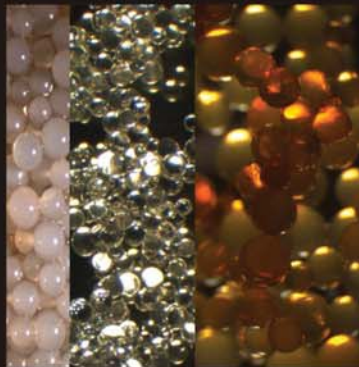
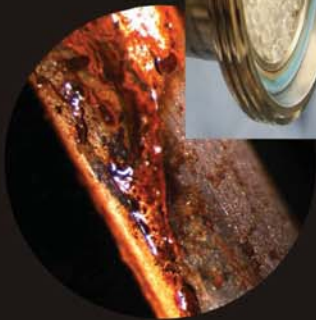
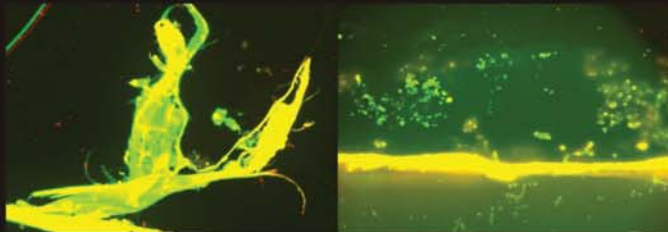
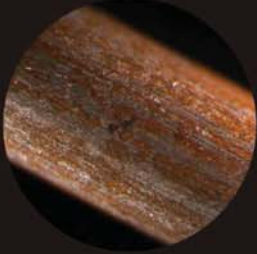
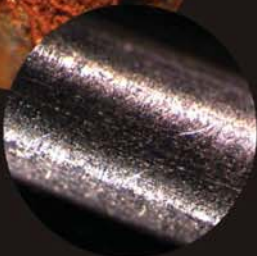
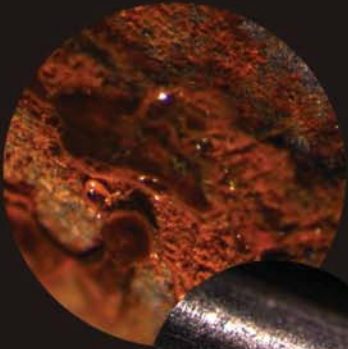


NATALIA A. HOOG

**STUB RESONATORS
TRANSMISSION
- LINE - BASED
WATER SENSORS**



STUB RESONATORS
TRANSMISSION – LINE – BASED WATER SENSORS

Natalia Alexandrovna Hoog

Graduation committee

Chairmen

Prof. Dr. Ir. P.M.G. Apers University of Twente

Prof. Dr. Ir. J.H.A. de Smit University of Twente

Promotor

Prof. Dr. Ir. A. van den Berg University of Twente

Assistant promoters

Dr. Ir. W. Olthuis University of Twente

Dr. H. Miedema WETSUS

Committee members

Prof. Dr. H. Morgan University of Southampton

Prof. Dr. Ir. P.J. French Delft University of Technology

Prof. Dr. Ir. F.B.J. Leferink University of Twente

Prof. Dr. Ir. F.E. van Vliet University of Twente

Dr. Ir. M.J.J. Mayer EasyMeasure

Stub resonators transmission – line – based water sensors
N.A. Hoog, PhD Thesis, University of Twente, The Netherlands

ISBN: 978-90-365-3705-6

Cover design by Valentin Dolgov: taigartgallery, Tomsk, Russia

Copyright © N.A. Hoog, Enschede, 2014
All rights reserved.

Printed by: Gildeprint Drukkerijen - The Netherlands

STUB RESONATORS
TRANSMISSION – LINE – BASED WATER SENSORS

DISSERTATION

to obtain

the degree of doctor at the University of Twente,

on the authority of the rector magnificus,

Prof. Dr. H. Brinksma

on account of the decision of the graduation committee,

to be publicly defended

on Friday the 12th of September 2014 at 12:45

by

Natalia Alexandrovna Hoog

born on the 25th of January 1980

in Shevchenko, USSR

This dissertation has been approved by the promotor

Prof. Dr. Ir. A. van den Berg

The BIOS Lab-on-a-chip group,
MESA+ Institute for Nanotechnology,
University of Twente, The Netherlands

*To my husband, Richard Hoog,
who has been a great source of motivation and inspiration for me...*

Table of Contents

Chapter 1: General Introduction and Thesis Outline	10
Chapter 2: On-line fingerprinting of fluids using coaxial stub resonator technology	24
Chapter 3: Modeling and Simulations of the Amplitude-Frequency Response of Transmission Line Type Resonators Filled with Lossy Dielectric Fluids	52
Chapter 4: On - line Method for Assessing the Ethanol Content of Solutions Using Coaxial Stub Resonator Technology	88
Chapter 5: Stub Resonators for On - line Monitoring Early Stages of Corrosion	100
Chapter 6: On - line Monitoring of Biofouling Using Coaxial Stub Resonator Technology	142
Chapter 7: A Coaxial Stub Resonator-Based Sensor for the On-line Monitoring of the Loading of Ion Exchange Resins	196
Chapter 8: General discussion and perspectives	238
Summary	257
Samenvatting	259
List of publications and patents	262
Acknowledgments	264
About the author	269



Leeuwarden



Chapter 1

General Introduction and Thesis Outline

Abstract

The research presented in this thesis describes practical investigations in using stub resonator (as a transmission line) technology for different (on-) inline sensor applications in the field of water technology. In addition, a substantial part of the research has been devoted to provide an adequate theoretical description of transmission line based sensors. The main purpose of the project was to come up with the conceptual proof of principle for using this technology for a large variety applications, ranging from fluid composition (ethanol content of fluids) and surface modification (corrosion detection (onset) and biofouling) to the chemical adsorption capacity (loading) of ion exchange resins. The Introduction gives an overview of basic principles of on-line monitoring dielectric properties of fluids, the role of dielectrometry and finally the potential role of stub resonators. The introduction concludes with summarizing the research objectives and an outline of the subsequent chapters of the thesis.

1.1 On-line monitoring of fluids

An old and well-known English proverb says: “forewarned is forearmed”. This wisdom is not less true in the world of sensing than it is in daily life. But how applicable it might be, one key aspect is implicitly assumed but certainly not explicitly stated. The factor time! Only if the information comes in on time can appropriate action be undertaken. In the context of sensors, this statement translates into the need for in-line and on-line sensing devices that allow continuous monitoring. Only then are the benefits optimal. Examples of successful on-line sensing that substantially improved the production process can be found in the dairy industry where on-line light scattering sensors monitor cheese manufacturing [1]. As for clinical applications, one can think about how on-line glucose level monitoring really improved the life of diabetes [2].

The water sector industry, the context of my research, can also benefit enormously from on-line sensing devices, also because the ever increasing demand for water of high quality [3-4]. Lots of effort is indeed devoted to develop a new generation of sensors, including those possessing software for advanced modeling and statistical methods.

There is no single, generic measure of water quality. For one thing, how do we define water quality? From the practical point of view, quality can only refer to parameters that can be measured. The parameters of water that can be tested fall in three categories:

physical characteristics: e.g., temperature, color, suspended solids and turbidity;

chemical characteristics: e.g., nutrients, minerals, metal ions and oxides, oxygen, organic compounds and a wide range of pollutants (e.g., pesticides, hydrocarbons, pharmaceuticals etc.);

biological characteristics: e.g., all types of bacteria, protozoa, parasites, algae, invertebrates, plants and other organisms.

The traditional method of monitoring water is one of collecting samples, taking them to a lab and perform the analysis. However, this procedure is laborious and thus expensive. The future is definitely for robust (on-) and in-line sensors. The water sector starts to realize this as well and an overview of currently existing on-line monitoring technologies for water can be found for instance in [5 - 6]. Whatever new type of sensor one intends to design and develop for the water industry, crucial criteria for all of them are an optimized geometry, easy access to data, low cost and low maintenance, and indeed on-line.

The main goal of these is to use the same type of sensing platform for different applications whether it aquatic quality monitoring, monitoring of water distribution systems, and/or fouling monitoring. In addition, an ideal sensor should obey the unifying principle of design, implying that one and the same design can be used for different applications [7].

1.2 Role of a physics based sensor in the water industry

According to [8], the definition of a physics based sensor is a device that provides information about a physical property of a system. Examples of physics based sensors are for instance those used to measure temperature or pressure [10-12]. Note that the definition categorizes on the nature of the parameters to be measured rather than on the application. Following this line of thought, the stub resonator discussed in Chapter 4 of this thesis used to determine the ethanol content of fluids by measuring its dielectric properties (physical parameter) is definitely a physical sensor even though the purpose of the sensor is to measure fluid composition, more a chemical than physical property of the system.

The two parameters defining the dielectric properties of a fluid are (complex) dielectric permittivity ϵ_r and the dielectric loss tangent $\tan\delta_{eff}$. The general expression of the complex dielectric permittivity of an isotropic material is given by [13]:

$$\epsilon_r = \epsilon_{re} - j\epsilon_{im} \quad (1)$$

$$\tan\delta_{eff} = \frac{\omega\epsilon_{im} + \sigma}{\omega\epsilon_{re}} \quad (2)$$

where ϵ_r [-] is the relative complex permittivity, ω the angular frequency [rad/s], σ the conductivity [S/m], ϵ_0 the permittivity of vacuum ($=1/(\mu_0 \cdot c)^{-1/2} \approx 8.85 \cdot 10^{-12}$ F/m) and $\tan\delta_{eff}$ [-] the dielectric loss tangent associated with all dielectric losses apart from those due to conductivity.

Dielectric properties can be assessed by studying the response of the system by exposing it to well-defined electric field conditions evoked by applying alternating current (AC) of given frequency. The sensitivity of this class of sensors depends in general to a large extent on dielectric properties and the geometry of the system, e.g., the geometry of the electrodes and the distance between them. This dependence thus allows optimization of the sensor for these parameters. Even though there are thus certain design requirements, the type of sensor described in this thesis offer a large degree of freedom. The main aim of my research was to design a sensor platform that can be used for several applications, instead of a sensor for just one parameter. The results show the versatility of the technology as the presented applications range from the determination of fluid composition and ion exchange loading to monitoring corrosion and biofilm formation. The next section discusses several examples of sensors that measure the dielectric properties of fluids.

1.3 Dielectrometry methods

Dielectrometry refers to dielectric spectroscopy techniques that measure changes of different physical parameters of a polar material, like polarization, permittivity, and conductivity, in response to an AC current, at one or a range of frequencies [14-15]. Many sensors rely on dielectrometry and their applications can be found in many different fields, among them fluid properties [15 - 22].

The two types of dielectrometry-based sensors currently most widely used are based on either capacitive measurements [23] or microwave technology, using sections of transmission lines or waveguides as sensitive elements. Both technologies will be discussed briefly.

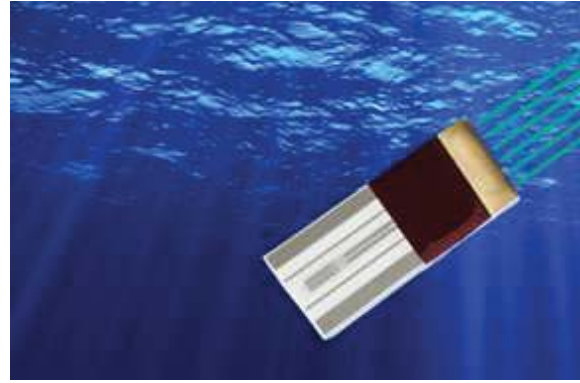
Capacitive measurements to determine dielectric properties

The easiest way to convert a measured capacitance into an informative signal is connecting the sensitive element to an inductor and measuring the resonant frequency of the obtained resonant circuit. The main two advantages of these sensors are their accuracy and the fact that they represent a non-invasive method of measuring [24]. The best-known examples of capacitive sensors are the parallel-plate capacitor and the coaxial cylindrical capacitor. However, due to the high impedance of the capacitive element, the resonant frequency of these systems is very sensitive to errors caused not only by the finite resistance of the fluid to be measured but in addition also to other sources of error, e.g., the parasitic capacitance of all elements comprising the measuring circuit. The total capacitance of the system can easily be of the same order of magnitude as this parasitic capacitance of the measuring circuit. As a result, the main disadvantage of the capacitive sensor that its working range is limited to low frequencies [25].

Despite this disadvantage, the water sector makes use already of existing commercially available capacitive sensors from e.g., BEDIA and IST AG Innovative Sensor Technology (Fig. 1.).



Capacitive Level Sensor NR160 is designed to monitor liquids from BEDIA [26].



Conductivity sensor from IST AG Innovative Sensor Technology [27]

Fig. 1. Examples of commercial available sensors based on the capacitive measurements.

Microwave technology based on transmission lines to determine dielectric properties

Transmission line based microwave technology to determine the dielectric properties of fluids is based on measuring the reflection coefficient at a defined reference plane, usually at the interface of the test dielectric. Advantages of this technology is the low dependence of the resonant frequency on measuring circuit parameters, a high resolution due to the high frequencies applied and, finally, the high absolute sensitivity [28]. Disadvantages are the rather complex measuring setup, implying high cost of the required equipment.

1.4 Motivation for this thesis research

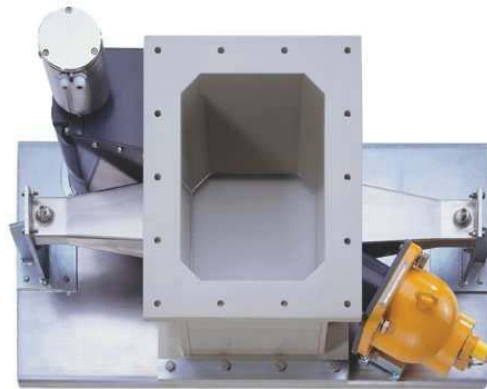
The aim of the study presented here was to investigate the feasibility of a new type of sensor for the finger printing of water based on a quarter or half wave coaxial stub resonator with the water to be investigated present as dielectric between its two electrodes. The sensor should have high accuracy and the cost price should be low (enough). Furthermore, the sensor was assumed to operate in- and on-line.

Most important advantage of sensors based on the concept of transmission line technology is their broad frequency range of operation, i.e., from low frequency to frequencies in the microwave range. In addition, the attenuation properties of stub resonators can be measured as well over a broad frequency range. Because of this the signal response can be presented as so-called amplitude – frequency (AF) plots. The AF plot provides information about the resonance frequency as well as the quality factor of the resonator, both related to the composition of the fluid sample applied as dielectric. This type of sensor thus offers a, from the electronics point of view, an easy undemanding way to gain information of the dielectric properties of a fluid without the need for chemical modification or physical invasion.

Fig. 2 shows two commercially available sensors for application in the water sector.



The Stevens Hydra Probe represents the advanced and robust soil moisture sensor from STEVENS [29].



Microwave Moisture Analyzer MicroPolar LB 567 / LB 568 from BERTHOLD TECHNOLOGIES GmbH & Co. KG [30]

Fig. 2. Examples of commercial available sensors based on the microwave technology.

1.5 Modeling of transmission lines

Modeling the behavior of transmission line type of sensors requires the theoretical description over a rather broad frequency range of both the resonance frequencies (resonances) and total attenuation (losses). For an ideal resonator, i.e., one without any losses [31], the resonance frequencies f_{res} of an open ended ($\lambda/4$) and closed ended ($\lambda/2$) resonator are given by Eqs. 3a and 3b, respectively.

$$f_{res} = \frac{2n-1}{2 \cdot \pi \cdot \sqrt{LC}} = \frac{c \cdot (2n-1)}{4l \sqrt{\epsilon_{re} \epsilon_0 \mu_{re} \mu_0}} \quad (3a)$$

$$f_{res} = \frac{n}{2 \cdot \pi \cdot \sqrt{LC}} = \frac{c \cdot n}{2l \sqrt{\epsilon_{re} \epsilon_0 \mu_{re} \mu_0}} \quad (3b)$$

where

n , the order number of f_{res} (Hz);

l , the length of the resonator (m),

c , speed of light in vacuum (m/s);

μ_0 , magnetic permeability of free space (vacuum permeability) ($\text{H} \cdot \text{m}^{-1}$): $\mu_0 = 4\pi \cdot 10^{-7}$;

μ_r , relative magnetic permeability (-);

ϵ_0 , dielectric permittivity of free space (vacuum permittivity) ($\text{F} \cdot \text{m}^{-1}$): $\epsilon_0 = 1/(\mu_0 \cdot c)^2$.

In case a transmission line based sensor, i.e., a stub resonator as shown in Fig. 3, is connected to a spectrum analyzer with tracking generator, an electrical circuit equivalent shown in Fig. 3 is obtained

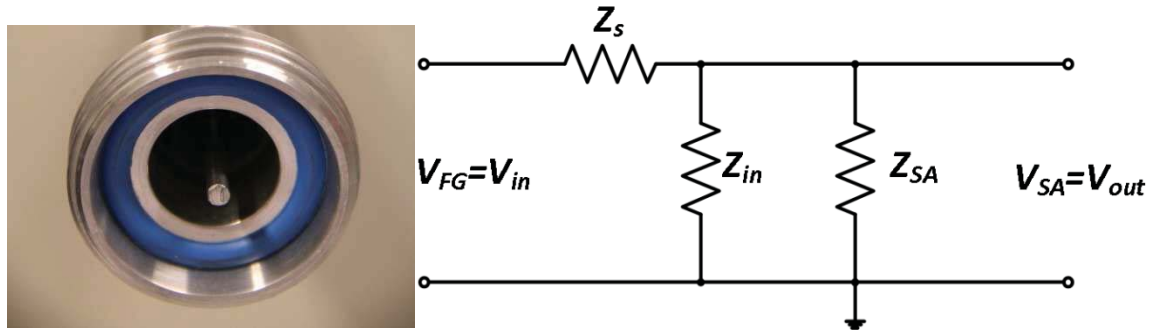


Fig. 3. Photo of the coaxial stub resonator showing inner and outer conductor and the equivalent electric circuit used for most of the modeling presented in this thesis.

A typical response curve of the sensor system in Fig. 3, is shown in Fig. 4.

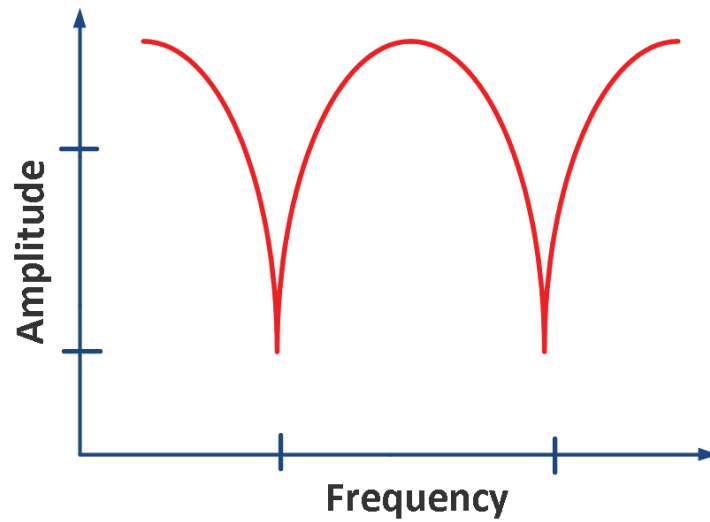


Fig. 4. Schematic AF response of a transmission line based sensor showing two resonances.

The AF response in figure X is affected by sensor geometry, ohmic losses in the conductors of the resonator and the complex dielectric properties of the (composite) dielectric material in the sensor. In a nutshell, changes in the real part of dielectric permittivity of the dielectric between inner and outer conductors result in a shift of the resonant frequency of the resonator i.e., a shift of the minima in the AF plot towards higher or lower frequencies. Ohmic losses in the conductors and dielectric losses result in a lower quality factor of the resonances i.e., in “broadening of the AF response curves and a “shift of the minima in the AF response curves” towards higher amplitude and to some extent, also in a shift of the resonant frequencies.

Extensive modeling of a transmission line based sensor, including all losses in the system, opens possibilities to relate measured changes in the AF plot of a resonator filled a fluid to a change of the properties of that fluid.

Transmission line behavior suffers from losses of the following nature [31]:

$$\alpha_{total} = \alpha_C + \alpha_D + \alpha_G + \alpha_R \quad (4)$$

where

α_C , attenuation due to properties of metal (Np/m) or (dB/m);

α_D , attenuation due to dielectric loss tangent (Np/m) or (dB/m);

α_G , attenuation due to conductivity (Np/m) or (dB/m);

α_R , attenuation due to radiation (Np/m) or (dB/m).

In a model predicting the dielectric properties of lossy fluids all these different types of losses have to be taken into account. However, in the models presented in this thesis the attenuation due to radiation α_R was excluded because of its very low contribution to the total loss.

As for the modeling, different models can be distinguished. As shown in Fig. 5, the extensive model applied in this thesis [32, 33] covers both lumped element modeling [34], applicable only for a single resonance frequency (resonance) [35], and a modeling of transmission lines with low loss [31].

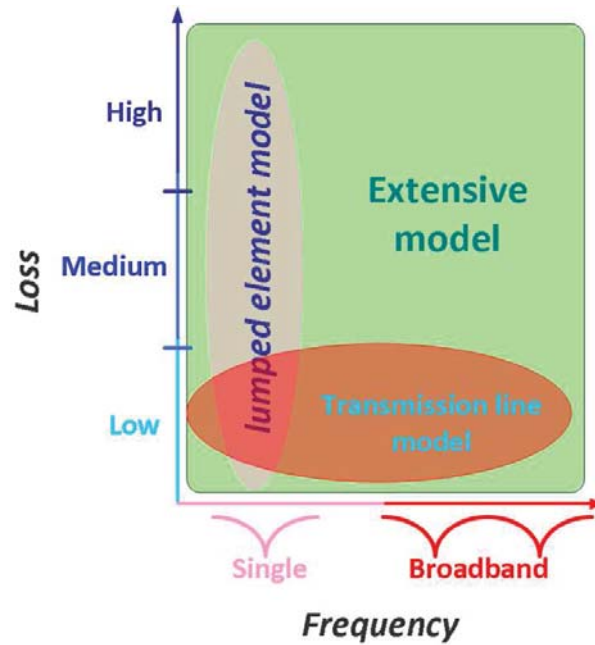


Fig. 5. The schematic overview of the problem in modeling of lossy transmission lines.

1.6 Research objectives

The research presented here aimed the following objectives (in order of the subsequent chapters in this thesis):

- Demonstrate the proof-of-principle of using transmission line based sensors for assessing the dielectric properties of fluids.
- Providing a theoretical description of transmission line behavior, predicting the dielectric properties of fluids from experimentally obtained AF plots.
- Extensive modeling of transmission line based sensors and validation of the model with experiments.
- Demonstrate the ability of the sensor to monitor the content of organic mixtures.
- Explore the possibility to use the sensor as an early warning system for corrosion detection.
 - Investigate the feasibility of the sensor to monitor the onset of biofilm growth.
 - Investigate the feasibility of the sensor to monitor the load degree of ion exchange resin columns.
- Application of the extensive model for the sensor applications investigated i.e., to explain and quantify the effects of corrosion, biofilm formation and loading of ion exchange resin on the sensor response.

1.7 Outline of the thesis

Chapter 2 shows the proof-of-principle of a coaxial stub resonator to assess the dielectric properties of fluids.

Chapter 3 deals with modeling and simulations of the amplitude-frequency response of transmission line type resonators filled with lossy dielectric fluids.

Chapter 4 demonstrates the ability of the sensor evaluate bulk solvent properties of ethanol-containing fluids.

Chapter 5 provides the proof-of-principle to apply the sensor for (early stages) of corrosion formation.

Chapter 6 demonstrates that coaxial stub resonators can be used to detect early stages of biofilm formation.

Chapter 7 shows that the sensor can be applied to measure the load degree of ion exchange resin with humic acids.

Chapter 8 discusses the results obtained in a wider context and places the findings into perspective and /or recommendations for further research to further develop stub resonator technology.

1.8 References

1. C.C. Fagan, M. Leedy, M. Castillo, F.A. Payne, C.P. O'Donnell, D.J. O'Callaghan, Development of a light scatter sensor technology for on-line monitoring of milk coagulation and whey separation, *Journal of Food Engineering*, Volume 83, Issue 1, November (2007), pp. 61-67, ISSN 0260-8774, <http://dx.doi.org/10.1016/j.jfoodeng.2006.12.014>.
2. I.B. Hirsch, D. Armstrong, R.M. Bergenstal, B. Buckingham, B.P. Childs, W.L. Clarke, A. Peters, H. Wolpert, Clinical application of emerging sensor technologies in diabetes management: consensus guidelines for continuous glucose monitoring (CGM), *Diabetes Technol Ther.* 2008 Aug;10(4):232-44; quiz 245-6, <http://dx.doi.org/10.1089/dia.2008.0016>.
3. EU. 2000. Water Framework directive. In UNION TEPATCOTE, ed. Official Journal L 327, pp 1-73.
4. <http://dwi.defra.gov.uk/stakeholders/legislation/index.htm>
5. M.V. Storey, Br. van der Gaag, B.P. Burns, Advances in on-line drinking water quality monitoring and early warning systems, *Water Research*, Volume 45, Issue 2, January 2011, Pages 741-747, ISSN 0043-1354, <http://dx.doi.org/10.1016/j.watres.2010.08.049>.
6. W. Bourgeois, J.E Burgess and R. M Stuetz, Review On-line monitoring of wastewater quality: a review, *Journal of Chemical Technology & Biotechnology*, John Wiley & Sons, Ltd., 76, pp. 337-348, 2001 <http://dx.doi.org/10.1002/jctb.393>
7. L.A O Rocha, S. Lorente, Ad. Bejan, *Constructal Law and the Unifying Principle of Design*, Springer New York; 2013 edition (December 3, 2012)-320 pages, ISBN 978-1-4614-5048-1.
8. Ad. Hulanicki, S. Glab and F. Ingman, Chemical sensors: definitions and classification, *Pure Appl. Chem.*, 1991, Vol. 63, No. 9, pp. 1247-1250, <http://dx.doi.org/10.1351/pac199163091247>
9. J.R. Stetter, W.R. Penrose, Sh. Yao, Sensors, Chemical Sensors, Electrochemical Sensors, and ECS, *Journal of The Electrochemical Society*, 150 (2) S11-S16 (2003).
10. B. Jakoby, M. J. Vellekoop, Physical sensors for water-in-oil emulsions, *Sensors and Actuators A: Physical*, Volume 110, Issues 1-3, 1 February (2004), Pages 28-32, ISSN 0924-4247, <http://dx.doi.org/10.1016/j.sna.2003.08.005>.
11. <http://www.sengenuity.com/viscositysensor.html>
12. <http://www.analog.com/en/mems-sensors/digital-temperature-sensors/products/index.html>
13. J. Krupka, Frequency domain complex permittivity measurements at microwave frequencies, *Measurement Science and Technology*, 17 R55-R70, 2006 doi: <http://dx.doi.org/10.1088/0957-0233/17/6/R01>
14. J. D. Menczel, R. Bruce Prime, *Thermal Analysis of Polymers: Fundamentals and Applications*, ISBN: 978-0-471-76917-0, pp. 696, Copyright © 2009 by John Wiley & Sons, Inc.
15. K. Asami, T. Yonezawa, H. Wakamatsu, and N. Koyanagi, *Dielectric Spectroscopy of Biological Cells, Bioelectrochemistry and Bioenergetics*, vol. 40, no. 2, pp. 141-145, Aug. (1996).
16. D.D. Denton, J. B. Camou, and S. D. Senturia, Effects of Moisture Uptake on the Dielectric Permittivity of Polyimide Films, *Proceedings of the 1985 International Symposium on Moisture and Humidity*, 1985, pp. 505-513.
17. V. Mamishev, Y. Du, B. C. Lesieutre, and M. Zahn, Measurement of Moisture Spatial Profiles in Transformer Pressboard, *IEEE Conference on Electrical Insulation and Dielectric Phenomena*, (1998), pp. 323-326.
18. H. Beving and G. Eriksson, *Dielectric-Spectroscopy of Human Blood*, *European Journal of Surgery*, pp. 87-89, (1994).
19. T.Yu. Shchegoleva, V. G. Kolesnikov, Research of controlling connection systems of cell macromolecular mechanisms by method of dielectrometry in the MM range of radiowaves, *Physics and Engineering of Millimeter and Submillimeter Waves*, 1998. MSMW '98. Third International Kharkov Symposium , vol.2, no., pp.760,762 vol.2, 15-17 September (1998): doi: 10.1109/MSMW.1998.755586
20. V. Modenov, Waveguide-resonance method of dielectrometry, *Microwaves and Radar*, 1998. MIKON '98., 12th International Conference on , vol.2, no., pp.648,652 vol.2, 20-22 May (1998): doi: 10.1109/MIKON.1998.740940
21. M.V Zubez, V.G. Kolesnikov, Development of non-destructive methods of semen quality control, *Physics and Engineering of Millimeter and Sub-Millimeter Waves*, 2001. The Fourth International Kharkov Symposium on , vol.2, no., pp.926,928 vol.2, 2001: doi: 10.1109/MSMW.2001.947360

22. G.A. Alexeyev, Impedance dielectrometry of a dissipative medium, Microwave and Telecommunication Technology, 2001. CriMiCo 2001. 11th International Conference on , vol., no., pp.590,591, 14-14 Sept. (2001)
23. <http://www.capacitive-sensing.com/>
24. Application Note 380-1, Dielectric constant measurement of solid materials using the 16451B dielectric test fixture, Agilent literature number 5950-2390, September 1998
25. Basics of Measuring the Dielectric Properties of Materials - Application Note, Agilent literature number, May (2014).
26. http://radel.co.za/website/index.php?page=shop.browse&manufacturer_id=13&category_id=56&option=com_virtuemart&Itemid=57
27. <http://www.ist-ag.com/>
28. Yu. N. Pchelnikov, Slow-Wave Structures-Based Method of Measurements, IEEE Transaction on Instrumentation and Measurement, Vol. 51, # 5, October (2002), pp. 891-896.
29. <http://www.stevenswater.com/>
30. <https://www.berthold.com/>
31. D.M. Pozar, Microwave Engineering, Wiley, 2004.
32. N.A. Hoog-Antonyuk, W. Olthuis, M.J.J. Mayer, H. Miedema, F.B.J. Leferink, A. van den Berg, Extensive Modeling of a Coaxial Stub Resonator for Online Fingerprinting of Fluids, Procedia Engineering, Volume 47, 2012, Pages 310-313, ISSN 1877-7058, <http://dx.doi.org/10.1016/j.proeng.2012.09.145>.
33. N.A. Hoog, M.J.J. Mayer, H. Miedema, W. Olthuis, F.B.J. Leferink, A. van den Berg, Modeling and Simulations of the Amplitude-Frequency Response of Transmission Line Type Resonators Filled with Lossy Dielectric Fluids, Sensors and Actuators A: Physical, Volume 216, 1 September (2014), pp. 147-157, <http://dx.doi.org/10.1016/j.sna.2014.05.006>.
34. O. Zinke, H. Brunswig, Hochfrequenztechnik 1, Hochfrequenzfilter, Leitungen, Antennen, 6. Auflage, Berlin: Springer 2000, pp. 86-88.
35. N.A. Hoog-Antonyuk, W. Olthuis, M.J.J. Mayer, D. Yntema, H. Miedema, A. van den Berg, On-line fingerprinting of fluids using coaxial stub resonator technology, Sensors and Actuators B: Chemical, Volume 163, Issue 1, 1 March (2012), pp. 90-96, ISSN 0925-4005, <http://dx.doi.org/10.1016/j.snb.2012.01.012>.
36. Jia-Sh. G. Hong, M.J. Lancaster, Microstrip Resonators for RF/Microwave Application, John Wiley & Sons, pp. 488, (2004).



Grenoble, France, Workweek BIOS, Spring 2012



Chapter 2

On-line Fingerprinting of Fluids Using Coaxial Stub Resonator Technology

Abstract

Here we demonstrate the proof-of-principle of a coaxial stub resonator to assess the dielectric properties of fluids. This radio-frequency spectroscopy method is based on coaxial stub technology and comprises quarter wave length open-ended resonators that are filled with a liquid sample as dielectric between inner and outer conductor. Changes in the dielectric properties of the liquid sample result in changes in the electric properties of the resonator, e.g., its resonance frequency and quality factor. In addition to a batch resonator, results obtained with a flow-through resonator indicate that the concept can be further developed into a cost-efficient and low-maintenance sensor for the on-line fingerprinting of the dielectric properties of fluids, such as drinking or waste water, ethanol and glycerol.

This chapter is based on the article published as:

N.A. Hoog-Antonyuk, W. Olthuis, M.J.J. Mayer, D. Yntema, H. Miedema, A. van den Berg, *On-line fingerprinting of fluids using coaxial stub resonator technology*, *Sensors and Actuators B: Chemical*, Volume 163, Issue 1, 1 March 2012, Pages 90-96, <http://dx.doi.org/10.1016/j.snb.2012.01.012>.

2.1 Introduction

In drinking water, surface water, waste water and industrial process fluids, a large number of toxic or otherwise undesired components can be present at a wide range of concentration levels. In order to safeguard water quality, the early detection of pollutants in water is mandatory. However, currently existing (bio) chemical detection methods are labor-intensive and by implication expensive. Even more important, all these methods are off-line providing a momentary signature only. The aim of the present study was to develop a fingerprinting sensing device that operates on-line instead and that is based on recording a physical rather than a (bio) chemical parameter representative for water quality.

Examples of physical parameters to monitor and track the composition of a fluid are those related to its dielectric properties, e.g., dielectric permittivity and loss tangent. This can be achieved by using high or microwave frequency techniques with capacitors or (coaxial) resonators as sensitive elements [1 - 10]. Both techniques will now be discussed briefly.

In a capacitance-based measurement, the capacitance (as a sensing element) can be connected to an inductor to create a resonant circuit with a characteristic resonant frequency. However, due to the high impedance of the capacitive element, the resonant frequency of the circuit is rather sensitive to errors caused not only by the finite resistance of the monitored liquid, but also, for instance, by the parasitic capacity of all elements forming the measuring circuit. As a result, the total capacitance of the system can be of the same order of magnitude as the parasitic capacitance of the measuring circuit, especially at high frequencies [11, 12].

Microwave technology to determine the dielectric permittivity of a fluid is based on measuring the reflection coefficient at a defined reference plane, usually the one at the interface of the dielectric to be investigated. Advantages of these microwave based systems are a high resolution resulting from the high frequencies applied and a high absolute sensitivity [13, 14].

Apart from these advantages, there are some disadvantages such as the complicated and, consequently, high construction costs, off-line sample analysis and, since the measurements are based upon reflection, the prerequisite that at the micro scale the test solution can be considered homogeneous [15 - 16]. Other studies assess dielectric properties of fluids in stub resonators through so-called scattering or S-parameter measurements requiring relatively expensive equipment [17 - 22]. Additionally, the interpretation of S-parameter models is less straight forward which complicates the analysis [23].

Among the different techniques a cavity perturbation technique using split-ring resonators can be shown as an example of the sensor based on the microwave theory. The main advantage of ring resonators is the lack of radiation loss [24]. But this benefit comes

with a disadvantage as well; measuring the dielectric constant using microstrip ring resonators is limited to materials having low dielectric constants. The reason is that the cavity perturbation method is inherently limited to materials having low dielectric constants (citation) [25]. Obviously, with a water epsilon of 80, this technology is less applicable to measure on watery solutions.

The present contribution deals with the feasibility of a quarter wave length open ended coaxial stub resonator as a flow-through and on-line sensing element for tracking changes in the dielectric properties of a fluid. The fluid is present as the dielectric between the inner and outer conductor of the resonator. This technique is less sensitive to errors as compared to the previously mentioned reflection techniques. On-line analysis is realized by pumping the sample continuously through the resonator using an inlet and outlet for the fluid to be investigated. Since the sensor system can be designed such that the fluid volume between inner and outer conductor is relatively large, it is envisaged that the sensor can also be applied for analysis of heterogeneous mixtures. In principle, the concept outlined here creates the possibility for on-line complex dielectric permittivity measurements in resonant circuits at high frequencies with a high quality factor, i.e., at radio frequencies between 3 and 30 MHz (HF), at frequencies in the range of 30 MHz to 300 MHz (VHF) and at frequencies in the microwave range between 300 MHz and 300 GHz (both UHF and EHF) [26]. The on-line flow-through system enables fast, cost-efficient sample analyses.

2.2 Sensing technique

Fig. 1 gives a schematic overview of the coaxial resonator described in this study and its connection to the coaxial transmission line between the function generator (FG) and the spectrum analyzer (SA).

The sensing system comprises a function generator (FG), with an internal output resistance of $Z_s=50 \Omega$, connected to a spectrum analyzer (SA), with an internal input resistance of $Z_{SA}=50 \Omega$, both connected by a coaxial transmission line with a characteristic impedance of 50Ω . To this coaxial transmission line, a quarter wave length open ended coaxial stub resonator (RE) is connected. The advantage of an open ended coaxial stub resonator over a closed ended one is that its base resonant frequency is a factor of 2 lower. As a result, the required length of the resonator can be reduced without compromising the frequency range of the response. The resonator consists of an inner conductor positioned in the center of a hollow outer conductor. The sample to be analyzed is present as dielectric between inner and outer conductor.

In addition to Fig. 1 Fig. 2 gives a detailed schematic overview of the coaxial stub resonator itself.

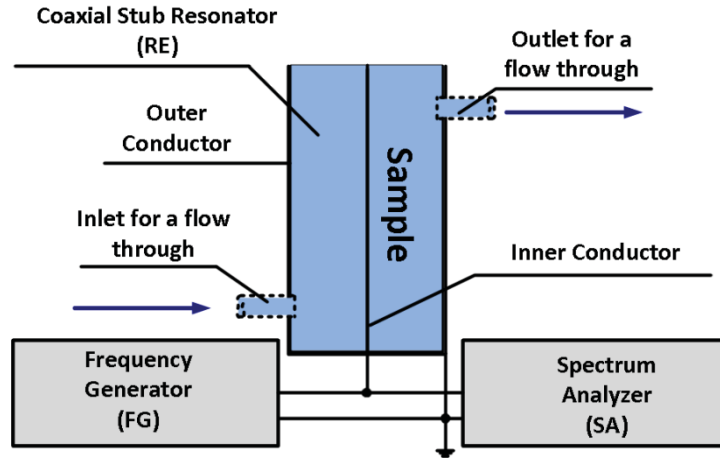


Fig. 1. Basic principle of the coaxial stub resonator sensing system consisting of a function generator (FG), a spectrum analyzer (SA) and the coaxial resonator (RE). The dotted structures indicate the inlet and the outlet of the flow-through resonator. Apart from lacking the in- and outlet, the design of the batch resonator is essentially the same.

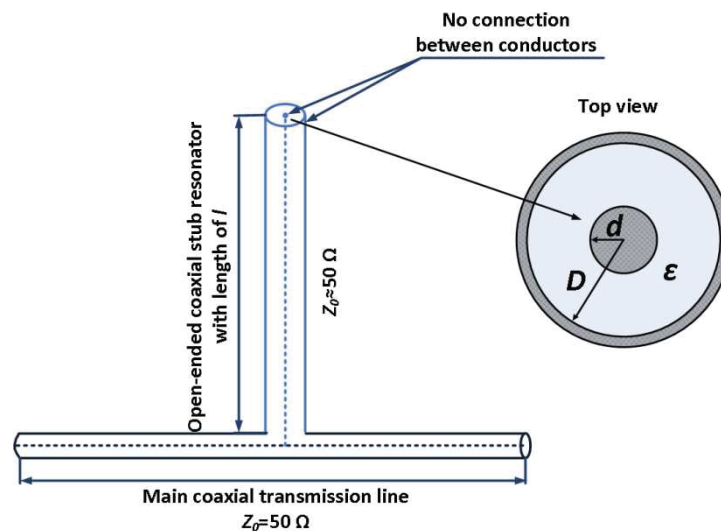


Fig. 2. The schematic representation of the open ended coaxial stub resonator of length l and its connection to the transmission line between function generator FG and spectrum analyzer SA. Z_0 is the characteristic impedance of the transmission line and of the coaxial stub. Note that the inner and outer conductors at the end of the coaxial stub are not connected. The inset shows a top view of the coaxial stub.

Fig. 3 shows the electrical equivalent circuit of the device shown in Figs. 1 and 2, with the quarter wave length coaxial stub resonator represented as a lumped element series resonant circuit. As shown and discussed later on, Fig. 3 presents an adequate circuit analog of our device for frequencies close to the base frequency of the resonator [27].

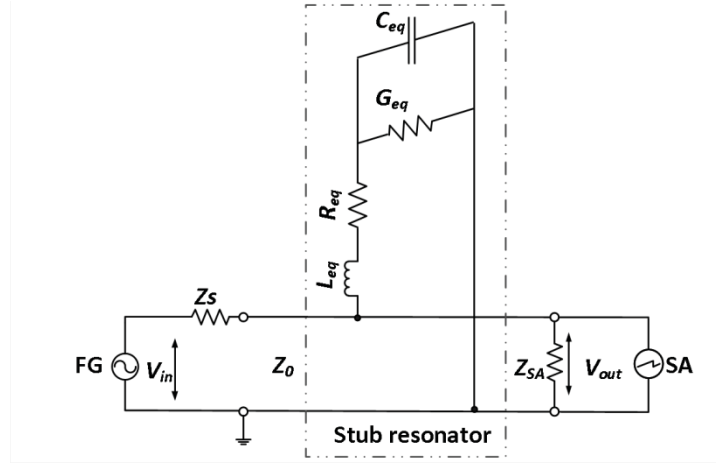


Fig. 3. The electrical equivalent circuit of the sensor system of Figs. 1 and 2. Parameters L_{eq} , C_{eq} , G_{eq} and R_{eq} represent the lumped element inductance of the resonator, the lumped element capacitance of the resonator, the conductivity of the dielectric and losses due to the skin effect in the inner and outer conductors of the coaxial resonator, respectively.

It is noted that a lumped element circuit as shown in Fig. 3 predicts one resonant frequency only, whether that is the first or one of the higher resonances. In contrast, the coaxial sensing element records all resonances within a defined frequency range. Even though the model used can be extended to account for these odd resonances, using the Telegrapher's equations [28 - 32], such aim was considered beyond the scope of the present study.

The propagation velocity of electromagnetic waves is affected by the dielectric between the inner and outer conductor of the resonator [28 - 32]. Therefore, the resonant frequency f_{res} of a quarter wave length open ended coaxial resonator with effective length l is given by Eq. 1:

$$f_{res} = \frac{c \cdot (2n - 1)}{4l \sqrt{\epsilon_{re} \epsilon_0 \mu_{re} \mu_0}} \quad (1)$$

where

f_{res} , resonance frequency (Hz);

c , speed of light in free space (m/s);

l , length of coaxial resonator (m);

μ_r , relative magnetic permeability (-);

μ_0 , magnetic permeability of free space (vacuum permeability) ($\text{H} \cdot \text{m}^{-1}$): $\mu_0 = 4\pi \cdot 10^{-7}$;

ϵ_{re} dielectric co dielectric permittivity: real part of the complex dielectric permittivity
 $\epsilon_r = \epsilon_{re} - j\epsilon_{im}$ where ϵ_{im} represents the imaginary part of ϵ_r : (-);

ϵ_0 , dielectric permittivity of free space (vacuum permittivity), $\epsilon_0=1/(\mu_0 \cdot c)^{1/2}$ (F·m⁻¹);

n , resonance number.

By filling the resonator of Fig. 1 with a fluid sample, and making an amplitude – frequency (AF) plot using the frequency generator and spectrum analyzer, the base resonant frequency as well its odd resonances can be determined from the minimums in the plot. Substitution of the experimentally determined value of f_{res} and the stub resonator length l in Eq. 1 enables the calculation of the relative dielectric permittivity of the fluid sample assuming $\mu_r=1$.

Besides the resonant frequency, the shape of the amplitude – frequency plot also provides information on the dielectric losses in the fluid between inner and outer conductor G_{eq} and on the skin effect in the inner and outer conductors R_{eq} . In order to quantify the values of G_{eq} and R_{eq} near the base resonant frequency of the stub resonator, the transfer function V_{out}/V_{in} needs to be derived.

The inductance L , series resistance R , capacitance C and dielectric conductance G of a coaxial transmission line (all expressed per unit length) are given by [28, 32]:

$$L = \frac{\mu_0 \mu_r}{2\pi} \ln\left(\frac{D}{d}\right) + \frac{\mu_0 \mu_r}{2\pi} \sqrt{\frac{\rho}{2\omega \mu_0 \mu_r}} \left(\frac{1}{d} + \frac{1}{D}\right) \quad (2)$$

$$R = \frac{\rho}{2\pi \delta_s} \left(\frac{1}{0.5 \cdot D} + \frac{1}{0.5 \cdot d}\right) \quad (3)$$

$$C = \frac{2\pi \epsilon_0 \epsilon_{re}}{\ln(D/d)} \quad (4)$$

$$G = \omega \cdot C \cdot \tan \delta_{eff} \quad (5)$$

where

μ_r , relative magnetic permeability (-);

ω , angular frequency, $\omega=2\pi f$ (rad/s);

ω_0 , angular resonance frequency, $\omega_0=2\pi f_0$ (rad/s);

D , (inner) diameter of outer conductor (m);

d , (outer) diameter of inner conductor (m);

R_s , surface resistance of the metal, $R_s = \sqrt{\frac{\omega\mu_0\mu_r\rho}{2}} = \frac{\rho}{\delta_s}$ (Ω);

δ_s , depth of penetration, $\delta_s = \sqrt{\frac{2\rho}{\omega\mu_r\mu_0}}$ (m);

ρ , specific resistance of the metal, $\rho=1/\sigma$ ($\Omega\cdot\text{m}$);

σ , conductivity (S/m);

$\tan\delta_{eff}$, dielectric loss tangent (-).

For frequencies applied in this study ($f > 5$ MHz), the contribution of internal inductance to L is negligible [28]. Hence, starting from Eq. 2, the following approximation holds (Eq. 6):

$$L \approx \frac{\mu_0\mu_r}{2\pi} \ln\left(\frac{D}{d}\right) \quad (6)$$

Note that this approximation turns L into a frequency-independent parameter. The distributed parameters in Eqs. 3 - 6 can be related to the lumped element values L_{eq} , C_{eq} , G_{eq} and R_{eq} by comparing the general solution of the Telegrapher's equation for a quarter wavelength open ended coaxial stub with the solution for the lumped element model near the base resonant frequency f_{res} (Eqs. 7 - 10), [27]:

$$L_{eq} = L \cdot \frac{l}{2} \quad (7)$$

$$C_{eq} = C \cdot \frac{8l}{\pi^2} \quad (8)$$

$$G_{eq} = G \cdot \frac{8l}{\pi^2} \quad (9)$$

$$R_{eq} = R \cdot \frac{l}{2} \quad (10)$$

It is noted that the base resonant frequency of the quarter wave length coaxial stub can be derived directly from Eqs. 4 - 8 and the resonance criterion $LC=1/(\omega^2)$, which results from Eq. 1 for $n=1$.

For the transfer function, relating the voltage of the input signal supplied by the function generator V_{in} to the voltage of the output signal recorded by the spectrum analyzer V_{out} , the following relation is obtained (Eq. 11):

$$\frac{V_{out}(\omega)}{V_{in}(\omega)} = \frac{1/\left(\frac{1}{j\omega L_{eq} + 1/(j\omega C_{eq} + G_{eq}) + R_{eq}} + \frac{1}{Z_{SA}}\right)}{\left(Z_s 1/\left(\frac{1}{j\omega L_{eq} + 1/(j\omega C_{eq} + G_{eq}) + R_{eq}} + \frac{1}{Z_{SA}}\right)\right)} \quad (11)$$

where

V_{in} , voltage of the input signal supplied by FG (V);

V_{out} , voltage of the output signal recorded by SA (V);

Z_s , internal resistance of the frequency generator (Ω);

R_{eq} , resistance of the coaxial antenna, per unit length (Ω);

Z_{SA} , internal resistance of the spectrum analyzer (Ω).

For our fluid-filled coaxial stub resonator, the first step in the analysis to obtain the relative dielectric constant of the fluid is the determination of the resonant frequency of the AF plot using Eq. 1. The experimentally observed shape of the AF plot can be compared to model simulations using Eqs. 3 - 11. Since the AF plot renders the value of the dielectric constant the only remaining unknown parameters in Eqs. 3 - 11 are the values of G_{eq} and R_{eq} .

According to the lumped element circuit in Fig. 3, the total impedance Z_{tot} of the coaxial stub resonator is given by Eq. 12:

$$Z_{tot} = j\omega L_{eq} + \frac{1}{j\omega C_{eq} + G_{eq}} + R_{eq} \quad (12)$$

For the imaginary part of Z_{tot} i.e., $Im(Z_{tot})$ the following expression can be derived (Eq. 13):

$$\text{Im}(Z_{tot}) = \frac{G_{eq}(G_{eq}\omega L_{eq} + \omega C_{eq}R_{eq}) - \omega C_{eq}(1 - \omega^2 L_{eq}C_{eq} + R_{eq}G_{eq})}{G_{eq}^2 + \omega^2 C_{eq}^2} \quad (13)$$

At resonance, with $\omega = \omega_{res}$ and $\text{Im}(Z_{tot}) = 0$, ω_{res} can be expressed in terms of L_{eq} , C_{eq} and G_{eq} (Eq. 14):

$$\omega_{res} = \frac{1}{\sqrt{L_{eq}C_{eq}}} \sqrt{1 - G_{eq}^2 \frac{L_{eq}}{C_{eq}}} \quad (14)$$

For $\text{Re}(Z_{tot})$, the following expression can be derived (Eq. 15):

$$\text{Re}(Z_{tot}) = \frac{G_{eq}(1 - \omega^2 L_{eq}C_{eq} + R_{eq}G_{eq}) + \omega^2 C_{eq}(G_{eq}L_{eq} + C_{eq}R_{eq})}{G_{eq}^2 + \omega^2 C_{eq}^2} \quad (15)$$

Substitution of Eq. 14 into Eq. 15 provides the following expression for R_{tot} at resonance (Eq. 16):

$$R_{tot} = R_{eq} + \frac{G_{eq}L_{eq}}{C_{eq}} \quad (16)$$

At resonance, the electrical equivalent circuit of Fig. 3 is reduced to a simple resistive voltage divider (Fig. 5):

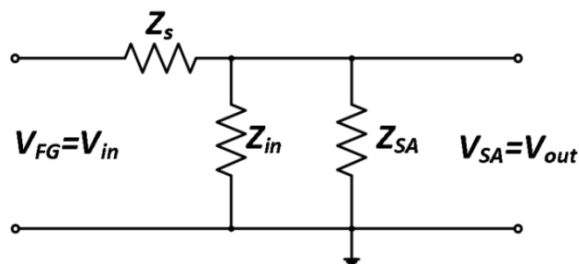


Fig. 4. Representation of the electrical equivalent circuit in Fig.3 at resonance as a simple resistive voltage divider.

Since the internal impedance of both the function generator and the spectrum analyzer equals 50Ω , the value of R_{tot} can be calculated from V_{out} and V_{in} at resonance by the use of equation (17).

$$R_{tot} = 50 \cdot V_{out} / (V_{in} - 2 \cdot V_{out}) \quad (17)$$

R_{eq} in Eq. 16 represents the series resistance in the resonant circuit caused, predominantly, by the skin effect in inner and outer conductor. The value of R_{eq} can be determined using Eq. 18 after constructing a second coaxial stub resonator but filled with air as dielectric and resonating at the same resonant frequency as the one filled with fluid sample. It is noted that the coaxial stub resonator filled with air is longer than the one filled with fluid since the relative dielectric constant of the fluid is larger than that of air.

Since the dielectric losses in air are negligible, i.e., $G_{eq}=0$, the total resistance $R_{tot}=R_{eq}$. The skin effect is proportional to the length of inner and outer conductor of the resonator. Since the two resonators, one filled with air, the other with fluid, resonate at the same frequency but have different length, $R_{eq(fluid)}$ needs to be corrected for the resonator length according to:

$$R_{eq(fluid)} = R_{eq(air)} \cdot l_{(fluid)} / l_{(air)} \quad (18)$$

Once the value of $R_{eq(fluid)}$ has been determined, the single unknown parameter left in Eq. 16 is the conductance G_{eq} , representing dielectric losses in the fluid between the inner and outer conductor of the stub resonator. The value of G_{eq} can now be determined from the AF plot obtained with the resonator filled with fluid and using Eqs. 16-18.

Finally, the dielectric loss tangent at resonance, describing the phase angle between the lumped element capacitor voltage and capacitor current is given by Eq. 19:

$$\tan \delta_{eff} = G_{eq} / (\omega \cdot C_{eq}) \quad (19)$$

Once the values of R_{eq} and G_{eq} have been determined, all parameters in Eqs. 2 - 11 are known. As a result, the AF plot can be simulated and compared to the one experimentally obtained.

2.3 Experimental

The experiments were performed with a HAMEG HMS3010 3 GHz Spectrum Analyzer with Tracking Generator, both with an internal resistance Z_s of 50 Ω . In order to check the internal resistance of the function generator, its output amplitude was measured with a high impedance oscilloscope to amount 1.34 V. Subsequently, the output was loaded with a 50 Ω resistor, resulting in output amplitude of 0.67 V. This result proves that the internal resistance of the internal frequency generator of the spectrum analyzer is indeed very close to 50 Ω . The interconnecting transmission lines have characteristic impedance Z_0 of 50 Ω .

For the experiments, two types of coaxial resonators were designed: a batch resonator and a flow-through resonator. Apart from the (in) ability of flowing through the measured solutions, both coaxial resonators are essentially of the same design but with different dimensions, as summarized in Table 1. When filled with the same dielectric solution and according to Eq. 1, both types of resonators have a different resonant frequency.

Table 1

Geometric parameters of the coaxial batch and flow-through resonators. The outer and the inner conductors of both resonators were made from copper.

Parameter	Flow-through resonator	Batch resonator
Length, l	1.01 (m)	$34 \cdot 10^{-2}$ (m)
Inner conductor diameter, d	$0.5 \cdot 10^{-3}$ (m)	$0.5 \cdot 10^{-3}$ (m)
Inner diameter of the outer conductor, D	$22.0 \cdot 10^{-3}$ (m)	$22.0 \cdot 10^{-3}$ (m)
Diameters of the fluid inlet and outlet	$7.0 \cdot 10^{-3}$ (m)	
Conductivity of copper, σ	$5.7 \cdot 10^7$ ($S \cdot m^{-1}$)	

Both inner and outer conductors are made of copper. The transmission lines were connected to the resonator by using SMA (SubMiniature version A) connectors with a total length of 20 mm.

To investigate the performance of both types of resonators, the following solutions were tested as dielectric between inner and outer conductor: demineralized water with a conductivity of $1 \cdot 10^{-4}$ S/m, ethanol (100% denatured with 2-Propanol 2.5%) supplied by BOOM B.V., glycerol (100%) supplied by VNR.

The characteristic impedance of the coaxial stub resonator equals to Eq. 20 (see also the Supplementary Information for a detailed discussion):

$$Z_0 = \frac{1}{2\pi} \sqrt{\frac{\mu_0 \mu_r}{\epsilon_0 \epsilon_r}} \ln\left(\frac{D}{d}\right) \quad (20)$$

The characteristic impedance of both resonators as calculated with Eq. 20 was 39.8 Ω for water, 72.3 Ω for ethanol and 55.5 Ω for glycerol. An inevitable consequence, and hence accepted compromise, of the range of characteristic impedance of the different solutions used (39.8-72.3 Ω) is that the resonator was not perfectly matched to the function generator, spectrum analyzer and transmission lines, all with an impedance of 50 Ω .

Experiments were performed at 20 °C and repeated 11 times. From the base frequency obtained for each experiment, the relative dielectric permittivity ϵ_r was calculated using Eq. 1. Subsequently, the mean value of ϵ_r was calculated for the set of 11 experiments. The experiments in the flow-through resonator were executed at recycling conditions i.e., by pumping the liquid under investigation from a 5 liter container through the vertically-positioned resonator in bottom-to-top direction and with the outflow returning into the feed container. In order to deal with the relatively high viscosity of glycerol, a Master flex peristaltic pump, model 77200-60 was used for this purpose.

It is noted that over time and depending on the dielectric and the process conditions, both the inner conductor and the outer conductor of the flow-through resonator may be covered by a thin layer of metal oxide. This effect was observed when the flow-through resonator was operated continuously with a copper inner conductor for a period of 1 month when filled with drinking water. In that particular case the resonator can be considered to be constructed with two concentric dielectrics: one dielectric of metal oxide around the inner conductor and the dielectric under investigation. It appears that, in this particular case, the small layer of metal oxide dielectric around the inner conductor may have a significant influence on the effective dielectric permittivity i.e., on the resonant frequency of the coaxial resonator. This problem can be solved by isolating the inner conductor with a thin inert coating and by correcting for the influence of this coating on the resonant frequency. Prior to all experiments reported in this contribution, both inner and outer conductors of the coaxial resonators were inspected to ensure that neither of them was coated by a small layer of metal oxide.

In order to check whether the measurements are influenced by coupling or radiation effects, the experimental set-up was placed in a Faraday cage with a characteristic size of 70.0 cm and a wall thickness of 3.0 mm. Based on a coaxial stub of 34.0 cm length, filled with demineralized water as dielectric, results were compared to those obtained without using a Faraday cage. It was found that, within experimental error, application of a Faraday cage did not result in a frequency shift whereas the difference in amplitude at the base frequency amounted to less than 4%. We therefore concluded that under the laboratory conditions applied measurements were free of environmental interferences.

2.4 Results and Discussion

Fig. 5 shows the AF plot for water, ethanol and glycerol as obtained with the batch resonator and the experimental set-up in Fig. 1.

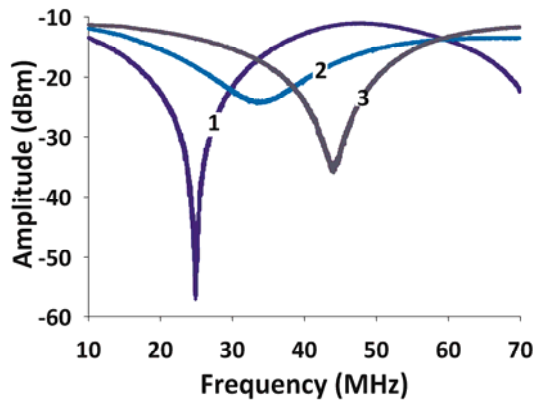


Fig. 5. AF plot for demineralized water (1), glycerol (2) and ethanol (3) as obtained with the batch resonator and the experimental set-up in Fig. 1. All experiments were executed at 20 °C.

Substitution of the obtained base resonant frequencies (24.8 MHz for water, 44.1 MHz for ethanol and 33.9 MHz for glycerol) into Eq. 1 results in dielectric permittivity values of re: $\epsilon_{water}=80.2\pm 0.9$ (78.76 (79.5) according to [34], $\epsilon_{ethanol}=25.4\pm 0.3$ (24.35 (25.13) according to [34] and $\epsilon_{glycerol}=41.8\pm 0.8$ (42.49) according to [34], with reported literature values given in between brackets. These results thus reveal that the batch resonator performs well with water, ethanol and glycerol as dielectrics. Resonance in all AF plots showed up as a minimum at a frequency predicted by reported values obtained with different experimental methods. We, therefore, conclude that it is technically feasible to determine the dielectric permittivity of a liquid by using this batch resonator.

As mentioned in the sensing technique section, the shape of the AF plots in Fig. 5 are mainly determined by the skin effect in inner and outer conductors of the coaxial stub resonator and by dielectric losses in the fluid between them. The AF plot of ethanol will further be investigated using the lumped element model described in section 2.2. In order to quantify the skin effect i.e., the value of R_{eq} , a coaxial stub resonator with a length of 1.70 m was constructed (see also Supplementary Information). The other characteristic dimensions of the stub resonator, such as construction material, diameter of the inner and outer conductors were identical to those listed in Table 1. Air was applied as dielectric between inner and outer conductor. The length of the coaxial stub resonator was chosen as such that its resonant frequency with air as dielectric was about 44 MHz, i.e., approximately the same as the resonant frequency of the smaller stub resonator filled with ethanol. Since the 1.70 m coaxial stub was filled with dry air, the dielectric losses in the stub were

negligible so that $G_{eq}=0$. The values for the voltage input of the function generator V_{in} and the recorded voltage by the spectrum analyzer V_{out} at the resonant frequency of the 1.70 m coaxial stub resonator were measured to amount 66.83 mV and 2.51 mV respectively, see also Table 2. Substitution of these values in Eq. 18 provides a R_{eq} value of 0.98 Ω . Since the coaxial stub resonator applied for the experiments with ethanol has a length of 34 cm, see also Table 2, its value of R_{eq} i.e., $R_{eq(fluid)}$, is smaller than that of the 1.70 m stub resonator filled with air. Substitution of these values in Eq. 17 results in $R_{eq(fluid)}= 0.20 \Omega$ at the resonant frequency of 44 MHz. Since $R_{eq(fluid)}$ is known, the value of G_{eq} , representing the dielectric loss in the fluid, can now be calculated from the attenuation at the resonant frequency of 44 MHz for the 0.34 m coaxial stub resonator filled with ethanol. The values for the voltage input of the function generator V_{in} and the recorded voltage by the spectrum analyzer V_{out} at the resonant frequency of the 0.34 m coaxial stub resonator filled with ethanol were measured to amount 60.74 mV and 3.55 mV respectively. Substitution of the determined values for V_{in} , V_{out} and R_{eq} in Eqs.16 - 18 provides the value for $G_{eq}=1.07 \cdot 10^{-3}$ S. Substitution of this value into Eq. 19 provides the dielectric loss tangent: $\tan\delta_{eff}=0.04$.

Once all parameters defining the AF plot with the use of Eqs. 3 - 11 have been determined, an AF plot for the lumped element circuit in Fig. 3 can be calculated and compared to the experimentally determined one. The result is show in Fig. 5. The simulations were executed by the use of MATLAB 7.9.0 (R2009b) software.

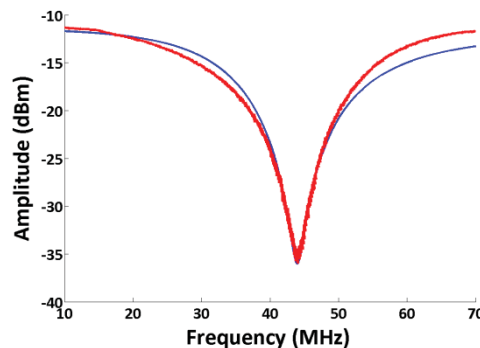


Fig. 6. AF plot for experimental data of ethanol (red) and modeling (blue) for the batch resonator using Eqs. 3 - 11 and the parameters in Table 2.

Fig. 6 reveals a good agreement between the simulated and experimentally determined AF plots. Hence, it is concluded that the open ended quarter wave length batch coaxial stub resonator performs as expected and that the lumped element circuit in Fig. 3 describes the behavior of the coaxial stub resonator well near its base resonant frequency.

Fig. 7 shows an AF plot for water as obtained with the batch resonator but now over a broader frequency range as compared to Fig. 5, i.e., for a frequency range from 10 to 150 MHz.

Table 2

Measurements with a 1.70 m quarter wavelength coaxial stub resonator with air as dielectric and with a 0.34m quarter wavelength coaxial stub resonator filled with ethanol in order to assess the values for R_{eq} and G_{eq} representing losses as a result of the skin effect and dielectric losses respectively.

Dielectric	Input amplitude (dBm)	Resonance amplitude (dBm)	V_{in} (mV)	V_{out} (mV)	R_{tot} (Ω)	R_{eq} (Ω)	L_{eq} (H)	C_{eq} (F)	G_{eq} (S)	$\tan\delta_{eff}$ (-)
Air	10.5	39	66.83	2.51	0.98	0.98	$6.43 \cdot 10^{-7}$	$2.02 \cdot 10^{-11}$	0	
Ethanol	11.33	36	60.74	3.55	1.55	0.20	$1.29 \cdot 10^{-7}$	$1.01 \cdot 10^{-10}$	$1.07 \cdot 10^{-3}$	0.04

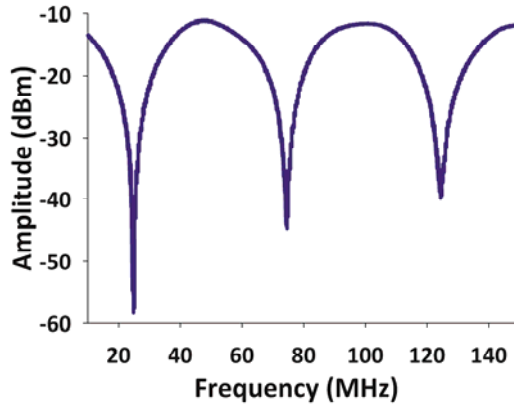


Fig. 7. AF frequency plot for demineralized water obtained with the batch resonator at 20 °C. Resonant frequencies for the first, second and third resonances are 24.8 MHz, 74.3 MHz and 124.7 MHz respectively.

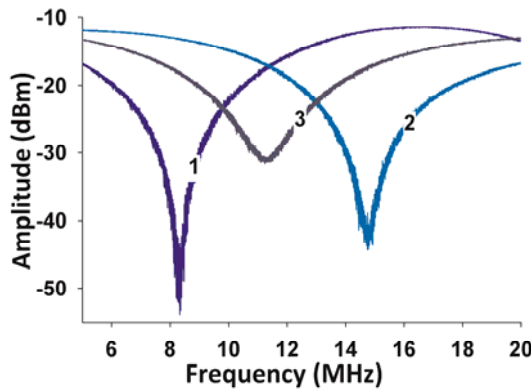


Fig. 8. AF plot for demineralized water (1), glycerol (2) and ethanol (3) as obtained with the flow-through resonator and the experimental set-up in Fig. 1. All experiments were executed at 20 °C.

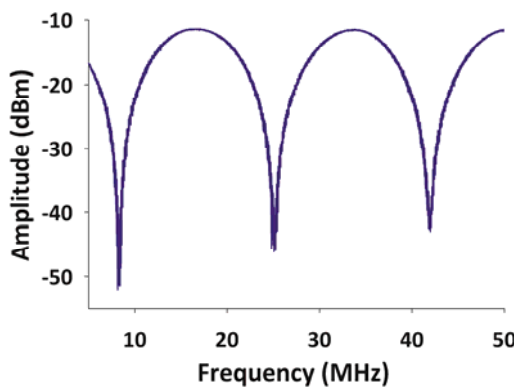


Fig. 9. AF plot for demineralized water obtained with the flow-through resonator at 20 °C. Resonance frequency for the first, second and third resonances are 8.3 MHz, 25.07 MHz, 41.99 MHz, respectively.

Fig. 7 shows that apart from the base frequency (or 1st resonance); the batch resonator detects the higher resonances also. The dielectric permittivity of demineralized water as calculated from the first, second and third resonance in Fig. 7 are 80.2 ± 0.89 , 79.4 ± 0.51 and 78.9 ± 0.54 , respectively. The decline in amplitude of the signal with increasing frequency can be explained by an increase of energy loss mainly as a result of the decreasing penetration depth of the current in the inner and outer conductors due to an increased skin effect with increasing frequency.

We also tested the flow-through resonator and Fig. 8 shows AF plot for water, ethanol and glycerol.

Compared to Fig. 5, obtained with the batch resonator, results are very similar. Substitution of the resonant frequencies determined from Fig. 7 in Eq. 1 results in the following dielectric permittivity values of water, ethanol and of glycerol: $\epsilon_{water} = 79.9 \pm 0.86$ (78.76 (79.5) according to [34]), $\epsilon_{ethanol} = 24.2 \pm 0.50$ (24.35 (25.13) according to [34]) and $\epsilon_{glycerol} = 42.9 \pm 0.56$ (42.49) according to [34]. We conclude that the flow-through resonator performs well with the solutions tested because obtained values are close to reported experimental values by others (given in between brackets).

Fig. 9 shows an AF plot for water as obtained with the flow through resonator but now over a broader frequency range as compared to Fig. 9 i.e., for a frequency range from about 5 to 50 MHz.

As observed with the batch resonator, the flow through resonator is also able to reveal the higher resonances. When calculating the dielectric permittivity of demineralized water from the first, second and third resonance, we render values of 79.9 ± 0.86 , 78.7 ± 1.5 and 78.9 ± 1.2 , respectively.

An important characteristic of our coaxial stub is that resonance occurs at relative low frequencies. By implication, the use of commercially available but relatively expensive spectrum or network analyzers to delineate responses in the high frequency range is no longer required. Obviously, this reduces the investment costs for application substantially.

As was remarked already, not only the resonant frequencies but also the shape of the AF plots contains information on the dielectric properties of the samples. In case dielectric losses in the sample are high, the quality factor of the coaxial resonator will decrease. In addition, the AF plot will be affected by imperfections in the experimental set-up. It is expected that more detailed modeling of the resonator will guide us to gain more understanding of the system described here as well as the dielectric properties of fluids under investigation.

2.5 Conclusions

- The concept of a quarter wave length open-ended coaxial stub resonator as sensing device was successfully applied to measure the dielectric permittivity of water, ethanol and glycerol.
- The coaxial resonator presented in this study performs well both in the batch as in the flow-through mode of operation.
- The flow-through mode of operation allows the continuously on-line monitoring of fluid samples.
- It is expected that the coaxial resonator concept can be developed further into a cost-efficient and low maintenance sensor for dielectric spectroscopy in a broad field of specific applications.

2.6 Future steps

Based on the results presented in this study, we expect that the concept of the coaxial stub resonator as sensing device proves useful in a wide range of applications. Examples include the detection of (very early) corrosion or biofouling on the inner conductor surface of the coaxial stub, quality control in the food industry (e.g., milk, soft and alcoholic drinks) and measuring the load and/or saturation level of ion exchange resins and activated carbon applied as dielectrics in a coaxial stub-based device.

In addition, miniaturization of the coaxial stub sensor allows the application of much higher frequencies, i.e., frequencies in the GHz range. This, in turn, broadens the application range significantly as it gives way to complex dielectric radio-frequency spectroscopy for the detection of, for instance, molecular structures, micelles or microorganisms in liquid samples.

2.7 Acknowledgement

This work was performed in the TTIW-cooperation framework of Wetsus, Centre of Excellence for Sustainable Water Technology (www.wetsus.nl). Wetsus is funded by the Dutch Ministry of Economic Affairs, the European Union Regional Development Fund, the Province of Fryslân, the City of Leeuwarden and the EZ/Kompas program of the “Samenwerkingsverband Noord-Nederland”. The authors thank the participants of the research theme Sensoring for the fruitful discussions and their financial support.

Furthermore, the authors wish to thank Prof. Dr. Ir. F.B.J. (Frank) Leferink and Prof. Dr. Ir. F. E. (Frank) van Vliet for their large scientific contribution to this work.

2.8 References

1. A. Fabbri, T. Fen-Chong, O. Coussy, Dielectric capacity, liquid water content, and pore structure of thawing–freezing materials, *Regions Science and Technology*, Volume 44, Issue 1, January 2006, 52-66.
2. H. Eller, A. Denoth, A capacitive soil moisture sensor, *Journal of Hydrology*, Volume 185, Issues 1-4, 1 November 1996, 137-146.
3. F. Kizito, C.S. Campbell, G.S. Campbell, D.R. Cobos, B.L. Teare, B. Carter, J.W. Hopmans, Frequency, electrical conductivity and temperature analysis of a low-cost capacitance soil moisture sensor *Journal of Hydrology*, Volume 352, Issues 3-4, 15 May 2008, 367-378.
4. T. Fen-Chong, A. Fabbri, J.-P. Guilbaud, O. Coussy, Determination of liquid water content and dielectric constant in porous media by the capacitive method *Comptes Rendus Mecanique*, Volume 332, Issue 8, August 2004, 639-645.
5. U. C. Hasar, M. T. Yurtcan, A microwave method based on amplitude-only reflection measurements for permittivity determination of low-loss materials *Measurement*, Volume 43, Issue 9, November 2010, 1255-1265.
6. A. García, J. L. Torres, E. Prieto, M. De Blas, Dielectric properties of grape juice at 0.2 and 3 GHz *Journal of Food Engineering*, Volume 48, Issue 3, May 2001, 203-211.
7. F. N. Dalton, M. Th. Van Genuchten, The time-domain reflectometry method for measuring soil water content and salinity *Geoderma*, Volume 38, Issues 1-4, September 1986, 237-250.
8. D. M. Hagl, D. Popovic, S. C. Hagness, J. H. Booske, M. Okoniewski, Sensing volume of open-ended coaxial probes for dielectric characterization of breast tissue at microwave frequencies, *Microwave Theory and Techniques*, *IEEE Transactions on*, Volume: 51, Issue:4, 08 Apr 2003, pages 1194 – 1206, DOI: 10.1109/TMTT.2003.809626.
9. Y. Wang and M. N. Afsar, Measurement of complex permittivity of liquids using waveguide techniques, *Progress In Electromagnetics Research*, Vol. 42, 131-142, 2003.
10. V.V. Komarov, S. Wang, J. Tang, Permittivity and measurements, *Wiley Encyclopedia of RF and Microwave Engineering*. Volume 4, 2005, 3693-3711.
11. I. Ciofi, M. R. Baklanov, Z. Tókei, G. P. Beyer, Capacitance measurements and k-value extractions of low-k films *Microelectronic Engineering*, Volume 87, Issue 11, November 2010, 2391-2406.
12. U. Kaatzte and V. Uhlendorf, *Z. Physik. Chem. NF* 126, 1981.
13. J. Baker-Jarvis, M.D. Janezic, P.D. Domich, R.G. Geyer, Analysis of an open-ended coaxial probe with lift-off for nondestructive testing, *Instrumentation and Measurement*, *IEEE Transactions on*, Volume 43, Issue:5, Oct 1994, 711 – 718.
14. J. Sheen, Study of microwave dielectric properties measurements by various resonance techniques, *Measurement*, Volume 37, Issue 2, March 2005, 123-130.
15. M.S. Venkatesh, G.S.V. Raghavan, An Overview of Dielectric Properties Measuring Techniques, *Canadian Biosystems Engineering*, Volume 47, 2005, 15-7.30.
16. M. V. Storey, B. van der Gaag, B. P. Burns, Advances in on-line drinking water quality monitoring and early warning systems *Water Research*, Volume 45, Issue 2, January 2011, 741-747.
17. D. Singwong, N. Siripon, A wide-band bandpass filter using a novel embedded short-circuited stub resonator, *Microwave Conference Proceedings (APMC)*, 2010 Asia-Pacific, March 2011, 1086 – 1089.
18. G H. Huff, S Goldberger, A Coaxial Stub Microfluidic Impedance Transformer (COSMIX), *IEEE Microwave and Wireless components Letters*, Volume 20, March 2010.
19. J. Lamb, The Experimental Behaviour of the Coaxial Line Stub, *Electrical Engineers - Part III: Radio and Communication Engineering*, *Journal of the Institution of Electrical Engineers*, Volume 93 Issue:23, May 1946, 188-190.
20. J. Carroll, M. Li, and K. Chang, New Technique to Measure Transmission Line Attenuation, *IEEE Transactions On Microwave Theory And Techniques*, Volume. 33, January 1995.
21. J. M. Drozd and W. T. Joines, A Capacitively Loaded Half-Wavelength Tapped-Stub Resonator, *IEEE Transactions On Microwave Theory And Techniques*, Volume. 45, July 1997.
22. Y.-H. Chou, M.-J. Jeng, Y.-H. Lee, and Y.-G. Jan, Measurement of RF PCB Dielectric Properties And Losses, *Progress In Electromagnetics Research Letters*, Vol. 4, 2008, 139–148.
23. H. Heck, Module 5: Advanced Transmission Lines Topic 5: 2 Port Networks & S-Parameters, OGI EE564, 2008, (<http://home.comcast.net/~howard.heck/>).

24. T.C. Edwards, M. B. Steer, *Foundations of Interconnect and Microstrip design*, Wiley, 2000.
25. P.A. Bernard; J.M. Gaubray, Measurement of dielectric constant using a microstrip ring resonator, *Microwave Theory and Techniques*, IEEE Transactions on , vol.39, no.3, pp.592,595, Mar 1991; doi: 10.1109/22.75310.
26. D.M. Pozar, *Microwave Engineering* Addison, Wesley Publishing Company. ISBN 0-201-50418-9, 1993.
27. O. Zinke, H. Brunswig, *Hochfrequenztechnik 1, Hochfrequenzfilter, Leitungen, Antennen*, 6. Auflage, Berlin: Springer 2000, pp86-88.
28. D. M. Pozar, *Microwave Engineering*, Wiley, 2004.
29. R. E. Collin, *Foundations for Microwave Engineering*, Wiley IEEE, 2000.
30. F. Leferink, C. Roeloffzen, *Handout Transmission Media: Transmission Lines*, University of Twente, 2007.
31. Shicong Ma Xu, Bingyin Bo, Zhiqian Klimek, Andrew, The research on lumped parameter equivalent circuit of transmission line, *Advances in Power System Control, Operation and Management (APSCOM 2009)*, 8th International Conference, November 2009, 1-5.
32. A Niknejad, *Lossy Transmission Lines and the Smith Chart*, University of California, Berkeley, Course EECS 117, Lecture 6. (<http://rfic.eecs.berkeley.edu/~niknejad/ee117/pdf/lecture6.pdf>)
33. O. Coufal, Inductance of coaxial cable, *Energyspectrum*, 2008, vol. 3, no. 1, p. 1-5. ISSN: 1214-7044.
34. C. Wohlfarth, M. D. Lechner, *Static Dielectric Constants of Pure Liquids and Binary Liquid Mixtures*, Supplement to IV/6, Series: Landolt-Börnstein: Numerical Data and Functional Relationships in Science and Technology - New Series, Vol. 17, Subseries: Physical Chemistry, 2008, 203.

2.9 Supplementary Information

Appendix A

Characteristic impedance considerations

In this section the influence of the characteristic impedance of the stub resonator Z_{c_STUB} on the behavior of the sensing system shown in Fig.1, section 2.2 is briefly discussed. Figure A.1 gives a schematic overview of two transmission lines i.e., TL1 with characteristic impedance Z_{c_TL1} in series with TL2 with characteristic impedance Z_{c_TL2} , using a connector with characteristic impedance $Z_{connector}$.

Fig. A.2 shows a schematic representation of the AF - response of this series of transmission lines assuming that TL1 is connected to a function generator and TL2 is connected to a spectrum analyzer.

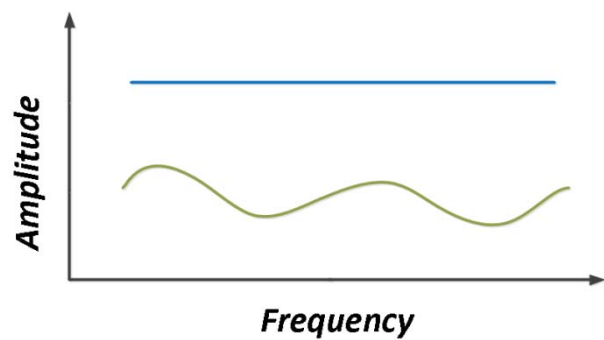
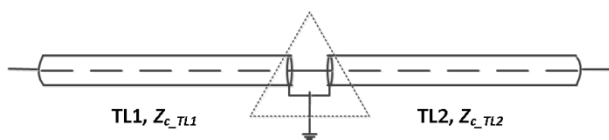


Fig. A.1. Schematic representation of two transmission lines TL1 with Z_{c_TL1} and TL2 with Z_{c_TL2} in series, using a connector with characteristic impedance $Z_{connector}$ (represented by the dotted triangle).

Fig. A.2. Shape of the AF-response for the series of two transmission lines shown in Fig. A.1 for $Z_{c_TL1} = Z_{connector} = Z_{c_TL2}$ (blue curve) and for an unmatched system such as $Z_{c_TL1} = Z_{connector} \neq Z_{c_TL2}$ (green curve).

In case $Z_{c_TL1} = Z_{connector} \neq Z_{c_TL2}$, reflections will occur at the connection point of the connector and TL2.

Fig. A.3 gives a very schematic overview of the coaxial stub resonator sensing system with TL1, TL2, TLstub connected by the use of a T connector. The function generator connected to TL1, and the spectrum analyzer was connected to TL2, see also Fig. 1, section 2.2.

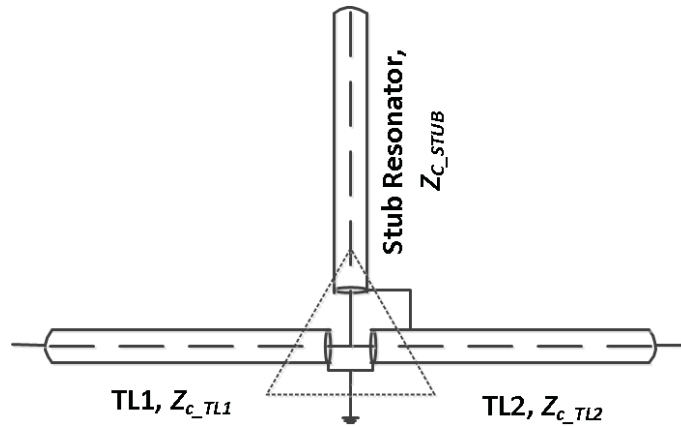


Fig. A.3. The schematic representation of the stub resonator sensing system. TL1, TL2, TLstub are connected using a T connector, the function generator is connected to TL1 and the spectrum analyzer to TL2, according to Fig. 1 in section 2.2.

In practice $Z_{c_TL1}=Z_{c_TL2}=Z_{c_connector} = 50 \Omega$. This means that, the system in Fig. A.3 with stub resonator is not matched and that reflections will occur at the connection of TL1, TL2, Z_{c_STUB} .

Fig. A.4 shows the effect of the lossless transmission lines the AF – response for stub resonators with different values of Z_{c_STUB} .

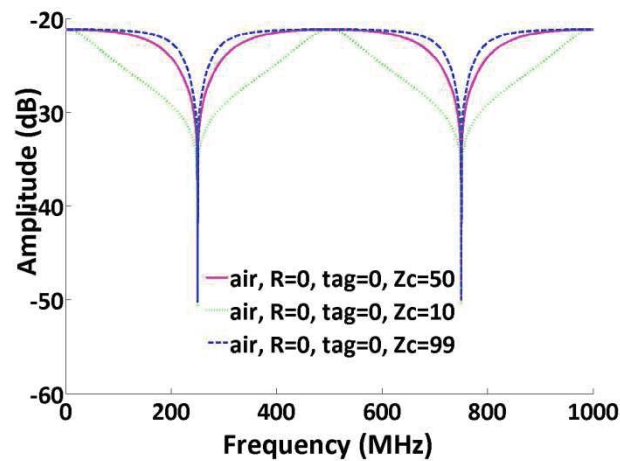


Fig. A.4. Simulated AF-plots assuming Z_{c_STUB} to be 50, 10 or 99 Ω and air ($\epsilon_r=1$) as dielectric. The ohmic losses (R) and dielectric losses (loss tangent tag) were assumed to be zero.

Fig. A.5. shows simulated AF-responses for different values of Z_{c_STUB} for a resonator filled with lossy dielectric (water) without ohmic losses ($R=0$).

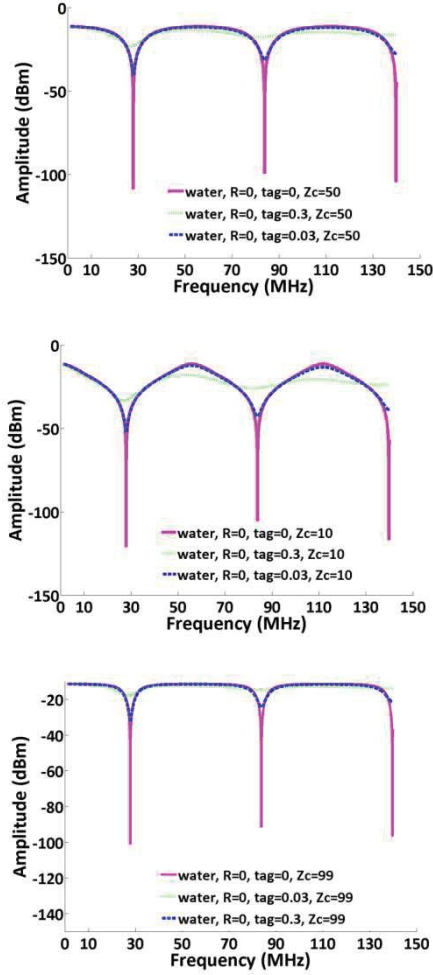


Fig. A.5. Simulated AF plots as in Fig. 1 for Z_{c_STUB} values of 50, 10 and 99 Ω with water as dielectric and for different values of loss tangent.

The value of Z_{c_STUB} can be defined as:

$$Z_{c_STUB} = \sqrt{\frac{R + j\omega L}{G + j\omega C}} \quad (\text{A.1})$$

where the inductance L is related to both the inner diameter of the outer conductor D and the outside diameter of the inner conductor d . The capacitance C is apart from geometry determined by the dielectric permittivity ϵ_r of the dielectric under study, as given by Eq. 20 in Ch. 2 of this thesis.

As an example how geometry and dimensions affect Z_{c_STUB} , Table 1 summarizes the dimensions of inner and outer conductor required to obtain a Z_{c_STUB} value of either 10, 50 or 99 Ω .

Table A.1

Values of Z_{c_STUB} in relation to the dimensions of the inner (D) and outer conductor (d) of the coaxial resonator applied in this study.

Dielectric	$Z_{c_STUB}=50 (\Omega)$		$Z_{c_STUB}=10 (\Omega)$		$Z_{c_STUB}=99 (\Omega)$	
	$D (mm)$	$d (mm)$	$D (mm)$	$d (mm)$	$D (mm)$	$d (mm)$
Air	25	10	25	21	25	5
Water	25	0.015	25	6	25	0.00001

Of course, there is the freedom of design of resonators with inner conductors of different dimensions. However, deviations from commercially available standard geometries will increase the total cost price of the sensor.

It should be also noted that from Eq. 3, it is obvious that increasing the diameter of the inner conductor d will decrease the ohmic losses R thereby affecting Z_c (Eq. A1). Besides, Z_{c_STUB} depends on the ratio of the diameters of outer conductor D and inner conductor d (Eq. 20) and will decrease with increasing inner conductor diameter d (assuming that this effect is larger than the aforementioned decrease of R). In other words: increasing the diameter of the inner conductor d of the resonator will result in both a lower value of Z_c and a lower value of R (less ohmic losses). However, increasing the diameter of the outer conductor as well results in a reduction of the cutoff frequency and consequently the combined effects of the evanescent mode and multiple modes may occur which could be applied in future work to increase the sensitivity of the system.

Fig. A.6 shows that different coaxial stub resonator designs are possible with the same Z_c values. The figure was added to illustrate that the sensitivity of the sensor system for changes in ohmic losses R in the conductors can be adjusted by scaling of the resonator geometry.

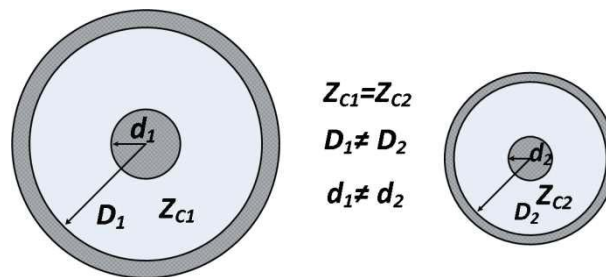


Fig. A.6. The schematic representation of the transmission lines with a different geometry (D and d) and the same characteristic impedance Z_c .

In conclusion, a characteristic impedance that is not too extreme, such as e.g. $5 < Z_c < 500 \Omega$, avoids practical problems and still leaves freedom for optimizing a measurement setup.

Appendix B

Additionally, the skin effect as an important parameter of this study will be discussed.

The skin effect is a tendency for alternating current (AC) to flow mostly near the outer surface of an electrical conductor, such as metal wire. The effect becomes more and more apparent as the frequency increases.

The main problem with the skin effect is that it increases the effective resistance of a wire for AC at moderate to high frequencies, compared with the resistance of the same wire at direct current (DC) and low AC frequencies. The effect is most pronounced in radio-frequency (RF) systems, especially antennas and transmission lines [<http://whatis.techtarget.com/definition/skin-effect>].

As an example, the skin depth for the copper and stainless steel wires both at 50 MHz was calculated: 9.2 μm and 59.1 μm , respectively.

To model the current distribution in a round wire the following references can be used:

1. Y. Shibuya, Skin Effects in Straight Wires, Wolfram Demonstrations Project Published: November 5, 2012 (<http://demonstrations.wolfram.com/SkinEffectsInStraightWires/>).
2. Gl. S. Smith, A simple derivation for the skin effect in a round wire, 2014 Eur. J. Phys. 35 025002. doi:10.1088/0143-0807/35/2/025002.
3. Sv. Koerner, Skin Effect Calculation, 10 Jul 2012 (Updated 10 Jul 2012), <http://www.mathworks.com/matlabcentral/fileexchange/37443-skin-effect-calculation>.

Fig. B.1 demonstrates the results of modeling the current distribution in a round copper wire of 1mm at 50 MHz using program code of Sv. Koerner.

Furthermore, the formulas to estimate and optimize the practical significance of the skin effect for particular cases are given and described in [2, this section].

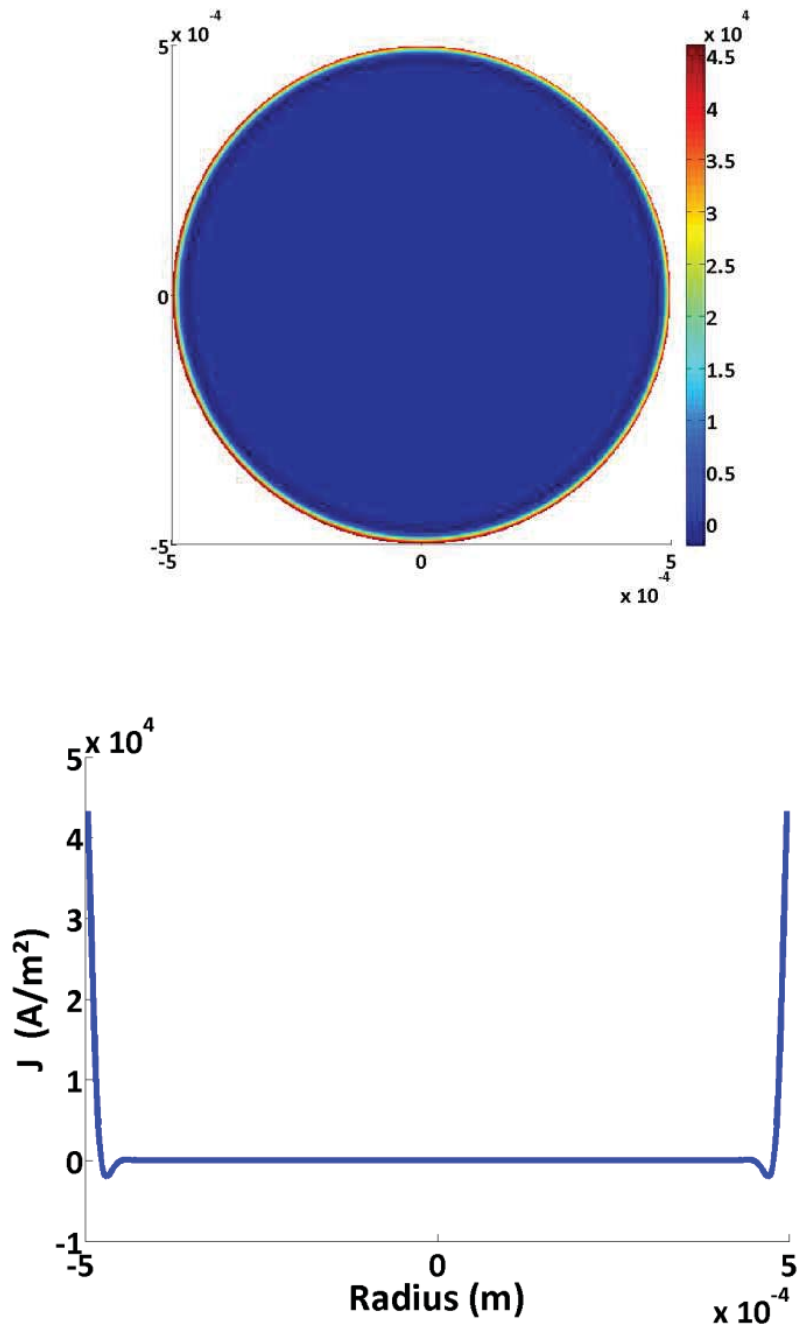


Fig. B.1. Simulation of the current density distribution in a round copper wire.



Krakow, POLAND, EUROSENSORS 2012

Chapter 3

Modeling and
Simulations of the
Amplitude - Frequency
Response of
Transmission Line
Type Resonators
Filled with Lossy
Dielectric Fluids



Abstract

Stub resonators can be used to assess the dielectric properties of fluids. The resonance frequencies, determined from the amplitude versus frequency (AF) response of such resonators, are mainly determined by the permittivity of the fluid while damping arises from dielectric losses. Even though this methodology has been extensively reported in the literature, without almost any exception these studies refer to (near) ideal behavior regarding for example, geometry and negligibly low conductivity of the fluid studied. On-line stub resonator-based sensors (i.e., flow-through) in use for industrial applications, however, quite often suffer from high dielectric losses, non-ideal material choice of the conductors from an electrical point of view and unconventional resonator geometry. Therefore, in order to ensure correct data interpretation, a straightforward model accounting for the effects of dielectric losses, conductor losses (skin effect) and impedance mismatches on the AF response is highly desirable. In addition, such a model can help to optimize future sensor designs. Here, we present a lumped parameter model, essentially based on telegrapher's equations, that accounts for the skin effect, dielectric losses and impedance mismatches between the transmission lines to the resonator and the resonator respectively. The adequacy of the method, even in the case of impedance mismatch, is demonstrated by comparing these model simulations with experimentally obtained AF curves for both flow-through coaxial stub resonators and microstrip resonators immersed in the fluid under investigation.

This chapter is based on the article published as:

N.A. Hoog, M.J.J. Mayer, H. Miedema, W. Olthuis, F.B.J. Leferink, A. van den Berg: *Modeling and Simulations of the Amplitude-Frequency Response of Transmission Line Type Resonators Filled with Lossy Dielectric Fluids*, Sensors and Actuators A: Physical, Volume 216, 1 September 2014, Pages 147-157. <http://dx.doi.org/10.1016/j.sna.2014.05.006>

3.1 Introduction

There are different ways to determine the dielectric permittivity of fluids. In dielectric spectroscopy [1-3], an alternating electric field is applied across two capacitor plates with the fluid under investigation as dielectric [4-7]. Measuring the impedance of the system as a function of frequency gives the dielectric permittivity, loss tangent, as well as their frequency dependence. Another known technique to assess the dielectric properties of a fluid is to apply a quarter wave length coaxial stub resonator as a sensing element by placing the fluid under investigation between its inner and outer conductor [2, 3]. Since this method is based on the concept of a transmission line, it is less sensitive to errors caused by the parasitic capacitance and inductance of all elements in the measurement set-up as compared to the previously mentioned capacitance-based measurements, especially at high frequencies [8-10]. In a previous attempt we applied a lumped element model to a quarter wave length open-ended coaxial stub resonator [2, 3]. Even though this first model was shown to adequately predict the amplitude versus frequency plot near the base resonant frequency of the stub resonator, it was limited to the fundamental (basic) resonant frequency. In the present contribution, we extend our first model for lossy stub resonator systems to a model that describes all resonance frequencies within a defined frequency range. The model, based on transmission line theory, comprises a general solution of the telegrapher's equations and takes into account both the skin effect and dielectric losses [11, 12]. A particular challenge arises when the impedance of the stub resonator does not match the impedance of the transmission lines, the latter typically 50 Ω . The feasibility of our method is demonstrated and discussed by comparing model simulations with experimentally obtained data using either a coaxial stub resonator or a microstrip line resonator. The results show that even if the system elements are unmatched, achieved by adapting the geometry of the resonator, the model still describes the experimental data quite well.

3.2 Model of the lossy stub resonator system

Fig. 1 gives a schematic overview of the coaxial stub resonator sensing system used in this study for analysing the dielectric properties of a fluid.

Fig. 2 shows the equivalent electrical circuit used of the experimental set-up in Fig. 1 comprising the frequency generator (FG) with internal impedance Z_s ; transmission line TL1, connecting the function generator with the coaxial stub resonator, and transmission line TL2, connecting the coaxial stub resonator to spectrum analyzer (SA) with internal impedance Z_{SA} . The coaxial stub resonator T, including a connector, are represented as transmission line TL3 with characteristic impedance Z_{CRE} and described by a distributed element model.

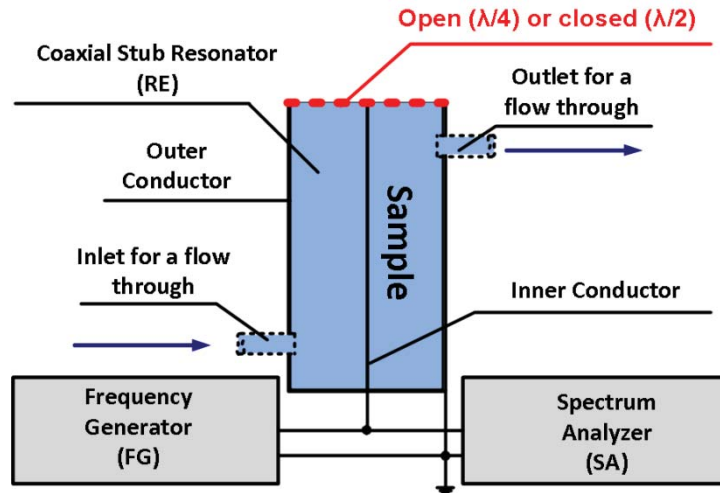


Fig. 1. Schematic outline of the coaxial stub resonator sensing system consisting of a function generator (FG), a spectrum analyzer (SA) and the coaxial stub resonator (RE). The dotted Inlet and Outlet indicate that the batch resonator can be optionally used as flow-through resonator. The liquid sample under investigation is applied as dielectric between inner and outer conductor of the coaxial stub resonator.

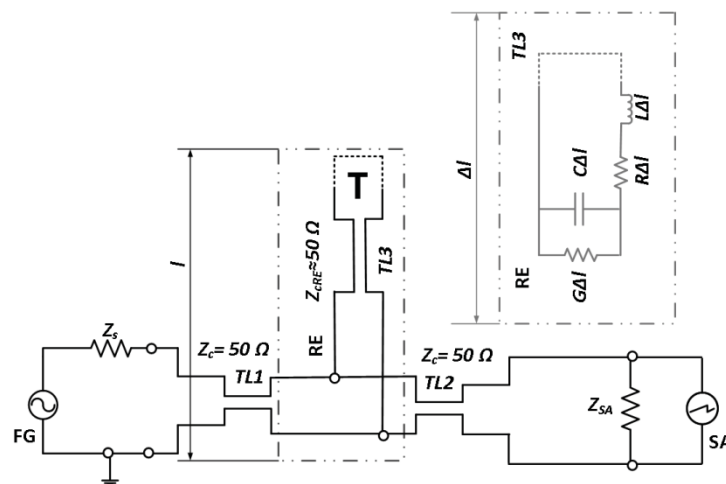


Fig. 2. The equivalent electrical circuit of the sensor system shown in Fig. 1. Parameters $L\Delta l$, $C\Delta l$, $G\Delta l$ and $R\Delta l$ represent the resonator's distributed element inductance, capacitance, conductivity and resistance, respectively, all with length Δl . The dotted line on T indicates either an open or closed (short) circuit, representing a $\lambda/4$ or $\lambda/2$ resonator, respectively.

Based on the equivalent electric circuit of the sensor system in Fig. 2, we will now derive a straightforward model for predicting the amplitude versus frequency (AF) plot of a coaxial sensing system. The model is straightforward in the sense that it is based on and by implication follows directly from the classic telegraph equations.

Given a resonator length l of $\lambda/4$, the distributed element inductance L , resistance R , capacitance C and conductance G of a coaxial transmission line are expressed by Eqs.1-6, respectively [11, 14]:

$$L = \frac{\mu_0 \mu_r}{2\pi} \ln\left(\frac{D}{d}\right) + \frac{\mu_0 \mu_r}{2\pi} \sqrt{\frac{\rho}{2\omega \mu_0 \mu_r}} \left(\frac{1}{d} + \frac{1}{D}\right) \quad (1)$$

$$R = \frac{\rho}{2\pi \delta_s} \left(\frac{1}{0.5 \cdot D} + \frac{1}{0.5 \cdot d}\right) \quad (2)$$

$$\delta_s = \sqrt{\frac{2\rho}{\omega \mu_r \mu_0}} \quad (3)$$

$$R_s = \sqrt{\frac{\omega \mu_0 \mu_r \rho}{2}} = \frac{\rho}{\delta_s} \quad (4)$$

$$C = \frac{2\pi \epsilon_0 \epsilon_r}{\ln(D/d)} \quad (5)$$

$$G = \omega \cdot C \cdot \tan \delta_{eff} \quad (6)$$

where

μ_0 , magnetic permeability of free space (vacuum permeability) ($\text{H} \cdot \text{m}^{-1}$): $\mu_0 = 4\pi \cdot 10^{-7}$;

μ_r , relative magnetic permeability (-);

ω , angular frequency $\omega = 2\pi f$ (rad/s);

ω_0 , angular resonance frequency, $\omega_0 = 2\pi f_0$ (rad/s);

ϵ_0 , dielectric permittivity of free space (vacuum permittivity) ($\text{F} \cdot \text{m}^{-1}$): $\epsilon_0 = 1/(\mu_0 \cdot c)^{-1/2}$;

c , speed of light in vacuum (m/s);

ϵ_r , relative dielectric permittivity (-);

D , (inner) diameter of outer conductor (m);

d , (outer) diameter of inner conductor (m);

R_s , surface resistance of the metal (Ω);

- δ_s , depth of penetration (m);
 ρ , specific resistance of the metal ($\Omega \cdot m$): $\rho=1/\sigma$;
 σ , conductivity (S/m);
 $\tan\delta_{eff}$, dielectric loss tangent (-).

The resistance R in Eq. 2 is related to two physical parameters, the depth of penetration δ_s in both inner and outer conductor (skin effect) and the surface resistance of the metal R_s [11, 15].

It is noted that the inner and outer conductor should be made of the same material; otherwise the model should account for two different values of the specific resistance of the metal ρ in Eq. 1.

Apart from the geometry of the device (D and d), medium property μ_r and material characteristics ρ , Eqs.1-6 contain two (unknown) parameters needed to calculate L , C and G , i.e. ϵ_r and $\tan\delta_{eff}$. The loss tangent, $\tan\delta_{eff}$, in Eq. 6 represents dielectric losses in the fluid sample under investigation and is, like ϵ_r , a key parameter characterizing dielectric fluid properties. For pure, single component fluids, values of these parameters may be found in the literature. If the resonator is filled with a fluid of unknown composition, both can be determined by fitting the model simulations developed in this study against experimentally determined AF plots with the real part of the complex dielectric permittivity ϵ_{re} and $\tan\delta_{eff}$ as free fitting parameters.

In an ideal resonator without any losses (i.e. $R=G=0$) or, in general, whenever $\frac{R}{L} = \frac{G}{C}$ [15], the resonance frequency f_{res} of an open ended ($\lambda/4$) and closed end ($\lambda/2$) resonator are given by Eqs. 7a and 7b, respectively [2]. In these special cases, the dielectric constant ϵ_{re} can be determined directly from equations 7a and 7b [11, 12]:

$$f_{res} = \frac{2n-1}{2 \cdot \pi \cdot \sqrt{LC}} = \frac{c \cdot (2n-1)}{4l \sqrt{\epsilon_{re} \epsilon_0 \mu_{re} \mu_0}} \quad (7a)$$

$$f_{res} = \frac{n}{2 \cdot \pi \cdot \sqrt{LC}} = \frac{c \cdot n}{2l \sqrt{\epsilon_{re} \epsilon_0 \mu_{re} \mu_0}} \quad (7b)$$

where

- n , the order number of f_{res} (Hz);
 l , the length of the resonator (m).

In all other cases with losses, the minimum in the AF response obtained with the set-up shown in Fig. 1 is not defined exclusively by L and C but also by dielectric losses and losses in the conductors. As a result, the real part of the dielectric permittivity cannot be determined directly from the minimum in the AF plot.

In order to determine ϵ_{re} and $\tan\delta_{eff}$ from an experimentally determined AF response of an unknown fluid, the following procedure was applied.

The relative complex dielectric permittivity ϵ_r is defined as:

$$\epsilon_r = \epsilon_{re} - j\epsilon_{im} \quad (8)$$

where ϵ_{re} and ϵ_{im} represent the real and imaginary part of ϵ_r , respectively. ϵ_{re} is related to the stored energy within the dielectric, i.e., the fluid under investigation, whereas ϵ_{im} is related to the dissipation of energy within the dielectric. Note that the capacitance C in Eq. 5 is determined solely by ϵ_{re} .

The effective loss tangent $\tan\delta_{eff}$, which is a measure for the dielectric losses in the system, is expressed by Eq. 9:

$$\tan\delta_{eff} = \frac{\omega\epsilon_{im} + \sigma}{\omega\epsilon_{re}} \quad (9)$$

where σ represents the conductivity of the solution in S/m and $\omega=2\pi f_{res}$ the angular frequency in rad/s.

In Eq. 9, ϵ_{im} and σ reflect the polarization losses and the conductivity losses in the dielectric, respectively. It is noted that in the literature, polarization losses and dielectric losses are sometimes lumped into one parameter i.e., into ϵ_{im} [13]. In this contribution, ϵ_{im} is defined in terms of Eq. 9, implying ϵ_{im} solely includes those losses due to polarization.

It should be mentioned that ϵ_{im} plays a significant role especially in the high frequency range and, according to Eq. 9, affects $\tan\delta_{eff}$. Note that $\tan\delta_{eff}$ is affected by σ and ϵ_{re} as well, with σ and ϵ_{re} both functions of frequency

Once L , R , C and G are determined, the complex characteristic impedance Z_c and the complex propagation constant γ can be calculated as function of ω [11, 16] and are expressed by Eqs. 10, 11:

$$Z_c = \sqrt{(R + j\omega L)/(G + j\omega C)} \quad (10)$$

$$\gamma = \sqrt{(R + j\omega L) \cdot (G + j\omega C)} = \alpha + j\beta \quad (11)$$

where

Z_c , complex characteristic impedance of the lossy coaxial stub resonator (Ω);

γ , complex propagation constant (m^{-1});

α , attenuation of propagation constant γ (Np/m).

β , phase of the propagation constant γ (rad/m);

The attenuation of propagation constant γ i.e., $Re(\gamma)=\alpha$ represents all losses in the stub resonator due to metal losses (in inner and outer conductors) and dielectric losses (in the fluid under investigation).

The next step is to calculate the input impedance Z_{in} of the coaxial stub resonator of length l from [16] expressed by Eq. 12:

$$Z_{in} = Z_c \frac{Z_l / Z_c + \tanh(\gamma l)}{1 + Z_l / Z_c \cdot \tanh(\gamma l)} \quad (12)$$

where

Z_l , load impedance of the coaxial stub resonator, [Ω].

In case of a closed-ended ($Z_l=0$) and open-ended ($Z_l=\infty$) stub resonator, Eq. 12 reduces to Eqs.13 and 14, respectively:

$$Z_{in} = Z_c \tanh(\gamma l) \quad (13)$$

$$Z_{in} = Z_c \coth(\gamma l) \quad (14)$$

Eq. 12 represents the input impedance Z_{in} of a coaxial stub resonator of length l , characteristic geometry D and d , conductor losses R and filled with a liquid (dielectric) of conductance G as a function of frequency ω .

Finally, in order to be able to construct the AF plot, an expression must be derived relating the output voltage V_{out} recorded by the spectrum analyzer to the input voltage V_{in} applied by the function generator. Close inspection of Fig. 2 reveals that the input

impedance Z_{in} of the stub resonator, i.e., the input impedance of transmission line TL3, is in parallel with the internal resistance of the spectrum analyzer Z_{SA} and in series with the internal resistance of the function generator Z_S , see also Fig.3.

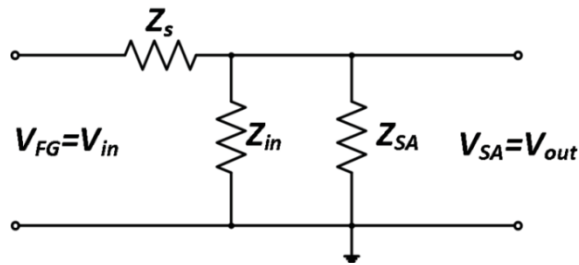


Fig. 3. The equivalent electric circuit of Fig. 2, with Z_{in} representing the input impedance of the coaxial stub resonator i.e., of transmission line TL3.

Given the equivalent circuit of Fig. 3, we can now derive V_{out} as function of V_{in} (Eq. 15):

$$V_{out} = V_{in} \frac{(Z_{in} \cdot Z_{SA})}{(Z_S \cdot Z_{SA} + Z_S \cdot Z_{in} + Z_{in} \cdot Z_{SA})} \quad (15)$$

Note that V_{out} is complex and that the signal measured by the spectrum analyzer equals the modulus of V_{out} . Further, that the internal resistance of the function generator Z_S , and the internal resistance of the spectrum analyzer Z_{SA} are both usually 50Ω and that Z_{in} can be calculated from Eq. 12.

Equations 1 to 6 and 8 to 15 define the behavior of the experimental set-up in Figs. 1-3 and can be used to simulate AF plots, i.e., obtaining V_{out} as a function of frequency. In case the dielectric properties of the fluid in the stub resonator are not known, the model can be used to estimate the dielectric properties of the fluid under investigation by fitting simulated AF plots against experimental data with the unknowns ϵ_{re} and $\tan\delta_{eff}$ as the two free-fitting parameters. For this purpose a fitting routine was written in Matlab (R2012b), see Appendix D for a detailed description. It is noted that each of the parameters ϵ_{re} , ϵ_{im} , σ and ω (and by implication $\tan\delta_{eff}$ as well) change with frequency. This is important to realize since it means that the fitting procedure should be applied over a sufficiently small frequency range so that ϵ_{re} and $\tan\delta_{eff}$ are not changing significantly over the frequency range considered. For this reason, we determined in this study values of ϵ_{re} and $\tan\delta_{eff}$ over each resonance separately. As a result, we obtained average values of ϵ_{re} and $\tan\delta_{eff}$ “valid” within the frequency range of each resonance.

Microstrip line stub resonator

It should be emphasized that Eqs. 10-15 provide a general solution of the telegrapher's equations and apply to any type of transmission line operating in the Transverse Electromagnetic Mode or TEM. If, for example, a microstrip line (MSL) is used as a sensing element in the experimental set-up of Figs. 1 and 2, the dielectric properties of a fluid sample in which the MSL is placed can be determined analogous to the procedure described for the coaxial stub resonator i.e., by solving Eqs. 1-6 and 8-15. However, if applied to MSL, the expressions for the distributed elements R , C , L and G have to be adapted for the particular geometry of the MSL used. The left panel of Fig.4 shows the geometry of an MSL used in this study whereas the right panel shows a cross section of the MSL in more detail with E-lines and H-lines indicated. A difference with the coaxial type of resonator is that the MSL operates in the so-called quasi-TEM mode compared to the strictly TEM mode of operation of the coaxial stub resonator.

Fringing effects are quite significant so that the capacitance of the MSL is larger than calculated from the assumption that it behaves like an ideal plate capacitor between the strip conductor and ground plane. It is for this reason that the system is defined by an effective dielectric permittivity with a value in between that of the substrate and the working medium.

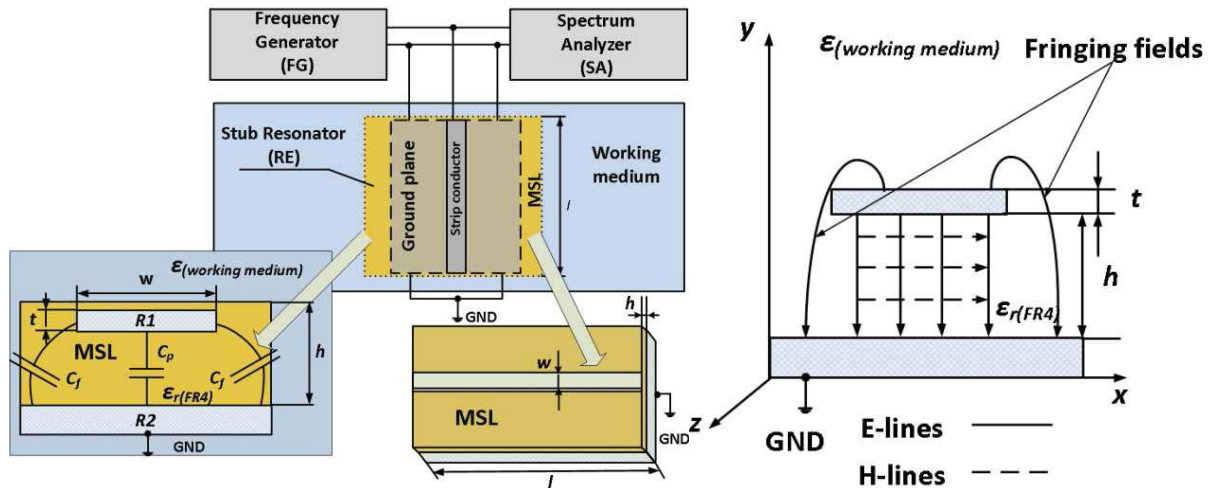


Fig. 4. Left: Schematic overview of the MSL used in this study: here l is the length (m), w is the width (m), h is the substrate thickness (m), t is the strip metallization thickness (m), $\epsilon_{r(FR4)}$ is the effective dielectric permittivity of substrate FR4, a composite material of woven fiberglass cloth and an epoxy resin, R_1 is the normalized series distributed resistance for the microstrip and R_2 is the normalized series distributed resistance for the ground planes of the MSL.

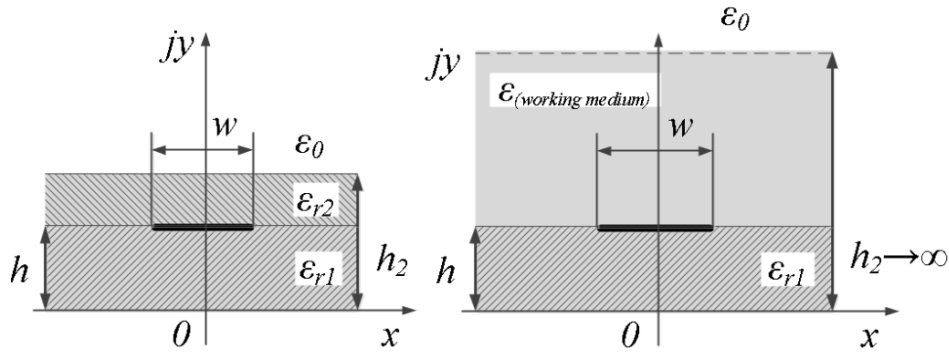


Fig. 5. Schematic overview of the three-layer MSL. On the left, as depicted in [17] and on the right in dimensions specifically adapted to this study.

The advantage of MSL-based designs above coaxial resonators is that they are well defined, and very feasible for cost effective mass production as a consumable (disposable sensor part) thereby reducing maintenance of a practical implementation of the MSL sensor. Additionally, MSL based designs allow further miniaturization [30 - 33]. A potential application of the MSL concept can be testing e.g. specific polymers or for that matter other types of coatings the stripline is covered with for their adsorption or absorption properties through dielectric measurements.

There are different ways to obtain the values of the inductance L , capacitance C , dielectric conductance G and series resistance, R , per unit length of microstrip transmission line. A first method is to determine these parameters, empirically. However, in contrast to the coaxial resonator, for MSL this procedure is quite extensive. Another way is theoretically by performing a full wave (3D) simulation. A third, more widely-used approach (and followed here as well) is based on the analysis of multilayer microstrip lines by a conformal mapping method [18], as outlined by J. Svacina in [19]. They derived and validated semi-empirical expressions for the effective dielectric permittivity ϵ_{eff} and characteristic impedance Z_c of a three-layer microstrip line with strip width w , substrate height h and substrate dielectric permittivity ϵ_{r1} , a dielectric on top of the substrate of height h_2 and dielectric permittivity ϵ_{r2} and the permittivity of air ϵ_0 . In the present study, ϵ_{r2} functions as working medium. Importantly, because our stripline is completely immersed in fluid, implying ϵ_{r2} equals ϵ of the fluid tested and the factual absence of ϵ_0 , h_2 is assumed to extend into infinity, as depicted in Fig.5.

Using $h_2 \rightarrow \infty$, and consequently $w/h \leq 1$, implies that the original equation for the filling factor q_2 in [19] can be reduced to:

$$q_2 = 0.5 - 0.9/\pi \cdot \ln(8h/w) \quad (16)$$

To derive the capacitance C and inductance L , as based on the corresponding value of the characteristic impedance Z_c , requires the propagation velocity v as functions of L , C and ϵ_{eff} :

$$v = \frac{1}{\sqrt{LC}} = \frac{1}{\sqrt{\mu_r \epsilon_{eff} \cdot \mu_0 \epsilon_0}} = \frac{c}{\sqrt{\mu_r \epsilon_{eff}}} \quad (17)$$

The characteristic impedance Z_c for lossless transmission lines is given by:

$$Z_c = \sqrt{L/C} \quad (18)$$

Implying L and C are expressed by:

$$L = Z_c^2 \cdot C \quad (19)$$

$$C = L/Z_c^2 \quad (20)$$

Substitution of Eqs. 19 and 20 results in:

$$L = Z_c \cdot \sqrt{\epsilon_{eff}} / c \quad (21)$$

$$C = \sqrt{\epsilon_{eff}} / (Z_c \cdot c) \quad (22)$$

The effective inductance of large ground planes has been described in details in [20]. Increasing the surface area of the ground plate hardly affects the MSL capacitance. Actually, this lack of effect was checked experimentally (see Supplementary information, Appendix A).

Considering that the MSL stub is connected to the main transmission line by the combination of two SMA (SubMiniature version A) connectors with a total length of 25 mm, the additional parallel capacitance of the coaxial insertion C_{SMA} and the series inductance

L_{SMA} must be taken into account in Eqs. 21 and 22, respectively, and can be calculated according to [2] and is applied in the program code is shown in Appendix D: (the effect of SMA connectors on the resonance frequency is shown in Appendix B).

The distributed resistance for microstrip R_1 can be obtained using the following approximation [23] as it is expressed by Eq. 23:

$$\frac{R_1 W}{R_s} = LR \left(\frac{1}{\pi} + \frac{1}{\pi^2} \ln \frac{4\pi\pi}{t} \right) \quad (23)$$

where R_s represents the surface resistance of the conductors and the loss ratio LR is given by Eq. 24:

$$\begin{aligned} LR &= 1 & u &\leq 0.5 \\ LR &= 0.94 + 0.132 \cdot u - 0.0062 \cdot (u)^2 & 0.5 < u &\leq 10 \end{aligned} \quad (24)$$

The distributed resistance for ground R_2 can be approximated by [15] and is given by Eq. 25:

$$\frac{R_2 W}{R_s} = \frac{u}{u + 5.8 + 0.03 \cdot 1/u} \quad 0.1 \leq u \leq 10 \quad (25)$$

This results in a total distributed resistance R of the microstrip line as it is expressed by Eq. 26:

$$R = R_1 + R_2 \quad (26)$$

As for the coaxial stub resonators, the distributed conductance G is given by Eq. 6:

However, in contrast to coaxial stub resonators, $\tan\delta_{eff}$ is defined by losses in both the fluid under investigation and the substrate material of the MSL. Therefore in this study, the dielectric loss $\tan\delta_{eff}$ should be considered as a qualitative parameter rather than a quantitative parameter to characterize the properties of a fluid under investigation.

Using Eqs. 6, 8-15 and 16-26, the dielectric properties of the fluid can be determined analogous to the fitting procedure described for the coaxial stub resonator systems [24 - 27]. It is worth noting that, according to [21 - 22]; radiation losses in the MSL become significant in case of a low characteristic impedance of the MSL, thick substrates and a low dielectric constant. For the MSL resonator applied in this study, it was shown that radiation losses are negligible as compared to the skin effect and dielectric losses.

3.3 Experimental

All experiments were performed with a HAMEG HMS3010 3 GHz Spectrum Analyzer with Tracking Generator, both with internal impedance Z_S and Z_{SA} of 50 Ω .

Table 1 and Table 2 give an overview of the dimensions of the two coaxial stub resonators and the MSL applied in this study, respectively; see also Figs. 1 and 4. The dimensions were chosen as such that (by approximation) the impedance of the system elements matched. In contrast, the dimensions of the resonator listed in Table 3 resulted in a mismatch of characteristic impedance.

In order to test our model and compare it with the performance of the resonators, the following solutions were used as dielectric fluid sample: demineralized water with a conductivity of $1 \cdot 10^{-4}$ S/m produced by a commercially available demineralization installation Milli-Q Advantage A10 Ultrapure Water Purification System (EMD Millipore), ethanol (100% denatured with 2-Propanol 2.5%) supplied by BOOM B.V. (Netherlands), and glycerol (100%) supplied by VNR (Netherlands).

The main algorithm for the model simulations was written in MATLAB code (MATLAB R2012b, Appendix D).

Table 1

Geometric parameters of the coaxial batch and flow-through resonators. The outer and the inner conductors of both resonators were made from copper.

Parameter	Flow-through resonator	Batch resonator
Length, l	1.01 (m)	$34 \cdot 10^{-2}$ (m)
Inner conductor diameter, d	$0.5 \cdot 10^{-3}$ (m)	$0.5 \cdot 10^{-3}$ (m)
Inner diameter of the outer conductor, D	$22.0 \cdot 10^{-3}$ (m)	$22.0 \cdot 10^{-3}$ (m)
Diameters of the fluid inlet and outlet	$7.0 \cdot 10^{-3}$ (m)	
Conductivity of copper, σ	$5.7 \cdot 10^7$ (S·m ⁻¹)	

Table 2

Geometric parameters of the MSL resonator. The outer and the inner conductor were made from HASL (hot air solder leveling).

Parameter	MSL resonator
Length, l	$33 \cdot 10^{-2}$ (m)
Substrate thickness, h	$1.93 \cdot 10^{-3}$ (m)
Width, w	$1.70 \cdot 10^{-4}$ (m)
Strip metallization thickness, t	$1.70 \cdot 10^{-4}$ (m)
Effective dielectric permittivity of substrate (FR4), ϵ_r	4.8 (-)
Conductivity of tin, σ^1	$8.7 \cdot 10^6$ (S·m ⁻¹)
Conductivity of copper, σ^1	$5.7 \cdot 10^7$ (S·m ⁻¹)

¹ The conductivity of HASL is mostly determined by conductivity σ of copper. The model simulations for the MSL system were executed with the conductivity σ of copper. The results of simulation for MSL with different conductors can be found in Appendix C.

Table 3

Geometric parameters of the coaxial batch resonator with mismatched characteristic impedance. The outer and the inner conductors of both resonators were made from stainless steel 316L.

Parameter	Batch resonator
Length, l	$42 \cdot 10^{-2}$ (m)
Inner conductor diameter, d	$5 \cdot 10^{-3}$ (m)
Inner diameter of the outer conductor, D	$12 \cdot 10^{-3}$ (m)
Conductivity of stainless steel 316L, σ	$7.7 \cdot 10^6$ (S·m ⁻¹)

3.4 Results and Discussion

Figs. 6 - 8 show AF plots for water, ethanol and glycerol as determined with the experimental set-up shown in Fig. 1; using either the batch or flow-through resonator of Table 1 (red curves). Blue curves indicate model simulations performed according to the procedure outlined in the previous section.

Table 4 summarizes the major modeling results.

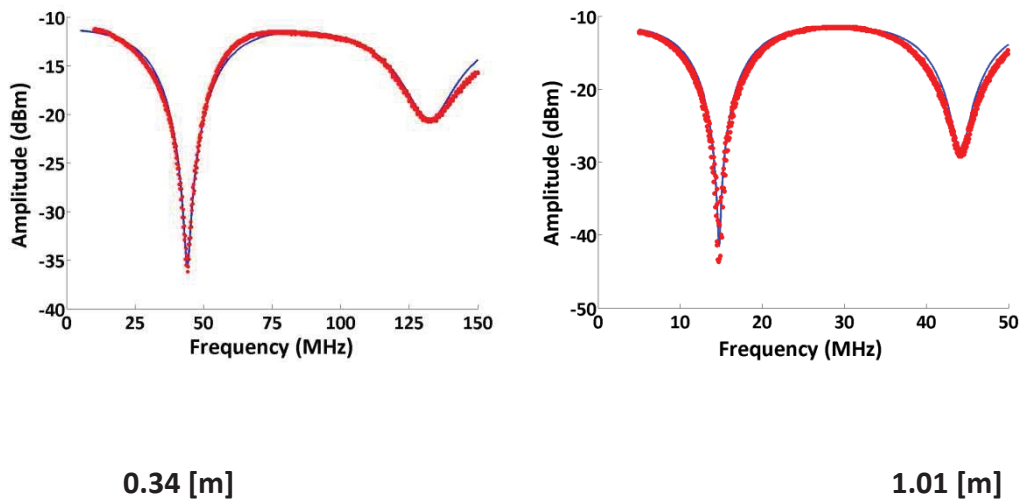


Fig. 6. Experimentally obtained amplitude versus frequency plot of ethanol (red) using a quarter wave length open-ended batch resonator (left panel) or flow-through resonator (right panel). Simulation data are shown for comparison (blue).

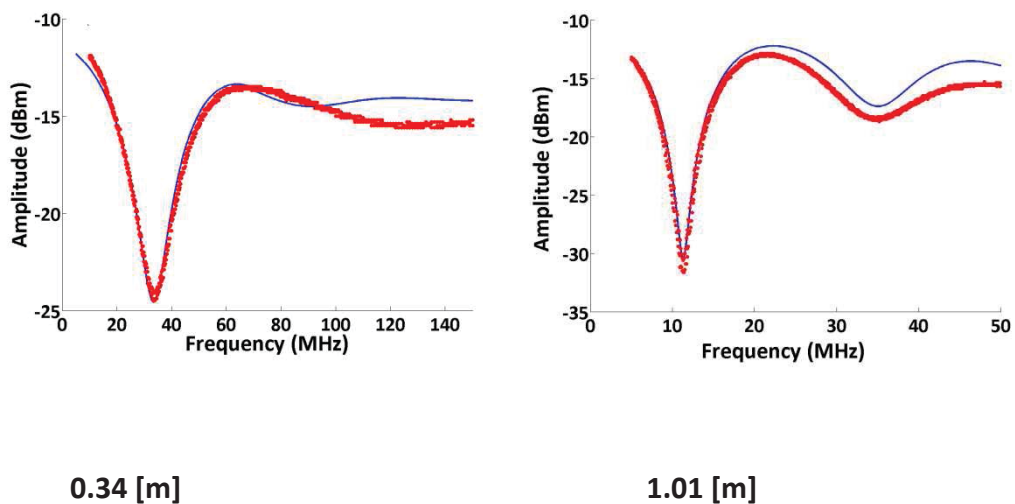


Fig. 7. Experimentally obtained amplitude versus frequency plot of glycerol (red) using a quarter wave length open-ended batch resonator (left panel) or a flow-through resonator (right panel). Simulation data are shown for comparison (blue).

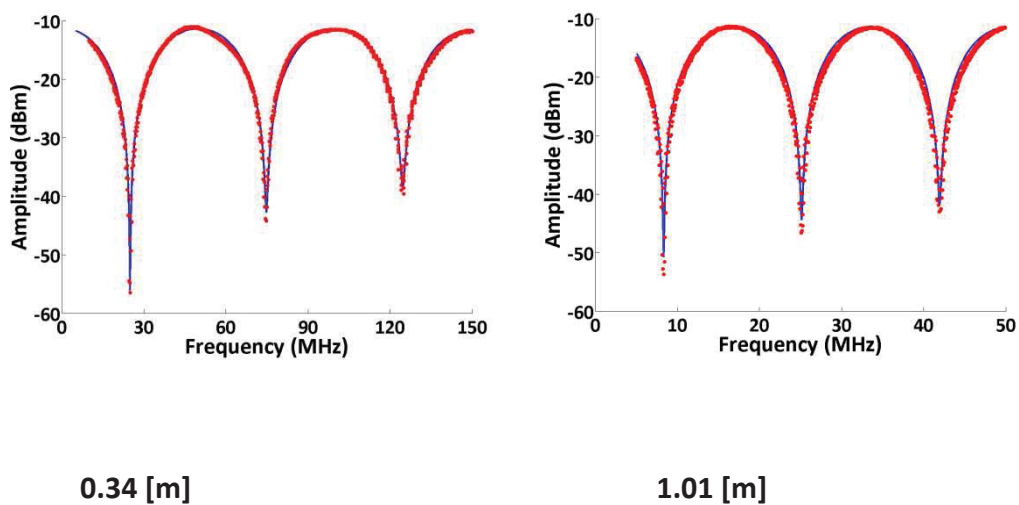


Fig. 8. Experimentally obtained amplitude versus frequency plot of demineralized water (red) using a quarter wave length open-ended batch resonator (left panel) or a flow-through resonator (right panel). Simulation data are shown for comparison (blue).

Table 4

Modeling results for the coaxial resonator stubs parameterized in Table 1, filled with either ethanol, water or glycerol. Literature ϵ_r values are indicated directly underneath the headings of the columns.

Res. Freq. ²	Ethanol (ϵ_r (-), 25.13; 24.35) ^[29]				Water (ϵ_r (-), 79.5; 78.76) ^[29]				Glycerol (ϵ_r (-), 42.49) ^[29]				
	f_{res} (MHz)	ϵ_r (-)	R (Ω/m)	$\tan\delta_{eff}$ (-)	f_{res} (MHz)	ϵ_r (-)	R (Ω/m)	$\tan\delta_{eff}$ (-)	f_{res} (MHz)	ϵ_r (-)	R (Ω/m)	$\tan\delta_{eff}$ (-)	
Batch	1 st	43.8	25.2	1.0	0.040	24.7	78.2	0.8	0.001	33.9	42.1	0.9	0.267
	2 nd	131.9	24.7	1.8	0.112	74.5	78.9	1.3	0.007	-	-	-	-
	3 rd	-	-	-	-	123.9	78.3	1.7	0.008	-	-	-	-
Flow-through	1 st	14.7	25.4	0.6	0.013	8.4	79.5	0.4	0.001	11.4	42.7	0.5	0.105
	2 nd	44.4	25.4	1.0	0.035	25.1	78.5	0.8	0.002	33.3	38.7	0.9	0.258
	3 rd	-	-	-	-	41.9	78.2	1.0	0.002	-	-	-	-

² Number of the resonance frequency.

From Figs. 6 - 8 it is concluded that there is good agreement between the model simulations and the experimentally determined AF plots over a wide frequency range covering two or even three resonance frequencies. This is true for both resonator geometries and with either ethanol or water as dielectric. The results in Table 4 also show good agreement between the determined values of ϵ_{water} and $\epsilon_{ethanol}$ and reported literature values. In addition, experimentally obtained values of the loss tangent $\tan\delta_{eff}$ are consistent. For instance, using the batch resonator filled with ethanol, the loss factor determined at 43.8 MHz (1st resonance frequency) is 0.040. Using the ethanol-perfused flow-through resonator instead, the loss factor as determined at 44.4 MHz (2nd resonance frequency) turns out to be 0.035.

For glycerol, there is also good agreement between the experimentally determined AF plots and the model simulations, at least for its 1st resonance frequency. However, at the second resonance frequency dielectric losses become too high for the model to accurately predict the performance of the resonator. The reason that the model no longer accounts for the behavior of the resonator might be that the latter starts to deviate from the TEM mode. Even though the model is rather inadequate to account for such behavior shown by high-loss fluids, the AF response can still be fitted to the model with the loss tangent as free parameter. For instance, a fit of the glycerol data of Fig. 7 results in a loss tangent of 0.258 and the amplitude of the 2nd resonance very similar to the one observed experimentally.

Figs. 9 - 11 show AF plots for the MSL resonator, described in Fig. 4 and Table 2, submerged in either ethanol, glycerol or water as dielectric, respectively. Table 5 summarizes some major modeling results.

Figs. 9 - 11 and Table 5 show that also for the MSL resonator model and experimentally obtained AF response match closely, implying that the resonant frequency, attenuation and quality factor of the resonator are predicted well, at least when immersed in the liquids investigated. For glycerol, differences between the experimentally determined and simulated AF plot near the second resonance frequency are less pronounced as compared to the results with the coaxial resonators. This effect may be caused by that fact that in the MSL, not only the fluid under investigation but also the substrate of the MSL is a dielectric. Since the dielectric losses of the MSL substrate are very small, overall dielectric losses are smaller compared to those observed during coaxial resonator experiments. The fact that the substrate of MSL-type resonators contributes to the overall apparent dielectric compromises (FR4, which has a dielectric constant of 4.6 or 4.8 tangent loss of 0.02 and a conductivity of $40.5 \cdot 10^{-3}$ [30 - 31] (to more or lesser extent) its sensitivity towards (changes in) the dielectric of the fluid to be measured. It should also be mentioned that variations in the wire width of the conductor on the MSL add to deviations between simulation and experimental data. Additionally, the electrical length of the immersed MSL resonator is longer than its physical length. In future designs we will (partly) remedy this artifact by perforating the substrate of such MSL-based devices.

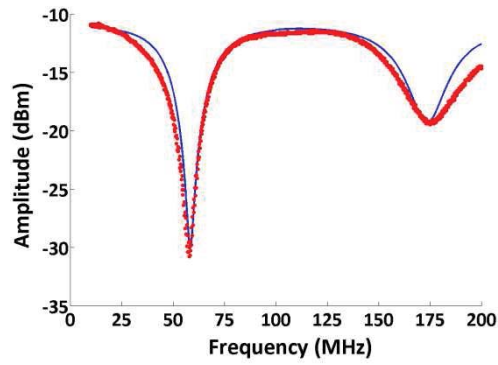


Fig. 9. Experimentally obtained amplitude versus frequency plot of ethanol (red) using a quarter wave length open-ended MSL resonator. Simulation data are shown for comparison (blue).

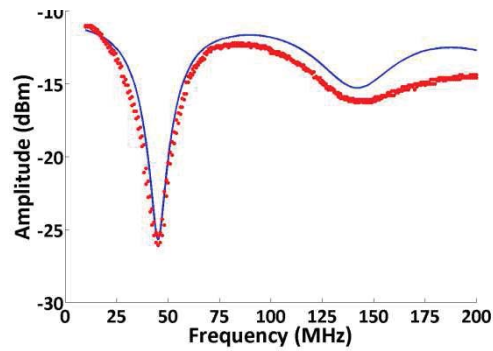


Fig. 10. Experimentally obtained amplitude versus frequency plot of glycerol (red) using a quarter wave length open-ended MSL resonator. Simulation data are shown for comparison (blue).

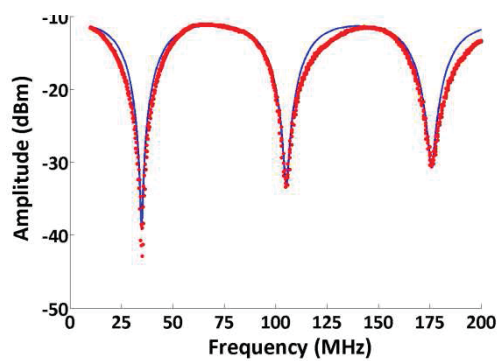


Fig. 11. Experimentally obtained amplitude versus frequency plot of demineralized water (red) using a quarter wave length open-ended MSL resonator. Simulation data are shown for comparison (blue).

Table 5

Modeling results for the MSL resonator of Table 2 filled with either ethanol, water or glycerol as dielectric Literature ϵ_r values are indicated directly underneath the headings of the columns.

MSL	Res. Freq. ³	Ethanol					Water					Glycerol					
		f_{res} (MHz)	ϵ_r (-)	R (Ω/m)	$\tan\delta_{eff}$ (-)	f_{res} (MHz)	ϵ_r (-)	R (Ω/m)	$\tan\delta_{eff}$ (-)	f_{res} (MHz)	ϵ_r (-)	R (Ω/m)	$\tan\delta_{eff}$ (-)	f_{res} (MHz)	ϵ_r (-)	R (Ω/m)	$\tan\delta_{eff}$ (-)
	1 st	57.9	27.5	7.22	0.033	35.1	81.2	6.32	0.002	45.7	48.11	6.27	0.10	-	-	-	-
	2 nd	175.0	27.4	11.13	0.076	105.0	80.0	9.90	0.004	-	-	-	-	-	-	-	-
	3 rd	-	-	-	-	176.2	80.0	12.16	0.005	-	-	-	-	-	-	-	-

³ Number of the resonance frequency.

We supported our experimental data with a newly developed model. The model alone suffices to describe the AF plot of our resonator, given the dielectric and loss tangent $\tan\delta_{eff}$ of the sample liquid are known within the frequency range considered, in other words if the resonator is filled with a liquid of known ϵ_r and $\tan\delta_{eff}$.

In case the dielectric properties of the fluid under investigation are unknown, the values of ϵ_{re} and $\tan\delta_{eff}$ within a frequency range of interest can be determined by fitting the model simulations against experimental data using the procedure described in the previous section.

In order to further investigate the predictive value of the model, systems with a significant impedance mismatch between the resonator and the transmission lines ($Z_c=50 \Omega$) were studied.

Figs. 12 - 14 show the results obtained with a coaxial resonator of large diameter. Even though in this case the characteristic impedance of stub resonator and transmission line mismatch: 5.9 Ω , 10.5 Ω , 8.1 Ω for demineralized water, ethanol and glycerol respectively, the model still predicts the shape of the response curve with reasonable accuracy. Table 6 summarizes the major modeling results. These results show the validity of the model for a wide range of geometries (i.e, match-mismatch conditions).

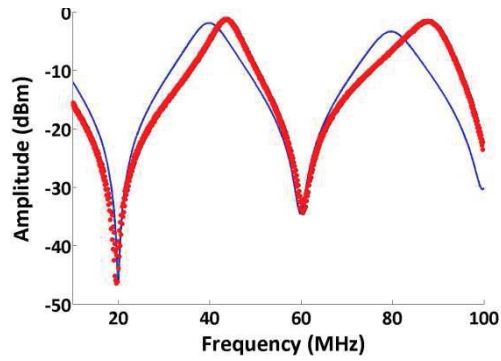


Fig. 12. Experimentally obtained amplitude versus frequency plot of demineralized water (red) using a quarter wave length open-ended batch resonator with mismatched characteristic impedance. Simulation data are shown for comparison (blue).

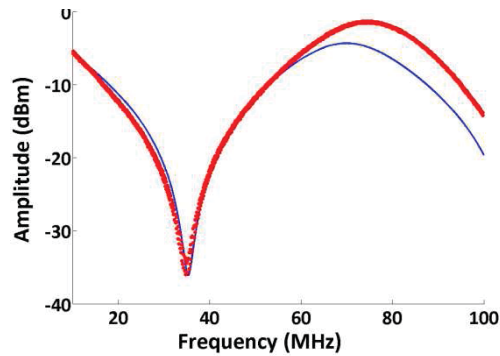


Fig. 13. Experimentally obtained amplitude versus frequency plot of ethanol (red) using a quarter wave length open-ended batch resonator with mismatched characteristic impedance. Simulation data are shown for comparison (blue).

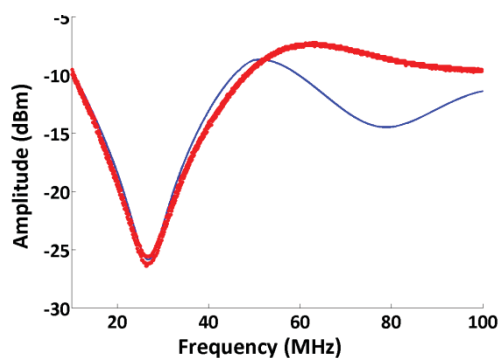


Fig. 14. Experimentally obtained amplitude versus frequency plot of glycerol (red) using a quarter wave length open-ended batch resonator with mismatched characteristic impedance. Simulation data are shown for comparison (blue).

Table 6

Modeling results for the resonator with mismatched (RM) characteristic impedance in Table 3 filled with either ethanol, water or glycerol as dielectric Literature ϵ_r values are indicated directly underneath the headings of the columns.

Res. Freq. ⁴	Ethanol				Water				Glycerol			
	f_{res} (MHz)	ϵ_r (-)	R (Ω/m)	$\tan\delta_{eff}$ (-)	f_{res} (MHz)	ϵ_r (-)	R (Ω/m)	$\tan\delta_{eff}$ (-)	f_{res} (MHz)	ϵ_r (-)	R (Ω/m)	$\tan\delta_{eff}$ (-)
1 st	35.3	25.4	0.8	0.052	19.9	80.0	0.6	0.020	27.1	42.5	0.9	0.25
2 nd	-	-	-	-	60.2	80.8	1.1	0.029	-	-	-	-

⁴ Number of the resonance frequency.

We recorded on three fluids of different physico-chemical nature, water, ethanol and glycerol. For instance, polar and non-polar solvents are clearly distinctive in the sense that dielectric permittivity ϵ_r and $\tan\delta_{eff}$ of polar liquids exhibit stronger frequency dependence. Even though we did not quantify the match between experimental data and model predictions in more detail, Figs. 6-11 clearly show that the resonators described here and/or the model itself perform better with water and ethanol than with glycerol as dielectric. Given the followed procedure to construct the AF response, as outlined above, the model is expected to predict the AF response more accurately when filled with fluids of high ϵ_r and /or low complex conductivity G because both parameters contribute to the overall loss factor. This explains that the low loss in demineralized water is due to its low G , and the high ϵ_r of water. For ethanol the overall loss is also relatively low but significantly higher than that of water. It is noted that the complex conductivity G consists of a real part accounting for the movement of free charge that is in phase with the electric field and an imaginary part accounting for out of phase movement of dipoles that are aligned by the electrical field. Ethanol has a slightly higher G than water in the frequency range studied as well as a considerably lower ϵ_r . As compared to water and ethanol, glycerol has a considerably higher G in the frequency range studied and a value of ϵ_r that is between water and ethanol, resulting in an increased loss level.

A very interesting alternative approach to assess the properties of fluids was developed by Valentin et al., Filiâtre et al. and more recently Cassiède et al. [34 - 37]. Their approach comprises the characterization of the behaviour of quartz crystal resonators that are fully immersed in a fluid under investigation. In a nutshell, the resonant frequency and impedance characteristics of the immersed quartz crystal depend strongly on the properties of the rigid thin fluid film attached to the resonator surface and the influence of interfacial effects on energy dissipation. In x and y, it was shown that the quartz-crystal resonator system can be modeled by an acoustic equivalent to the electrical transmission line model based on the telegraphers equations. Since the model in the present study and the quartz-crystal system have different focus i.e., focus on the characterization of the dielectric permittivity and dielectric losses in a fluid and focus on the fluid flow characteristics respectively, combination of both techniques may result in a powerful sensor system. It is noted that both techniques are sensitive to the conductivity of the fluid under investigation asking for addition measures to operate the systems at these conditions.

So far, we tested the sensor, and by implication the model, for analytical solutions only, i.e. solutions of known composition. To demonstrate the practical application of the sensor and the model we extended our measurements to an “unknown” sample, in this case Russian vodka of conductivity of 2 $\mu\text{S}/\text{cm}$ and temperature of 20 °C. Following the fitting routine described in Appendix D, the obtained values for ϵ_{re} (Eq.8) and $\tan\delta_{eff}$ were 63.91 and 0.008, respectively (Fig. 15). According to [29], the static dielectric permittivity of demineralized water with 30% - 40% ethanol falls in between 66.08 (66.00) and 59.67 (59.60). The recorded 63.91 for the vodka sample seems sensible given the specification of the manufacturer that the vodka contains 37.5% ethanol (v/v).

With $2 \mu\text{S}/\text{cm}$, ethanol is a fluid of low conductivity. Due to increasing losses, the shape of the AF response changes at higher solution conductivity, ultimately resulting in the total disappearance of any resonance frequency peak. In such case, the system is not working as a resonator anymore. As an example, and for comparison with the vodka sample, Fig. 16 shows data obtained with Dutch red wine of conductivity of $2.32 \text{ mS}/\text{cm}$ (i.e., 3 orders of magnitude higher than the conductivity of the tested vodka) and temperature of 18°C and containing 10.5% ethanol (v/v). As in agreement with the quartz-crystal resonator, the AF response shown here does not provide any information any more about the liquid sample, a direct result of the high conductivity of the fluid sample.

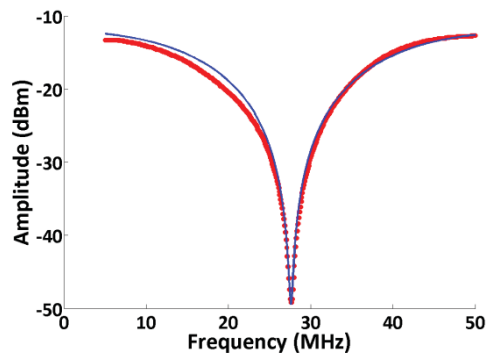


Fig. 15. Experimentally obtained amplitude versus frequency plot of vodka (red) using a quarter wave length open-ended batch resonator. Fitting data are shown for comparison (blue).

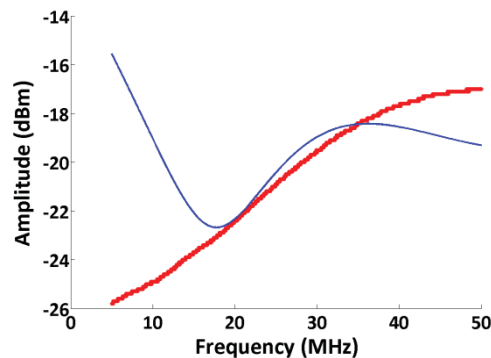


Fig. 16. Experimentally obtained amplitude versus frequency plot of wine (red) using a quarter wave length open-ended batch resonator. Fitting data are shown for comparison (blue).

3.5 Conclusions

The model predicting the AF response of a stub resonator operated with a fluid as dielectric presented here accounts for dielectric losses, conductor losses including the skin effect, the characteristic impedance of the resonator and impedance mismatch between the stub resonator and measuring equipment connected to it.

The model was successfully applied to predict the behavior of coaxial stub resonators and MSL resonators with deionized water, ethanol and glycerol as dielectric over a frequency range of 1 to 3 resonances. Calculated ϵ_r values derived from the experimental data are close to reported values in the literature, for water as well as for ethanol and glycerol. When exposed to fluids of “unknown” composition (in this case vodka and wine), both resonator and model gave results as anticipated by the large difference between the conductivity of the two fluids. To the best of our knowledge, in contrast to the currently existing models, our model includes all parameters needed to simulate to a rather large extent of accuracy the AF response of a dielectric. . Even though applied to only two different types of resonators, the model may be useful for all those sensors based on lossy transmission line theory. We tested different designs, a coaxial batch and flow-through resonator and a microstrip line resonator. Results obtained with these different systems are in close agreement. The different types of resonators all have their specific pro’s and contra’s. The coaxial flow-through and MSL-type resonators offer the ability for continuous, on-line measurements. We foresee most applications of this type of sensors as early warning systems for the quality control of e.g. drinking water, industrial process water or for that matter any other kind of fluid contaminated with impurities. Since these sensors are characterized by high dielectric losses and unconventional resonator geometry, extensive modeling can be a helpful tool to both optimize the sensor design and analyse experimental data.

3.6 Acknowledgement

This work was performed in the TTIW-cooperation framework of Wetsus, Centre of Excellence for Sustainable Water Technology (www.wetusus.nl). Wetusus is funded by the Dutch Ministry of Economic Affairs, the European Union Regional Development Fund, the Province of Fryslân, the City of Leeuwarden and the EZ/Kompas program of the “Samenwerkingsverband Noord-Nederland”. The authors thank the participants of the research theme Sensoring for the fruitful discussions and their financial support.

3.7 References

1. P. Natarajan, Micro coaxial transmission lines for integrated microwave circuits, Theses and Dissertations, Paper 2298, Scholar Commons Citation, University of South Florida, 2007, pp. 17-19.
2. N.A. Hoog-Antonyuk, W. Olthuis, M.J.J. Mayer, D. Yntema, H. Miedema, A. van den Berg, On-line fingerprinting of fluids using coaxial stub resonator technology, *Sensors and Actuators B* 163 (2012) 90-96, doi: dx.doi.org/10.1016/j.snb.2012.01.012.
3. M.J.J. Mayer, N. Hoog, RF antenna filter as a sensor for measuring a fluid, WO Patent 005084, 2011.
4. Fabbri, T. Fen-Chong, O. Coussy, Dielectric capacity, liquid water content, and pore structure of thawing-freezing materials, *Regions Science and Technology*, Volume 44, Issue 1, January 2006, pp. 52-66.
5. H. Eller, A. Denoth, A capacitive soil moisture sensor, *Journal of Hydrology*, Volume 185, Issues 1-4, 1 November 1996, pp. 137-146.
6. Hong-Tao Sun, Liang-Ying Zhang, Xi Yao, Wojciech Wlodarski, AT-cut quartz resonators for determination of viscoelastic and dielectric properties of water/glycerol, *Sensors and Actuators A: Physical*, Volume 43, Issues 1-3, May 1994, pp. 208-212.
7. T. Fen-Chong, A. Fabbri, J.-P. Guilbaud, O. Coussy, Determination of liquid water content and dielectric constant in porous medium by the capacitive method, *Comptes Rendus Mecanique*, Volume 332, Issue 8, August 2004, pp. 639-645.
8. D.M. Hagl, D. Popovic, S.C. Hagness, J.H. Booske, M. Okoniewski, Sensing volume of open-ended coaxial probes for dielectric characterization of breast tissue at microwave frequencies, *Microwave Theory and Techniques, IEEE Transactions on*, Volume: 51, Issue:4, 08 Apr 2003, pp. 1194 – 1206.
9. Y.Wang and M.N. Afsar, Measurement of complex permittivity of liquids using waveguide techniques, *Progress In Electromagnetics Research*, Vol. 42, 2003, pp. 131-142.
10. V.V. Komarov, S. Wang, J. Tang, Permittivity and measurements, *Wiley Encyclopedia of RF and Microwave Engineering*. Volume 4, 2005, pp. 3693-3711.
11. D.M. Pozar, *Microwave Engineering*, Wiley, 2004.
12. O. Zinke, H. Brunswig, *Hochfrequenztechnik 1, Hochfrequenzfilter, Leitungen, Antennen*, 6. Auflage, Berlin: Springer 2000, pp. 86-88.
13. W. Richards, Yuen Lo, D. Harrison, An improved theory for microstrip antennas and applications, *Antennas and Propagation, IEEE Transactions on* , vol.29, no.1, pp.38,46, 1981.
14. O. Coufal, Inductance of coaxial cable, *Energyspectrum*, 2008, vol. 3, no. 1, p. 1-5. ISSN: pp. 1214-7044.
15. R.E. Collin, *Foundations for Microwave Engineering*, Wiley IEEE, pp.156-157, 2000.
16. F. Leferink, C. Roeloffzen, *Handout Transmission Medium: Transmission Lines*, Universty of Twente, 2007.
17. http://ewh.ieee.org/r8/serbia_montenegro/education/EdSoc_SCG_002_1.pps#277,1, Software Tools for Microwave Research, Design, and Education.
18. W. Olthuis, W. Streekstra, P. Bergveld, Theoretical and experimental determination of cell constants of planar-interdigitated electrolyte conductivity sensors, *Sensors and Actuators B: Chemical*, Volume 24, Issues 1-3, March 1995, Pages 252-256, ISSN 0925-4005.
19. J. Svacina, Analysis of multilayer microstrip lines by a conformal mapping method, *Microwave Theory and Techniques, IEEE Transactions on*, vol.40, no.4, Apr 1992, pp.769-772.
20. F.B.J. Leferink, M.J.C.M. van Doom, Inductance of printed circuit board ground planes, *Electromagnetic Compatibility*, 1993. Symposium Record., 1993 IEEE International Symposium on 9-13 Aug, 1993, pp. 327-329.
21. L. Lewin, Radiation from discontinuities in strip-line, *Proc. Inst. Elec. Eng.*, vol. 107C, pp. 163-170, 1960.
22. L. Lewin, Spurious radiation from microstrip, *Proc. Inst. Elec. Eng.*, vol. 125, July 1978, pp. 633-642.
23. H.A. Wheeler, Formulas for the skin effect, *Proc. IRE*, Vol. 30, No. 9, September 1942, pp. 412-4124.
24. K. Verna, Nasimuddin and A.S. Omar, Microstrip resonator sensor for determination of complex permittivity of materials in sheet, liquid and paste form, *IEE Proc.- Microw. Anteenas Propag.* Vol 152, NO. 1, February 2005.
25. Liu, Yang Pu, A microstrip resonator with slotted ground plane for complex permittivity measurements of liquids, *IEEE Microwave and Wireless components letters*, vol. 18, No 4, April 2008.
26. A. Rashidian, M.T. Aligodarz, D.M. Klymyshyn, Dielectric characterization of materials using a modified microstrip ring resonator technique, *IEEE Transactions on Dielectrics and Electrical Insulation*, Volume 19 , Issue 4, 2012.

27. K. Saeed, A.C. Guyette, I.C. Hunter, R.D. Pollard, Microstrip Resonator Technique for Measuring Dielectric Permittivity of Liquid Solvents and for Solution Sensing, Microwave Symposium, IEEE/MTT-S International, 2007.
28. F.B.J. Leferink, M.J.C.M. van Doom, Inductance of printed circuit board ground planes, Electromagnetic Compatibility, 1993. Symposium Record., 1993 IEEE International Symposium on 9-13 Aug, 1993, pp. 327-329.
29. Ch. Wohlfarth, M.D. Lechner, Static Dielectric Constants of Pure Liquids and Binary Liquid Mixtures, Supplement to IV/6, Series:Landolt-Börnstein: Numerical Data and Functional Relationships in Science and Technology - New Series, Vol. 17, Subseries:Physical Chemistry, 2008, p. 203.
30. F.A. Ayoub, Analysis of Rectangular Microstrip with Air Substrates, Journal of Electromagnetic Waves and Applications, Volume 17, Issue 12, 2003, pp. 1755-1766.
31. J.R Aguilar, M. Beadle, P.T. Thompson and M.W. Shelley, The microwave and RF characteristics of FR4 substrates, Low Cost Antenna Technology (Ref. No. 1998/206), IEE Colloquium on 24 Feb., 1998.
32. A. K. Skrivervik, J.-F. Zürcher, O. Staub, J. R. Mosig, PCS Antennas: The Challenge of Miniaturization, IEEE AP magazine, Aug. 2001.
33. J. Joubert, Spiral microstrip resonators for narrow-stopband filters, Microwaves, Antennas and Propagation, IEE Proceedings , vol.150, no.6, Dec 2003 , pp.493,496.
34. M. Cassiède, J.-L. Daridon, J.H. Paillol, J. Pauly, Characterization of the behaviour of a quartz crystal resonator fully immersed in a Newtonian liquid by impedance analysis, Sensors and Actuators A: Physical, Volume 167, Issue 2, June 2011, pp. 317-326.
35. C. Filiâtre, G. Bardèche, M. Valentin, Transmission-line model for immersed quartz-crystal sensors, Sensors and Actuators: A Physical 44, 1994, pp. 137–144.
36. M. Valentin, C. Filiâtre, Application of the impedance transformation on transmission lines to electrochemical microbalance, Journal de physique III 4 (1994), pp. 1305–1319.
37. M. Cassiède, J.H. Paillol, J. Pauly, J.-L. Daridon, Electrical behaviour of AT-cut quartz crystal resonators as a function of overtone number, Sensors and Actuators A: Physical, Volume 159, Issue 2, May 2010, pp. 174-183.

3.8 Supplementary Information

Appendix A

Fig. A shows that a larger ground plane of the MSL resonator does not significantly affect the resonance frequency f_{res} .

Appendix B

Fig. B shows simulation data (blue and pink) on the influence of the use of SMA connectors on resonance frequency f_{res} . For comparison, experimental data are also shown (red).

Appendix C

Figure C shows simulation data on the effect of the nature of the conductors of the MSL resonator, i.e., tin, copper or gold, on the AF response.

The discrepancy between experimentally obtained and simulation data is partly due to radiation losses, not included in the simulation, notably at higher frequencies (e.g. 4th resonance frequency) [18, 19].

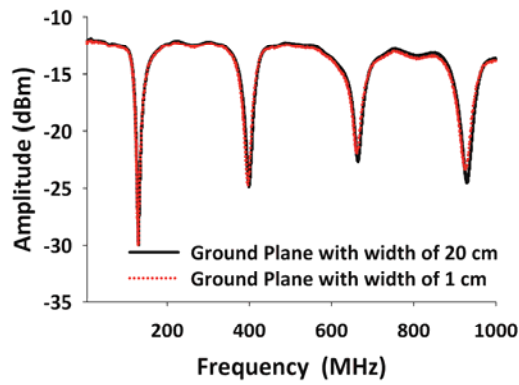


Fig. A. Experimentally obtained AF plot of air using a quarter wave length open-ended MSL resonator with a ground plane width of either 1 cm or 20 cm.

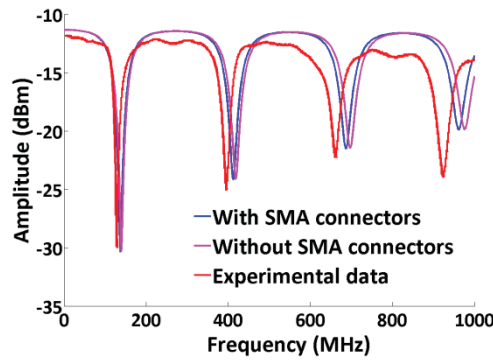


Fig. B. AF plot of air using a quarter wave length open-ended MSL resonator. Simulation data refer to a system with (blue) and without SMA connectors (pink). Experimental data are also shown (red).

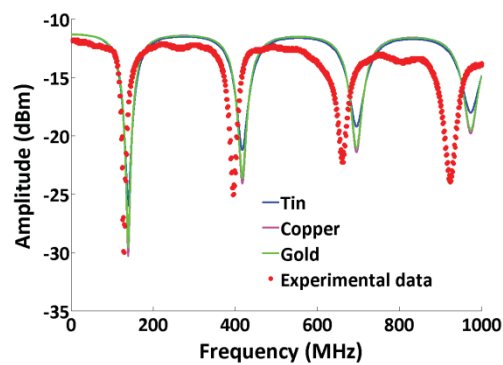


Fig. C. Simulated AF data for a quarter wave length open-ended MSL resonator with conductors made of either tin, copper or gold. Experimental data (obtained with copper) are shown for comparison.

Appendix D

Here we demonstrate an example of the MATLAB code and data file to realize the fitting of the static dielectric permittivity ϵ_{re} and effective loss tangent $\tan\delta_{eff}$ as parameters of function of the output voltage V_{out} .

Main program for parameter estimation for coaxial resonator:

```
clear all % Clear all variables in function workspace
close all % Close all figures
clc % Clear command window
load testethanol1011.txt % load the file "testethanol1011.txt"
%- See the Supplementary Information
f=testethanol1011(:,1); % Load experimental data; frequency
amplitude=testethanol1011(:,2); % Load experimental data; amplitude
f=f*1e+6; % Frequency conversion
%- Plot experimental data
plot(f, amplitude, 'ob')
hold on
x0 = [0.001 25];
ya0 = myfun3(x0,f);
%- Plot initial values
hold on;
plot(f,ya0,'--m')
%-Boundary conditions
LB = [0 10]; % Lower bounds
UB = [1 100]; %Upper bounds
% -Solving nonlinear least-squares curve fitting
[x,resnorm] = lsqcurvefit('coax_resonator',x0,f,amplitude, LB, UB)
ya = coax_resonator(x,f);
%- Plot fit results
Hf = plot(f,ya,'r');
set(Hf, 'LineWidth',2)
hold on
```

Function evaluates the model the amplitude-frequency response of coaxial transmission line type resonators filled with lossy dielectric fluids:

```
function F = coax_resonator(x,f)
len =1.01; % length of the coax resonator [m]
b = 22e-3; % inner diameter of the outer conductor [m]
a = 0.5e-3;% outer diameter of the inner conductor [m]
c=3*1e+8; % speed of light in vacuum [m/s]
E = x(2) * 1/(4*pi*1e-7*c*c); % vacuum permeability [H/m]
Ur=1; %relative dielectric permeability of the dielectric between inner and outer conductors [-]
u = Ur*4*pi*1e-7; % magnetic permeability of the dielectric [H/m]
sigma=6.64e-4;%conductivity of the dielectric between inner and outer conductors [S/m]
sigma_copper=57e+6;%conductance of the metal applied for inner and outer conductors (copper) [1/(Ohm*m)]
C = ((2*pi*E)/log(b/a)); % capacitance of the open ended coaxial stub resonator [F]
L = ((u/(pi*2))*log(b/a));% inductance of the open ended coaxial stub resonator [H]
%Define the input voltage supplied by the function generator [V]
vin=121.48e-3; %input voltage supplied by the function generator [V]
omega = 2*pi*f;% angular frequency [rad/s]
Eim=((omega.*E.*x(1))-sigma)./omega;%imaginary part of complex dielectric permittivity
skin_depth=sqrt(2./(omega.*u.*sigma_copper));%skin_depth
Rs=1./(sigma_copper.*skin_depth);% surface resistivity of the inner and outer conductor of the resonator
R=(Rs/(2*pi)*(1/(0.5*a)+1/(0.5*b)));% distributed element resistance R of the resonator [Ohm/m]
G=(omega.*Eim+sigma).(omega.*E).*omega.*C;%distributed element conductance of the resonator [F/(m*s)]
gamma =(sqrt((R+1i.*omega.*L).(G+1i.*omega.*C)));%complex propagation constant [1/m]
%notes on gamma: Re(gamma)=alfa = attenuation constant representing losses [Np/m];
Im(gamma)=beta=phase of the propagation constant [rad/m]
%since the signal is oscillating in time with omega rad/s, the propagation velocity of the wave [m/s] =
omega/beta; also, beta = 2*pi/wavelength.
Zc=sqrt(((R+1i.*omega.*L)/(G+1i.*omega.*C)));% complex characteristic impedance of the resonator [Ohm]
Zin=Zc.*coth(gamma.*len);%complex input impedance of the resonator [Ohm]
vout=sqrt((real(Zin.*(vin./(50+2*Zin))))^2+(imag(Zin.*(vin./(50+2*Zin))))^2);%modulus of vout, the is the
recorded voltage by the spectrum analyzer [V]
F =20.*log10(vout)+13;%vout as a power ratio in dBm i.e., the measured power referenced to one mWatt and
the underlying assumption of a 50 Ohm load resistance
```

Main program for parameter estimation for microstrip resonator:

```
clear all % Clear all variables in function workspace
close all % Close all figures
clc % Clear command window
load msl_ethanol.txt % load the file "msl_ethanol.txt"
%- See the Supplementary Information

f=msl_ethanol(:,1); % Load experimental data; frequency
amplitude=msl_ethanol(:,2); % Load experimental data; amplitude

f=f*1e+6; % Frequency conversion
```



```

%- Plot experimental data
plot(f, amplitude, 'or')
hold on
x0 = [0.001 10];
ya0 =msl_resonator(x0,f);
% % - Plot initial values
hold on;
plot(f,ya0,'--m')
%-Boundary conditions
LB = [0 1]; % Lower bounds
UB = [1 100]; %Upper bounds
% -Solving nonlinear least-squares curve fitting
[x,resnorm] = lsqcurvefit('msl_resonator',x0,f,amplitude, LB, UB)
ya = msl_resonator(x,f);
%- Plot fit results
Hf = plot(f,ya,'b');
set(Hf, 'LineWidth',2)
hold on
xlabel('Frequency, (Hz)');
ylabel('Amplitude, (dBm)');
grid on
hold on

```

Function evaluates the model the amplitude-frequency response of microstrip transmission line type resonators immersed in lossy dielectric fluids:

```

function F = msl_resonator(x,f)
c=3*1e+8; % speed of light in vacuum [m/s]
E = x(2) * 1/(4*pi*1e-7*c*c); % vacuum permeability [H/m]
c=3*1e+8; % speed of light in vacuum [m/s]
mr=1; %relative dielectric permeability of the dielectric between inner1 and outer1 conductors [-]
m0=4*pi*1e-7; % magnetic permeability of the dielectric [H/m]
m = mr*m0; % magnetic permeability of the dielectric [H/m]

sigma=6e-4;%conductivity of the dielectric under test [S/m]
sigma_copper1=57e+6;%conductance of the metal applied for inner1 and outer1 conductors (stainless steel)
[1/(Ohm*m)]
h=0.00193;%thickness ('height') of substrate [m]
t=0.00017;%thickness of strip metallization [m]
w=0.00017; %width of microstrip [m]
u=w/h;% magnetic permeability of the dielectric [H/m]
lensma=5.4e-3+17.25e-3
len=0.33+lensma; % length of the microstrip resonator [m]
er1=4.8; % static dielectric permittivity of FR4
%relative dielectric permeability of the dielectric [-]
e0=1/(4*pi*1e-7*c*c); % vacuum permeability [H/m]
q1= 0.5+ 0.9/(pi*log(8*h/w)) % filling factor (by J. Svacina)
q2= 0.5-0.9/(pi*log(8*h/w)) % filling factor (by J. Svacina)
e_eff=er1*q1+x(2)*((1-q1)*(1-q1))/(x(2)*(1-q1-q2)+q2) % effective permittivity (by J. Svacina)
Zc=60*log(8*h/w)/sqrt(e_eff) % characteristic impedance (by J. Svacina)
Cmsl=sqrt(e_eff)/(Zc*c) % capacitance of msl [H/m]
Lmsl=Zc*sqrt(e_eff)/(c) % inductance of msl [H/m]
Lsma= 3.9452e-07; % inductance of sma [H/m]

```

```

Csma= 6.2063e-11; % capacitance of sma [H/m]
L=(Lsma*lenssma/(lenssma+len))+(Lmsl*len/(lenssma+len)) % inductance of msl resonator+sma [H]
C=(Csma*lenssma/(lenssma+len))+(Cmsl*len/(lenssma+len)) % capacitance of msl resonator+sma [F]
%
%Define the input voltage supplied by the function gener1ator [V]

vin=129.48e-3; %input voltage supplied by the function gener1ator [V]
omega = 2*pi*f;% angular frequency [rad/s]
Eim=((omega.*E.*x(1))-sigma)./omega;%imaginary part of complex dielectric permittivity
skin_depth=sqrt(2./(omega.*m.*sigma_copper1));%skin_depth
%
% distributed element resistance R of the msl resonator [Ohm/m] by Collin et al.
if (u<=0.5) please put comment and / or reference
    LR=1; ;% Loss ratio [by Collin]
else
    LR=0.94+0.132*u-0.0062*u^2; % Loss ratio [by Collin]
end
Rs=1./(sigma_copper1.*skin_depth);% surface resistivity of the inner1 and outer1 conductor of the resonator
R1=(Rs*LR*(1/pi+1/pi^2*log(4*pi*w/t)))/w; % Normalized series resistance of for the microstrip [by Collin]
R2=(Rs*(u/(u+5.8+0.03*1/u)))/w;% Normalized series resistance of the ground plane [by Collin]
R=R1+R2;% distributed element resistance R of the resonator [Ohm/m]
%
G=(omega.*Eim+sigma).(omega.*E).*omega.*C;%distributed element conductance of the resonator [F/(m*s)]
gamma =(sqrt((R+1i.*omega.*L).(G+1i.*omega.*C)))/omega;%complex propagation constant [1/m]
%notes on gamma: Re(gamma)=alfa = attenuation constant representing losses [Np/m];
Im(gamma)=beta=phase of the propagation constant [rad/m]
%since the signal is oscillating in time with omega rad/s, the propagation velocity of the wave [m/s] =
omega/beta; also, beta = 2*pi/wavelength.
Zc=sqrt(((R+1i.*omega.*L)/(G+1i.*omega.*C)));% complex characteristic impedance of the resonator [Ohm]
Zin=Zc.*coth(gamma.*len);%complex input impedance of the resonator [Ohm]
vout=sqrt((real(Zin.*(vin./(50+2*Zin))))^2+(imag(Zin.*(vin./(50+2*Zin))))^2);%modulus of vout, this is the
recorded voltage by the spectrum analyzer1 [V]

F =20.*log10(vout)+13;%vout as a power ratio in dBm i.e., the measured power referenced to one mWatt
and the underlying assumption of a 50 Ohm load resistance
    
```

Additional program to calculate the L and C for SMA connectors:

```

clc
%This program allows to calculate the inductance and capacitance of
%different combinations of sma connectors
len = 5.4e-3+17.25e-3 % Total length of sma for PCB and sma T [m]
b = 7.76e-3;% Outer conductor [m]
a = 1.08e-3; % Inner conductor [m]
Er = 2.2; % The inner dielectric material of sma is teflon
%Dielectric permittivity of teflon is 2.2
Ur = 1;
E = Er * 8.854e-12; %Permittivity
u = Ur*1.257e-6; %Permeability
C = (2*pi*E)/(log(b/a)) % Capacitance
L = (u/(pi^2))*log(b/a) %Inductance
    
```



Tomsk, Tomsk State University of Control Systems and Radioelectronics (TUSUR)



Chapter 4

On-line Method for
Assessing the Ethanol
Content of Solutions
Using Coaxial
Stub Resonator
Technology

Abstract

Here we demonstrate the proof-of-principle of a new type of sensor to evaluate bulk solvent properties of ethanol. Our sensing device is based on the operating principle of a quarter wave length open-ended coaxial stub resonator. This technique is feasible for in-line measurements in a flow-through sensor that, if desirable, can be embedded in existing process piping or equipment. The adequacy of the method is demonstrated by comparing experimental data with different mathematical models predicting the dielectric properties of binary mixtures. Even though we used a coaxial stub resonator to assess the properties of binary water – ethanol mixtures, the potential applicability of the technique reaches further. Indeed, the method introduced here might be a useful tool in the field of food industry, organic chemistry, biochemistry and microbiology for on-line monitoring the content of ethanol.

This chapter is based on the article submitted as:

N.A. Hoog, H. Miedema, M.J.J. Mayer, W. Olthuis, S. G. Kataev, A. van den Berg, *On-line Method for Assessing the Ethanol Content of Solutions Using Coaxial Stub Resonator Technology*, Measurement

4.1 Introduction

The direct real-time determination of ethanol is an essential tool in the production process of alcoholic beverages like spirits, wine and beer, among others [1, 2]. Despite the diversity of existing technologies [3, 4], there is a lack of sensors that can operate both in-line and off-line and can analyze both large and small fluid volumes.

Coaxial stub resonators consist of an inner and outer conductor separated by a dielectric medium, in our particular case water, possibly containing different levels of ethanol. With an input signal of constant amplitude but variable frequency, the frequency of lowest load impedance, i.e., the resonance frequency (f_{res}), is determined. The value of f_{res} solely depends on the resonator length, the relative magnetic permeability of the material the sensor is made of and the dielectric permittivity of the fluid. The amplitude output at f_{res} depends on the characteristic impedance of the resonator, which, in turn, depends on material and geometrical parameters (e.g., ratio of inner and outer conductor diameter) and fluid characteristics (dielectric permittivity). Apart from f_{res} and the output amplitude, the shape (e.g., width of the resonance peak) of the amplitude-frequency or AF response depends on losses in both conductors (e.g., skin effect) and dielectric losses in the fluid (e.g., due to the conductivity of ions present). In two previous publications [5, 6] we showed that a sensor based on this principle can be used to monitor the composition of the fluid that acts as dielectric in between the two conductors. In addition, it was possible to adequately model and predict the experimentally observed response, including all the losses. It is also worth to mention that the inline sensor based on stub resonator technology can be realized using standard commercially available electronic components like a microcontroller, function generator chip and ADC. We thus developed a sensor to determine the ethanol content in watery solutions that is easy in use and low cost in both manufacturing and operation.

4.2 Sensor description

The coaxial transmission line-based stub resonator (with flow-through ability) has been discussed in detail previously [5, 6]. Here we apply this technology to assess the dielectric permittivity of ethanol containing watery solutions and by that their ethanol content. In an ideal resonator without any losses, the resonance frequency f_{res} of an open ended ($\lambda/4$) and closed end ($\lambda/2$) resonator are given by Eqs. 1a and 1b, respectively. In these special cases, the dielectric constant ϵ_{re} can be determined directly from equations 1a and 1b:

$$f_{res} = \frac{2n-1}{2 \cdot \pi \cdot \sqrt{LC}} = \frac{c \cdot (2n-1)}{4l \sqrt{\epsilon_{re} \epsilon_0 \mu_{re} \mu_0}} \quad (1a)$$

$$f_{res} = \frac{n}{2 \cdot \pi \cdot \sqrt{LC}} = \frac{c \cdot n}{2l \sqrt{\epsilon_{re} \epsilon_0 \mu_{re} \mu_0}} \quad (1b)$$

where

n , the order number of f_{res} (Hz);

l , the length of the resonator (m),

c , speed of light in vacuum (m/s);

μ_0 , magnetic permeability of free space (vacuum permeability) ($\text{H} \cdot \text{m}^{-1}$): $\mu_0 = 4\pi \cdot 10^{-7}$;

μ_r , relative magnetic permeability (-);

ϵ_0 , dielectric permittivity of free space (vacuum permittivity) ($\text{F} \cdot \text{m}^{-1}$): $\epsilon_0 = 1/(\mu_0 \cdot c)^2$.

ϵ_{eff} is a complex parameter:

$$\epsilon_{eff} = \epsilon_{re} + j\epsilon_{im} \quad (2)$$

where ϵ_{re} and ϵ_{im} represent the real and imaginary part of ϵ_{eff} , respectively.

Apart from an effect on ϵ_{eff} , the presence of ethanol in water changes the loss tangent $\tan\delta_{eff}$ of the mixture:

$$\tan\delta_{eff} = \frac{\omega\epsilon_{im} + \sigma}{\omega\epsilon_{re}} \quad (3)$$

where σ represents the conductance of the solution in S/m and $\omega=2\pi f_{res}$ the angular frequency in rad/s.

Changes of ϵ_{eff} and $\tan\delta_{eff}$ become visible as changes in the amplitude versus frequency (AF) response of the sensor. The coaxial-type resonator applied in this study consisted of a function generator (FG) and a spectrum analyzer (SA), both implemented in a HAMEG HMS3010 spectrum analyzer with tracking generator. All interconnecting transmission lines had characteristic impedance (Z_0) of 50 Ω and SMA-type connectors of 25 mm length (SubMiniature version A) were used. Table 1 gives an overview of the physical dimensions of the quarter-wave ($\lambda/4$) open-ended coaxial stub resonator applied in this study.

Table 1

Geometric parameters of the flow-through resonator with outer and inner conductors made from stainless steel 316L.

Parameter	Flow-through resonator
Length, l	$29 \cdot 10^{-1}$ (m)
Inner conductor diameter, d	$1.5 \cdot 10^{-3}$ (m)
Inner diameter of the outer conductor, D	$25 \cdot 10^{-3}$ (m)
Diameters of the fluid inlet and outlet	$15 \cdot 10^{-3}$ (m)
Conductivity of stainless steel 316L, σ	$7.7 \cdot 10^6$ ($S \cdot m^{-1}$)

4.3 Models to calculate ϵ_{eff} of binary mixtures

In the case of mixtures, ϵ_{eff} is a function of the dielectric permittivity ϵ_i and volume fraction V_i of the components present. Most frequently used models for the calculation of ϵ_{eff} include:

1) Maxwell Garnett Model (MGM) for two dielectric composites with a dilute conductive phases, based on dispersion theory [7-10] and expressed by:

$$\epsilon_{eff} = \epsilon_1 \frac{\epsilon_2 + 2\epsilon_1 + 2V_2(\epsilon_2 - \epsilon_1)}{\epsilon_2 + 2\epsilon_1 - V_2(\epsilon_2 - \epsilon_1)} \quad (4)$$

2) Lichtenecker logarithmic law (LLL), also based on dispersion theory [7, 9] and expressed by:

$$\lg \varepsilon_{eff} = \sum_{i=1} V_i \cdot \lg \varepsilon_i \quad (5)$$

3) Refractive mixing dielectric model (GRMDM) [11], expressed by:

$$\sqrt{\varepsilon_{eff}} = (1 - V_2) \sqrt{\varepsilon_1} + V_2 \sqrt{\varepsilon_2} \quad (6)$$

4.4 Material and methods

The performance of the sensor was tested using homogeneous mixtures of demineralized water (conductivity of $1 \cdot 10^{-4}$ S/m) and absolute analytical ethanol (C_2H_5OH ; Merck KGaA).

4.5 Results and discussion

Fig. 1 shows the AF plots for pure H_2O (black) and pure C_2H_5OH (red), whereas Fig. 2 depicts AF responses obtained for water containing different volume fractions (V_i) of ethanol. For clarity reasons here only the first resonance is shown.

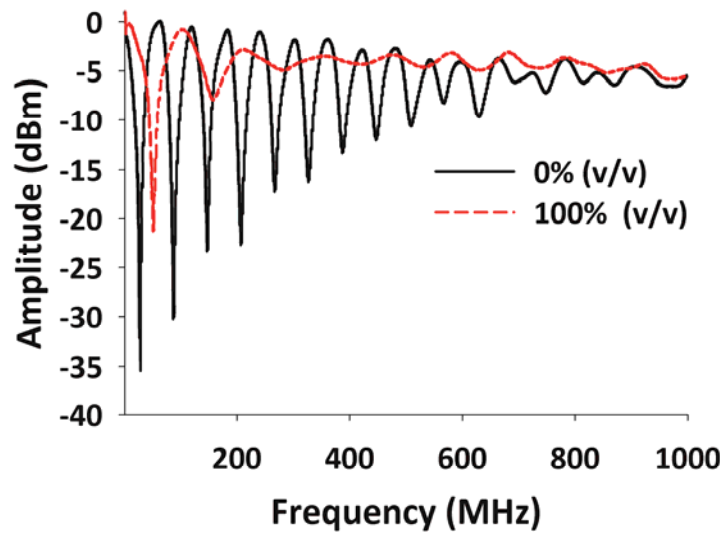


Fig. 1. AF plots recorded for pure H_2O (black) and pure C_2H_5OH (red) (1000 points/scan).

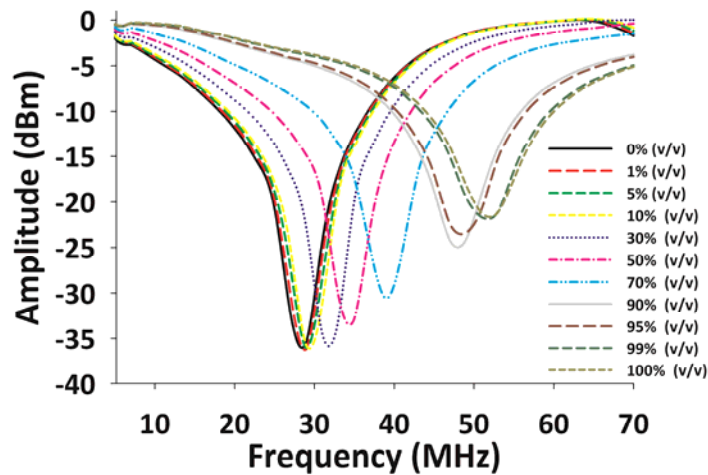


Fig. 2. First resonance of AF plots recorded for $H_2O-C_2H_5OH$ mixtures of different composition (1000 points/scan).

At low frequencies, the AF response is mainly determined by ϵ_{re} of ϵ_{eff} (Eqs. 2, 3) and the conductivity of the dielectric. At higher frequencies, the influence of ϵ_{im} on ϵ_{eff} increases (Eqs. 2, 3). Consequently, the sensitivity of the sensor increases with increasing frequency, an effect already obvious from Fig. 2, e.g. compare the difference between 0% and 10% v/v response versus the one between 90% and 100% v/v.

Resonance in all AF plots shows up as a minimum in the AF plot at f_{res} . Substitution of f_{res} (29.0 and 52.1 MHz for pure water and pure ethanol, respectively) into Eq. 1 renders $\epsilon_{water}=79.5$ and $\epsilon_{ethanol}=24.6$. Reported ϵ_{water} and $\epsilon_{ethanol}$ values, all obtained at 20 °C but with different experimental methods [12, 13], range from 78.8 to 79.5 for water and 24.4 to 25.1

for ethanol [15]. Apart from the experimental method, the way the analytical ethanol has been produced might affect its final ethanol content, e.g., due to fermented residues of sugar. Noteworthy, at lower concentration the (effective) ethanol concentration in solution is lowered by ethanol sticking to the inner wall of the resonator, thereby changing the AF response to lower frequencies [14].

Despite the variation in reported ϵ_{water} and $\epsilon_{ethanol}$ values, we conclude that the values obtained with the stub resonator are in close agreement with those found in the literature.

Fig. 3 compares experimentally obtained data for the first resonance and the models (see also [15]) addressed in section 3 for calculating ϵ_{eff} . Whereas all models accurately predict ϵ_{eff} for pure solutions, be that water or ethanol, for reasons unknown they all underestimate ϵ_{eff} of mixtures containing 20-80% ethanol. Note that experimental data (blue) reported in [15] is also more in accordance with our experimental data than with data generated by the different models. The inset shows the same experimental data but linearly fitted, resulting in a regression coefficient >0.99 . The linear response implies sensor sensitivity independent of the ethanol percentage of the solution, a key characteristic from a practical point of view, notably for the calibration protocol.

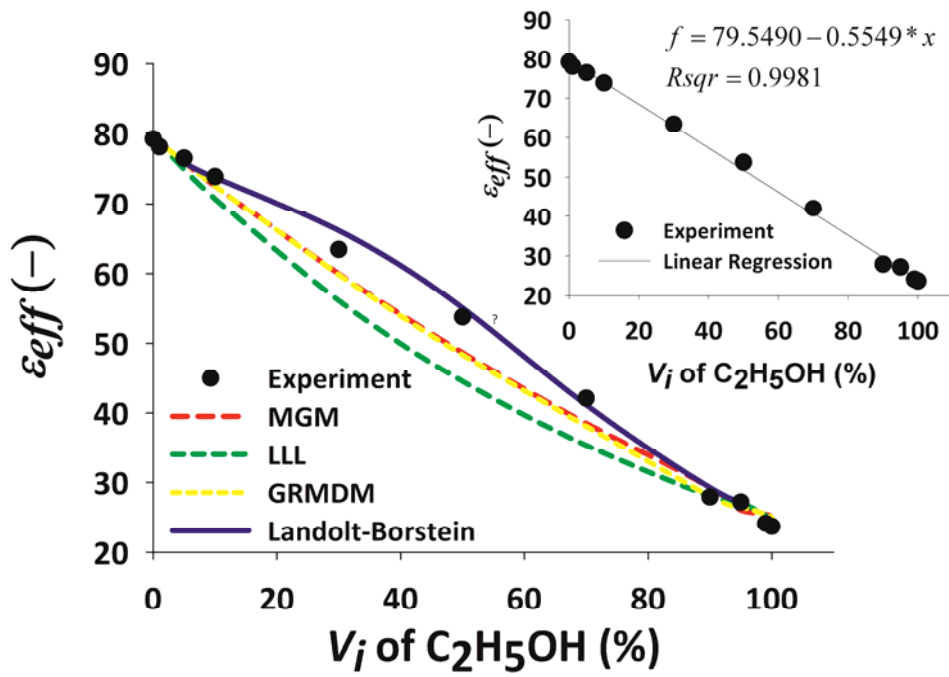


Fig. 3. Comparison between $1^{st} f_{res}$ calculated from the models and obtained experimentally applying different concentrations of C_2H_5OH in H_2O solutions.

4.6 Conclusions

The concept of a $\lambda/4$ length open-ended coaxial stub resonator as sensing device was successfully applied to measure the dielectric permittivity of binary ethanol-water mixtures. The close agreement between calculated values of ϵ_{water} and $\epsilon_{ethanol}$ and those reported previous makes us conclude that the coaxial stub resonator can be used to determine the dielectric permittivity of a liquid, and by that its ethanol content. The flow-through mode of operation allows the continuously on-line monitoring of fluid samples. It is expected that the coaxial resonator concept can be developed further into a cost-efficient and low maintenance sensor for assessing the ethanol content in a broad field of specific applications.

4.7 Acknowledgement

This work was performed in the TTIW-cooperation framework of Wetsus, Centre of Excellence for Sustainable Water Technology (www.wetusus.nl). Wetusus is funded by the Dutch Ministry of Economic Affairs, the European Union Regional Development Fund, the Province of Fryslân, the City of Leeuwarden and the EZ/Kompas program of the “Samenwerkingsverband Noord-Nederland”. The authors thank the participants of the research theme Sensoring for the fruitful discussions and their financial support.

4.8 References

1. E. Kress-Rogers, *Instrumentation and Sensors for the Food Industry*, 2nd Edition, Published by Woodhead Publishing Ltd, (2001), ISBN-13: 978-1-85573-560-6, ISBN: 1-85573-560-1.
2. K. M. Dombek, L.O. Ingram, Determination of the intracellular ethanol concentration of ethanol in *Saccharomyces cerevisiae* during fermentation. *Appl. Environ. Microbiol.*, 51, pp. 197-200, (1986).
3. D. A. Skoog, *Principles of Instrumental Analysis*, 3rd Ed. Saunders: New York, USA (1985).
4. E. A. L. Gattas, C.R.C.S. Tininis, C. Laluca, C. Cheap assay of malate, glycerol and ethanol in fermented musts and food samples, *Clin. Chem. Lab. Med.*, 41, pp. 383-386, (2003).
5. N.A. Hoog-Antonyuk, W. Olthuis, M.J.J. Mayer, D. Yntema, H. Miedema, A. van den Berg, On-line fingerprinting of fluids using coaxial stub resonator technology, *Sensors and Actuators B* 163, pp. 90-96 (2012).
6. N.A. Hoog-Antonyuk, W. Olthuis, M.J.J. Mayer, H. Miedema, F.B.J. Leferink, A. van den Berg, Extensive Modeling of a Coaxial Stub Resonator for Online Fingerprinting of Fluids, *Procedia Engineering* pp. 310-313, (2012).
7. D. M. Pozar, *Microwave Engineering*, Wiley, (2004).
8. M. Campbell, *Measurements and analysis of the microwave dielectric properties of tissues*, PhD thesis, University of Glasgow, (1990).
9. W. R. Tinga, *Mixture laws and microwave-material interactions*, *Dielectric Properties of Heterogeneous Materials*, vol. Pier 6, Progress in Electromagnetics Research, A. Priou, Ed. New York, Amsterdam, London, Tokyo: Elsevier, pp. 1-40, (1992).
10. G., J. C. Maxwell, Colours in metal glasses and metal films, *Philos. Trans. R. Soc. London, Sect. A*, Vol. 3, 385-420, (1904).
11. M. I. Epov, V. L. Mironov, P. P. Bobrov, I. V. Savin, A. V. Repin, Dielectric spectroscopy of oil-bearing rocks at 0.05–16 GHz, *Russian Geology and Geophysics - RUSS GEOL GEOPHYS*, vol. 50, no. 5, pp. 470-474, 2009.
12. Y.S. Joshi, P.G. Hudge, A.C. Kumbharkhane, S.C. Mehrotra, The dielectric relaxation study of 2(2-alkoxyethoxy)ethanol–water mixtures using time domain reflectometry, *Journal of Molecular Liquids*, Volume 163, Issue 2, pp. 70-76, 2011.
13. M. Mohsen-Nia, H. Amiri, Measurement and modelling of static dielectric constants of aqueous solutions of methanol, ethanol and acetic acid at $T = 293.15$ K and 91.3 kPa, *The Journal of Chemical Thermodynamics*, Volume 57, pp. 67-70, 2013.
14. M. K. Jain, C. A. Grimes, Effect of surface roughness on liquid property measurements using mechanically oscillating sensors, *Sensors and Actuators A: Physical*, Volume 100, Issue 1, pp. 63-69, 2002.
15. C. Wohlfarth, M. D. Lechner, *Static Dielectric Constants of Pure Liquids and Binary Liquid Mixtures*, Supplement to IV/6, Series: Landolt-Börnstein: Numerical Data and Functional Relationships in Science and Technology - New Series, Vol. 17, Subseries: Physical Chemistry, 2008, 203.



Prague, Czech Republic, IC-MAST 2013



Chapter 5

Stub Resonators for On-line Monitoring Early Stages of Corrosion

Abstract

Here we demonstrate the proof-of-principle of a new type of sensor to assess effects due to corrosion of metal surfaces. The method can be applied to all situations where metals are exposed to a corrosive (fluidic) environment, including, for instance, the interior of pipes and tubes. The sensing device is based on the operating principle of a quarter wave length open-ended stub resonator. In the absence of corrosion, inner and outer conductors of the resonator are separated by a single dielectric, i.e., a fluid. Oxidation of the metal surface of inner and/or outer conductor changes the properties of the dielectric between inner and outer conductor because it introduces a dielectric permittivity that differs from that of the fluid. Additionally, corrosion affects the skin effect and the effective resistance of the corroding inner and outer conductors of the stub resonator. As a result the recorded amplitude-frequency (AF) plot shows a shift of the resonance frequency and/or a change of shape of the resonance peak(s). The two types of transmission line designs explored are coaxial and coplanar stripline (CPS). Irrespective the design, the method outlined here offers an equipment-undemanding, low maintenance and cost-efficient in-line early warning system to detect (the onset of) corrosion. The additional advantage of the system is the freedom of design as for its geometry, from coax to one embedded in printed circuit boards, both designs with hardly any constraints on the particular dimensions. Depending on the precise geometry, the sensor may be able to detect corrosion in tap water after just one hour. Experimental data (recorded after 4 days) is in close agreement with simulation data representing a 17 μm homogeneous oxide layer.

This chapter is based on the article published as:

N.A. Hoog, M.J.J. Mayer, H. Miedema, R.M. Wagterveld, J. Tuinstra, M. Saakes, W. Olthuis, A. van den Berg, *Stub Resonators for Online Monitoring Early Stages of Corrosion*, Sensors and Actuators B: Chemical, Volume 202, 31 October 2014, Pages 1117-1136, ISSN 0925-4005, <http://dx.doi.org/10.1016/j.snb.2014.06.026>.

5.1 Introduction

The economic cost due to corrosion can hardly be overestimated. As calculated by the National Association of Corrosion Engineers, in the USA alone, the total cost involved in 2012 amount to above \$1 trillion, no less than 6.2% of GDP [1]. Corrosion may and often does result in failures of utilities possibly leading to dangerous situations, for example, when occurring in the transportation sector. Apart from cost and safety, there is the issue of sustainability. Corrosion leads to (irreversible) material losses with the corroded metals commonly ending up in the environment [2-12]. It is exactly for all these reasons that over the last decades technologies have been developed to detect (and eventually of course prevent) corrosion in an as early stage as possible. Without the pretention to be complete, currently existing technologies include: corrosion coupons, electrical resistance (ER), inductive resistance probes, linear polarization resistance (LPR), electrochemical impedance spectroscopy (EIS), electrochemical frequency modulation, resonance analysis, electrochemical noise (EN), zero resistance amperometry (ZRA), potentiodynamic polarization, thin layer activation (TLA) and gamma radiography, electrical field signature method (EFSM), acoustic emission (AE). Apart from these direct techniques there are several indirect technologies to measure corrosion: corrosion potential, hydrogen flux monitoring and chemical analyses [13, 14]. Whether direct or indirect, the techniques listed above are either intrusive or non-intrusive and off- or on-line.

Despite the diversity of existing technologies, we present an alternative that is easy to use, low cost, and low maintenance. The sensor described here is based on transmission line theory and classified as a quarter wave length open-ended stub resonator. For this reason, it can be operated at high frequencies without introducing parasitic distributed inductance and capacitance elements. This allows complex dielectric spectroscopy and analyzing resonances over a broad frequency range. An additional advantage is that scaling of the inner conductor not only changes the dielectric properties of the system but also affects the effective resistance of the inner conductor. The latter effect increases with frequency because of the skin-effect. From the design point of view we discuss two types, the coaxial and the coplanar stripline resonator (CPS) transmission line. Both systems can be realized using standard electronic components to obtain a (flow-through) sensor that represents the analog of a (automated) spectrum analyzer. Both designs are expected to suit different applications and were chosen to demonstrate the general applicability of the concept in terms of stub resonator geometry. For instance, the coaxial type seems most appropriate for monitoring industrial processes. The CPS design, on the other hand, can be used to test oxidation inhibitors, to mention just one potential application. It should also be remarked that the design can set limits to particular applications.

Stub resonators consist of an inner and outer conductor separated by a dielectric, in our particular case a fluid. With an input signal of constant amplitude but variable frequency, the frequency of lowest load impedance, i.e., the resonance frequency (f_{res}) is determined. Whereas f_{res} itself solely depends on the resonator length, the relative magnetic

permeability and the dielectric permittivity of the fluid, the amplitude output at f_{res} depends on the characteristic impedance of the resonator, which, in turn, depends on material and geometrical parameters (e.g., inner and outer conductor ratio) and fluid characteristics (dielectric permittivity). Apart from f_{res} and the output amplitude, the shape (e.g., width of the resonance peak) of the amplitude-frequency or AF response depends on losses in both conductors (e.g. skin effect), dielectric losses in the fluid (e.g., due to the conductivity of ions present) and, finally, losses due to impedance mismatch, notably between the coaxial transmission lines and the resonator. In two previous publications [14, 17] we showed that a sensor based on this principle can be used to monitor the composition of the fluid that acts as dielectric in between the two conductors. In addition, it was quite well possible to adequately model and predict the experimentally observed response, including all the losses.

Instead of focusing on fluid composition, here we discuss an entire different application of stub resonators, one with the inner conductor as sensitive element and susceptible to the formation of an oxide layer on its outer surface. This can be realized by making the entire sensor, except the inner conductor, out of (corrosion-resistant) stainless steel. The inner conductor, in turn, can be made out of the material to be investigated. Suppose, for example, that a particular piece of process equipment shows susceptibility to corrosion. A stainless steel coaxial resonator with the inner conductor made from the same material as the equipment under investigation can be installed in the process liquid feed stream. Corrosion results in the formation of a second dielectric surrounding the inner conductor. Instead of a system with both conductors separated by a single dielectric (i.e., the fluid), inner and outer conductor are now separated by two concentric layers of different permittivity. With both conductors made of corrosion-sensitive material, the same oxidation process will of course occur at the surface of the outer conductor as well, resulting in a three-layer dielectric. However, as will be discussed later on also in this case will the change in AF response predominantly determined by the corrosion layer on the inner conductor.

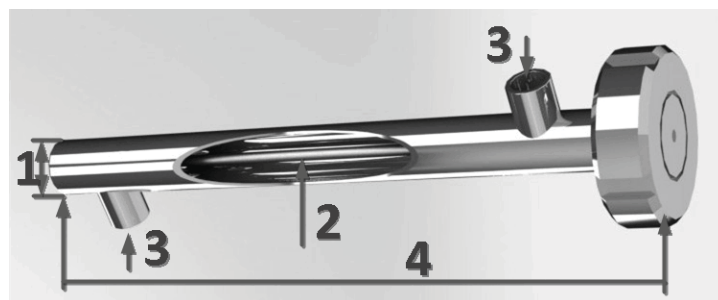


Fig. 1. Schematic 3D image of the coax sensor with outer conductor of diameter of D (1); inner conductor of diameter of d (2); input and output ports for fluid flow-through (3) and tube length l (4). Note that the inner conductor has been made visible by making the outer conductor partly transparent.

Fig. 1 shows a schematic 3D image of the coax resonator. Corrosion of the inner and/or outer conductor will be monitored as a change in the AF (amplitude-frequency) response of the device. In the ideal scenario, measures can be taken before actual damage has occurred

in those parts of the process installation that are made of the same construction material as the inner conductor of the sensor, on which corrosion was detected. So in this case, the sensor is used as an early warning system. In case of just a corrosive inner conductor, the sensor is simply reactivated by replacing the partly oxidized metal rod with a new one. Indeed, an additional advantage of this design is the ease by which the inner metal rod can be replaced. We thus developed a corrosion sensor that is easy in use and low cost in manufacturing and operation.

5.2 Sensor description

Coaxial stub resonator

Fig. 2 shows the coaxial-type resonator implemented in a circuit consisting of a function generator (FG) and spectrum analyzer (SA), both implemented in a HAMEG HMS3010 spectrum analyzer with tracking generator. It should be noted that the spectrum analyzer is calibrated in dBm (dimension in power). The interconnecting transmission lines all had characteristic impedance (Z_0) of 50Ω . In order to minimize the size of the connectors, we used connectors of the type SMA (SubMiniature version A) with a length of just 20 mm. Note the two possible configurations of the stub resonator, closed or open, the mode exploited in this study. Also note that the device can operate under batch or flow-through conditions. The resonator outlined here has been described by the authors in more detail previously [14-24].

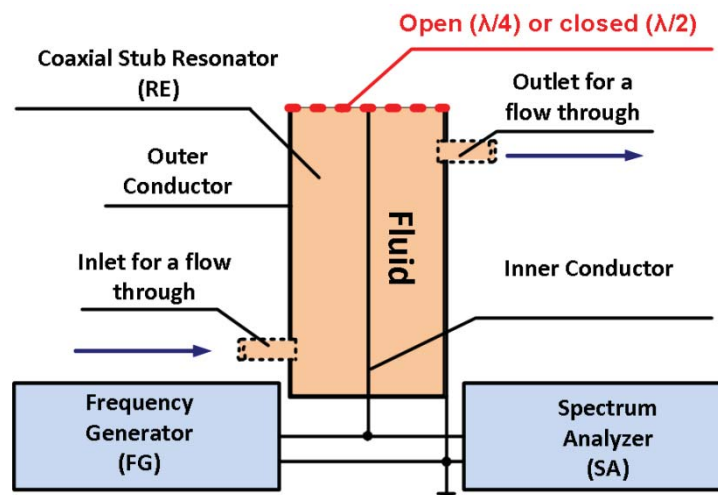


Fig. 2. Schematic outline of the coaxial stub resonator sensing system consisting of a function generator (FG), a spectrum analyzer (SA) and the coaxial stub resonator (RE). The dotted inlet and outlet indicate that the flow-through resonator can be optionally used as batch resonator.

Table 1 gives an overview of the physical dimensions of the quarter-wave coaxial stub resonators applied in this study, see also Fig. 1. Two sizes of inner conductor were tested with a diameter of either 2 or 15 mm.

Table 1

Geometric parameters of the flow-through resonator. The outer and the inner conductors of the resonator were made from stainless steel 316L and steel, respectively. Note the two different sizes of inner conductor that were tested.

Parameter		
Length, l	$29 \cdot 10^{-1}$	(m)
Inner conductor diameter, d	$2 \cdot 10^{-3}$ or $15 \cdot 10^{-3}$	(m)
Inner diameter of the outer conductor, D	$25 \cdot 10^{-3}$	(m)
Diameters of the fluid inlet and outlet	$15 \cdot 10^{-3}$	(m)
Conductivity of stainless steel 316L, σ	$1.45 \cdot 10^6$	(S · m ⁻¹)
Conductivity of steel, σ	$6.99 \cdot 10^6$	(S · m ⁻¹)

The corrosion of steel, i.e. the oxidation of iron to iron (II) (ferrous-) and eventually to iron (III) (ferric-), in the presence of water, is given by Eqs. 1, 2:



Apart from the possible formation of Fe_2O_3 , the hydrated ferric oxide, orange to red-brown in color, makes up for most of the oxidation products.

The outer conductor is corrosion resistant because it has been manufactured from stainless steel. As a result, only the inner conductor will suffer from corrosion. For now we will assume that the oxide forms a homogeneous layer (but see Discussion). Fig. 3 gives a schematic cross section of the coaxial stub resonator with the inner conductor covered with an oxide layer.

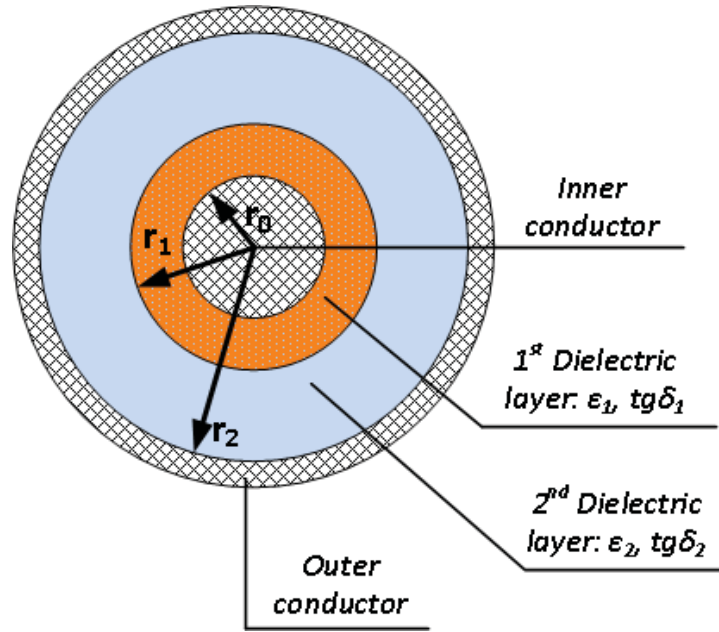


Fig. 3. Schematic cross section of the coaxial stub resonator with two dielectric layers in between inner and outer conductor: corrosion layer (r_1 , orange, dielectric permittivity ϵ_1) and fluid (r_2 , blue, with dielectric permittivity ϵ_2).

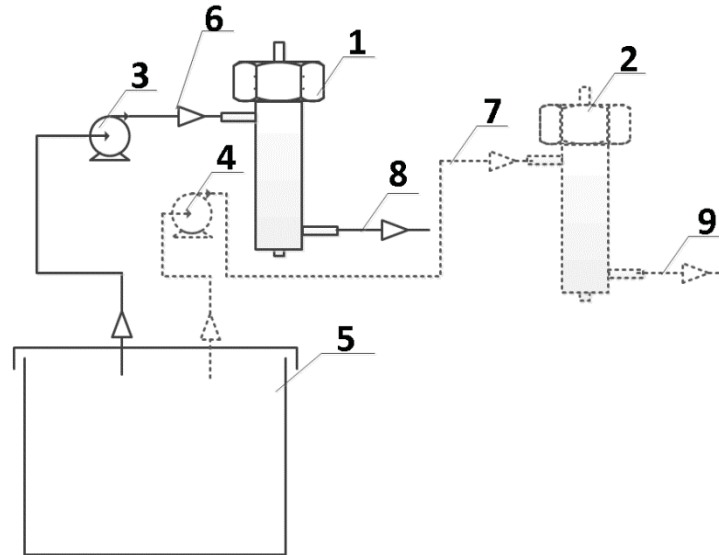


Fig. 4. Schematic view of the experimental set-up consisting of the coaxial resonator (1); The presented 2nd resonator, labeled (2) and drawn in dotted lines, indicate that the system can be extended with n resonators, all depending on the precise aim of the particular experiment. Also indicated pumps (3, 4); reservoir tank for tap water (5); inlet ports (6, 7) and outlet ports (8, 9).

The electrical parameters of the stub resonator are the distributed element inductance L , resistance R , capacitance C and conductance G , see also [14, 17, 26] for detailed

description. When these parameters are known, the behavior of the resonator can be described in terms of AF response, using the setup shown in Fig. 1.

The effective dielectric permittivity ϵ_{eff} and the effective loss tangent $\tan\delta_{eff}$ of a coaxial resonator with multiple concentric layers of different dielectric permittivity have been described in [14, 17] and is expressed by:

$$\epsilon_{eff} = f(\epsilon_{r1}, \epsilon_{r2}, \dots, \epsilon_{rn}) \quad (3)$$

$$\tan\delta_{eff} = f(\tan\delta_1, \tan\delta_2, \dots, \tan\delta_n) \quad (4)$$

In an ideal resonator without any losses, the resonance frequency f_{res} of an open ended ($\lambda/4$) and closed end ($\lambda/2$) resonator are given by Eqs. 5a and 5b, respectively. In this special case, the dielectric constant ϵ_{re} can be determined directly from Eqs. 5a and 5b [17].

$$f_{res} = \frac{2n-1}{2 \cdot \pi \cdot \sqrt{LC}} = \frac{c \cdot (2n-1)}{4l \sqrt{\epsilon_{re} \epsilon_0 \mu_{re} \mu_0}} \quad (5a)$$

$$f_{res} = \frac{n}{2 \cdot \pi \cdot \sqrt{LC}} = \frac{c \cdot n}{2l \sqrt{\epsilon_{re} \epsilon_0 \mu_{re} \mu_0}} \quad (5b)$$

where c represents the speed of light in vacuum (m/s), n the order number of f_{res} (Hz), l the length of the resonator (m), μ_r relative magnetic permeability of the dielectric between inner and outer conductors (-), μ_0 the absolute vacuum permeability (H/m), ϵ_0 the absolute vacuum permittivity (F/m), and ϵ_{re} the relative effective dielectric constant (-).

Note that the capacitance C in Eqs. 5a and 5b is determined by the real part ϵ_{re} of ϵ_r :

For a lossy resonator, polarization and conductivity losses in the dielectric under investigation, as well as resistance losses in the inner and outer conductors, must be taken into account. A detailed model accounting for these losses, essentially based on telegrapher's equations, is explained in [17].

In order to describe the behavior of the corrosion sensor i.e., a lossy resonator, the model described in [17] was extended with expressions for both the effective dielectric permittivity ϵ_r and the effective loss tangent $\tan\delta_{eff}$ of the composite dielectric consisting of oxide metal and water.

For a lossy dielectric, complex dielectric permittivity can be described as:

$$\epsilon_r = \epsilon_{re} - j\epsilon_{im} \quad (6)$$

where ϵ_{re} and ϵ_{im} represent the real and imaginary part of ϵ_r , respectively.

The effective loss tangent $\tan\delta_{eff}$ (-), which is a measure for the dielectric losses in the system, is expressed by Eq. 7:

$$\tan\delta_{eff} = \frac{\omega\epsilon_{im} + \sigma_{eff}}{\omega\epsilon_{re}} \quad (7)$$

where ϵ_{im} and σ_{eff} reflect the polarization losses and the conductivity losses in the dielectric respectively. and $\omega=2\pi f_{res}$ represents the angular frequency (rad/s).

The effective conductivity σ_{eff} , of the fluid volume and the oxide layer, i.e., the composite dielectric between inner and outer conductors is a parameter hard to assess. The difficulty is related to the extent the conductor is covered with an oxide layer. In case only a small surface area is covered with metal oxide, σ_{eff} will be mainly determined by the fluid conductance. In contrast, a very thin homogeneous layer of metal oxide on the inner conductor may result in electrical isolation of the inner conductor. In this case σ_{eff} will be almost completely determined by the conductivity of the metal oxide layer. For this reason, σ_{eff} was lumped into $\tan\delta_{eff}$ (see Eq. 7), which, in turn, was used in the model as a fitting parameter. It is noted that lumping of σ_{eff} into $\tan\delta_{eff}$ is common practice [18].

ϵ_r and $\tan\delta_{eff}$ can also be expressed in terms of the capacitance and tangent loss of the individual system elements:

$$\epsilon_r = C_{eff} / C_{vacuum} \quad (8)$$

where C_{vacuum} is the capacitance of the resonator with vacuum between both conductors.

According to [19], the effective capacitance (C_{eff}) of a coaxial capacitor with a two-layer dielectric is given by Eqs. 9 and 10:

$$C_{eff} = \left[\frac{1}{C_1} + \frac{1}{C_2} \right]^{-1} \quad (9)$$

where C_1 and C_2 are the capacitances related to the corrosion layer and the fluid, respectively, each given by:

$$C_1 = \frac{2\pi\epsilon_0\epsilon_1}{\ln(r_1/r_0)} \quad \text{and} \quad C_2 = \frac{2\pi\epsilon_0\epsilon_2}{\ln(r_2/r_1)} \quad (10)$$

where

ϵ_1 , dielectric permittivity of an oxide layer (-);

ϵ_2 , dielectric permittivity of a fluid (-);

r_0 , radius of the inner conductor of the resonator (m);

r_1 , radius of the occurred oxide layer (m);

r_2 , inner radius of the outer conductor (m).

Taking into account Eqs. 9 - 10, ϵ_{eff} of a cylindrical capacitor with dielectrics ϵ_1 and ϵ_2 in radial direction can be expressed by Eq. 11 [20]:

$$\epsilon_{eff} = \frac{\epsilon_1\epsilon_2 \ln\left(\frac{r_2}{r_0}\right)}{\epsilon_1 \ln\left(\frac{r_2}{r_1}\right) + \epsilon_2 \ln\left(\frac{r_1}{r_0}\right)} \quad (11)$$

Eqs. 3-11 give a full description of the behavior of the stub resonator.

Coplanar stripline (CPS) stub resonator

Apart from the coaxial type, we also investigated a sensor based on a coplanar stripline transmission line, shown schematically in Fig. 5.

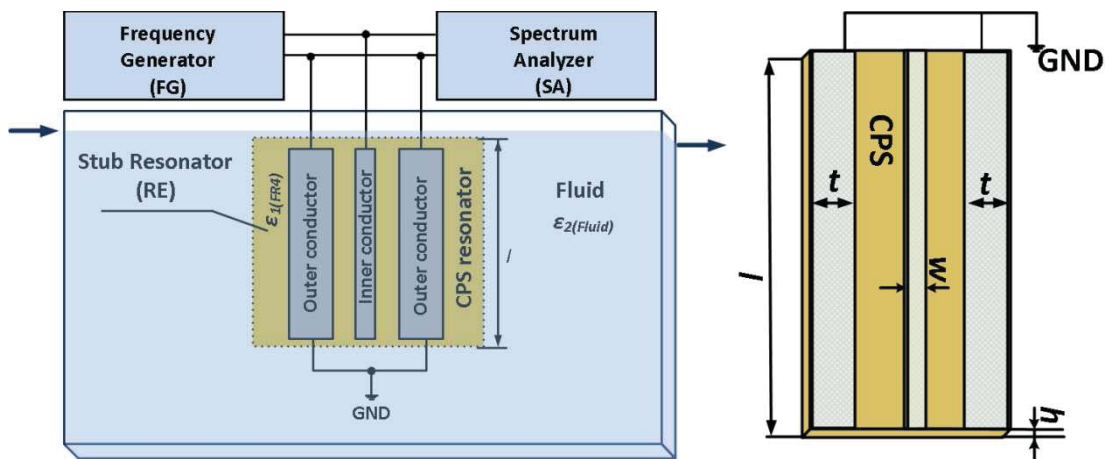


Fig. 5. Schematic overview of the CPS used in this study. Here, l represents the length, w the width of the signal wire, h the substrate thickness, t the width of ground signal, $\epsilon_{1(FRA)}$ the dielectric permittivity of substrate, $\epsilon_{2(FIuid)}$ the dielectric permittivity of the fluid. On the left panel, the fluid level is indicated by arrows.

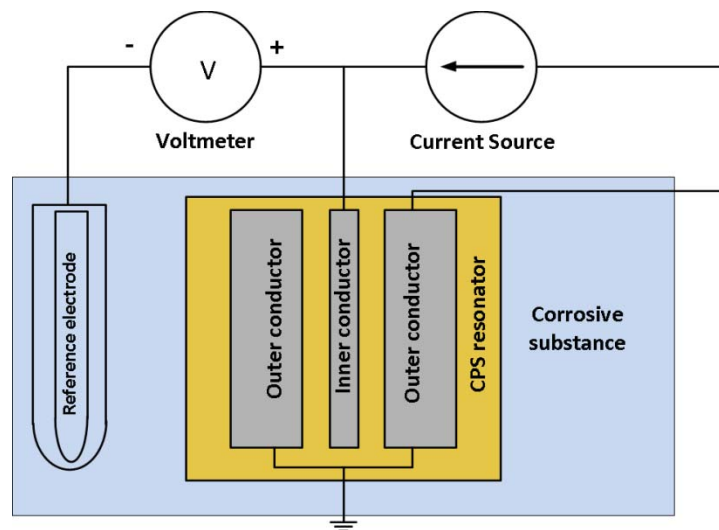


Fig. 6. Schematic representation of a test cell for a CPS-based transmission line. The inner and outer conductor functions as working and auxiliary electrode, respectively. Corrosion tests can be performed with the sensor either fully or partly immersed into the electrolyte solution as well as during constant or periodic exposure to the corrosive electrolyte.

Analogous to the coaxial stub resonator, the behavior of the CPS resonator is defined by its electrical parameters: the distributed element inductance L , resistance R , capacitance C and conductance G [27, 28]. Knowing these parameters allows accurate modeling of its AF response [17].

Table 2 gives an overview of the relevant dimensions of the CPS resonator used in this study. As a dielectric substrate, laminated epoxy resin fiberglass composite sheets (FR4) were used.

Table 2

Geometric parameters of the CPS resonator. The outer and the inner conductor were made from Sn-Ag alloy.

Parameter		
Length, l	$34 \cdot 10^{-2}$	(m)
Substrate thickness, h	$1.93 \cdot 10^{-3}$	(m)
Width of the signal wire, w	$7.60 \cdot 10^{-4}$	(m)
Width of ground wire, t	$2.2 \cdot 10^{-3}$	(m)
Effective dielectric permittivity of substrate (FR4), ϵ_r	4.8	(-)
Conductivity of tin, σ	$8.7 \cdot 10^6$	(S · m ⁻¹)

Both the inner and outer conductor of the CPS were made of tin-silver or Sn-Ag alloy, with tin (Sn) being the predominant surface-active component [35]. In order to study the effect of oxidation we applied a 10 mA dc-current to accelerate the corrosion process. Given a surface area of the (working) inner electrode of 1 cm², the current density was 10 mA/cm². The dc-current induced corrosion test experiments were performed in a sodium hydroxide (NaOH) solution, a highly corrosive condition for Sn. Due to a dissolution-precipitation mechanism, a thin layer of either stannous hydroxide Sn(OH)₂ and/or oxide SnO develops on the electrode surface. At higher anodic potentials this layer of Sn(OH)₂ and SnO is further oxidized to Sn(OH)₄ and SnO₂. Apart from the oxidation of Sn, oxidation of Ag and H₂O might occur as well.

The resonator's AF response is also sensitive to the ionic species present in the solution, with a high ionic conductivity causing increased dielectric losses. Calculation of the change in solution composition is however not feasible because the relative contributions of the oxidation of Sn, Ag and H₂O remain unknown. But because oxidation will affect the ionic species present in the solution, the change in AF response due to dc-current induced oxidation needs to be separated from the one due to dc-current induced change in solution composition. We therefore worked along the following protocol:

1. Perform the control (non-corroded conductor) according to Fig. 6 and in MilliQ water.
2. Mount the CPS resonator into a vessel containing 1 liter 2 mM NaOH.
3. Apply a dc-current of 10 mA for one hour using the circuit of Fig. 6 and a Ag/AgCl reference electrode.
4. Wash the specimen with demineralized water and dry under laboratory conditions.
5. Repeat the measurement of step 1 but with (partly) corroded conductor.
6. Repeat steps (2-5) for 2 and 3 hours, respectively.

5.3 Material and Methods

The conductivity of the solutions was measured using a pH/Cond 340i-WTW electrode (VWR).

The Ag/AgCl reference electrode used for the dc-current induced corrosion experiments was of the type +0.200 V vs. NHE (ProSense QiS, The Netherlands).

Scanning electron microscopy (SEM) was used to characterize and visualize the surface of the inner and/or outer conductors.

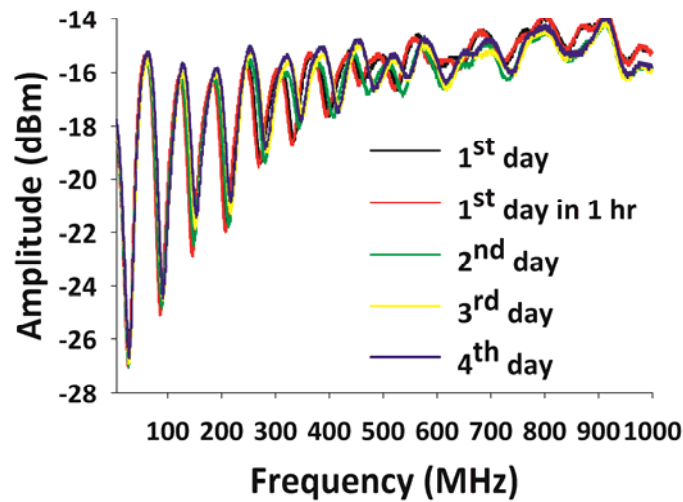
Chemicals were purchased from VWR International BVBA.

5.4 Results

Coaxial resonator

All experiments with the (flow-through) coaxial resonator were performed using tap water with conductivity of $545 \cdot 10^{-4}$ S/m (compared to 10^{-4} S/m of milliQ water), and at a temperature of 18 ± 0.5 °C. Fig. 7 shows a typical series of AF responses indicating corrosion of the inner conductor over a time period of four days using an inner conductor diameter of either 2 mm (A) or 15 mm (B). The differences in the AF responses are mainly caused by larger dielectric losses when using the 15 mm inner conductor (larger conductor surface area, shorter distance between both conductors). For that reason, all further experiments were performed with inner conductors of 2 mm. As shown by Fig. 7A, an effect is already observable after one hour of operation (red curve), notably at higher frequencies. Another conclusion arising from Fig. 7A is that, in general, effects of corrosion are more pronounced at higher frequencies. There are two reasons for this. Firstly, according to Eq. 5 and given a certain change in ϵ_r , the shift of f_{res} (Δf_{res}) is proportional to $c(2n-1)/4l$, implying a larger shift at higher n , i.e., at higher resonance frequencies. Secondly, as for the amplitude, e.g. the skin effect is more dominant at higher frequencies.

A



B

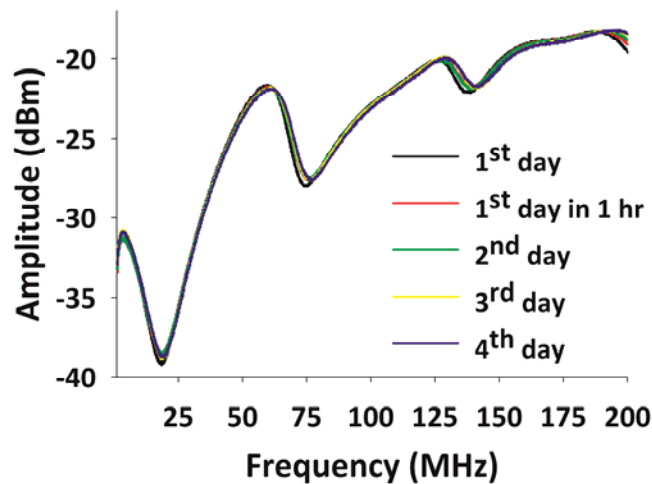


Fig. 7. AF plots in response to corrosion over a time period of 4 days using an inner conductor of 2 mm (A) or 15 mm (B). (1000 point/scan).

These first four resonances of Fig. 7A are shown in more detail in Fig. 8. For comparison, Table 3 shows results obtained after fitting the experimental data (red dots) of Fig. 8 to Eq. 2 in [17] and/or Eqs. 1-12 in [22] and Eqs. 3-11 presented here, using the *lsqcurvefit* option in MATLAB (2012B). This fitting procedure renders the thicknesses of the oxide layer and $\tan\delta_{eff}$, both at each day of the experiment (see Eq. 7). Table 3 confirms this assumption in that the highest agreement between experimental and simulation data is, in general, observed at the minimum of the curves. Table 3 further suggests that Fig. 7A has been recorded (after four days) in the presence of an oxide layer with a thickness of 17 μm (see also Discussion).

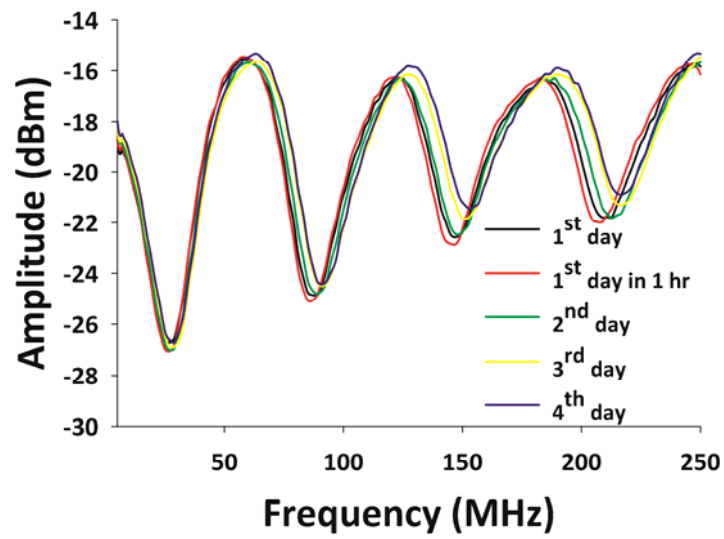


Fig. 8. The experimentally obtained first four resonances of Fig. 7A shown at higher resolution, i.e., in a frequency range between 5MHz-250MHz.

Table 3

Simulations of the 3rd resonance shown in Fig. 8 and Fig. 10, with the radius r of an oxide layer and the effective loss tangent $\tan\delta_{eff}$, as fitting parameters. Drawn curves all refer to simulation data whereas the red dots represent experimental data obtained with the resonator used for Fig. 7A and Fig. 8.

Day of experiment	Results of simulation 3 rd resonance	$\tan\delta_{eff}$, (-)	r^* , (μm)
1 st day		0.14	8

1st day

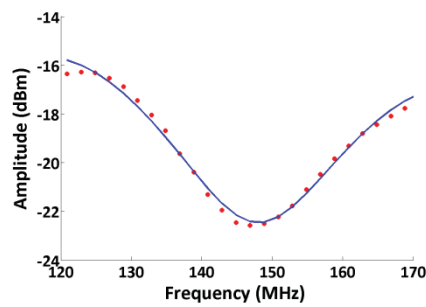
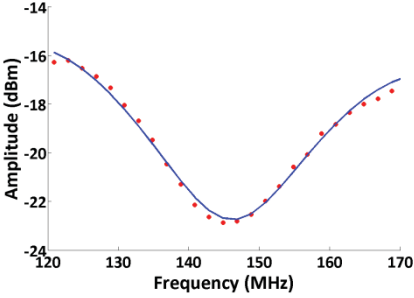
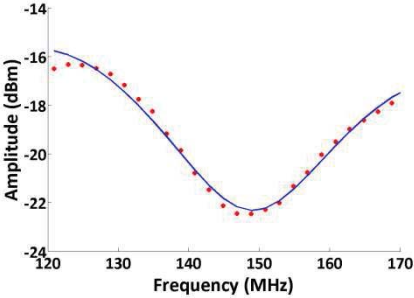
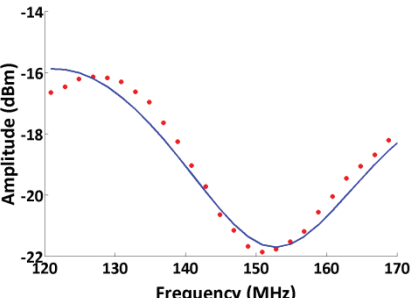
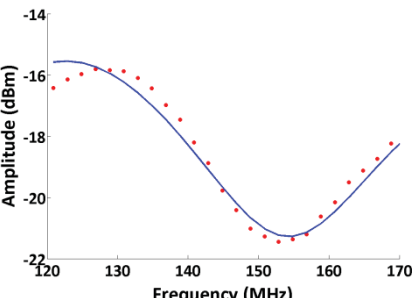


Table 3 (Continued)

Day of experiment	Results of simulation 3 rd resonance	$\tan\delta_{eff}$, (-)	r^* , (μm)
1 st day in 1 hr		0.13	6
2 nd day		0.14	10
3 rd day		0.16	15
4 th day		0.16	17

*Radius of an oxide layer

These first four resonances shown in Fig. 8 were used to get a clearer picture of the observed AF responses. We therefore plotted the resonance frequency and amplitude as a function of time. The result is shown in Fig. 9. Even though the precise shape differs, the trend of resonance frequency as well as amplitude is essentially the same (perhaps except for the amplitude plot of the first resonance). This similarity is an important observation as it strengthens the hypothesis for the shift of each resonance, i.e., the formation of a corroded oxide layer on the inner conductor's surface.

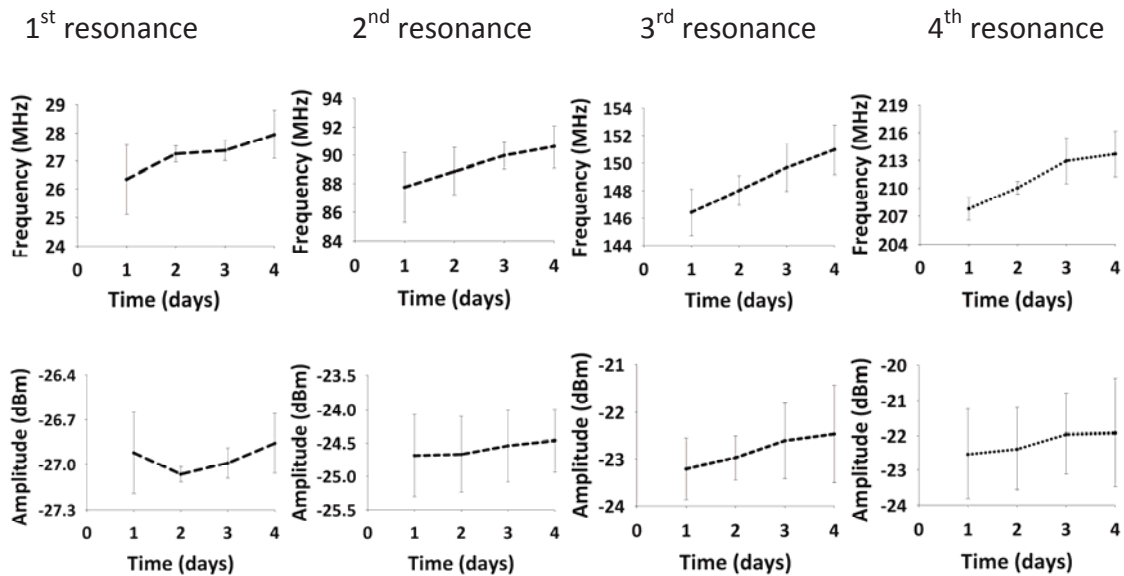


Fig. 9. Changes of resonance frequency f_{res} (top row) and amplitude (bottom row) during 4 days and plotted separately for the first 4 resonances.

At higher frequencies we observed an increased dispersion of the signal. Fig. 9 demonstrates this phenomenon, showing the correlation between the shift in resonance frequency and in amplitude, plotted for the first four resonances and each monitored over a time frame of four days. Whereas the data points for the first two resonance frequencies almost overlap, those of the 3rd and 4th clearly start to diverge, an effect due to enhanced dielectric losses.

Importantly, Fig. 9 is based on a triple set of data, also measurements were repeated 10 times but with resonator tubes of different length (0.3, 0.61 or 1.01 m), different outer diameter (20 or 70 mm) and an inner conductor diameter of 1.5, 15 or 60 mm. (see Supplementary Information Figs. A.2-A.4). Despite this difference in experimental set up, the trend in the data was always the same (i.e., as shown in Fig. 9), an observation that makes us conclude that the method is reproducible

At low frequencies, the AF response is mainly determined by the real part of ϵ_r in Eq. 6 and the conductivity of the dielectric. Polarization losses and conductivity losses of the solution both increase the relative contribution of the imaginary part of ϵ_r in Eq. 6 with increasing frequency [14, 17]. Fig. 10 shows the 3rd resonance over time at higher resolution. After an initial shift in the direction of lower frequencies after just one hour (red curve), the response starts to shift in the opposite direction, i.e. to higher frequencies.

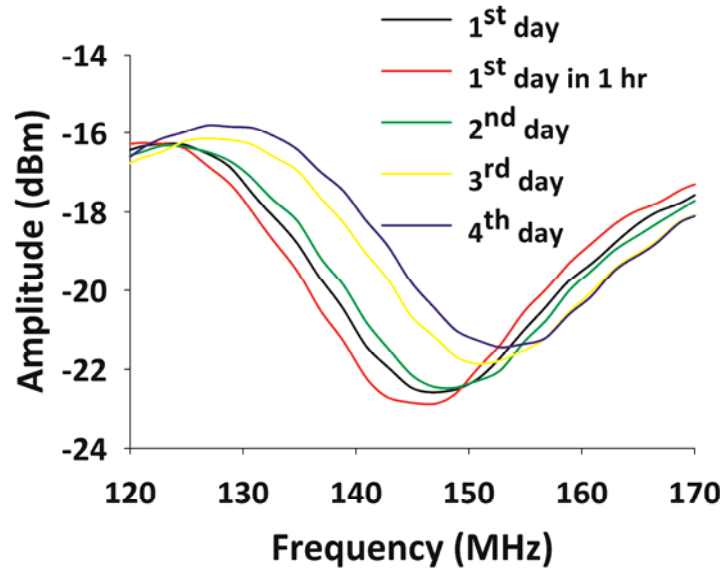


Fig. 10. AF plot of 3rd resonance frequency showing the shift in frequency and amplitude caused by corrosion during 1, 2, 3 or 4 days.

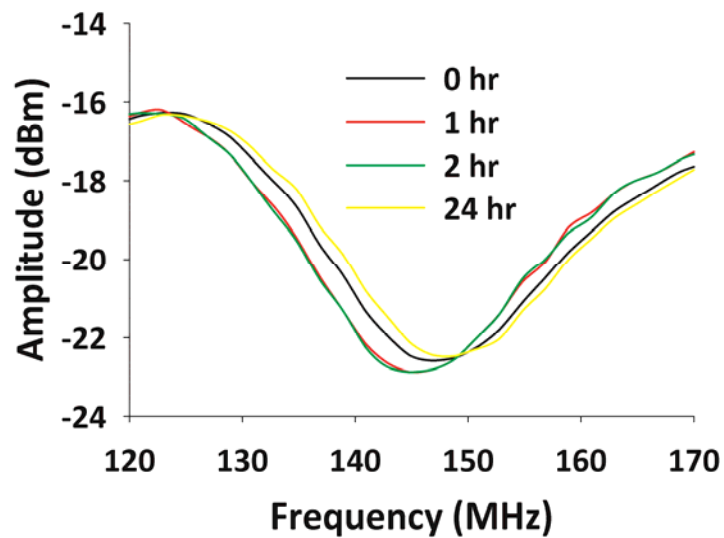


Fig. 11. AF response of 3rd resonance frequency after 1, 2 and 24 hrs of corrosion shown at higher resolution.

We investigated this phenomenon in more detail and measured the AF response after 1, 2 and 24 hrs of corrosion (Fig. 11). We now observed a shift to the left during the first two hours followed by one to the right after 24 hrs.

To correlate, at least at the qualitative level, the shown changes in AF response with visual corrosion effects, we also obtained SEM pictures of the surface of the inner conductor with corrosion progressing over time (Fig. 12). Whereas we do see spots of corrosion appearing at the surface during the first two hours (A, B), it is only after 24 hrs that the surface is completely covered with oxide (D). In addition, SEM pictures were made from cross sections of the inner conductor, with estimated thicknesses of the observed oxide layer covering its surface (Fig. 13).

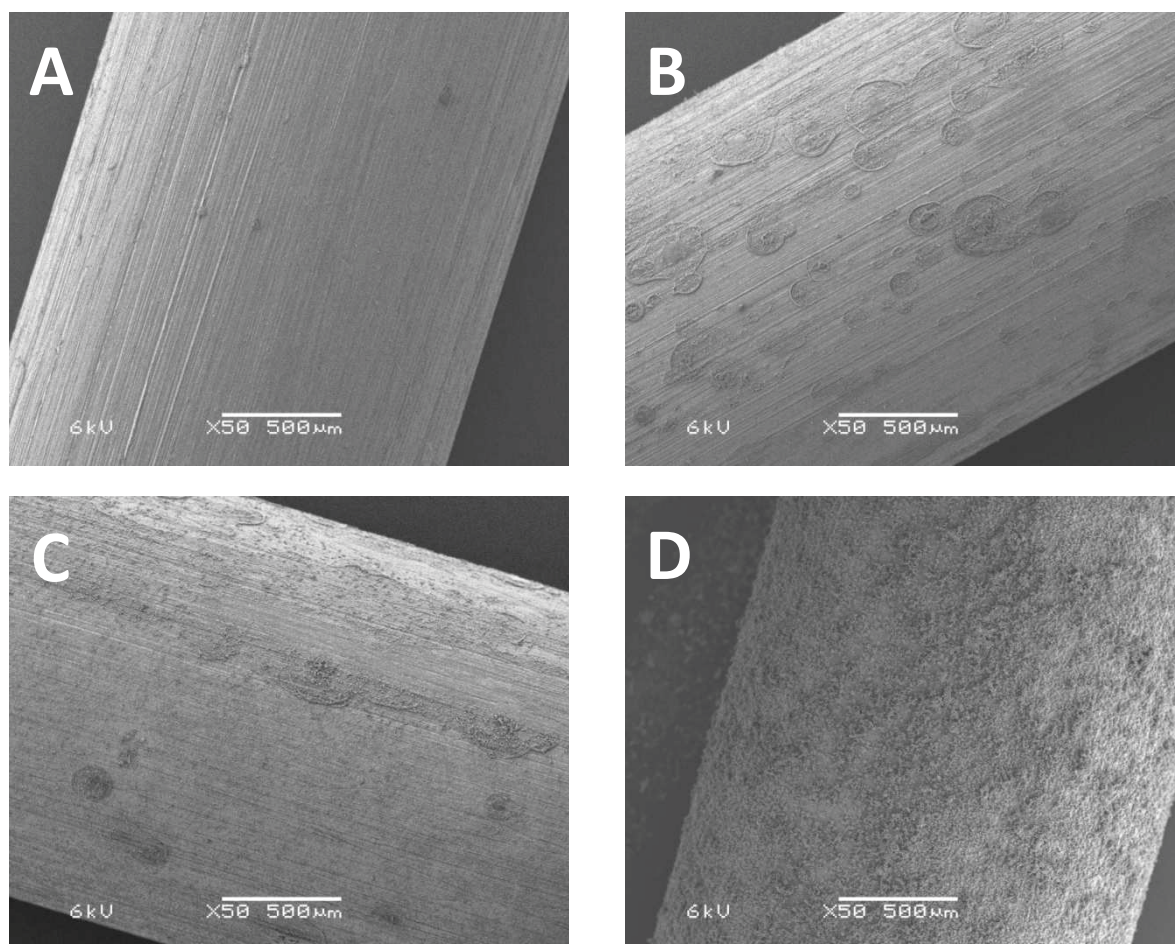


Fig. 12. SEM images showing the non-corroded (A) and corroded inner conductor surface after 1 hr (B), 2 hrs (C) and 24 hrs (D).

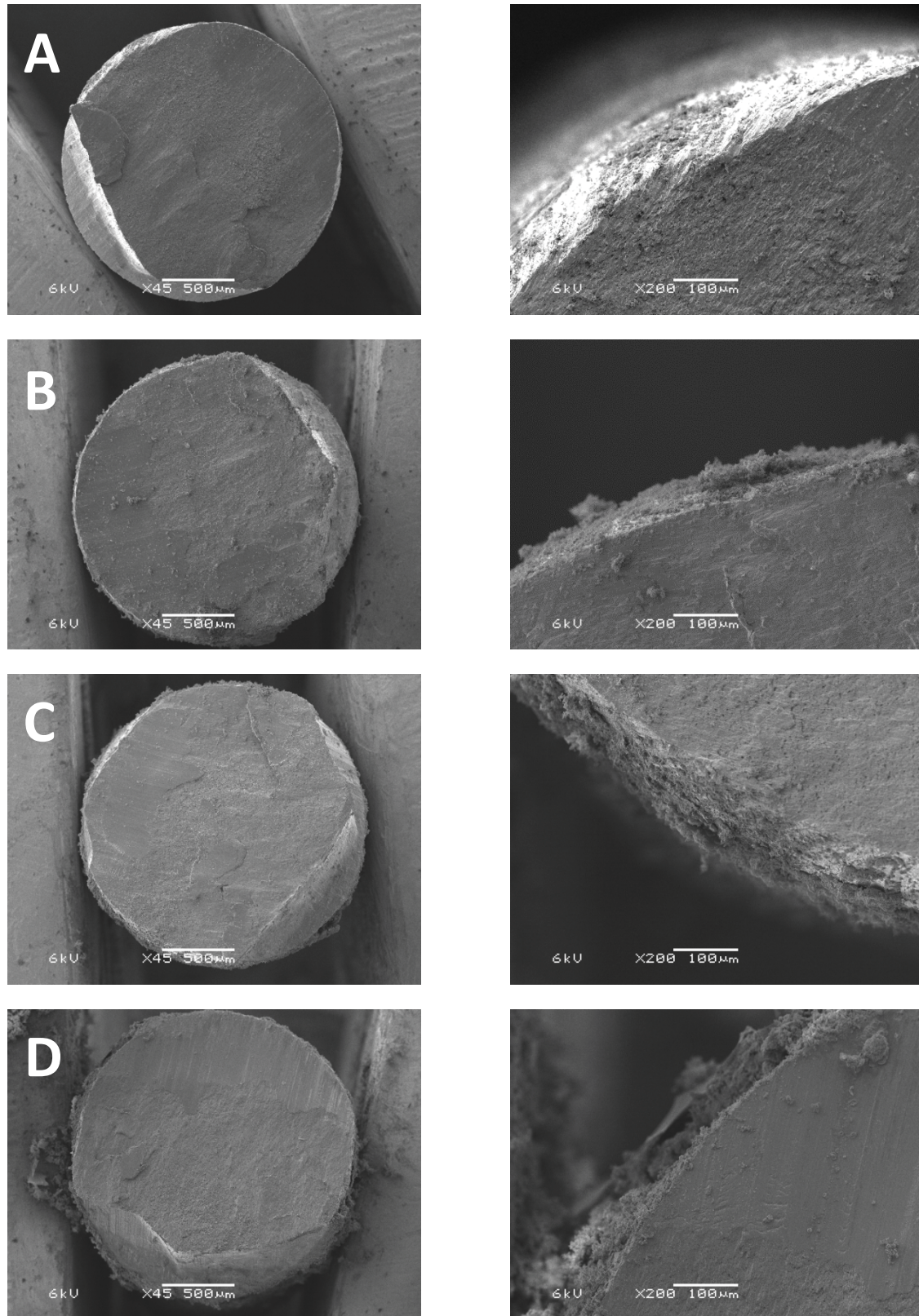


Fig. 13. SEM images showing cross sections the inner conductor during 4 days of experiment. Row A: 1st day, after 1 hr; Row B: 2nd day; Row C: 3rd day and Row D: 4th day. In both panels, the oxide layer at the outer surface is clearly visible. Note the difference in scale bars used, 500 μm in the left panels versus 100 μm in the right panels. Left and right panel in each row were obtained from the same specimen.

The SEM images shown in Fig. 13 were analyzed using open source software IMAGEJ (image processing and analysis in java) [46], resulting in estimated oxide layer thicknesses summarized in Table 4.

Table 4

Estimated thickness of the developed oxide layers over time obtained from the SEM images shown in Fig. 14. Each thickness has been based on three independent measurements on the same specimen.

No measurement	Day		
	2	3	4
1	12 (μm)	27 (μm)	62 (μm)
2	7 (μm)	22 (μm)	30 (μm)
3	5 (μm)	25 (μm)	16 (μm)

It is worth to mention that the stub resonator is much more sensitive for corrosion of the inner conductor surface as compared to the outer conductor surface. The converging of electric field lines near a surface depends on the curvature of the particular surface. It is for this reason that the electric field near the inner conductor is stronger than that near the outer conductor surface. This effect of geometry becomes apparent also when calculating the change in ϵ_{eff} upon the formation of an oxide layer on either the inner or outer conductor surface. Based on the resonator geometry listed in Table 1, covering the *inner* conductor with a 17 μm layer of metal oxide ($\epsilon=2.4$) lowers, according to Eq. 11, ϵ_{eff} from 72.47 to 66.36. Repeating this calculation but for an oxide layer of the same thickness on the outer conductor surface hardly affects ϵ_{eff} at all as it lowers ϵ_{eff} from 72.47 to just 72.46. Note also that the 17 μm oxide layer on the outer conductor surface represents a much larger metal oxide volume than a similar layer on the surface of the inner conductor, thereby emphasizing the much higher sensitivity of the inner conductor to corrosion effects.

The difference in sensitivity of both conductors is also shown graphically in Fig. 14, representing simulations of AF responses in the absence and presence of a 17 μm oxide layer on the surface of either the inner or outer conductor.

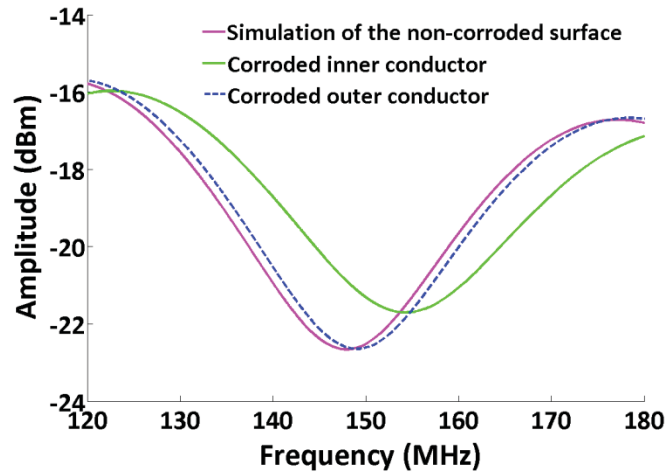


Fig. 14. Simulations of the 3rd resonance shown in Fig. 8 and Fig. 11 of the manuscript.

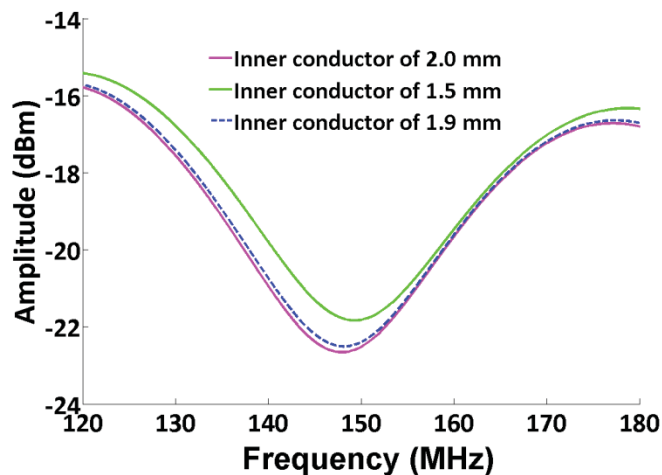


Fig. 15. Simulations of the 3rd resonance shown in Fig. 8 and Fig. 10 for different dimensions of the inner conductor.

The oxide layer forms and functions as an insulating layer for the conductor. It is also for this reason that the sensor is much more sensitive to the formation of the first oxide layer compared to the subsequent progressively increasing layer thickness over time.

Apart from an increase in thickness, over time the oxide layer becomes more porous and with that more brittle. As a result and promoted by flowing through the resonator, oxide particles may actually detach from the inner conductor surface thereby reducing its diameter. Alternatively, the corrosion product may also leave the resonator as metal ions instead of as metal oxide particles, thereby reducing its inner conductor diameter as well. As

the AF response is a function of the diameter of the inner conductor, the thinning of the inner conductor and eventually washing out of oxide products affects the resonator behavior. Fig. 15 simulates this effect by reducing the inner conductor diameter from 2.0 to 1.5 mm.

The high sensitivity of the inner conductor to corrosion is also evident when replacing this conductor with one made of stainless steel, rendering an inert, corrosion resistant electrode (Fig. 16). Compared to Fig. 8, the AF response hardly changes over a period of 4 days.

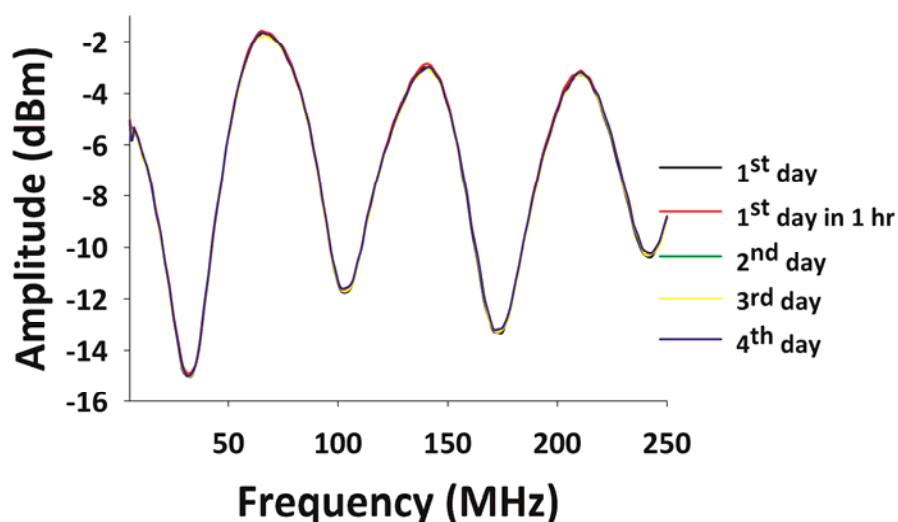


Fig. 16. AF response of a resonator with a stainless steel inner conductor, in the frequency range of 5MHz-250MHz.

Coplanar stripline (CPS) stub resonator

The working principle of the CPS stub resonator is essentially the same as the one of the coaxial stub resonator, it just exploits a different geometry. Fig. 17 shows the AF-response of the 1st resonance with the CPS (completely) immersed in 2 mM NaOH ($533 \cdot 10^{-4}$ S/m), while applying a dc-current current of 10 mA. During these dc-current induced corrosion experiments, the potential difference between the inner conductor and the Ag/AgCl reference electrode changed from -0.537 V at the start to a value in the range of 3.75 V - 4.19 V after applying dc-current for 3 hrs. The variability of the monitored voltage difference after three hours may reflect differences in oxide layer composition (see Discussion).

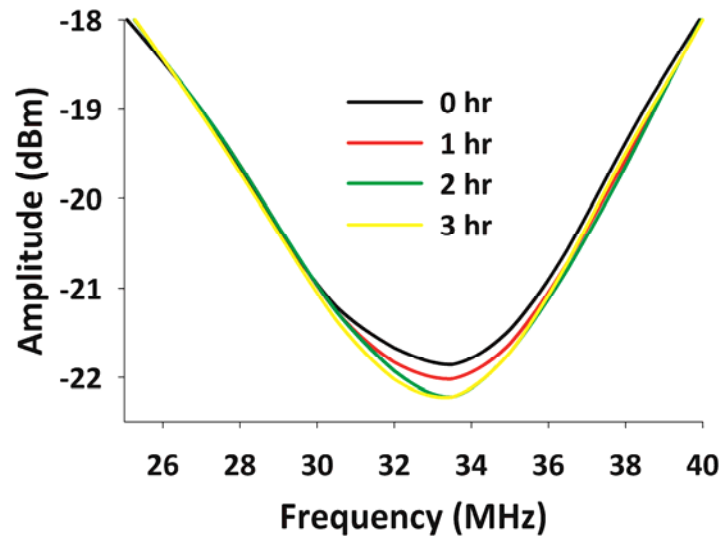


Fig. 17. AF plots of the CPS resonator showing the shift in resonance frequency and amplitude of the 1st resonance due to the effect of 3 hrs of corrosion, induced by a dc-current of 10 mA (1000 point/scan). Measurements were performed in the presence of 2 mM NaOH.

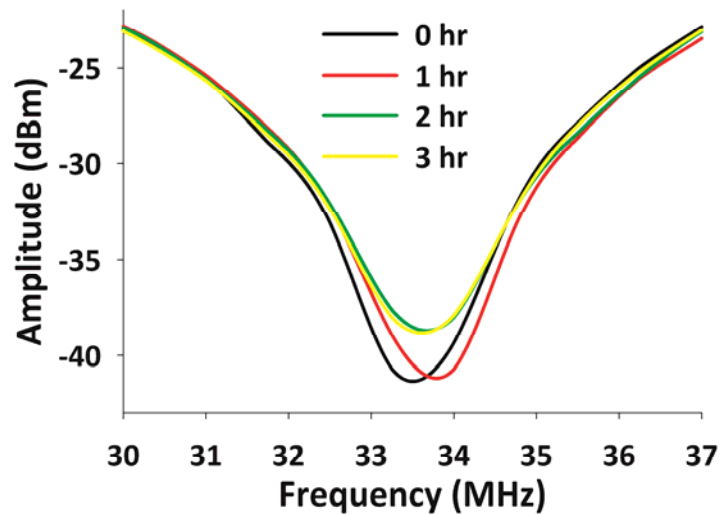


Fig. 18. AF plots of the CPS resonator showing the shift in resonance frequency and amplitude of the 1st resonance due to the effect of 3 hrs of corrosion, induced by a dc-current of 10 mA (1000 point/scan). Measurements were performed in MilliQ, i.e., in the absence of NaOH.

The result shows the response of a single inner conductor but recorded after different times of exposure to NaOH, for up to three hours. Both the resonance frequency f_{res} and the amplitude were affected by corrosion. As already remarked, dc-current induced corrosion will change the composition of the solution. Therefore, the response shown in Fig. 17 represents both the effect due to surface corrosion and change in solution composition. In order to isolate the response caused by the oxidation of the surface, we repeated the experiment but following the protocol outlined in Section 2 of Paragraph “Coplanar stripline (CPS) stub resonator”. While corrosion was performed in 2 mM NaOH, the actual measurement was recorded in MilliQ (after carefully rinsing the CPS with MilliQ). The result is shown in Fig. 18. Compared to Fig. 17, the effect of corrosion of the AF response is more profound. The reason is the rather high background of ionic conductance in the experiment of Fig. 17 due to the presence of 2 mM NaOH. The enhanced losses resulting from this ionic effect predominantly shapes the AF response and partly masks the effect due to surface corrosion. This is also the reason that we show the 1st instead of the 3rd resonance (as with the coaxial type) because the response is so much more sensitive to losses at higher frequencies. The reason for the almost identical response after 2 and 3 hours is twofold. Firstly, once an oxide layer has been formed, the sensor becomes less sensitive to further oxide formation. Secondly, the (accelerated) oxidation dissolves the inner conductor and by that increases the relative contribution of the oxidation of the outer conductor, also resulting in a compromised sensitivity.

As we did for the coax resonator, the CPS inner conductor surface was also characterized by SEM (Fig. 19). Because the outer conductor of the CPS resonator is made from tin as well, this conductor is also susceptible to oxidation. We therefore also examined samples of the outer conductor with SEM and examples are shown in Fig. 20. After 2 hrs (Fig. 20B), the outer conductor suffered less from oxidation compared to the inner conductor shown in Fig. 19C.

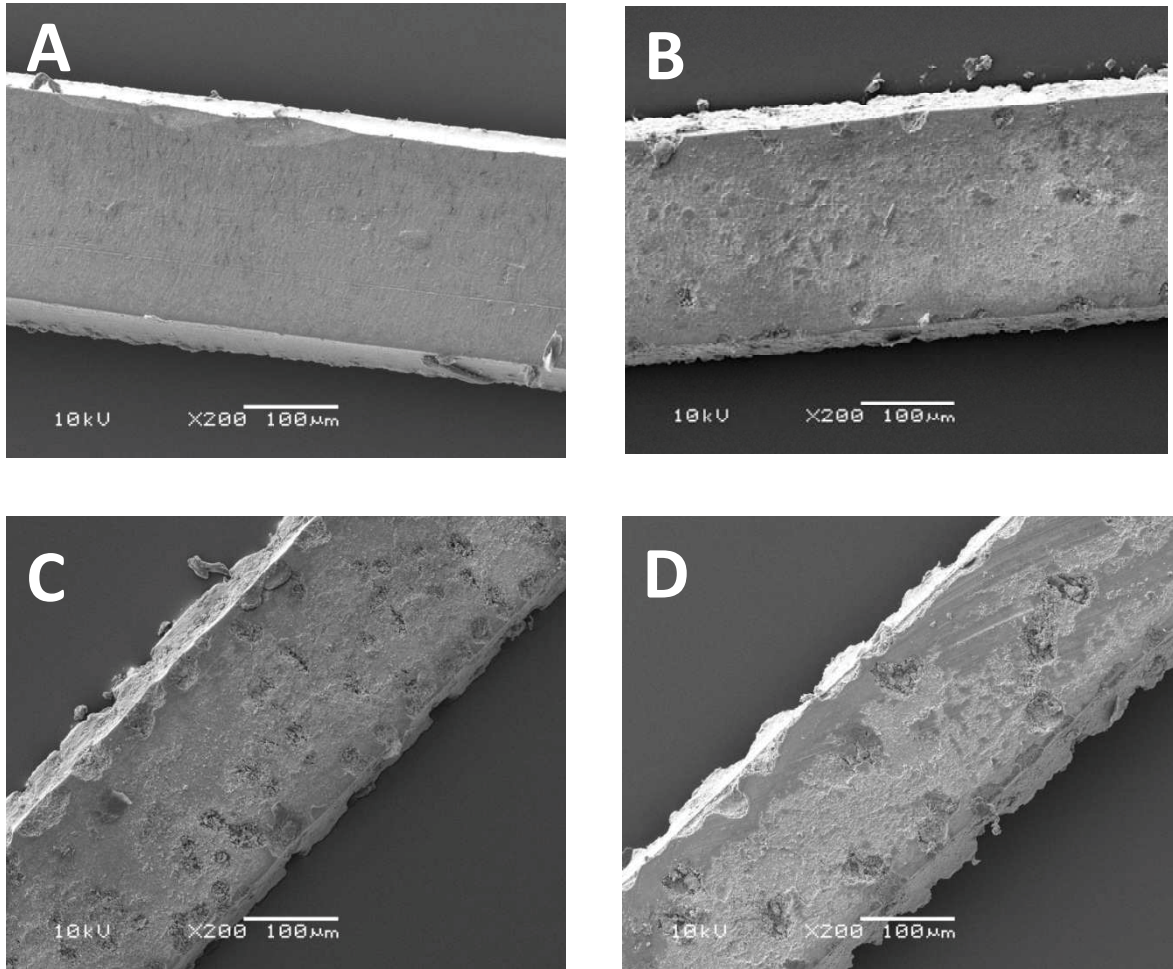


Fig. 19. SEM images showing non-corroded (A) and corroded parts of the inner conductor of the CPS resonator after 1 (B), 2 (C) and 3 hrs (D) of oxidation.

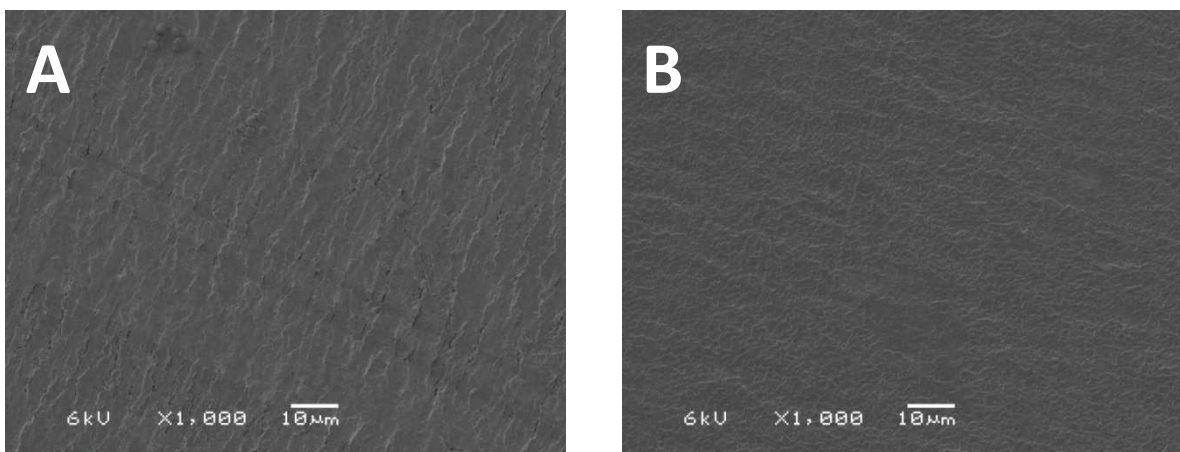


Fig. 20. SEM images showing non-corroded (A) and corroded parts of the outer conductor of the CPS resonator after 2 hrs (B) of oxidation.

5.5 Discussion

In this study we explored the possibility to use a stub resonator-based sensor for the detection of metal corrosion. These first results are encouraging but a number of questions remains to be answered. For example, in case of the coaxial resonator, how to explain the initial shift of the AF response to the left, followed by the one to the right (Fig. 10, Fig. 11). We hypothesize that even though corrosion occurs during the first two hours already, the effects remain limited to the appearance of isolated spots of oxide on the inner conductor's surface. When corrosion progresses the surface becomes covered by a concentric oxide layer completely isolating the conductor resulting in a significant shift of minimum in the AF plot to higher frequencies. Remains the question what causes the initial shift to lower frequencies? We have two possible explanations. The first one assumes the presence of small air bubbles on the (rough) metal surface prior to immersing the conductor in solution. Upon immersion, these air bubbles will (partly) dissolve or escape into the bulk solution thereby replacing a dielectric of low permittivity (air) for one of much higher permittivity (water). As a result, the resonance frequency will shift to lower frequencies, i.e., to the left. The next explanation offers an answer in quite different direction. The presence of (non-conducting) metal oxide spots intruding the conductor surface will make the total current pathway through the conductor longer resulting in an increase of the resonator inductance [29, 31]. The larger surface area due to increased roughness leads to a higher resonator capacitance [29, 31]. Both the increase of the resonator inductance and the resonator capacitance will shift the (resonant frequencies in the) AF plot to the left i.e., towards lower frequencies. Finally, the increased roughness also affects the resistance of the inner conductor. All effects mentioned above increase with increasing frequency, implying changes in AF response can be used to recognize pitting corrosion. However, studying pitting corrosion was considered to be beyond the scope of this study and the authors did not (yet) explore this potential application in more detail.

Even though we made a distinction between steel and stainless steel, suggesting the latter to be corrosion resistant, it should be realized that the main difference between the two types of steel refers to the rate they corrode. Corrosion rates depend on a number of parameters including temperature, composition of the corrosive medium the metal is exposed to and the type of metal itself. For example, according to [32], the corrosion rate of stainless steel at room temperature and in 5 g/l of NaCl is $1.85 \cdot 10^{-2}$ mpy. The corrosion rate of stainless steel type 316 L in drinking water and at room temperature is reported to be <0.1 mpy [33].

In comparison, the corrosion rate of steel can be as high as 40 mpy [34], i.e., a value 400 times higher than the one for stainless steel.

Correlation of the oxide layer thickness with the (change in) AF response requires knowledge of the layer thickness and dielectric permittivity of the oxide layer and the

thickness of this layer. Experimental determination of the layer thickness is challenging since corrosion forms all but a homogeneous layer.

A further complication arises from the (unknown) composition of the oxide layer. Even though $\text{Fe}(\text{OH})_3$ might be the predominant form with a dielectric permittivity in the range of 1.5-2.3 [39, 40], $\text{Fe}(\text{OH})_2$, $\text{Fe}_5\text{HO}_8 \cdot 4\text{H}_2\text{O}$, Fe_3O_4 , FeO , polymorphs of either FeOOH or Fe_2O_3 and any combination between them, may form as well. Reported dielectric permittivity values for these mentioned oxidation products range from 12.7-14.2 to 24 [41] to a value as high as 32.8 [42].

Despite the difficulty to establish the aforementioned correlation we did compare experimental results with model predictions. As already remarked, effects are more enhanced at higher resonances. To do so we assumed the inner conductor covered with a homogenous oxide layer consisting exclusively of $\text{Fe}(\text{OH})_3$ with an ϵ_r value of 2.3. By minimizing the difference between measured (26.97 MHz) and calculated resonance frequency of the 1st resonance with the layer thickness as free fitting parameter, we obtain an oxide layer thickness of 17 μm , a value close to the one derived by eye from Table 3. It remains hard to judge to what extent this estimate deviates from its actual (effective) value but according to the SEM picture of Fig. 13 such value seems quite realistic. Because of the heterogeneity of the oxide layer, any theoretical description based on homogenous layers is at least incomplete. This is true even more because prior to the actual recording standard procedure holds to sandpaper the inner conductor surface in order to remove the protection layer. This treatment improves surface roughness and affects surface resistance in a way simulation cannot account for, implying a further deviation between simulated and experimental data.

It is noted that the sensor is most sensitive for the first thin layer of metal oxide formed on the inner conductor, even if this metal oxide layer is not homogeneously distributed over the inner conductor surface. This makes the sensor concept feasible to detect corrosion at an early stage. Once the inner conductor is completely covered with a homogeneous layer of metal oxide, the signal shift in the AF plot per micron formed metal oxide layer thickness will decrease. This feature of the sensor is an advantage to detect early stages of corrosion but makes the sensor less sensitive for recording progressive corrosion.

The sensor described here monitors processes at a metal surface, notably that of the inner conductor. Apart from such surface effects, the behavior of the stub resonator depends on the dielectric properties of the fluid located in between inner and outer conductor as well as the geometry of the system. Attempts to include temperature [see 43, 44] and the conductivity of the fluid under investigation (now lumped in $\tan\delta_{eff}$) in the model used for the AF response simulations by the authors look most promising and are close to finalization (results not shown). Noteworthy, a relatively larger conductor surface will not per se make the device more sensitive. According to Eqs. 9-11, a larger diameter lowers the sensitivity. Also, the relative contribution of losses caused by the conductivity of the dielectric will increase because of the larger electrode surface. In addition, a larger inner

diameter will decrease the distance between both conductors, thereby increasing conductivity losses in the solution. Another argument deals with the necessity to keep the resonator impedance matched. Changing the diameter of the (not yet corroded) inner conductor from 2 to 15 mm reduced the impedance of the resonator; when filled with tap water from 19.1 to 3.5 Ω . As a result and due to significantly increased mismatch-related losses the behavior of the resonator totally changed, notably at higher frequencies (Fig. 7). On the other hand, reducing the diameter of the inner conductor increases the characteristic impedance Z_c of the system, which at Z_c values close to 100 Ω loses its ability to resonate (see also Appendix C and the Supplementary Information to the Chapter 2).

It is noted that the anode / cathode area ratio is an important factor in determining the corrosion rate and has an influence on the AF-response of the resonator. Therefore, in a real-life application, the inner conductor / outer conductor surface area ratio should reflect the actual anode / cathode surface area ratio, resulting in a relatively closer estimate of corrosion onset. However, it should be taken into account that changes in resonator geometry will result in changes of the characteristic impedance of the resonator which should be close to 50 Ω .

The sensor described here fulfills two (economic) requirements valid in general for all types of (ideal) sensors, i.e., easy to use and inexpensive. This is the case, for instance, if using a coaxial resonator of relatively large dimensions. Other advantages are: the sensor operates on - line and can be exposed to “real life process conditions” because it can be applied to, for instance, the interior of industrial piping systems. In addition, the sensitivity of the sensor can be adjusted by fine-tuning the inner and outer conductor surface area ratio, with, for instance, the inner conductor susceptible to corrosion but the outer conductor chemically inert. Another advantage of the stub resonator is that it responds to a number of different parameters affected by corrosion: skin effect, resonance frequency and dielectric losses.

In this study all results has been represented by AF responses. A Nyquist plot offers an alternative representation of the dielectric properties of a system showing the real and imaginary part of the input impedance. (see for an example Fig. A.1 in Supplementary Information). AF- and Nyquist plots are equivalent in terms of the information they render about the dielectric properties of the system under investigation. The reason we opted for AF plots is, first, that they relate more directly to the behavior of the resonator and, secondly, that they can be measured in a straightforward way, resulting in a practical and cost efficient sensor, i.e., a network analyzer for AF plots versus a more expensive impedance analyzer or network analyzer required for Nyquist representation. Further suggestions for cost reduction are given in the Supplementary Information.

According to [47, 48], for a non-ideal capacitor, the constant phase element Q (CPE) is a very helpful parameter for fitting experimental impedance data, even more so because it can be represented in terms of an equivalent electrical circuit. CPE behavior is generally attributed to distributed surface reactivity, surface inhomogeneity, roughness or fractal

geometry, electrode porosity, and to current and potential distributions associated with electrode geometry. Furthermore, observations on different types of diffusing species and electrode materials show that, in contrast to an ideal capacitance, the diffusive response of a non-ideal capacitance shows frequency dispersion in its low frequency tail, usually in the form of a CPE.

The model described in detail in [22] and applied in the present study accounts for dispersion of ϵ_{eff} , including the dispersion arising in the dielectric lossy part of the system. The real part ϵ_{re} of ϵ_{eff} can be considered to represent the behavior of an ideal capacitance, implying a f_{res} entirely defined by ϵ_{re} and not ϵ_{im} (see Eq. 5). For a non-ideal capacitance, i.e., for all real-life systems, f_{res} is defined by ϵ_{im} , σ and R as well.

As for potential application, we foresee most opportunities for the sensor as an early warning system where maintenance can be limited by replacing the inner conductor (just a metal rod) from time to time. After replacement, the corroded rod can easily be visually inspected for further detail. Depending on its precise application, the material of this metal rod can be adjusted (as long the permittivity of the particular oxide is known). Because of its relatively large dimensions, the metal rod can be produced in a cost effective and reproducible way. Another field of application can be a platform technology to test, for example, anti-corrosive compounds or other type of compounds that need to be tested for their dielectric properties. To do so, the (inner) conductor can be coated with an anti-corrosive compound. The rate at which the oxidation process proceeds upon dc-current application, compared to the resonator with uncoated electrodes, is a direct measure for the effectiveness of the anti-corrosive.

5.6 Concluding remarks

The results presented here are a first step towards the development of a stub resonator as an early warning system for the detection of corrosion. Future research will focus on a better understanding of the correlation between oxidation and the observed AF response. This is true even more for resonators with conductors made of alloys, implying more complex oxidation processes and kinetics. A related question still to be answered is, does passivation occur and if so how does it influence the AF response? The ultimate goal is to develop a sensor that monitors the rate of corrosion rather than one that just measures whether or not corrosion actually has happened.

Despite all the work still needed to come to the sensor outlined above, we do believe that compare to other currently existing technologies the stub resonator described in this study combines most of the advantages. For one thing, most of the techniques listed in the Introduction are intrusive and offline. The few techniques that are non-intrusive and on-line are either difficult to implement or require skilled personnel, implying higher operational cost.

5.7 Conclusions

The feasibility of using a flow-through coaxial stub resonator to detect the onset of corrosion was demonstrated for the corrosion of a steel inner conductor in tap water. Experimental data recorded during 4 days were in good agreement with model simulation data representing a 17 μm homogeneous oxide layer.

A coplanar stripline i.e., a 2 dimensional analog of the coaxial stub resonator was shown to successfully record the dc-current induced corrosion of a Sn/Ag alloy in water.

The large degree of freedom in sensor geometry design of transmission line resonators opens possibilities to operate the sensor in-line at “real life process conditions”, such as the interior of industrial piping systems. This feature, combined with limited maintenance of the system (e.g., replacing a metal inner conductor rod from time to time) opens possibilities to develop the sensor system to an early warning system.

5.8 Acknowledgement

This work was performed in the TTIW-cooperation framework of Wetsus, Centre of Excellence for Sustainable Water Technology (www.wetusus.nl). Wetusus is funded by the Dutch Ministry of Economic Affairs, the European Union Regional Development Fund, the Province of Fryslân, the City of Leeuwarden and the EZ/Kompas program of the “Samenwerkingsverband Noord-Nederland”. The authors thank the participants of the research theme Sensoring for the fruitful discussions and their financial support.

5.9 References

1. <http://www.g2mtlabs.com/2011/06/nace-cost-of-corrosion-study-update/>
2. J. Woodtli, R. Kieselbach, Damage due to hydrogen embrittlement and stress corrosion cracking, *Engineering Failure Analysis*, 7 (2000) 427-450, doi: [dx.doi.org/10.1016/S1350-6307\(99\)00033-3](https://doi.org/10.1016/S1350-6307(99)00033-3).
3. E. Rakanta, E. Daflou, G. Batis, Evaluation of corrosion problems in a closed air-conditioning system: a case study, *Desalination* 213 (2007) 9-17, doi: [dx.doi.org/10.1016/j.desal.2006.05.054](https://doi.org/10.1016/j.desal.2006.05.054).
4. B. Raj, U.K. Mudali, Materials development and corrosion problems in nuclear fuel reprocessing plants, *Progress in Nuclear Energy*, 48 (2006) 283–313, doi: [dx.doi.org/10.1016/j.pnucene.2005.07.001](https://doi.org/10.1016/j.pnucene.2005.07.001).
5. F. C. Robles Hernández, G. Plascencia, K. Kocha, Rail base corrosion problem for North American transit systems, *Engineering Failure Analysis*, 16 (2009) 281–294, doi: [dx.doi.org/10.1016/j.engfailanal.2008.05.011](https://doi.org/10.1016/j.engfailanal.2008.05.011).
6. M. Stern and A.L. Geary, Electrochemical Polarization, *J. Electrochem.Soc.*104, (1957) 56-63, doi: [10.1149/1.2428496](https://doi.org/10.1149/1.2428496).
7. C. Wagner and W. Traud, Z. The interpretation of corrosion phenomena by super-imposition of electrochemical partial reactions and the formation of potentials of mixed electrodes, *Zeitschrift fuer Elektrochemie und Angewandte Physikalische Chemie* (1938), 44, 391-402.
8. V.S. Agarwala, P.L. Reed, S. Ahmad, Corrosion Detection and Monitoring, - A Review Conference Paper, NACE International, CORROSION 2000, March 26 - 31, (2000).
9. C.F. Britton, Corrosion Monitoring and Inspection, *Shreir's Corrosion* 4 (2010) 3117-3166, doi: [dx.doi.org/10.1016/B978-044452787-5.00130-X](https://doi.org/10.1016/B978-044452787-5.00130-X).
10. P.R. Roberge, *Handbook of Corrosion Engineering*, McGraw-Hill Professional, New York, NY, (1999), ISBN-10/ASIN: 0070765162.
11. J. Mietz, B. Isecke, Monitoring of concrete structures with respect to rebar corrosion, *Construction and Building Materials*, Vol. 10, No. 5, July (1996), pp. 367-373.
12. H.J. De Bruyn, Current corrosion monitoring trends in the petrochemical industry, *International Journal of Pressure Vessels and Piping*, 66(1-3), (1996) 293-303.
13. F. Kuang, J. Jinna, Ch. Zou, T. Shi, Y. Wang, Sh. Zhang, H. Xu, Electrochemical Methods for Corrosion Monitoring: A Survey of Recent Patents, *Corrosion Science*, 2 (2010) 35-39, doi: [dx.doi.org/10.2174/1877610801002010034](https://doi.org/10.2174/1877610801002010034).
14. N.A. Hoog-Antonyuk, W. Olthuis, M.J.J. Mayer, D. Yntema, H. Miedema, A. van den Berg, On-line fingerprinting of fluids using coaxial stub resonator technology, *Sensors and Actuators B* 163 (2012) 90-96, doi: [dx.doi.org/10.1016/j.snb.2012.01.012](https://doi.org/10.1016/j.snb.2012.01.012).
15. D.M.Brasher, A.H.Kingsbury, Electrical measurements in the study of immersed paint coatings on metal. I. Comparison between capacitance and gravimetric methods of estimating water-uptake, *Journal of Applied Chemistry*, John Wiley & Sons, Ltd, <http://dx.doi.org/10.1002/jctb.5010040202>.
16. D. Bjegovic, J.J. Meyer, D. Mikulic, and D. Sekulic, Corrosion measurement in concrete utilizing different sensor technologies, NACE International, Paper No. 03435, (2003).
17. N.A. Hoog-Antonyuk, W. Olthuis, M.J.J. Mayer, H. Miedema, F.B.J. Leferink, A. van den Berg, Extensive Modeling of a Coaxial Stub Resonator for Online Fingerprinting of Fluids, *Procedia Engineering* (2012) pp. 310-313, doi: [10.1016/j.proeng.2012.09.145](https://doi.org/10.1016/j.proeng.2012.09.145).
18. W. Richards, Y. Lo, D. Harrison, An improved theory for microstrip antennas and applications, *Antennas and Propagation*, IEEE Transactions on , vol.29, no.1, pp.38, 46, (1981).
19. Z. Popovic, B. Popovic, *Introductory Electromagnetics*, Prentice Hall, (2000).
20. <http://www.microwaves101.com/encyclopedia/coaxdual.cfm>
21. P.S. Nikam, K.A. Pathan, Dielectric properties of Fe(OH)₃ thin films formed at solution-gas interface, *Bulletin of Materials Science* 01/(1994); 17(5):493-498.
22. N.A. Hoog, M.J.J. Mayer, H. Miedema, W. Olthuis, F.B.J. Leferink, A. van den Berg, Modeling and Simulations of the Amplitude-Frequency Response of Transmission Line Type Resonators Filled with Lossy Dielectric Fluids, *Sensors and Actuators A: Physical*, Volume 216, 1 September (2014), pp. 147-157, <http://dx.doi.org/10.1016/j.sna.2014.05.006>.
23. M.J.J. Mayer, N.A. Hoog, RF antenna filter as a sensor for measuring a fluid, WO Patent 005084, 13 January (2011).

24. M.J.J. Mayer, N.A. Hoog, Werkwijze en inrichting voor fingerprinting of het behandelen van een dielectricum in het algemeen en van water in het bijzonder, NL1038869, 16 August (2012).
25. D.M. Pozar, Microwave Engineering, Wiley, (2004).
26. Y.H. Suh, and K. Chang, Coplanar Stripline Resonators Modeling and Applications to Filters, IEEE Trans. Microwave Theory Tech. 50(5), 1289-1296 (2002).
27. M. Neshat, D. Saeedkia, S. Safavi-Naeini, Analysis of an Edge-Coupled Terahertz Photomixer Source Integrated with a Coplanar Stripline, in The Proceeding of the Joint 31st International Conference on Infrared and Millimeter Waves and 14th International Conference on Terahertz Electronics, (IEEE 2006), p. 526.
28. R.N. Simons, Coplanar Waveguide Circuits, Components, and Systems John Wiley & Sons, Inc., New York, (2001).
29. R.E. Collin, Foundations for Microwave Engineering, Wiley IEEE, (2000).
30. C.A. Moina, G.O. Ybarra, Study of passive films formed on Sn in the 7–14 pH range, Journal of Electroanalytical Chemistry, Volume 504, Issue 2, 18 May (2001), 175-183.
31. S.M. Guralnick, The Contexts of Faraday's Electrochemical Laws, Isis, Vol. 70, No. 1 (1979), 59-75.
32. N.M. Dawood, Corrosion of Stainless steel 316 L in Various Aqueous Salt Solutions, Collage of Materials Engineering-BabylonUniversity, <http://www.uobabylon.edu.iq/uobcoleges/filesshare/articles/Corrosion%20of%20Stainless%20steel%20316%20L%20with%20Time%20in%20Various%20Aqueous%20Salt%20Solutions.pdf>
33. Corrosion resistance of the austenitic chromium-nickel stainless steels in chemical environments, THE INTERNATIONAL NICKEL COMPANY, INC., One New York Plaza, New York, N.Y. 10004, 2nd Edition, 1970.
34. R.W. Revie (Editor), Uhlig's Corrosion Handbook, 3rd Edition, John Wiley & Sons, Inc., 2011 ISBN: 978-0-470-08032-0.
35. A. Ghoneim, M.A. Ameer, A.M. Fekry and F. El-Taib Heakal, Cyclic Voltammetric Studies on Selected Tin-Silver Binary Alloys in Sodium Hydroxide Solution, Corrosion, Vol. 66, No. 11, (2010).
36. F. Horn, J. W. Reynolds, and J. C. Rautio, Conductor Profile Effects on the Propagation Constant of Microstrip Transmission Lines, Microwave Symposium Digest (MTT), (2010) IEEE MTT-S International.
37. Y.Shlepnev, C. Nwachukwu, Roughness characterization for interconnect analysis, Electromagnetic Compatibility (EMC), 2011 IEEE International Symposium on.
38. Holloway, C. L.; Kuester, E. F. Power loss associated with conducting and rough surfaces, IEEE Trans. Microwave Theory Tech. 48: October, (2000), pp. 1601—1610.
39. <http://nl.krohne.com/nl/services/dielectric-constants/>
40. <http://www.deltacnt.com/99-00032.htm>
41. G. Kugel, C. Carabatos, B. Hennion, B. Prevot, Lattice dynamics of Wustite (FeO), Phys. Rev. B16, 378 (1977).
42. R.V. Pisarev, V.V. Druzhinin, N.N. Nesterova, Optical absorption of ferroelectrical iron boracites, Phys. Stat. Sol. 40, 503 (1977).
43. O. A. Nabokov and Yu. A. Lubimov, High-Frequency Dielectric Constant of Water and Determination of the Kirkwood Correlation Factor, Journal of Structural Chemistry, Volume 27, Number 5 pp. 731-736, 1987.
44. C. Guillou, W. Ellison, L. Eymard, K. Lamkaouchi, C. Prigent, G. Delbos, G. Balana, and S.A. Boukabara, Impact of new permittivity measurements on sea surface emissivity modeling in microwaves, Radio Sci., 33, 649-667, 1998 doi:10.1029/97RS02744.
45. Wohlfarth, M.D. Lechner, Static Dielectric Constants of Pure Liquids and Binary Liquid Mixtures, Supplement to IV/6, Series: Landolt-Bornstein: Numerical Data and Functional Relationships in Science and Technology – New Series, vol. 17, Subseries: Physical Chemistry, (2008), p. 203.
46. <http://imagej.nih.gov/ij/>
47. J. Bisquert, G. Garcia-Belmonte, P. Bueno, E. Longo, L.O.S. Bulhoes, Impedance of constant phase element (CPE)-blocked diffusion in film electrodes, Journal of Electroanalytical Chemistry, Volume 452, Number 2, 30 July 1998, pp. 229-234(6).
48. J.-B. Jorcin, M. E. Orazem, N. Pébère, B. Tribollet, CPE analysis by local electrochemical impedance spectroscopy, Electrochimica Acta, Volume 51, Issues 8–9, 20 January 2006, Pages 1473-1479, ISSN 0013-4686, <http://dx.doi.org/10.1016/j.electacta.2005.02.128>.

6.0 Supplementary Information

Appendix A

Nyquist representation

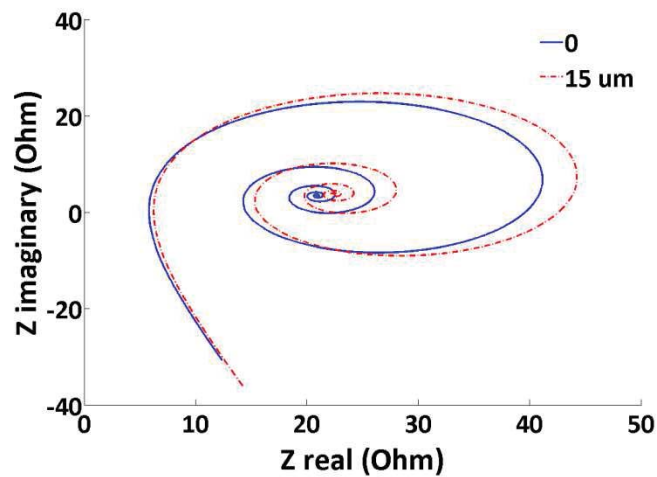


Fig. A.1. Nyquist plot calculated for the coaxial-type of resonator used for Figs. 7A and 8, in the absence (blue) or presence (red) of an oxide layer with an (assumed) thickness of 15 μm . Clearly visible are three sets of semicircles, from right to left, corresponding to the first three resonances shown in Figs. 7A and 8.

Appendix B

Here we demonstrate an example of the MATLAB code and data file to realize the fitting of the radius of the oxide layer, r and effective loss tangent $\tan\delta_{eff}$ from the measured output voltage V_{out} .

Main program for parameter estimation for coaxial resonator:

```
clear all % Clear all variables in function workspace
close all % Close all figures
clc % Clear command window
clearvars
format longE
load dayone.txt % load the file with data of the day of experiment
f=dayone(:,1); % Load experimental data; frequency
amplitude=dayone(:,2); % Load experimental data; amplitude
f=f*1e+6; % Frequency conversion
%- Plot experimental data
plot(f/1e+6, amplitude, 'or')
hold on
x0 = [0.01 0];
ya0 = corr_coax_resonator_main(x0,f);
%% - Plot initial values
% hold on;
% plot(f,ya0,'--m')
%-Boundary conditions
LB = [0.01 0]; % Lower bounds
UB = [1 1e-4]; %Upper bounds
```

```
% -Solving nonlinear least-squares curve fitting
[x,resnorm] = lsqcurvefit('corr_coax_resonator_main',x0,f,amplitude, LB, UB)
ya = corr_coax_resonator_main(x,f);
%- Plot fit results
Hf = plot(f/1e+6,ya,'b');
set(Hf, 'LineWidth',3)
hold on
xlabel('Frequency, (MHz)','fontsize',42,'fontweight','b');
ylabel('Amplitude, (dBm)','fontsize',42,'fontweight','b');
grid on
hold on
```

Function evaluates the model the amplitude-frequency response of coaxial transmission line type resonators filled with corroded inner conductor:

```
function F = corr_coax_resonator_main(x,f)
h=0.267+0.029; % the hgth of the coaxial resonator, [m]
h_polymer=0.042; % the hgth of the layer of the polymer layer, [m]
db=25e-3; % diameter of the resonator;
Vt=pi*h*db^2/4; %volume of the empty resonator [m^3]
f_polymer=(pi*h_polymer*db^2/4)/Vt %volume fraction of the polymer layer [m^3]
f_feed_t=1-f_polymer %volume fraction of the fluid [m^3]
e_polymer=2.2 % dielectric constant of the polymer layer
r2 = (25.4e-3)/2; %inner radius of the outer conductor, [m]
r0 = (2e-3)/2; %radius of the inner conductor of the resonator, [m]
Er1 = 2.4; %dielectric permittivity of an oxide layer, [-]
Er2 =80; % dielectric permittivity of a fluid substrate, [-]
Ur =1; %relative dielectric permeability of the dielectric between inner and outer conductors, [-]
e = 8.854e-12; % vacuum permeability [H/m]
u = Ur*1.257e-6;% magnetic permeability of the dielectric, [H/m]
r1=r0+x(2); %radius of the occurred oxide layer (m);
c=3*1e+8; % speed of light in vacuum, [m/s]
% capacitance of the open ended coaxial stub resonator, contains the oxide layer, [F/m]
C1=2*pi*e*Er1/(log(r1/r0))
% capacitance of the open ended coaxial stub resonator, contains a fluid, [F/m]
C2=2*pi*e*Er2/(log(r2/r1))
% total capacitance of the open ended coaxial stub resonator, [F/m]
C=1/(1/C1+1/C2)
% inductance of the open ended coaxial stub resonator, [H/m]
L = ((u/(pi^2))*log(r2/r0))
Ur=1; %relative dielectric permeability of the dielectric between inner and outer conductors, [-]
u = Ur*4*pi*1e-7; % magnetic permeability of the dielectric, [H/m]
sigma_stainless_steel=7.7e+6;%conductance of the metal applied for outer conductor (stainless steel), [1/(Ohm*m)]
sigma_steel=6.99e+6;%conductance of the metal applied for inner conductor ( steel), [1/(Ohm*m)]
Eeff_coax=(Er1*Er2*log(r2/r0))/((Er1*log(r2/r1)+Er2*log(r1/r0)))% effective dielectric constant of whole system, [-]
sigma_steel=7.7e+6;%conductance of the metal for the outer conductor(stainless steel) [1/(Ohm*m)]
Eeff=Eeff_coax*(f_feed_t)+e_polymer*f_polymer
E= Eeff * 1/(4*pi*1e-7*c*c); % vacuum permeability [H/m]
sigma_eff=0; % effective conductivity of the system, [S/m]
vin=120e-3; %input voltage supplied by the function generator, [V]
omega = 2*pi*f;% angular frequency, [rad/s]
Eim=((omega.*E.*x(1))-sigma_eff)./omega;%imaginary part of complex dielectric permittivity
skin_depth1=sqrt(2./(omega.*u.*sigma_stainless_steel));%skin_depth
```

```

skin_depth2=sqrt(2./(omega.*u.*sigma_steel));%skin_depth
Rs1=1./(sigma_stainless_steel.*skin_depth1);% surface resistivity of the outer conductor of the resonator
Rs2=1./(sigma_steel.*skin_depth2);% surface resistivity of the inner conductor of the resonator
R=Rs2/r0+Rs1/r2;% distributed element resistance R of the resonator [Ohm/m]
G=(omega.*Eim+sigma_eff)./(omega.*E).*omega.*C;%distributed element conductance of the resonator
[F/(m*s)]
gamma=(sqrt((R+1i.*omega.*L).*(G+1i.*omega.*C)));%complex propagation constant [1/m]
%notes on gamma: Re(gamma)=alfa = attenuation constant representing losses [Np/m];
Im(gamma)=beta=phase of the propagation constant [rad/m]
%since the signal is oscillating in time with omega rad/s, the propagation velocity of the wave [m/s] =
omega/beta; also, beta = 2*pi/wavehgt.
Zc=sqrt(((R+1i.*omega.*L)./(G+1i.*omega.*C)));% complex characteristic impedance of the resonator [Ohm]
Zin=Zc.*coth(gamma.*h);%complex input impedance of the resonator [Ohm]
vout=sqrt((real(Zin.*(vin./(50+2*Zin)))).^2+(imag(Zin.*(vin./(50+2*Zin)))).^2);%modulus of vout, the is the
recorded voltage by the spectrum analyzer [V]
F=20.*log10(vout)+13;%vout as a power ratio in dBm i.e., the measured power referenced to one mWatt and
the underlying assumption of a 50 Ohm load resistance

```

Appendix C

Decreasing the inner conductor diameter increases the characteristic impedance Z_c of the system. At values close to 100 Ω the system loses its ability to resonate, as shown in Fig. C. 1.

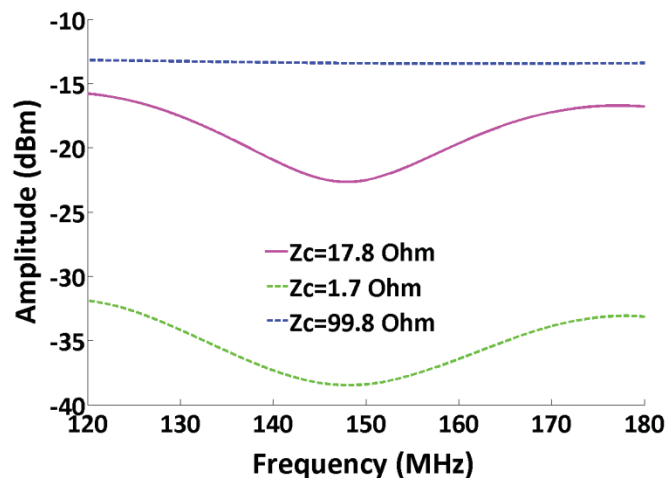


Fig. C.1. Simulations of the 3rd resonance shown in Fig. 8 and 11 of the manuscript by changing the diameter of the inner conductor from 2 mm (original value, pink) to 20 mm (green) and 0.02 mm (blue), respectively.

Mathlab code for the simulations in Fig. C.1

```

% _____ INNER CONDUCTOR_Day_1_2mm _____
format longE
h=0.267+0.029; % the length of the coaxial resonator
h_polymer=0.042; % the length of the layer of the polymer layer [m]
db=25e-3; % diameter of the resonator;
Vt=pi*h*db^2/4; %volume of the empty resonator [m^3]
Vt_polymer=pi*h_polymer*db^2/4 %volume of the polymer layer [m^3]
f_polymer=(pi*h_polymer*db^2/4)/Vt %volume fraction of the polymer layer [m^3]

```



```

Vt_feed=Vt-Vt_polymer %volume of the resonator with the polymer layer [m^3]
f_feed=Vt_feed/Vt
f_feed_t=1-f_polymer
e_polymer=2.2 % dielectric constant of the polymer layer
len = 0.267+0.029; %the length of the coaxial resonator, [m];
r2 = (25.4e-3)/2; %inner radius of the outer conductor, [m];
r0 = (2e-3)/2; %radius of the inner conductor of the resonator, [m];
Er1 = 2.4; %dielectric permittivity of an oxide layer, [-];
Er2 =80; % dielectric permittivity of a fluid substrate, [-],
Ur =1; %relative dielectric permeability of the dielectric between inner and outer conductors, [-]
e = 8.854e-12; % vacuum permeability [H/m]
u = Ur*1.257e-6;% magnetic permeability of the dielectric, [H/m]
r1=r0+8.202735219555178e-06; %radius of the occurred oxide layer (m);
c=3*1e8; % speed of light in vacuum, [m/s]
% capacitance of the open ended coaxial stub resonator, contains the oxide layer, [F]
C1=2*pi*e*Er1/(log(r1/r0))
% capacitance of the open ended coaxial stub resonator, contains a fluid, [F]
C2=2*pi*e*Er2/(log(r2/r1))
% total capacitance of the open ended coaxial stub resonator, [F]
C=1/(1/C1+1/C2)
% -----
% capacitance of the open ended coaxial stub resonator, contains air, [F]
Cair=2*pi*e/(log(r2/r0))
%Double check of the effective dielectric permittivity of the system
Dielectric_permittivity=C/Cair
% inductance of the open ended coaxial stub resonator, [H]
L = ((u/(pi*2))*log(r2/r0))
Ur=1; %relative dielectric permeability of the dielectric between inner and outer conductors, [-]
u = Ur*4*pi*1e-7; % magnetic permeability of the dielectric, [H/m]

sigma_feed=515e-4;%conductivity of a fluid between inner and outer conductors, [S/m]
sigma_stainless_steel=7.7e+6;%conductance of the metal applied for outer conductor (stainless steel),
[1/(Ohm*m)]
sigma_steel=6.99e+6;%conductance of the metal applied for inner conductor ( steel), [1/(Ohm*m)]
sigma_oxide=1e-4;%conductivity of an oxide layer, Reference [17] in the manuscript
Eeff_coax=(Er1*Er2*log(r2/r0))/((Er1*log(r2/r1)+Er2*log(r1/r0))% effective dielectric constant of whole
system, [-]
eps2=Eeff_coax
sigma_polymer=1.41e-7%conductivity of polymer layer
sigma_steel=7.7e+6;%conductance of the metal for the outer conductor(stainless steel) [1/(Ohm*m)]

Eeff=Eeff_coax*(f_feed_t)+e_polymer*f_polymer
E= Eeff * 1/(4*pi*1e-7*c*c); % vacuum permeability [H/m]
Vres=pi*r2^2*len
Voxide=pi*r1^2*len
sigma_eff_main=(sigma_oxide*Voxide+sigma_feed*(Vres-Voxide))/Vres
sigma_eff=sigma_eff_main*f_feed_t+sigma_polymer*f_polymer;
check_1=f_feed_t+f_polymer
% sigma_eff2= (sigma_feed*log(r2/r1) + sigma_oxide*log(r1/r0))/(log(r2/r0))
% Check volumes fractions
%v1=log(r2/r1)
%v2=log(r1/r0)
%v=(v1+v2)/(log(r2/r0))
vin=120e-3; %input voltage supplied by the function generator, [V]
f=120E+06:10000:180E+06;
omega = 2*pi*f;% angular frequency, [rad/s]

```

```

tg= 1.168018964411114e-01
Eim=((omega.*E.*tg)-sigma_eff)./omega;%imaginary part of complex dielectric permittivity
skin_depth1=sqrt(2./(omega.*u.*sigma_stainless_steel));%skin_depth
skin_depth2=sqrt(2./(omega.*u.*sigma_steel));%skin_depth
Rs1=1./(sigma_stainless_steel.*skin_depth1);% surface resistivity of the outer conductor of the resonator
Rs2=1./(sigma_steel.*skin_depth2);% surface resistivity of the inner conductor of the resonator
R=Rs2/r0+Rs1/r2;% distributed element resistance R of the resonator [Ohm/m]
G=(omega.*Eim+sigma_feed)./(omega.*E).*omega.*C;%distributed element conductance of the resonator
[F/(m*s)]
gamma =(sqrt((R+1i.*omega.*L).*(G+1i.*omega.*C)))/%complex propagation constant [1/m]
%notes on gamma: Re(gamma)=alfa = attenuation constant representing losses [Np/m];
Im(gamma)=beta=phase of the propagation constant [rad/m]
%since the signal is oscillating in time with omega rad/s, the propagation velocity of the wave [m/s] =
omega/beta; also, beta = 2*pi/wavelength.
Zc=sqrt(((R+1i.*omega.*L)./(G+1i.*omega.*C)))/% complex characteristic impedance of the resonator [Ohm]
Zc1=Zc
Zin=Zc.*coth(gamma.*len);%complex input impedance of the resonator [Ohm]
vout=sqrt((real(Zin.*(vin./(50+2*Zin))))).^2+(imag(Zin.*(vin./(50+2*Zin))))).^2);%modulus of vout, the is the
recorded voltage by the spectrum analyzer [V]
vout =20.*log10(vout)+13;%vout as a power ratio in dBm i.e., the measured power referenced to one mWatt
and the underlying assumption of a 50 Ohm load resistance
hF = figure
hA = axes
set(hA, 'XGrid', 'off', 'YGrid', 'on')
hold on
set(0,'DefaultFontSize',36,'DefaultFontName','Times New Roman', 'DefaultFontWeight', 'bold');
%- See the Supplementary Information
load dayone.txt % load the file
MHz=dayone(:,1); % Load experimental data; frequency
CH1=dayone(:,2); % Load experimental data; amplitude
frequency=MHz;
amplitude=CH1;
plot(frequency,amplitude,'LineStyle','none','Marker','.', 'MarkerEdgeColor','r', 'MarkerSize',40)
hold on
plot(f/1e+6,vout, 'm', 'LineWidth', 3);
xlabel('Frequency, (MHz)','fontsize',42,'fontweight','b');
ylabel('Amplitude, (dBm)','fontsize',42,'fontweight','b');
hold on
% _____ INNER CONDUCTOR_Day_1_20mm _____
format longE
h=0.267+0.029; % the length of the coaxial resonator
h_polymer=0.042; % the length of the layer of the polymer layer [m]
db=25e-3; % diameter of the resonator;
Vt=pi*h*db^2/4;%volume of the empty resonator [m^3]
Vt_polymer=pi*h_polymer*db^2/4 %volume of the polymer layer [m^3]
f_polymer=(pi*h_polymer*db^2/4)/Vt %volume fraction of the polymer layer [m^3]
Vt_feed=Vt-Vt_polymer %volume of the resonator with the polymer layer [m^3]
f_feed=Vt_feed/Vt
f_feed_t=1-f_polymer
e_polymer=2.2 % dielectric constant of the polymer layer
len = 0.267+0.029; %the length of the coaxial resonator, [m];
r2 = (25.4e-3)/2; %inner radius of the outer conductor, [m];
r0 = (20e-3)/2; %radius of the inner conductor of the resonator, [m];
Er1 = 2.4; %dielectric permittivity of an oxide layer, [-];
Er2 =80; % dielectric permittivity of a fluid substrate, [-],
Ur =1; %relative dielectric permeability of the dielectric between inner and outer conductors, [-]

```

```

e = 8.854e-12; % vacuum permeability [H/m]
u = Ur*1.257e-6;% magnetic permeability of the dielectric, [H/m]
r1=r0+8.202735219555178e-06; %radius of the occurred oxide layer (m);
c=3*1e+8; % speed of light in vacuum, [m/s]
% capacitance of the open ended coaxial stub resonator, contains the oxide layer, [F]
C1=2*pi*e*Er1/(log(r1/r0))
% capacitance of the open ended coaxial stub resonator, contains a fluid, [F]
C2=2*pi*e*Er2/(log(r2/r1))
% total capacitance of the open ended coaxial stub resonator, [F]
C=1/(1/C1+1/C2)
% -----
% capacitance of the open ended coaxial stub resonator, contains air, [F]
Cair=2*pi*e/(log(r2/r0))
%Double check of the effective dielectric permittivity of the system
Dielectric_permittivity=C/Cair
% inductance of the open ended coaxial stub resonator, [H]
L = ((u/(pi*2))*log(r2/r0))
Ur=1; %relative dielectric permeability of the dielectric between inner and outer conductors, [-]
u = Ur*4*pi*1e-7; % magnetic permeability of the dielectric, [H/m]
sigma_feed=515e-4;%conductivity of a fluid between inner and outer conductors, [S/m]
sigma_stainless_steel=7.7e+6;%conductance of the metal applied for outer conductor (stainless steel), [1/(Ohm*m)]
sigma_steel=6.99e+6;%conductance of the metal applied for inner conductor ( steel), [1/(Ohm*m)]
sigma_oxide=1e-4;%conductivity of an oxide layer, Reference [17] in the manuscript
Eeff_coax=(Er1*Er2*log(r2/r0))/((Er1*log(r2/r1)+Er2*log(r1/r0)))% effective dielectric constant of whole system, [-]
eps2=Eeff_coax
sigma_polymer=1.41e-7%conductivity of polymer layer
sigma_steel=7.7e+6;%conductance of the metal for the outer conductor(stainless steel) [1/(Ohm*m)]
Eeff=Eeff_coax*(f_feed_t)+e_polymer*f_polymer
E= Eeff * 1/(4*pi*1e-7*c*c); % vacuum permeability [H/m]
Vres=pi*r2^2*len
Voxide=pi*r1^2*len
sigma_eff_main=(sigma_oxide*Voxide+sigma_feed*(Vres-Voxide))/Vres
sigma_eff=sigma_eff_main*f_feed_t+sigma_polymer*f_polymer;
check_1=f_feed_t+f_polymer
vin=120e-3; %input voltage supplied by the function generator, [V]
f=120E+06:10000:180E+06;
omega = 2*pi*f;% angular frequency, [rad/s]
tg= 1.168018964411114e-01
Eim=((omega.*E.*tg)-sigma_eff)./omega;%imaginary part of complex dielectric permittivity
skin_depth1=sqrt(2./(omega.*u.*sigma_stainless_steel));%skin_depth
skin_depth2=sqrt(2./(omega.*u.*sigma_steel));%skin_depth
Rs1=1./(sigma_stainless_steel.*skin_depth1);% surface resistivity of the outer conductor of the resonator
Rs2=1./(sigma_steel.*skin_depth2);% surface resistivity of the inner conductor of the resonator
R=Rs2/r0+Rs1/r2;% distributed element resistance R of the resonator [Ohm/m]
G=(omega.*Eim+sigma_feed)/(omega.*E).*omega.*C;%distributed element conductance of the resonator [F/(m*s)]
gamma =(sqrt((R+1i.*omega.*L).*(G+1i.*omega.*C)))/omega;%complex propagation constant [1/m]
%notes on gamma: Re(gamma)=alfa = attenuation constant representing losses [Np/m];
Im(gamma)=beta=phase of the propagation constant [rad/m]
%since the signal is oscillating in time with omega rad/s, the propagation velocity of the wave [m/s] = omega/beta; also, beta = 2*pi/wavelength.
Zc=sqrt(((R+1i.*omega.*L)/(G+1i.*omega.*C)))/omega;% complex characteristic impedance of the resonator [Ohm]
Zc2=Zc
Zin=Zc.*coth(gamma.*len);%complex input impedance of the resonator [Ohm]

```

```

vout=sqrt((real(Zin.*(vin./(50+2*Zin))))).^2+(imag(Zin.*(vin./(50+2*Zin))))).^2;%modulus of vout, the is the
recorded voltage by the spectrum analyzer [V]
vout =20.*log10(vout)+13;%vout as a power ratio in dBm i.e., the measured power referenced to one mWatt
and the underlying assumption of a 50 Ohm load resistance
plot(f/1e+6,vout,'g--','LineWidth',3);
xlabel('Frequency, (MHz)','fontsize',42,'fontweight','b');
ylabel('Amplitude, (dBm)','fontsize',42,'fontweight','b');
hold on
% _____ INNER CONDUCTOR_Day_1_0.02mm _____
format longE
h=0.267+0.029; % the length of the coaxial resonator
h_polymer=0.042; % the length of the layer of the polymer layer [m]
db=25e-3; % diameter of the resonator;
Vt=pi*h*db^2/4; %volume of the empty resonator [m^3]
Vt_polymer=pi*h_polymer*db^2/4 %volume of the polymer layer [m^3]
f_polymer=(pi*h_polymer*db^2/4)/Vt %volume fraction of the polymer layer [m^3]
Vt_feed=Vt-Vt_polymer %volume of the resonator with the polymer layer [m^3]
f_feed=Vt_feed/Vt
f_feed_t=1-f_polymer
e_polymer=2.2 % dielectric constant of the polymer layer
len = 0.267+0.029; %the length of the coaxial resonator, [m];
r2 = (25.4e-3)/2; %inner radius of the outer conductor, [m];
r0 = (0.02e-3)/2; %radius of the inner conductor of the resonator, [m];
Er1 = 2.4; %dielectric permittivity of an oxide layer, [-];
Er2 =80; % dielectric permittivity of a fluid substrate, [-],
Ur =1; %relative dielectric permeability of the dielectric between inner and outer conductors, [-]
e = 8.854e-12; % vacuum permeability [H/m]
u = Ur*1.257e-6;% magnetic permeability of the dielectric, [H/m]
r1=r0+8.202735219555178e-06; %radius of the occurred oxide layer (m);
c=3*1e+8; % speed of light in vacuum, [m/s]
% capacitance of the open ended coaxial stub resonator, contains the oxide layer, [F]
C1=2*pi*e*Er1/(log(r1/r0))
% capacitance of the open ended coaxial stub resonator, contains a fluid, [F]
C2=2*pi*e*Er2/(log(r2/r1))
% total capacitance of the open ended coaxial stub resonator, [F]
C=1/(1/C1+1/C2)
% -----
% capacitance of the open ended coaxial stub resonator, contains air, [F]
Cair=2*pi*e/(log(r2/r0))
%Double check of the effective dielectric permittivity of the system
Dielectric_permittivity=C/Cair
% inductance of the open ended coaxial stub resonator, [H]
L = ((u/(pi*2))*log(r2/r0))
Ur=1; %relative dielectric permeability of the dielectric between inner and outer conductors, [-]
u = Ur*4*pi*1e-7; % magnetic permeability of the dielectric, [H/m]
sigma_feed=515e-4;%conductivity of a fluid between inner and outer conductors, [S/m]
sigma_stainless_steel=7.7e+6;%conductance of the metal applied for outer conductor (stainless steel),
[1/(Ohm*m)]
sigma_steel=6.99e+6;%conductance of the metal applied for inner conductor ( steel), [1/(Ohm*m)]
sigma_oxide=1e-4;%conductivity of an oxide layer, Reference [17] in the manuscript
Eeff_coax=(Er1*Er2*log(r2/r0))/((Er1*log(r2/r1)+Er2*log(r1/r0))% effective dielectric constant of whole
system, [-]
eps2=Eeff_coax
sigma_polymer=1.41e-7%conductivity of polymer layer
sigma_steel=7.7e+6;%conductance of the metal for the outer conductor(stainless steel) [1/(Ohm*m)]
Eeff=Eeff_coax*(f_feed_t)+e_polymer*f_polymer

```

```

E= Eeff * 1/(4*pi*1e-7*c*c); % vacuum permeability [H/m]
Vres=pi*r2^2*len
Voxide=pi*r1^2*len
sigma_eff_main=(sigma_oxide*Voxide+sigma_feed*(Vres-Voxide))/Vres
sigma_eff=sigma_eff_main*f_feed_t+sigma_polymer*f_polymer;
check_1=f_feed_t+f_polymer
vin=120e-3; %input voltage supplied by the function generator, [V]
f=120E+06:10000:180E+06;
omega = 2*pi*f;% angular frequency, [rad/s]
tg= 1.168018964411114e-01
Eim=((omega.*E.*tg)-sigma_eff)./omega;%imaginary part of complex dielectric permittivity
skin_depth1=sqrt(2./(omega.*u.*sigma_stainless_steel));%skin_depth
skin_depth2=sqrt(2./(omega.*u.*sigma_steel));%skin_depth
Rs1=1./(sigma_stainless_steel.*skin_depth1);% surface resistivity of the outer conductor of the resonator
Rs2=1./(sigma_steel.*skin_depth2);% surface resistivity of the inner conductor of the resonator
R=Rs2/r0+Rs1/r2;% distributed element resistance R of the resonator [Ohm/m]
G=(omega.*Eim+sigma_feed)./(omega.*E).*omega.*C;%distributed element conductance of the resonator
[F/(m*s)]
gamma =(sqrt((R+1i.*omega.*L).*(G+1i.*omega.*C)))/omega;%complex propagation constant [1/m]
%notes on gamma: Re(gamma)=alfa = attenuation constant representing losses [Np/m];
Im(gamma)=beta=phase of the propagation constant [rad/m]
%since the signal is oscillating in time with omega rad/s, the propagation velocity of the wave [m/s] =
omega/beta; also, beta = 2*pi/wavelength.
Zc=sqrt(((R+1i.*omega.*L)./(G+1i.*omega.*C)));% complex characteristic impedance of the resonator [Ohm]
Zc3=Zc
Zin=Zc.*coth(gamma.*len);%complex input impedance of the resonator [Ohm]
vout=sqrt((real(Zin.*(vin./(50+2*Zin))))^2+(imag(Zin.*(vin./(50+2*Zin))))^2);%modulus of vout, the is the
recorded voltage by the spectrum analyzer [V]
vout =20.*log10(vout)+13;%vout as a power ratio in dBm i.e., the measured power referenced to one mWatt
and the underlying assumption of a 50 Ohm load resistance
plot(f/1e+6,vout,'b--', 'LineWidth',3);
xlabel('Frequency, (MHz)','fontsize',42,'fontweight','b');
ylabel('Amplitude, (dBm)','fontsize',42,'fontweight','b');
legend ( 'Experimental data','Zc=17.8 Ohm', 'Zc=1.7 Ohm', 'Zc=99.8 Ohm')
hold on

```




Melbourne, Australia, Biosensors 2014



Chapter 6

On-line Monitoring of Biofouling Using Coaxial Stub Resonator Technology

Abstract

Here we demonstrate the proof-of-principle that a coaxial stub resonator can be used to detect early stages of biofilm formation. After promising field tests using a stub resonator with a stainless steel inner conductor as sensitive element, the sensitivity of the system was improved by using a resonator of shorter physical length, implying higher resonance frequencies (and by that a higher frequency range of operation) and improved sensitivity towards dispersion. In addition, the space between inner and outer conductor was filled up with glass beads, thereby exploiting the larger surface area available for biofilm formation.

Analysis of the biofilm and the stub resonator signal, both as function of time, indicates that the sensor allows detection of early stages of biofilm formation. In addition, the sensor signal clearly discriminates between the first stages of biofilm formation (characterized by separated, individual spots of bacterial growth on the glass beads) and the presence of a nearly homogeneous biofilm later on in time. Model simulations based on the transmission line theory predict a shift of the sensor response in the same direction and order of magnitude as observed in the biofouling experiments, thereby confirming the operating principle of the sensor.

This chapter is based on the article submitted as:

N.A. Hoog, M.J.J. Mayer, H. Miedema, W. Olthuis, A. A. Tomaszewska, A. H. Paulitsch-Fuchs, A. van den Berg, *On - line Monitoring of Biofouling Using Coaxial Stub Resonator Technology*, Sensing and Bio-Sensing Research (invited paper).

6.1 Introduction

Biofouling, i.e., the colonisation of an interface by a diverse array of organisms, affects surfaces and by that may have detrimental effects on the operation of processes in the field of water technology such as, raw water pre-treatment, drinking water production and distribution, wastewater treatment, industrial water cooling and water quality analysis [1-6].

Because of the high impact of biofouling on process operation and by implication high economic cost, in recent years there has been an increasing interest in developing an on - line sensor able to monitor biofilm formation in real time, especially in an early stage [7-9]. Despite all the efforts to engineer such a sensor, discussed in detail in [10-16], reliable detection technology for (the onset of) biofouling is still lacking.

Existing technologies rely on pressure drop changes [14, 17], differential heat transfer [10, 19] or differential turbidity [20]. Actually, none of these methods can reliably detect biofouling in an early stage. Changes are detected when it is already too late and the system operation already suffers from serious impairment.

Of all the different detection technologies to track biofouling, actuators that are either acoustic [21], optical [22] or electromagnetic [23] in nature are most reliable and most sensitive [10, 24]. A drawback of all these devices is however that the actual detector required is rather expensive whether that is e.g., an optical sensor [25], an analyser for scattering (S) parameters [18] or an impedance analyser [26].

The motivation to develop a new type of biofouling sensor was based, firstly, on the realization that we really need the detection of biofouling in a much earlier stage than currently available and, secondly, to offer a more cost effective alternative for existing technology. In the present study we demonstrate the feasibility of a (flow-through) coaxial stub resonator as a sensitive element of a biofouling sensor. Such resonator systems and their amplitude-frequency or AF response has been characterized, simulated and reported by the authors previously [27-30]. We discuss two different designs of such resonators. The first one has an inner and outer conductor separated by a fluid. The formation of a biofilm on the surface of the inner conductor (and on the surface of the outer conductor but to a much lesser extent) affects the skin effect of the inner conductor as well as the dielectric between inner and outer conductors thereby changing the AF response of the resonator. In the second type of resonator, the space in between both conductors is filled up with glass beads (Fig. 1).

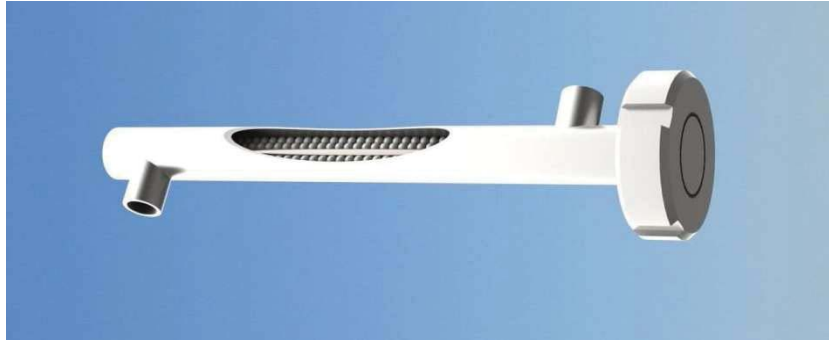


Fig. 1. Schematic 3D image of the coax sensor with a length of 30 cm and an outer conductor diameter of 25.4 mm filled with glass beads. Also indicated are the input and output ports used for fluid flow-through.

The changes in AF response are caused by both the formation of a biofilm on the surface of the glass beads and the reaction of the inner conductor surface to the amount of nutrients in the feed stream. In this case, the response is more related to an (apparent) change in composition of the feed solution. The sensor geometry and dimensions were designed such that the sensor can be operated at flow conditions that are relevant for process operation in industrial equipment and piping and that the required electronics equipment can be produced in a cost effective way. Additional advantages of our sensor compared to currently existing ones are that it operates as an early warning system and is low in maintenance.

6.2 Materials and methods

Sensor description

Fig. 1 shows a schematic outline and the basic elements of a sensor based on a stub resonator coaxial transmission line, discussed in detail previously [27-30].

The resonator itself consists of an inner and outer conductor separated by a fluid of certain dielectric permittivity. A change in this (effective) permittivity of the fluid, e.g., due to a change in fluid composition, will alter the resonator characteristics. Formation of a biofilm on the surface of the inner and/or outer conductor will also change the behaviour (i.e., resonant frequency and quality factor) of the resonator. In general, the system is more sensitive to changes at the surface of the inner conductor than of the outer conductor. Obviously, the larger the surface area covered with biofilm mass, the higher the volume fraction of biofilm dielectric between inner and outer conductor. As explained in a previous study [28], an inner conductor of larger diameter will however not result in a more sensitive sensor, an effect due to stronger converging electric field lines near an inner conductor of smaller diameter. There is however a way to enlarge the effective surface area without

compromising the sensor's sensitivity. Surface area enhancement can also be accomplished by filling up the space in between both conductors e.g., with glass beads (see Fig. 1). A schematic cross section of such system is shown in Fig. 3. The formation of a biofilm on the surface of the glass beads (in red) introduces a dielectric permittivity that differs from the permittivity of the glass and the fluid. As a result, the resonant frequency and quality factor (amplitude ratio) shift upon biofouling of the glass beads surface.

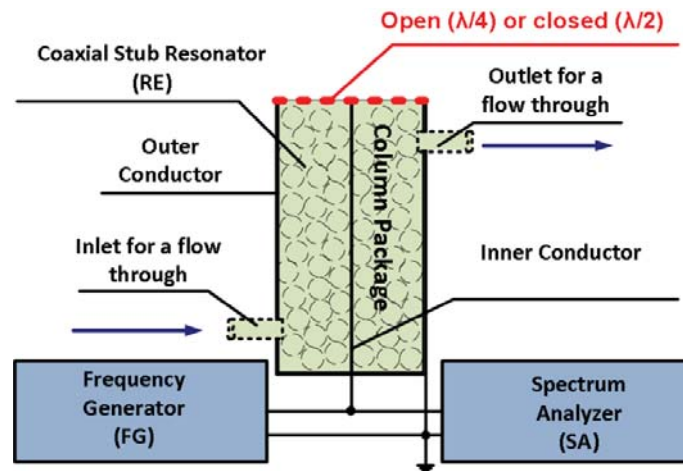


Fig. 2. Schematic outline of the coaxial stub resonator sensing system consisting of a function generator (FG), a spectrum analyzer (SA) and the coaxial stub resonator (RE). The dotted inlet and outlet indicate that the flow-through resonator can be optionally used as batch resonator.

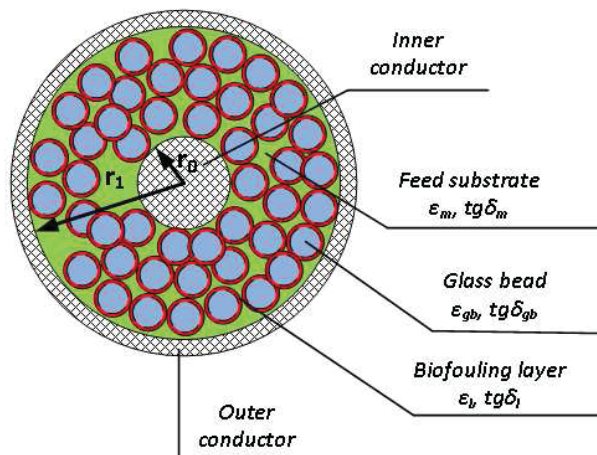


Fig. 3. Schematic cross section of the coaxial stub resonator filled with glass beads of which the surface is covered by a biofouling layer (red). We distinct three types of dielectric between inner and outer conductor: feed substrate (green, dielectric permittivity ϵ_m (-), loss tangent $\tan\delta_m$ (-), glass beads (blue, dielectric permittivity ϵ_{gb} (-), loss tangent $\tan\delta_{gb}$ (-) and biofouling layer (red, dielectric permittivity ϵ_l (-), loss tangent $\tan\delta_l$ (-).

The dielectric properties of a coaxial resonator filled with glass beads covered with a biofilm

The effective dielectric permittivity ϵ_{eff} and the effective loss tangent $\tan\delta_{eff}$ of a coaxial resonator with multiple concentric layers of different dielectric permittivity has been described in [32, 33] and is expressed by:

$$\epsilon_{eff} = f(\epsilon_{r1}, \epsilon_{r2}, \dots, \epsilon_{rn}) \quad (1)$$

$$\tan\delta_{eff} = f(\tan\delta_1, \tan\delta_2, \dots, \tan\delta_n) \quad (2)$$

In an ideal resonator without any losses, the resonance frequency f_{res} of an open ended ($\lambda/4$) and closed end ($\lambda/2$) resonator are given by Eqs. 3a and 3b, respectively. In this special case, the dielectric constant ϵ_{re} can be determined directly from Eqs. 3a and 3b [27, 28].

$$f_{res} = \frac{2n-1}{2 \cdot \pi \cdot \sqrt{LC}} = \frac{c \cdot (2n-1)}{4l \sqrt{\epsilon_{re} \epsilon_0 \mu_{re} \mu_0}} \quad (3a)$$

$$f_{res} = \frac{n}{2 \cdot \pi \cdot \sqrt{LC}} = \frac{c \cdot n}{2l \sqrt{\epsilon_{re} \epsilon_0 \mu_{re} \mu_0}} \quad (3b)$$

where c represents the speed of light in vacuum (m/s), n the order number of f_{res} (Hz), l the length of the resonator (m), μ_r relative magnetic permeability of the dielectric between inner and outer conductors (-), μ_0 the absolute vacuum permeability (H/m), ϵ_0 the absolute vacuum permittivity (F/m) and ϵ_{re} the real part of the relative effective dielectric constant. Note that the capacitance C in Eqs. 3a and 3b is determined by the real part ϵ_{re} of ϵ_r .

For a lossy resonator, polarization and conductivity losses in the dielectric under investigation, as well as resistance losses in the inner and outer conductors, must be taken into account. A detailed model accounting for these losses, essentially based on telegrapher's equations, is explained in [34].

In order to describe the behaviour of the biofouling sensor i.e., a lossy resonator packed with glass beads on which a film of biofouling can grow, the model described in [34] was extended with expressions for both the effective dielectric permittivity ϵ_r and the effective conductivity of the composite dielectric consisting of glass beads with biofilm, immersed in a feed substrate.

For a lossy dielectric, complex dielectric permittivity can be described as:

$$\epsilon_r = \epsilon_{re} - j\epsilon_{im} \quad (4)$$

where ϵ_{re} and ϵ_{im} represent the real and imaginary parts of ϵ_r , respectively.

The effective loss tangent $\tan\delta_{eff}$ (-), which is a measure for the dielectric losses in the system, is expressed by Eq. 5:

$$\tan\delta_{eff} = \frac{\omega\epsilon_{im} + \sigma_{eff}}{\omega\epsilon_{re}} \quad (5)$$

where ϵ_{im} and σ_{eff} reflect the polarization losses and the conductivity losses in the dielectric, respectively, and $\omega=2\pi f$ the angular frequency, in rad/s.

In the following, 2 models for the effective dielectric permittivity of the composite dielectric will be discussed.

For this, we consider the coaxial resonator packed with glass beads with dielectric permittivity ϵ_{gb} and volume fraction φ_{gb} [-] (see Fig. 3). The glass beads are covered with a biofouling layer with dielectric permittivity ϵ_l and volume fraction φ_l . The free space in between the beads is occupied by feed substrate with dielectric permittivity ϵ_m and volume fraction φ_m .

The first model is known as Lichtenecker's logarithmic law and is based on the assumption that the individual components in the mixture are randomly distributed over the total volume of that mixture [33].

According to Lichtenecker's logarithmic law the effective permittivity ϵ_{ceff} of the (composite) space between inner and outer conductor is given by:

$$\log \epsilon_{ceff} = \sum_{i=1}^n \varphi_i \cdot \log \epsilon_i \quad (6)$$

$$\log \epsilon_{ceff} = \varphi_{gb} \cdot \log \epsilon_{gb} + \varphi_l \cdot \log \epsilon_l + \varphi_m \cdot \log \epsilon_m \quad (7)$$

The second model for the effective dielectric permittivity, further on referred to as the “parallel dielectric layers model” is based on the assumption that the resonator is filled with subsequent layers of the individual components of the composite dielectric i.e., with a layer of glass, a layer of biofilm and a layer of feed substrate.

According to the “parallel dielectric layers model” the effective dielectric permittivity ϵ_{ceff} of the composite space between inner and outer conductor is given by:

$$\epsilon_{ceff} = \varphi_{gb} \cdot \epsilon_{gb} + \varphi_l \cdot \log \epsilon_l + \varphi_m \cdot \log \epsilon_m \quad (8)$$

The validity of both models for the composite system in Fig. 3 will now be discussed. From an electrical point of view, biofilm formation in a resonator, filled with feed substrate and a packed bed of glass beads as dielectric, can be seen as replacing feed substrate volume by biofilm volume. Therefore, the response changes of the resonator are primarily determined by the difference in dielectric properties of the biofilm and the feed substrate.

However, biofilm formation introduces a third dielectric in the resonator volume and a difference between the biofilm and the feed substrate is that the biofilm preferentially forms on the surface of the glass beads. This is important since the dielectric properties of the composite material in the resonator are not only determined by the volume fraction of the biofilm in the composite material but also by its distribution over the total composite volume. Since a packed bed of glass beads is present between the inner and outer conductors of the resonator, and since biofilm formation preferentially occurs at the glass bead surface, formation of biofilm may result in “thin biofilm sheet structures” throughout the resonator volume, connecting the inner conductor with the outer conductor. However, not all biofilm will be part of a “direct biofilm connection” between inner and outer conductors. A similar reasoning can be held for the packed bed of glass beads.

From the reasoning above, it becomes clear that the system in Fig. 3 cannot be considered as randomly distributed elements of biofilm, glass beads and feed substrate over the total dielectric volume. However, it can also not be considered as a volume filled with subsequent layers of the individual components of the composite dielectric. In reality, the value of ϵ_{ceff} is expected to be in between the results calculated by model 1 and model 2. In this contribution, both models will be applied as limiting cases to estimate the value of ϵ_{ceff} .

To calculate the effective loss tangent $\tan \delta_{eff}$ the effective conductivity of the system σ_{ceff} [S/m] was determined assuming that model 2 applies i.e., that the resonator volume is filled with subsequent layers of the individual components of the composite dielectric, resulting in eq. 9:

$$\sigma_{ceff} = \varphi_{gb} \cdot \sigma_{gb} + \varphi_l \cdot \sigma_l + \varphi_m \cdot \sigma_m \quad (9)$$

This assumption is considered reasonable for estimating σ_{ceff} since the feed substrate is the continuous phase (directly connecting the inner and outer conductors from an electrical point of view) and since it has a high conductivity as compared to the glass beads. This means that the term $\varphi_{gb} \cdot \sigma_{gb}$ is negligible in practice as compared to the term $\varphi_m \cdot \sigma_m$. The biofilm is present around the glass beads and its conductivity is also considerably higher than that of the glass beads. Further, as previously explained, “thin biofilm sheet structures” connect the inner and out conductors. So to some extent, the biofilm and feed substrate can be considered indeed to be present in the resonator according to model 2.

Biofouling formation and structure

In literature, several models on biofilm formation were proposed [8, 36-39]. Based on these models we have the following view on biofilm formation in the coaxial resonator system filled with glass beads:

- Almost immediately after bringing the glass beads in contact with feed substrate, containing a suspension of bacteria, its surface is covered by a so-called primary film (conditioning film), modifying the properties of the surface. Formation of such a layer of surface active molecules is the first step prior to the actual formation of the bacterial film and may last for a few seconds to minutes after the glass surface is exposed to the feed substrate [40].

- Primary film formation can be followed by a secondary colonization of bacteria that benefit from a protective environment in the biofilm and/or feed on the remnants of other bacteria. In this secondary community, better resource or space competitors may exclude less competitive organisms [41-43].

- Stable biofilms are composed primarily of microbial cells and extracellular polymeric substances (EPS) secreted by these cells. The EPS fraction consists basically of polysaccharides, accounting for up to 50% to 90% of the total organic carbon of biofilms and proteins. The polysaccharides can be considered the primary matrix material of the biofilm [44].

For describing the dielectric properties of the biofilm, following assumptions were made:

- The biofilm mainly consists of water i.e., the mass fraction of water in the biofilm is higher than about 0.90 and lower than about 0.98 [45, 53 - 56] and a good approximation of the biofilm is 1000 kg/m³ [60].

- The real part of relative dielectric permittivity ϵ_{re} of the viable bacteria and the EPS layer in the biofilm are 60 [51] and 70 [57], respectively.

– Even though the composition of the EPS layers most likely depends on the exact process conditions, its composition was considered to be constant during the course of the experiments of this study. Existing literature report polysaccharides [61] and proteins as dominant EPS components [62].

– According to [51] the overall composition formula of the biomass is expressed by Eq. 10:

$$\text{C:H(1.77):O(0.49):N(0.24)} \quad (10)$$

Experimental setups

Half-wave closed ended coaxial resonator

We started out with a half-wave (instead of quarter-wave) closed ended coaxial resonator. This resonator was essentially very similar to the one shown in Fig. 1 and Fig. 2 but without the glass beads. Table 1 summarizes the physical dimensions of this stub resonator.

Table 1

Geometric parameters of the flow-through resonator. The outer and the inner conductors of the resonator were both made from stainless steel 316L.

Parameter	Flow-through resonator
Length, l	1.05 (m)
Inner conductor diameter, d	$5 \cdot 10^{-3}$ (m)
Inner diameter of the outer conductor, D	$75 \cdot 10^{-3}$ (m)
Diameters of the fluid inlet and outlet	$27 \cdot 10^{-3}$ (m)
Conductivity of stainless steel 316L, σ	$1.45 \cdot 10^6$ ($\text{S} \cdot \text{m}^{-1}$)

Quarter-wave open-ended coaxial stub resonator

Fig. 4 shows a schematic overview of the experimental set-up used to monitor biofouling. The system comprises three identical flow-through systems, each of them equipped with a peristaltic pump (Masterflex), two tubes and a vessel of 120 L, with pump, tubes and vessel all interconnected to a closed configuration. The construction of the dummies which have the same geometry as a coaxial sensor excluding an inner conductor, the mode of operation and the experimental conditions were also exactly the same as those for the coaxial resonator. These five dummies, all running in parallel with the actual resonator tube, provided five independent controls. This set up made it possible to obtain a

control sample each day (up to five) the experiment was running without disturbing the process of biofilm formation in the remaining tubes, including the actual resonator. Feed substrate, 'contaminated' with bacteria cells, was dosed from a supply vessel into each tube by a peristaltic pump at a flow rate of $1.2 \text{ L}\cdot\text{h}^{-1}$.

Table 2 gives an overview of the dimensions of the quarter-wave coaxial stub resonators applied in this study, see also Fig. 1 and Fig. 2.

Table 2

Geometric parameters of the flow-through resonator (see also the "Supplementary Information"). The outer and the inner conductors of the resonator were both made from stainless steel 316L.

Parameter	Flow-through resonator	
Length, l	$29\cdot 10^{-1}$	(m)
Inner conductor diameter, d	$5\cdot 10^{-3}$	(m)
Inner diameter of the outer conductor, D	$25\cdot 10^{-3}$	(m)
Diameters of the fluid inlet and outlet	$27\cdot 10^{-3}$	(m)
Conductivity of stainless steel 316L, σ	$1.45\cdot 10^6$	($\text{S}\cdot \text{m}^{-1}$)

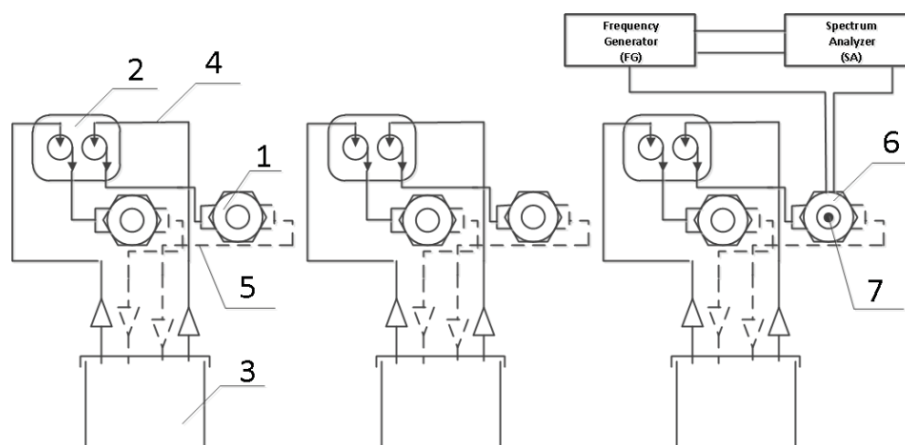


Fig. 4. Schematic of the experimental set-up consisting of 1) dummy (tube), 2) pump with double rotating shaft, 3) tank with feed substrate, 4) inlet hose, 5) outlet hose, 6)coaxial sensor connected to the frequency generator and spectrum analyzer, 7) an inner conductor of coaxial sensor.

In order to control variations in the resonance frequency and the shape of a response signal a HAMEG HMS3010 3 GHz Spectrum Analyzer with Tracking Generator was used. (It should be mentioned that this type of Spectrum Analyzer does not have a fixed input voltage of the tracking generator for each piece of equipment. In this study three different Spectrum Analyzer were used (see also MATLAB codes in the “**Supplementary Information**”)

The interconnecting transmission lines have all a characteristic impedance Z_0 of 50 Ohm. The transmission lines were connected to the resonator by using SMA (SubMiniature version A) connectors all with a total length of 20 mm.

To prevent corrosion of SMA connectors the sensors were filled with a 1-1.5 cm layer of epoxy resin at the bottom of the sensor, thereby fully immersing the SMA connectors in the resin. The real part of dielectric permittivity ϵ_{re} of epoxy resin is 3-6 [46].

It should be also mentioned that the difference of the total volume of the dummy and total volume of the resonator with the inner conductor of 5 mm is 4%. This difference in available internal volume is caused by the absence of an inner conductor in the dummies.

The differences in amount of glass beads 14% (the average amount of glass beads in the dummy (resonator without an inner conductor) is 2030 and the average amount in the resonator with an inner conductor 1750).

Feed substrate

In order to enhance bacterial growth the installation was fed with substrate consisting of a solution of NaCH_3COO , NaNO_3 and NaH_2PO_4 in tap water, resulting in a mass ratio C:N:P of 100:20:10 [45]. All chemicals were purchased in analytical grade (Boom B.V., Meppel, Netherlands) and dissolved in tap water. For the simulations, the value of ϵ_m of the feed substrate was set at 78 (see also the MATLAB code in the “**Supplementary Information**”).

Glass beads

The coaxial resonator tubes and dummies, all with a volume of 137.4 ml, were packed with glass beads of 4 mm diameter (Merck KGaA, Germany), with a total number of beads per tube of, on average, 2030. The surface area of a single glass bead is 0.5 cm^2 . The dielectric permittivity of glass ϵ_{gb} varies within a range of 3.8 to 19 [47-49]. The dielectric permittivity of quartz glass is 3.8 and that of regular window glass 7.6. Taking into account that the porosity of glass beads is less than that of regular window glass, in this study ϵ_{gb} was assumed to be 5.8 (see also MATLAB codes in the “**Supplementary Information**”).

Culture of *Escherichia coli*

Escherichia coli (*E. coli*) O157:H7 was cultured by incubating 200 mL standard Lysogeny broth (LB) media for 24 hours at 36°C [49]. The total cell number in the feed substrate solution at the start of the experiment was in the range of $5 \cdot 10^5$ and $10 \cdot 10^5$ cells mL^{-1} .

Sampling and analysis of glass beads

To determine the composition and the amount of accumulated biofouling as function of time, samples of the glass beads from the (dummy) resonator tubes and from the feed substrate (30 ml) were taken during each day of the experiment. Collected beads and sampled feed substrate were stored (at -20) in (disinfected) glass tubes until further investigation. Both types of samples were subjected to four different analyses: TCN, ATP, TOC, HPC, explained in more detail in the following paragraphs.

Total cell number (TCN)

For TCN determination, a Neubauer Improved Counting Chamber was used and the total number of cells in the sample was counted optically using a microscope (DM750, Leica, Wetzlar, Germany). Five squares, each with a volume of 1 [μL], were subjected to counting and the average value of two independent duplo measurements was taken. TCN [cells/ μL] is given by:

$$\text{TCN} = \frac{\text{number of cell counted}}{\text{number of squares counted}} \cdot \text{depth (mm)} \cdot \text{dilution factor} \quad (11)$$

Adenosine triphosphate (ATP)

As a relative measure for the active biomass content of the biofilm, the ATP concentration of the biofilm obtained from the glass bead surface was determined. For this purpose, the entire tube volume, containing all 2030 glass beads, was added to 100 mL of phosphate-buffered saline (PBS) solution (containing NaCl 8 g L⁻¹, KCl 0.2 g L⁻¹, Na₂HPO₄·7H₂O 1.15 g L⁻¹ and KH₂PO₄ 0.2 g L⁻¹; pH-adjusted to 7.3). In order to detach the biofilm from the glass bead surface, the suspension of glass beads in PBS was sonicated at 37 kHz for 5 minutes. After sonication, the suspension was further homogenized using a Vortex (Heidolph Reax Vortex Mixer, Germany). Finally, the suspension was centrifuged for 20 seconds at 2500 rpm. 20 ml of the supernatant was stored at -20 °C until further analysis by the Vitens laboratory in Leeuwarden (Exp. No. V131232127_F001).

The ATP measurement of the feed substrate was based on 150 ml samples, without further dilution.

Total organic carbon (TOC)

To determine the TOC content of the biofilm, all 2030 glass beads of a single tube were added to 100 mL of PBS in a TOC-free glass tube. Subsequently, the samples were sonicated at 35 kHz for 15 min (BANDELIN, Ultrasonic bath SONOREX DIGITEC, Germany). As for the feed substrate, 150 ml was mixed with 100 ml PBS in a TOC-free glass tube. The TOC concentration in both samples was measured with a TOC analyser (Shimadzu, Japan).

Heterotrophic plate counts (HPC)

100 ml PBS was added to 150 mL of glass beads (containing 2030 beads) and shaken for 20 minutes. Samples were diluted 10^3 , 10^6 and 10^8 times using 2 mm sterile polypropylene tubes. To determine CFU per cm^2 , LB agar plates were used. Therefore, 100 μL of diluted sample was spread on the plates. Plates were incubated at 37°C for 72 hours.

The HPC procedure for the feed substrate (105 ml) was essentially the same.

Experimental conditions

Temperature, conductivity, and operation time were controlled and stable for each set of experiments.

Table 3 contains information regarding experimental conditions.

Table 3

Temperature T ($^\circ\text{C}$) and conductivity σ (S/m) of the feed substrate for each set of experiment.

Main points of the experiment	Temperature, T ($^\circ\text{C}$)	Conductivity, σ (S/m)
WLN at Glimmen, The Netherlands: drinking water from Annen i.e., purified ground water (Fig. 5).	9.6 ± 1.0	$300 \cdot 10^{-4} \pm 54 \cdot 10^{-4}$
WLN at Glimmen, The Netherlands: the mixture of drinking water "De Punt" and raw ground water, creating a high iron(hydroxide) content and with that, a high fouling rate (Fig. 6).	10.3 ± 1.5	$300 \cdot 10^{-4} \pm 54 \cdot 10^{-4}$
WETSUS, The Netherlands: tap water (Fig. 7)	20.0 ± 1.5	$515 \cdot 10^{-4} \pm 20 \cdot 10^{-4}$
WETSUS, The Netherlands: using the substrate of the feed and E. coli culture (Fig. 8)	20.0 ± 1.5	$618 \cdot 10^{-4} \pm 20 \cdot 10^{-4}$
WETSUS, The Netherlands: using the substrate of the feed, E. coli culture and AgNO_3 (Fig. 14)	22.0	$620 \cdot 10^{-4}$

6.3 Results and discussion

In presenting the results we will follow the chronological order the sensor has been developed. This way the reader can witness the different phases of the project and, more importantly, follow the arguments that defined our research direction.

Starting point was a flow through half-wave closed ended resonator as shown in Fig. 2 but without the glass beads. In the absence of glass beads the system solely monitors biofilm formation at the surface of inner and outer conductor, both made from (corrosion-resistant) stainless steel. As explained earlier, the resonator is much more sensitive to biofilm formation on the inner conductor as compared to the outer conductor. In a previous contribution [27, 28], the authors have shown that such flow-through resonator can be operated in a stable and reproducible way and that it is feasible for measuring the dielectric properties of fluids.

Fig. 5 shows the results of a field test at a drinking water production facility and water quality centre of WLN at Glimmen, Netherlands. The field test was executed at the SenTec testing facility of WLN where different qualities of drinking water are available for testing sensors at “real life conditions”. The test was executed with drinking water from Annen i.e., purified ground water.

Even though we monitored biofilm formation for as long as 14 days, the results indicate minimal effects on the AF response. However, visual inspection of both inner and outer conductors revealed surface modification. Both inner and outer conductors of the flow through sensor were covered by a thin but visible slimy layer.

Although the observed lack of signal change in Fig. 5 might be caused by the limited fouling potency of the drinking water used for these experiments, it was concluded that the sensor should be sufficiently sensitive to detect the thin but visible biofilm that was observed after 14 days. In order to obtain more information on the sensor performance under field conditions, it was decided to expose it to water with much higher fouling capacity. For this purpose, the field test was executed with a mixture of drinking water from location “De Punt”, i.e., purified surface water, and raw ground water. Now, a clear signal shift was observed within just four days of operation (Fig. 6).

However, afterwards inspection and analysis of the resonator proved a response due to the deposition (scaling) of iron oxide on the inner conductor rather than biofilm formation. This observation actually pointed us in the direction of quite another application for our sensor, i.e., the monitoring of scaling and oxidation process (manuscript submitted).

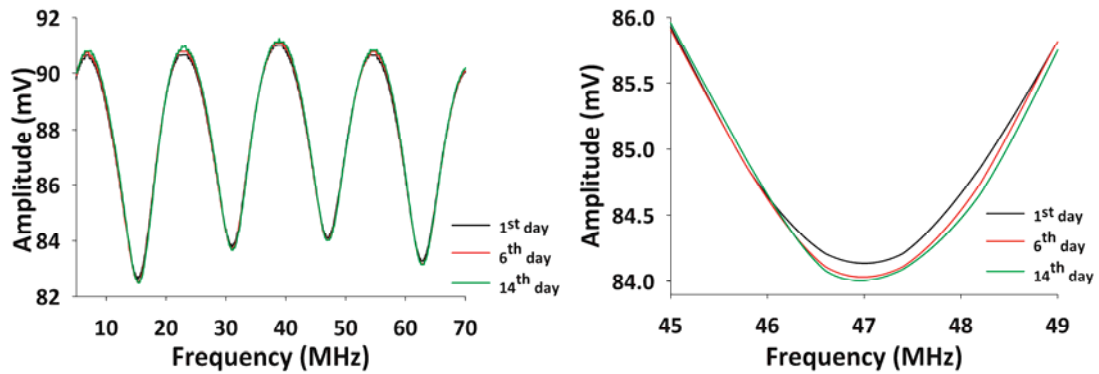


Fig. 5. Left and right panels show the amplitude versus or AF plots in the presence of biofilm on the surface of inner conductor during 12 days of operation using water from Annen in frequency range of 5-70 MHz and the 3rd resonance in more detail, respectively.

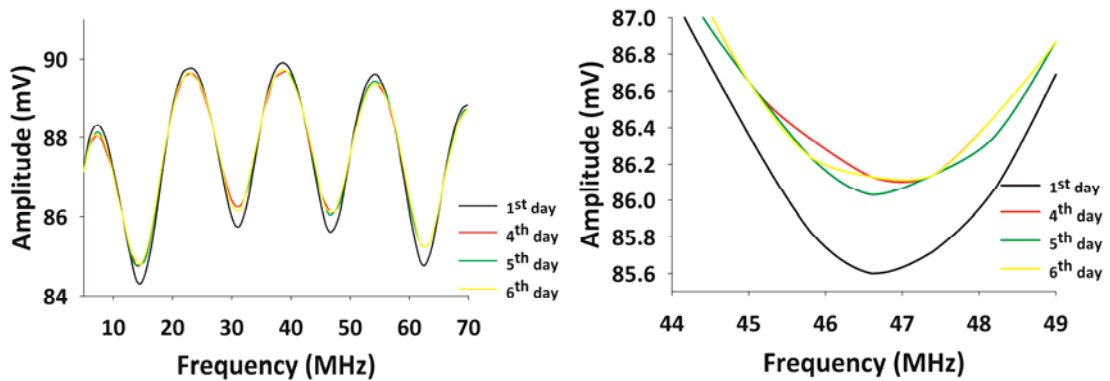


Fig. 6. Left and right panels show the amplitude versus frequency or AF plots in the presence of iron oxide on the surface of inner conductor during 6 days of operation using water from “De Punt” mixed with ground water in frequency range of 5-70 MHz and the 3rd resonance in more detail, respectively.

In order to evoke biofilm formation, our next step was to incubate the system with *E. coli* and perfuse the resonator with a (standard) feed solution promoting bacteria growth. The key adjustment was however to fill the resonator tube with glass beads to enhance the surface area for bacteria adherence.

To show the effect of the presence of glass beads, we run two experiments in parallel, one without (Fig. 7) and the other with glass beads (Fig. 8).

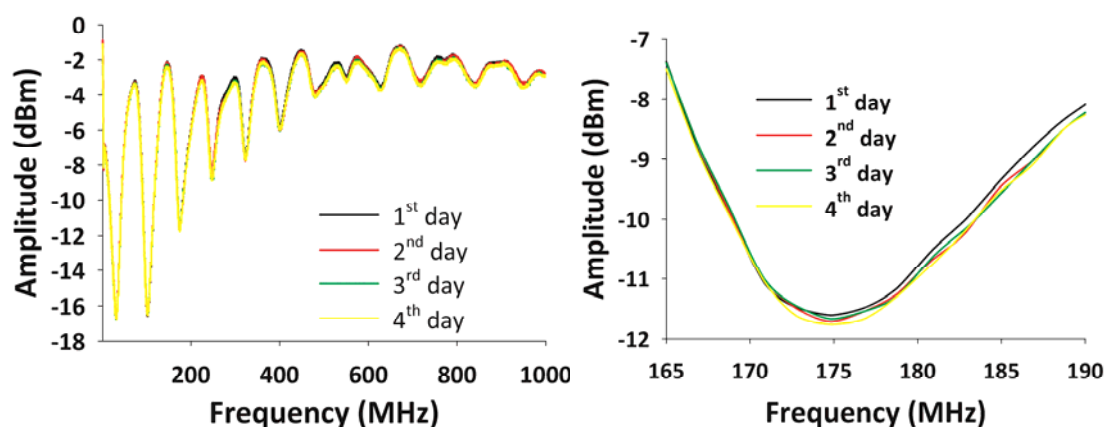


Fig. 7. Left and right panels show the amplitude versus frequency or AF plots in the presence of biofilm on the surface of inner conductor during 4 days of operation using the substrate of the feed and *E. coli* culture in frequency range of 1-1000 MHz and the 3rd resonance in more detail, respectively.

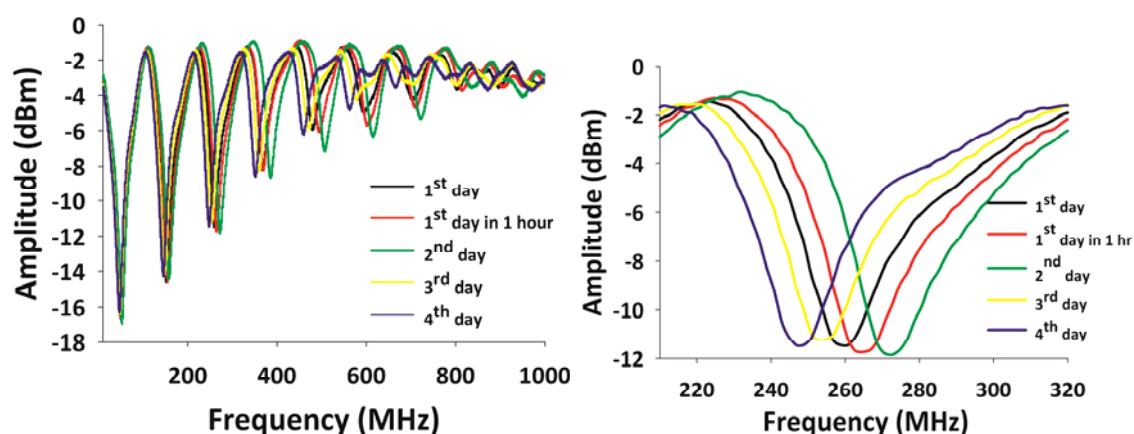


Fig. 8. Left and right panels show the amplitude versus frequency or AF plots in the presence of biofilm on the surface of inner conductor and glass beads during 4 days of operation using the substrate of the feed and *E. coli* culture in frequency range of 1-1000 MHz and the 3rd resonance in more detail, respectively.

Clearly, the presence of glass beads significantly increased the response sensitivity of the resonator to biofilm formation. This is reflected in the change of both resonant frequency and ratio of current amplitude. The results confirm the hypothesis that the AF responses mainly depend on the formation of biofouling on the surface of glass beads and less depend on multiplication of bacterial cells (*E. coli* in this study) in the feed substrate (see also the earlier). There is also growth of bacteria during biofilm formation. Note that the response shown in Fig. 8 is entirely different from the ‘scaling’ response shown in Fig. 6. Whereas deposition of $\text{Fe}(\text{OH})_3$ results in an upward shift of the AF response i.e. towards a

higher amplitude at the resonance frequency, biofilm formation shifts the response, first, towards higher resonance frequencies and slightly lower amplitudes, followed by a shift in opposite direction.(discussed later in more detail). This difference points to a different working mechanism responsible for the two different types of responses observed.

Fig. 9 delineates the changes of resonant frequency and amplitude ratio separately for the first five resonances in Fig. 8. The experiments ran for four days and each plot has a data point for each day. As can be seen, the changes over time for the resonances were very similar, notably in the case of the resonant frequency with a peak value at day 2. The similarity is valid for the amplitude ratio as well (but to a slightly lesser extent) and with a minimum value at day 2. From these similarities in response changes we conclude that the mechanism responsible is the same for each resonance. An important conclusion as it declassifies other, possible interfering, processes causing similar changes.

Fig. 10 correlates the observed change in resonant frequency and the one in amplitude, for the first five resonances and over a time period of four days. The increasing dispersion at higher frequencies (resonances) is evident as the individual data points for each resonance diverge with increasing resonance number. This conclusion is in line with decrease of the quality factor i.e., the broader band with of each resonance relative to its center frequency, with increasing resonance number in the AF plot, see the left panel of Fig. 8.

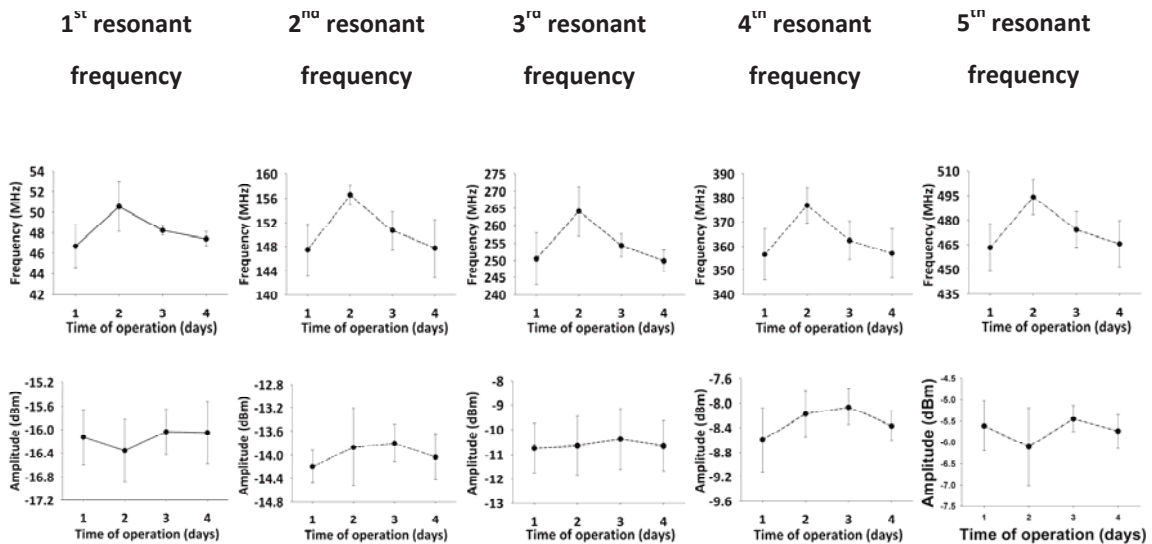


Fig. 9. Resonant frequencies and amplitudes of the first five days resonances over a time period of 4 days and in response to biofilm formation. Error bars represent the standard deviations of three independent experiments.

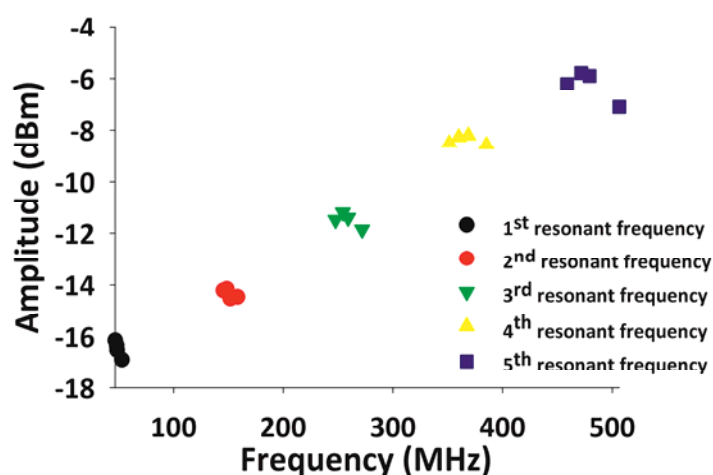


Fig. 10. Correlation between changes in resonant frequencies and amplitude for the first five resonances over a time period of four days and in response to biofilm formation.

In order to correlate the observed AF responses of the resonators to bacterial growth/biofilm formation, samples were taken simultaneously and used for total organic carbon (TOC), total cell number (TCN), colony forming units (CFU) and adenosine triphosphate (ATP) analysis (Fig. 11; n=3). The increase of TOC over time, obtained exclusively from the bead surface, demonstrates the 'deposition' of carbon. The observation that TCN and ATP simultaneously increase renders support for the conclusion that the increase of TOC reflects the presence of (living) bacteria on the bead surface rather than scaling effects due to the deposition of inorganic carbon. The temporal dip at day 3 seen simultaneously in the analysis of ATP, TCN and CFU indicates a 'real' effect rather than an artefact. The most plausible reason for this observation is carbon depletion of the feed solution (experiments were performed in a closed system at recycle conditions over the resonators and dummies). The carbon coming free after mass starvation of bacteria cells served as carbon source, resulting in a blooming bacteria culture at day 4.

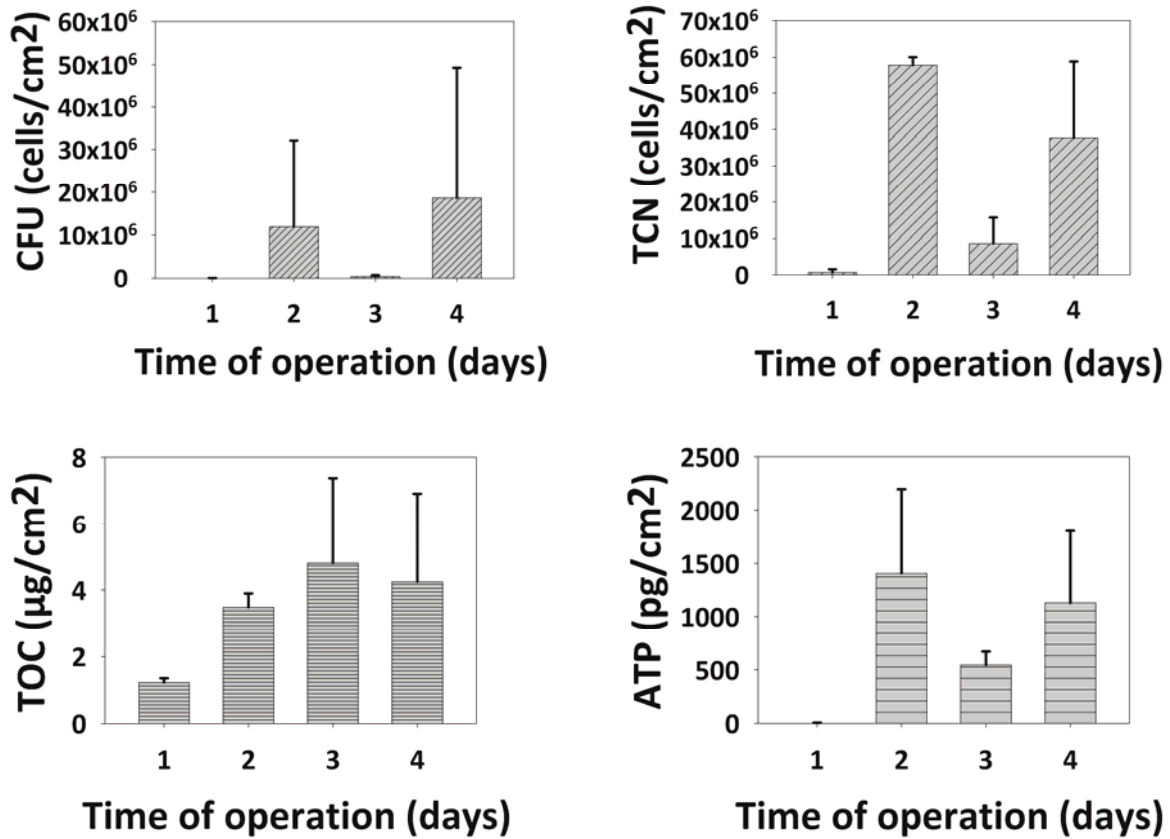


Fig. 11. Analysis of colony forming units (CFU); total cell number (TCN); total organic carbon (TOC) and adenosine triphosphate (ATP) over time and normalized for surface area. All samples used were collected exclusively from biofilm material on the surface of glass beads. Data based on three independent experiments.

In addition to the CFU, TCN, TOC and ATP measurements, the glass bead surface was examined by scanning electron microscopy (SEM) and examples are shown in Fig. 12, at magnifications of 5000. The SEM images indicate attachment of biofilm after day 1 but, in addition, also some detachment of biofilm between days 3 and 4, an effect possibly related to the observed mass starvation, as indicated by the data in Fig. 11, and subsequent blooming of the bacteria culture at day 4.

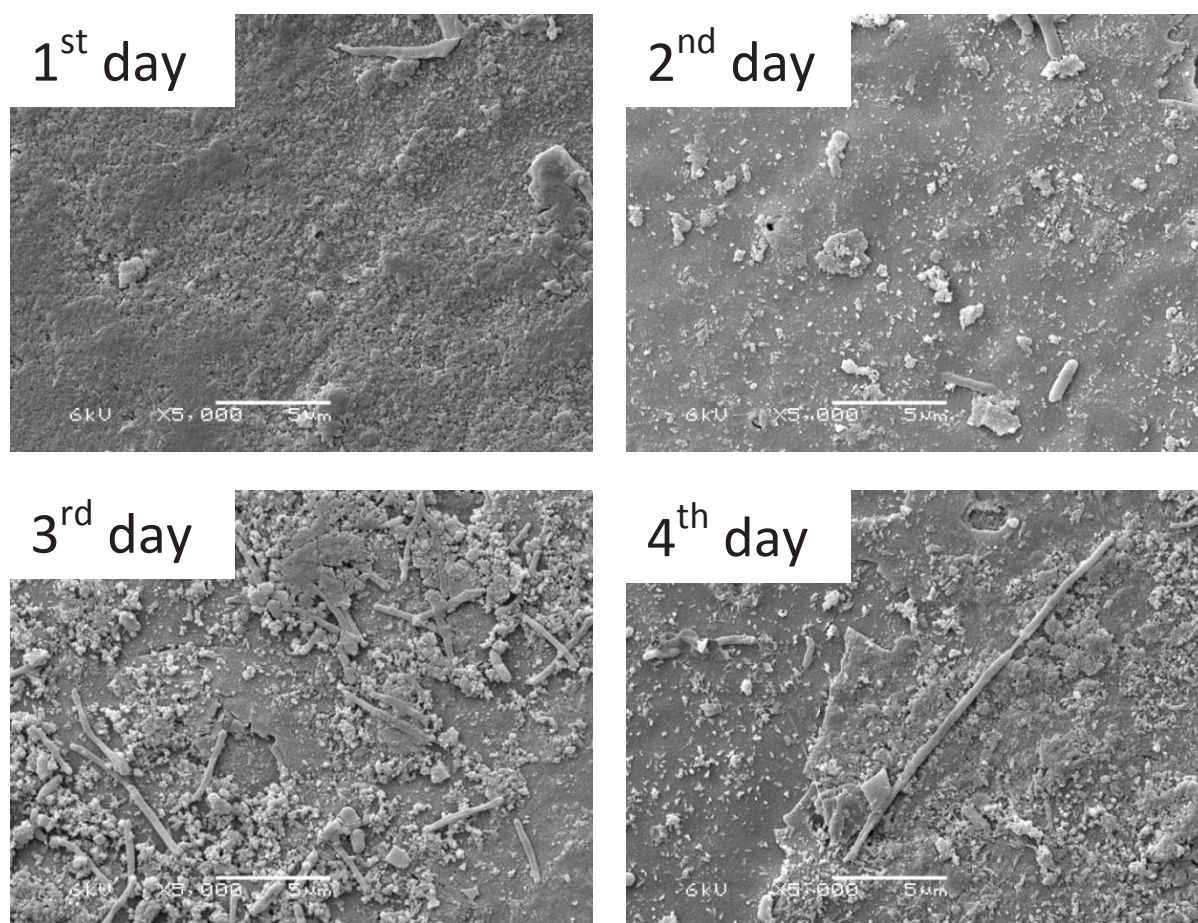


Fig. 12. SEM images of the glass bead surface, taken on 1st, 2nd, 3rd and 4th day of the experiment. Each image gives a qualitative reflection of the observed glass bead surface texture and was selected based on a microscopic scan of different surface areas.

In order to relate the observed sensor response shown in Fig. 8 to the biofilm formation on the glass beads, model simulations were executed. Major objective was to investigate whether the changes in the AF responses, measured during the biofilm experiment, can be explained by changes in the dielectric properties of the composite material in the resonator, applying the model explained in section 2.2.

A major challenge for the model simulations is to obtain a realistic estimate of the biofilm volume in the resonator, even more so because the % mass fraction of biomass in the biofilm strongly depends on process conditions. Reported values for the % mass fraction vary from 2% to 10%. [45, 53 - 56]. For this reason, the model simulations were executed for these two limiting cases as well as for an assumed biomass fraction of 5%. The total amount of biomass in the biofilm and subsequently the volume fraction of biofilm were derived from the TOC measurements according to the procedure outlined in the **“Supplementary Information”**.

Table 4 gives an overview of the calculated volume fractions of the biofilm on the glass beads from day 1 to day 4 assuming biomass fractions (%) of the biofilm of 2%, 5% and 10 %.

Table 4

The calculated biofilm volume fraction in the dielectric between inner and outer conductors ϕ_l at days 1 to 4 as derived from TOC measurements, assuming mass fractions (%) of biomass in the biofilm of 2%, 5% and 10%, respectively (see also the “**Supplementary Information**”).

Day	TOC _{lab} , [mg/ml]	2 % (w/w) biomass in biofilm	5 % (w/w) biomass in biofilm	10 % (w/w) biomass in biofilm
1	1.57±0.36	$1.38 \cdot 10^{-1} \pm 3.13 \cdot 10^{-2}$	$5.53 \cdot 10^{-2} \pm 1.25 \cdot 10^{-2}$	$2.76 \cdot 10^{-2} \pm 6.26 \cdot 10^{-3}$
2	3.29±1.11	$2.90 \cdot 10^{-1} \pm 9.81 \cdot 10^{-2}$	$1.16 \cdot 10^{-1} \pm 3.92 \cdot 10^{-2}$	$5.80 \cdot 10^{-2} \pm 1.96 \cdot 10^{-2}$
3	4.32±2.75	$3.81 \cdot 10^{-1} \pm 2.42 \cdot 10^{-1}$	$1.52 \cdot 10^{-1} \pm 9.69 \cdot 10^{-2}$	$7.62 \cdot 10^{-2} \pm 4.84 \cdot 10^{-2}$
4	4.16±2.35	$3.67 \cdot 10^{-1} \pm 2.07 \cdot 10^{-1}$	$1.47 \cdot 10^{-1} \pm 8.29 \cdot 10^{-2}$	$7.34 \cdot 10^{-2} \pm 4.14 \cdot 10^{-2}$

It should be mentioned that, as Table 4 shows, at the start of the experiment (i.e., the recording labeled Day 1) a significant amount of TOC was measured already. Most likely, this TOC concentration represents small amounts of TOC originating from the feed substrate attached to the glass bead surface during sampling.

The two key parameters characterizing changes in the dielectric properties of the composite material in the resonator are ϵ_{re} and $\tan \delta_{eff}$. The biofilm consists of *E. coli* and EPS with relative dielectric constants of 60 and 70, respectively. In the simulations, it was assumed that the dielectric constant of the biofilm layer $\epsilon_l = 60$, thereby implicitly assuming that, at day 2, the dielectric properties of the biofilm are determined by the presence of *E. coli* rather than EPS (extracellular polymeric substance).

Fig. 13 shows the measured and simulated third resonance AF plots for the biofouling experiments using the biofilm volume fractions in Table 4, for days 1 and 2. Two models were compared, Lichtenecker's logarithmic law for composite material (model 1, Eq. 7) versus a model description in terms of a system composed of parallel dielectric layers of glass, biofilm and feed substrate, respectively (model 2, Eq. 8). As explained in section 0, the “real life situation” is expected to represent an intermediate result between these two model simulations.

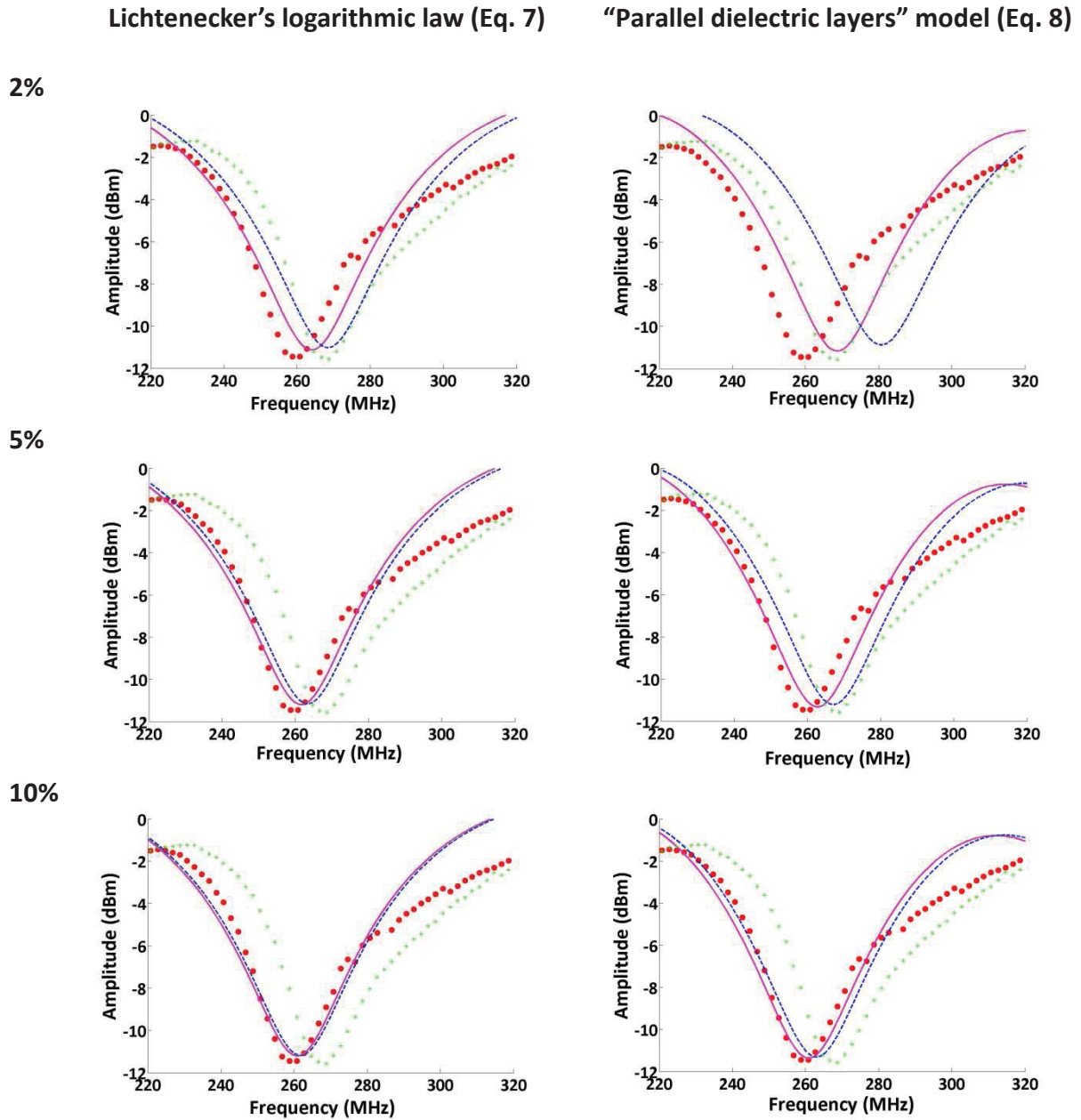


Fig. 13. The observed and simulated third resonance AF plots for the biofouling experiments comprising the resonators filled with glass beads. The experimental data for days 1 and 2 are represented by the red circles and green circles, respectively. The magenta and blue curves represent the model simulations for the first day and second day respectively.

Both the experimental data and the model simulations reveal that biofilm formation on the glass beads results in a shift of the minimum in the AF plots towards higher frequencies. This is expected since, from an electrical point of view, biofilm formation can be seen as replacing feed substrate dielectric ($\epsilon_m \sim 77$) by biofilm dielectric ($\epsilon_f \sim 60$). As a result, biofilm formation will decrease the effective dielectric constant ϵ_{eff} , resulting in a shift of the minimum in the AF plot towards higher frequencies, see also equation 3a (representing the ideal resonator case, the applied model is described in more detail in [28]). Fig. 13 further shows that application of Lichtenecker's logarithmic law predicts a smaller shift of the AF plot towards higher frequencies than the "parallel dielectric layers" model, which results directly from the lower value of ϵ_{re} predicted by the "parallel dielectric layers" model.

In spite of the large number of assumptions made, both for calculation of the biofilm volume fraction in the resonator and for the model simulations, Fig. 13 clearly demonstrates that, in case of biofouling on the glass beads, the measured sensor response (shift in AF plot) is in the same direction and order of magnitude as predicted by the model, thereby confirming that the operating principle of the sensor is (predominantly) defined by changes of ϵ_{eff} .

The results also reveal that a more detailed model, accounting for the exact geometric interactions between the different composite materials in the resonator, i.e., for the influence of glass beads with a shell of biofilm immersed in feed substrate on both dielectric permittivity and conductivity of the composite material, opens possibilities to use the model as a tool to relate signal change of the sensor more quantitatively to the volume fraction of biofouling in the system.

To further proof that the responses seen in Fig. 8 are indeed due to biofilm formation, a control experiment was performed in the presence of 3 mM/L of AgNO_3 , a potent bacteria growth inhibitor (Fig. 14). The results are affirmative. Compared to Fig. 8, over the first 2 days the response hardly changed. Even though the response was clearly affected in a later stage (day 5), the observed shift was in opposite direction of the one seen in the absence of AgNO_3 in the feed solution, indicating quite a different working mechanism. This hypothesis was confirmed by Energy Dispersive X-ray spectroscopy (EDX) that identified the spots as depositions of AgCl , due to its low solubility (see also the "**Supplementary Information**").

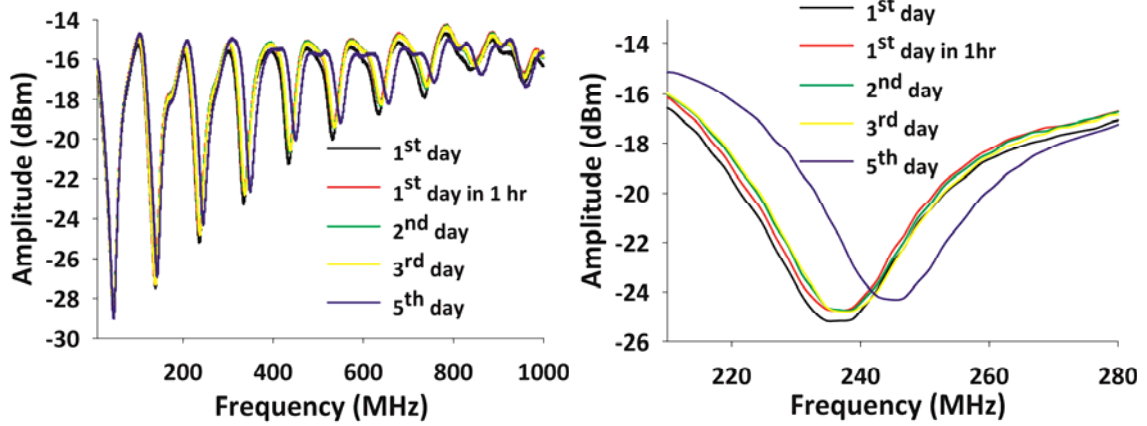


Fig. 14. AF response in the presence of 3 mM AgNO₃ during 5 days of operation in frequency range of 1-1000 MHz with the 3rd resonance plotted in more detail (right panel).

The AF responses of Fig. 15 were subjected to a similar analysis as those shown in Figs. 9 and 10. As in Fig. 9, the trend of the resonant frequency was identical for all resonances included in the analysis. As for the amplitude, we arrive at the same conclusion except for the first resonance. More importantly, the trends shown in Fig. 15 are essentially different from the one shown in Fig. 9. This distinction emphasizes the fact that the observed (shift in) response is due to a different cause, i.e., biofilm formation versus AgCl deposition, respectively.

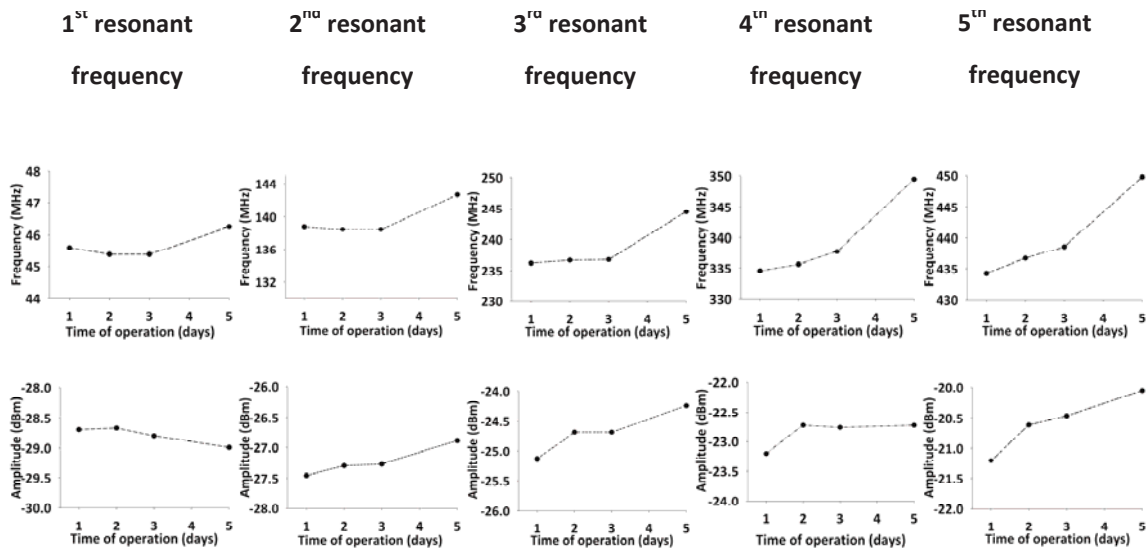


Fig. 15. Resonant frequency and amplitude of the first five resonances over a time period of four days and in response to AgCl deposition.

Fig. 16 correlates the observed change in resonant frequency and the one in amplitude, for the first five resonances and over a time period of five days. The increasing dispersion at higher frequencies (resonances) is evident as the individual data points for each resonance diverge with increasing resonance number.

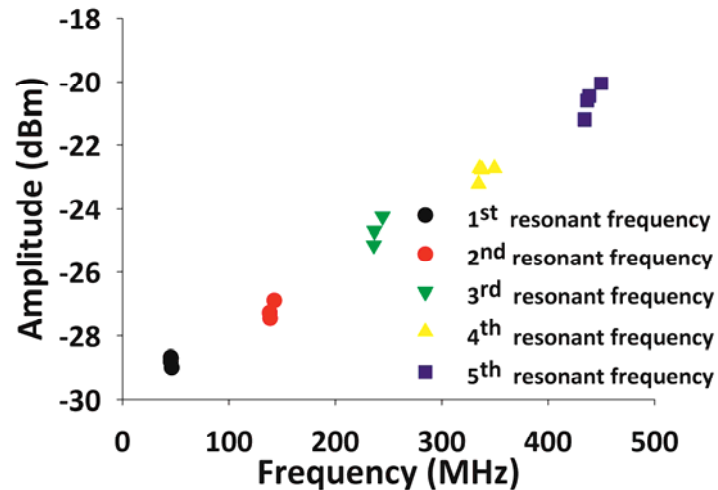


Fig. 16. Correlation between changes in resonant frequencies and amplitude for the first five resonances over a time period of five days and in response to AgCl deposition.

The difference between the glass bead surface covered with a biofilm and one with AgCl became also apparent from SEM images (Fig. 17). Whereas the images at day 1 of Fig. 12 and Fig. 17 are very similar, the images taken at day 4/5 are completely different with absolutely no bacteria cells attached in the presence of AgNO₃.

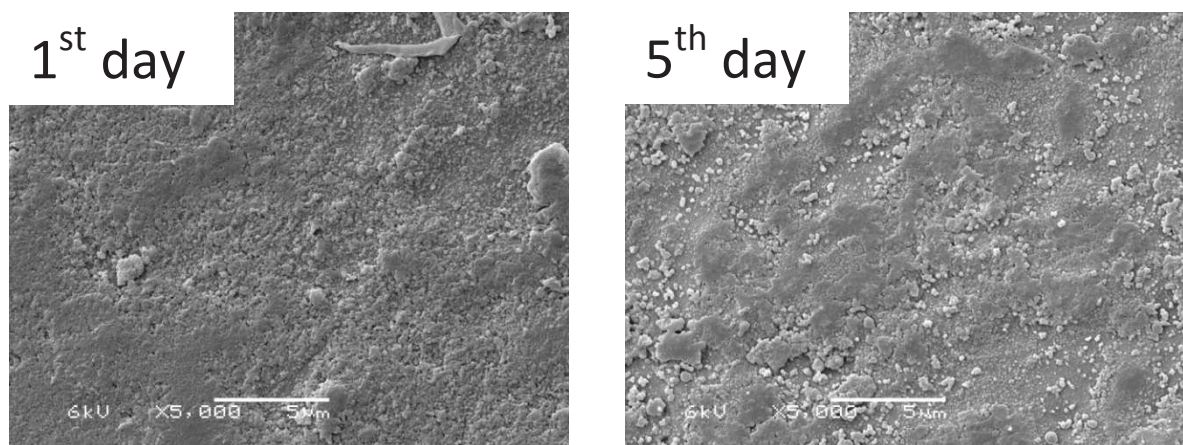


Fig. 17. SEM images of the glass bead surface before (left) and after (right) the deposition of AgCl.

Note that the observed shift in the AF response curve towards higher resonance frequencies (see Fig. 14) is in the anticipated direction since the static relative dielectric permittivity ϵ_{eff} of AgCl is 11.14 [65], thereby decreasing ϵ_{eff} of the dielectric between inner and outer conductors, see equation Eq.3a and increasing the resonance frequencies of the resonator, see equation Eq.3a.

6.5 Conclusions

- A flow-through stub resonator, with glass beads between inner and outer conductor as a surface for biofilm formation, was successfully applied to detect (early stages of) biofouling.
- Model simulations based on transmission line theory predict a shift in the amplitude versus frequency response of the sensor in the same direction and order of magnitude as observed experimentally, thereby confirming the operating principle of the sensor.
- The results indicate that isolated spots of biofilm and a homogenous biofilm layer result in a different AF response of the sensor, opening possibilities to discriminate between the onset of biofouling and a homogeneous biofilm layer
- The flow-through sensor design is relatively simple, robust and can be cleaned inline, opening possibilities to further develop it into a cost effective inline biofouling sensor.

6.6 Acknowledgement

This work was performed in the TTIW-cooperation framework of Wetsus, Centre of Excellence for Sustainable Water Technology (www.wetsus.nl). Wetsus is funded by the Dutch Ministry of Economic Affairs, the European Union Regional Development Fund, the Province of Fryslân, the City of Leeuwarden and the EZ/Kompas program of the “Samenwerkingsverband Noord-Nederland”. The authors thank the participants of the research theme Sensoring for the fruitful discussions and their financial support. Also authors are very grateful to Jelmer Dijkstra for help with SEM and EDX. Special thanks are also due to Tereza Rusková for her help with a large experimental part.

6.7 References

1. H.-C. Flemming, *Industrial Biofouling Materials Today*, Volume 14, Issue 11, (2011), p. 565.
2. J. Wingender, H.-C. Flemming, Biofilms in drinking water and their role as reservoir for pathogens *International Journal of Hygiene and Environmental Health*, Volume 214, Issue 6, (2011), pp. 417-423.
3. H.-C. Flemming, T. Griebe, G. Schaule, Antifouling strategies in technical systems — A short review, *Water Science and Technology*, Volume 34, Issues 5–6, (1996), pp. 517-524.
4. H. Ivnitsky, D. Minz, L. Kautsky, A. Preis, A. Ostfeld, R. Semiat, C. G. Dosoretz, Biofouling formation and modeling in nanofiltration membranes applied to wastewater treatment, *Journal of Membrane Science*, Volume 360, Issues 1–2, (2010), pp. 165-173.
5. S., Y. Oren, Z. Ronen, M. Herzberg, The influence of antiscalants on biofouling of RO membranes in seawater desalination, *Water Research*, Volume 47, Issue 10, (2013), pp. 3389-3398.
6. S. Dürr, J. C. Thomason, *Biofouling*, Wiley-Blackwell, (2009).
7. P. Henderson, *Fouling and antifouling in other industries: power stations, desalination plants, drinking water supplies and sensors*, Biofouling. Wiley-Blackwell, Chichester, (2010), pp 288–305.
8. H.-C. Flemming, Overview on fouling monitoring, Conference “Sensors4water”, Assen, the Netherlands, (2013).
9. T.R. Bott, D. M. Grant, Biofilms in flowing systems *Methods in Enzymology*, Volume 337, (2001), pp 88-103.
10. P. Janknecht, L. F. Melo, Online Biofilm Monitoring, *Reviews in Environmental Science and Biotechnology*, Volume 2, Issue 2-4, (2003) pp. 269-283.
11. E. Eguía, A. Trueba, B. Río-Calonge, A. Girón, J.J. Amieva, C. Bielsa, Combined monitor for direct and indirect measurement of biofouling, *Biofouling* 24 (2008), pp. 75–86.
12. R.P. George, P. Muraleedharan, R. K. Dayal, H. S. Khatak, Techniques for biofilm monitoring, *Corros. Rev.* 24 (2006), pp 123–150.
13. International Workshop Online sensors for fouling monitoring. Frankfurt am Main, Germany. <http://events.dechema.de/Biofouling.html>. 29–30 November, (2010).
14. L.F. Melo, T. R. Bott, Biofouling in water systems, *Experimental Thermal and Fluid Science* (1997).
15. L. Tamachkiarow, H.-C. Flemming, On-line monitoring of biofilm formation in a brewery water pipeline system with a fibre optical device, *Water Sci. Techn.* 47 (2003), pp19–24.
16. E. Kujundzic, A. Cristina Fonseca, E.A. Evans, M. Peterson, A.R. Greenberg, M. Hernandez, Ultrasonic monitoring of early-stage biofilm growth on polymeric surfaces, *J. Microbiol. Meth.* 68 (2007), pp 458–467.
17. J.S. Vrouwenvelder, M. C. M. van Loosdrecht, J.C. Kruithof, Early warning of biofouling in spiral wound nanofiltration and reverse osmosis membranes *Desalination*, Volume 265, Issues 1–3, (2011), pp. 206-212.
18. T. Piasecki, G. Guła, K. Nitsch, K. Waszczuk, Z. Drulis-Kawa, T. Gotszalk, Evaluation of *Pseudomonas aeruginosa* biofilm formation using Quartz Tuning Forks as impedance sensors, *Sensors and Actuators B: Chemical*, Volume 189, (2013), pp. 60-65.
19. T. Ruiz, E. E. Lopez, J. A. G. Celis, S. G. Gomez, A. S. Abelleira, Chemical treatments against biofouling on industrial equipment associated with marine related power generation technologies, a new approach to an old problem, In: *OCEANS, 2011, IEEE, Spain*, (2011), pp. 1–9.
20. J. Klahre, H.C. Flemming, Monitoring of biofouling in paper mill process waters, *Water Res.* 34 (2000), pp. 3657–3665.
21. Y. W. Kim, S. E. Sardari, M. T. Meyer, A. A. Iliadis, H. C. Wu, W. E. Bentley, R. Ghodssi, An ALD aluminum oxide passivated Surface Acoustic Wave sensor for early biofilm detection, *Sensors and Actuators B: Chemical*, Volume 163, Issue 1, (2012), pp. 136-145.
22. M. Fischer, M. Wahl, G. Friedrichs, Design and field application of a UV-LED based optical fiber biofilm sensor *Biosensors and Bioelectronics*, Volume 33, Issue 1, (2012), pp. 172-178.
23. L. Pires, K. Sachsenheimer, T. Kleintschek, A. Waldbaur, T. Schwartz, B. E. Rapp, Online monitoring of biofilm growth and activity using a combined multi-channel impedimetric and amperometric sensor *Biosensors and Bioelectronics*, Volume 47, (2013), pp. 157-163.

24. P. Lens, V. O'Flaherty, A. P. Moran, P. Stoodley, T. Mahony, *Biofilms in Medicine, Industry and Environmental Biotechnology Characteristics, Analysis and Control*, (2003) • ISBN: 9781843390190, pp. 608.
25. R. Philip-Chandy, P.J. Scully, P. Eldridge, H. J. Kadim, M. G. Grapin, M. G. Jonca, M. G. D'Ambrosio, F. Colin, An optical fiber sensor for biofilm measurement using intensity modulation and image analysis, *Selected Topics in Quantum Electronics, IEEE Journal of*, vol.6, no.5, (2000) pp.764,772.
26. J. Paredes, S. Becerro, F. Arizti, A. Aguinaga, J.L. Del Pozo, S. Arana, Interdigitated microelectrode biosensor for bacterial biofilm growth monitoring by impedance spectroscopy technique in 96-well microtiter plates, *Sensors and Actuators B: Chemical*, Volume 178, (2013), pp. 663-670.
27. N.A. Hoog-Antonyuk, W. Olthuis, M.J.J. Mayer, D. Yntema, H. Miedema, A. van den Berg, On-line fingerprinting of fluids using coaxial stub resonator technology, *Sensors and Actuators B* 163 (2012).
28. N.A. Hoog-Antonyuk, W. Olthuis, M.J.J. Mayer, H. Miedema, F.B.J. Leferink, A. van den Berg, Extensive Modeling of a Coaxial Stub Resonator for Online Fingerprinting of Fluids, *Procedia Engineering*, (2012) pp. 310-313.
29. M.J.J. Mayer, N. A. Hoog, RF antenna filter as a sensor for measuring a fluid, WO Patent 005084, 13 January 2011.
30. M.J.J. Mayer, N. A. Hoog, Werkwijze en inrichting voor ingerprinting of het behandelen van een dielectricum in het algemeen en van water in het bijzonder, NL1038869, 16 August 2012.
31. T. Kim, J. Kang, J.-H. Lee, J. Yoon, Influence of attached bacteria and biofilm on double-layer capacitance during biofilm monitoring by electrochemical impedance spectroscopy, *Water Research*, Volume 45, Issue 15, (2011), pp. 4615-4622.
32. D.M. Pozar, *Microwave Engineering*, Wiley, 2004.
33. R.E. Collin, *Foundations for Microwave Engineering*, Wiley IEEE, 2000.
34. N.A. Hoog, M. J.J. Mayer, H. Miedema, W. Olthuis, F. B. J. Leferink, A. van den Berg, Modeling and Simulations of the Amplitude-Frequency Response of Transmission Line Type Resonators Filled with Lossy Dielectric Fluids, Manuscript Number: SNA-D-13-01258R2 has been accepted for publication in *Sensors & Actuators: A. Physical* on the 12th of May, 2014, <http://dx.doi.org/10.1016/j.sna.2014.05.006>.
35. W.R. Tinga, Mixture laws and microwave-material interactions, *Dielectric Properties of Heterogeneous Materials*, vol. Pier 6, Progress in Electromagnetics Research, A. Priou, Ed. New York, Amsterdam, London, Tokyo: Elsevier, pp. 1-40, (1992).
36. Prakash, B. M. Veeragowda, and G. Krishnappa, Biofilms: a survival strategy of bacteria, *Current Science*, vol. 85, no. 9, (2003) pp. 1299–1307.
37. R.M. Donlan, W. O. Pipes, T. L. Yohe, Biofilm formation on cast iron substrata in water distribution systems, *Water Research*, Volume 28, Issue 6, (1994), pp. 1497-1503.
38. Z. Lewandowski, J. P. Boltz, 4.15 - Biofilms in Water and Wastewater Treatment, Reference Module in Earth Systems and Environmental Sciences, from *Treatise on Water Science*, Volume 4, 2011, Current as of 15 March (2013) pp. 529-570.
39. P. Stoodley, K. Sauer, D. G. Davies, J. W Costerton, Biofilms as complex differentiated communities, *Annu. Rev. Microbiol.*, 56, (2002), pp. 187–209.
40. Thome, M.E. Pettitt, M.E. Callow, J.A. Callow, M. Grunze, A. Rosenhahn, Conditioning of surfaces by macromolecules and its implication for the settlement of zoospores of the green alga *Ulva linza*, *Biofouling* 28, (2012), pp. 501-510.
41. W.G. Characklis, G. A. McFeters, K. C. Marshall, Physiological ecology in biofilm systems in *Biofilms*. John Wiley & Sons, New York, N.Y, (1990), pp 341–394.
42. R. Jackson, P. F. Churchill, and E. E. Roden. Successional changes in bacterial assemblage structure during epilithic biofilm development, *Ecology* 82, (2001), pp.555-566.
43. Hanning, R. Jarquin, M. Slavik, *Campylobacter jejuni* as a secondary colonizer of poultry biofilms, *Journal of Applied Microbiology*, 105(4), (2008).
44. Flemming H-C, Wingender J. Griegbe, C. Mayer, Physico-chemical properties of biofilms, In: Evans LV, editor. *Biofilms: recent advances in their study and control*, Amsterdam: Harwood Academic Publishers; (2000) pp. 19–34.
45. C. Dreszer, J.S. Vrouwenvelder, A.H. Paulitsch-Fuchs, A. Zwijnenburg, J.C. Kruithof, H.-C. Flemming, Hydraulic resistance of biofilms, *Journal of Membrane Science*, Volume 429, (2013), pp. 436-447.
46. M. S. Bhatnagar, EPOXY RESINS (Overview), *The Polymeric Materials Encyclopedia* © 1996 CRC Press, Inc.

47. <http://bettly.ru/tabulky/relativni-permitivita.htm> [in Russian].
48. J. Naka, S. Yamamoto, K. Komori, S. Yamakawa, T. Kokubo, Development of glass fiber with high dielectric constant, *Journal of Non-Crystalline Solids*, Volume 177, (1994), Pages 420-426.
49. Dziaugys, J. Banys, V. Samulionis, J. Macutkevicius, Y. Vysochanskii, V. Shvartsman and W. Kleemann, Chapter 9. Phase Transitions in Layered Semiconductor – Ferroelectrics, ISBN 978-953-307-455-9, (2011).
50. <http://www.medinalab.org/portal/protocols/48-recipes/81-lb-medium-and-lb-agar-plates>
51. U. von Stockar, J.-S. Liu, Does microbial life always feed on negative entropy? Thermodynamic analysis of microbial growth, *Biochimica et Biophysica Acta (BBA) - Bioenergetics*, Volume 1412, Issue 3, 4 August 1999, Pages 191-211, ISSN 0005-2728, [http://dx.doi.org/10.1016/S0005-2728\(99\)00065-1](http://dx.doi.org/10.1016/S0005-2728(99)00065-1).
52. H. Fricke, H.P. Schwan, K. Li, V. Bryson, A dielectric study of the low-conductance surface membrane in *E. coli*, *Nature*. 1956 Jan 21;177(4499):134-5.
53. W.-T. Tang, L.-Sh. Fan, Steady state phenol degradation in a draft-tube, gas-liquid-solid fluidized-bed bioreactor, *ChE Journal*, 01/1987; 33(2):239 - 249. DOI:10.1002/aic.690330210
54. W. Rauch, H. Vanhooren, P. A. Vanrolleghem, A simplified mixed-culture biofilm model, *Water Research*, Volume 33, Issue 9, June 1999, Pages 2148-2162, ISSN 0043-1354, [http://dx.doi.org/10.1016/S0043-1354\(98\)00415-1](http://dx.doi.org/10.1016/S0043-1354(98)00415-1).
55. D.L. Chopp, M. J. Kirisits, B. Moran, M. R. Parsek, A mathematical model of quorum sensing in a growing bacterial biofilm, *Journal of Industrial Microbiology and Biotechnology*, December 2002, Volume 29, Issue 6, pp 339-346.
56. O.K. Lyngberg, C. P. Ng, V. Thiagarajan, L. E. Scriven, M. C. Flickinger, Engineering the microstructure and permeability of thin multilayer latex biocatalytic coatings containing *E. coli*, *Biotechnology Progress*, 01/2001; 17(6):1169-79. DOI:10.1021/bp0100979.
57. J. Svagan, Anna J & Samir, My A S Azizi & Berglund, Lars A., Biomimetic polysaccharide nanocomposites of high cellulose content and high toughness; *Biomacromolecules*, 8, 2007.
58. X.-F. Zhou, G. H. Markx, R. Pethig, I. M. Eastwood, Differentiation of viable and non-viable bacterial biofilms using electrorotation, *Biochimica et Biophysica Acta (BBA) - General Subjects*, Volume 1245, Issue 1, 17 (1995), pp. 85-93.
59. Dw. K. Butler, Near-surface geophysics, Volume 13, Front Cover.. Society of Exploration Geophysicists, 2005 - Science - 732 pages.
60. R. Späth, H.-C. Flemming, S. Wuertz, Sorption properties of biofilms, *Water Science and Technology*, Volume 37, Issues 4–5, 1998, pp. 207-210.
61. J.W. Costerton, R.T. Irvin, K.-J. Cheng, The bacterial glycocalyx in nature and disease, *Ann Rev Microbiol* 35: (1981), pp. 299–324.
62. P. H. Nielsen, A. Jahn, R. Palmgren, Conceptual model for production and composition of exopolymers in biofilms, *Water Sci Technol* 36: (1997), pp. 9-11.
63. J. Svagan, M. A. S. A. Samir, and L. A. Berglund, Biomimetic Polysaccharide Nanocomposites of High Cellulose Content and High Toughness, *Biomacromolecules* 8, (2007) pp. 2556-2563
64. M. Elimelech, C. R. O'Melia, Kinetics of deposition of colloidal particles in porous media, *Environ. Sci. Technol.*, 24 (10), (1990), pp. 1528–1536.
65. Collaboration: Authors and editors of the volumes III/17B-22A-41B, Silver chloride (AgCl) refractive index, dielectric constants, II-VI and I-VII Compounds; Semimagnetic Compounds 41B: (1999), pp. 1-7.

6.8 Supplementary Information

Appendix A

For the model simulations, the exact resonator geometry was taken into account. In addition to the geometric parameters in Table 1, following parameters were accounted for in the model:

1. An inner conductor that is longer than the outer conductor, thereby slightly increasing the effective resonator length by 2.9 cm, see also Fig. A.1.
2. A polypropylene disc used in the top cap of the resonator with a thickness of 1 cm. This disc replaces feed substrate by polypropylene, see also Fig. A.1.
3. The presence of 1.5-2 cm epoxy resin at the bottom of the resonator in order to protect the SMA connector from corrosion

It is noted that the thickness of the epoxy resin layer and the thickness of the disc were lumped into one parameter ϵ_{epoxy} with a relative dielectric permittivity of 2.

The model simulations shown in Fig. 13 were performed according to the following procedure:

1. First the resonator filled with epoxy resin and air was simulated and the simulation was validated with experiments.
2. Subsequently, the resonator filled with epoxy resin, glass beads and air was simulated and also this simulation was validated with experiments.
3. Finally, the model was validated for a sensor filled with epoxy resin, glass beads and feed substrate, by comparing model simulation with experiments.

This validated model (together with the dielectric constant ϵ_r and $\tan\delta$ for glass beads, epoxy resin and feed substrate and) was used as starting point for the simulations in Fig. 13.

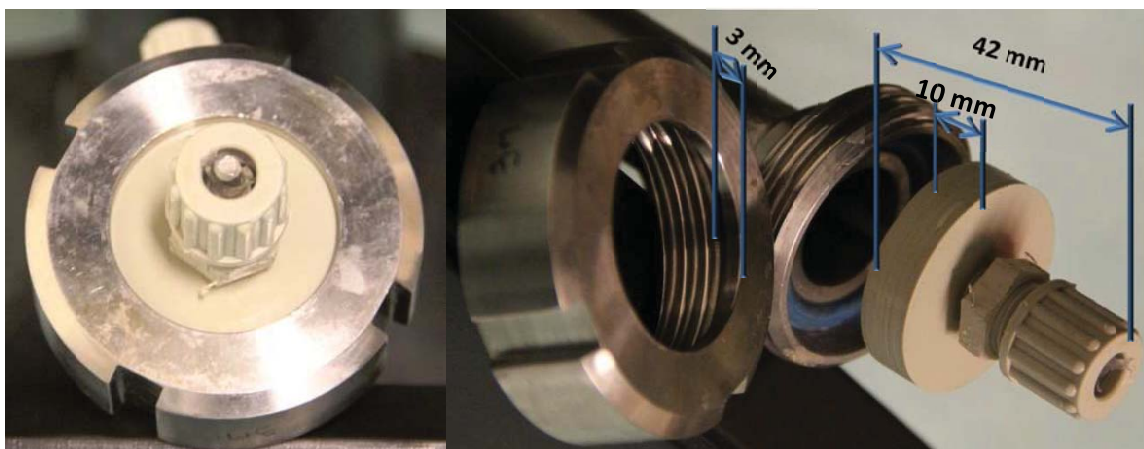


Fig.A.1. A photo of the coaxial resonator which includes the plastic cap on the top with dimensions.

To exclude the effect of the epoxy resin on the bottom of the resonator the following function was used:

```
function F = bio_air_epoxy_coax_resonator(x,f)
% The resonator was not closed, SO the polymer did not played role at all!!
em=1;      % dielectric permittivity of the feed substrate, [-]
h=0.267+0.029; % the total length of the resonator with epoxy on the bottom [m]
    % note: epoxy on the bottom of the sensor
h_epoxy=0.02; % the length of the layer of epoxy [m]
db=25e-3; % diameter of the resonator;
Vt=pi*h*db^2/4; %volume of the empty resonator [m^3]
Vt_epoxy=pi*h_epoxy*db^2/4 %volume of the epoxy resin [m^3]
f_epoxy=(pi*h_epoxy*db^2/4)/Vt %volume fraction of the epoxy resin [m^3]
Vt_air=Vt-Vt_epoxy %volume of the filled with epoxy resonator [m^3]
f_air=Vt_air/Vt
f_air_t=1-f_epoxy
len =0.267+0.029; % length of the coax resonator [m]
b = 25e-3; % inner diameter of the outer conductor [m]
a = 5e-3;% outer diameter of the inner conductor [m]
c=3*1e+8; % speed of light in vacuum [m/s]
Ur=1; %relative dielectric permeability of the dielectric between inner and outer conductors [-]
u = Ur*4*pi*1e-7; % magnetic permeability of the dielectric [H/m]
sigma_air=0;%conductivity of the dielectric between inner and outer conductors [S/m]
sigma_epoxy=1.41e-7%conductivity of the poxy resin
sigma_steel=7.7e+6;%conductance of the metal applied for inner and outer conductors (stainless steel)
[1/(Ohm*m)]
sigma_eff=sigma_air*f_air_t+sigma_epoxy*f_epoxy;
Eeff=em*(f_air_t)+x(2)*f_epoxy
E = Eeff * 1/(4*pi*1e-7*c*c); % vacuum permeability [H/m]
C = ((2*pi*E)/log(b/a)); % capacitance of the open ended coaxial stub resonator [F]
L = ((u/(pi*2))*log(b/a));% inductance of the open ended coaxial stub resonator [H]
%Define the input voltage supplied by the function generator [V]
vin=100e-3; %input voltage supplied by the function generator [V]
omega = 2*pi*f;% angular frequency [rad/s]
Eim=((omega.*E.*x(1))-sigma_eff)./omega;%imaginary part of complex dielectric permittivity
skin_depth=sqrt(2./(omega.*u.*sigma_steel));%skin_depth
Rs=1./(sigma_steel.*skin_depth);% surface resistivity of the inner and outer conductor of the resonator
R=(Rs/(2*pi)*(1/(0.5*a)+1/(0.5*b)));% distributed element resistance R of the resonator [Ohm/m]
G=(omega.*Eim+sigma_eff)./(omega.*E).*omega.*C;%distributed element conductance of the resonator
[F/(m*s)]
gamma =(sqrt((R+1i.*omega.*L).*(G+1i.*omega.*C)));%complex propagation constant [1/m]
%notes on gamma: Re(gamma)=alfa = attenuation constant representing losses [Np/m];
Im(gamma)=beta=phase of the propagation constant [rad/m]
%since the signal is oscillating in time with omega rad/s, the propagation velocity of the wave [m/s] =
omega/beta; also, beta = 2*pi/wavelength.
Zc=sqrt(((R+1i.*omega.*L)./(G+1i.*omega.*C)));% complex characteristic impedance of the resonator [Ohm]
Zin=Zc.*coth(gamma.*len);%complex input impedance of the resonator [Ohm]
vout=sqrt((real(Zin.*(vin./(50+2*Zin))))).^2+(imag(Zin.*(vin./(50+2*Zin))))).^2);%modulus of vout, the is the
recorded voltage by the spectrum analyzer [V]
F =20.*log10(vout)+13;%vout as a power ratio in dBm i.e., the measured power referenced to one mWatt and
the underlying assumption of a 50 Ohm load resistance
```

The main program was:

```
clear all % Clear all variables in function workspace
close all % Close all figures
clc % Clear command window
load air_new.txt % load the file with data of the day of experiment
%- See the Supplementary Information
f=air_new(:,1); % Load experimental data; frequency
amplitude=air_new(:,2); % Load experimental data; amplitude
f=f*1e+6; % Frequency conversion
%- Plot experimental data
plot(f/1e+6, amplitude, 'or')
hold on
x0 = [0 1];
ya0 = bio_air_epoxy_coax_resonator(x0,f);
% %- Plot initial values
% hold on;
% plot(f,ya0,'--m')
%-Boundary conditions
LB = [0 1]; % Lower bounds
UB = [1 100]; %Upper bounds
% -Solving nonlinear least-squares curve fitting
[x,resnorm] = lsqcurvefit('bio_air_epoxy_coax_resonator',x0,f,amplitude, LB, UB)
ya =bio_air_epoxy_coax_resonator(x,f);
%- Plot fit results
Hf = plot(f/1e+6,ya,'b');
set(Hf, 'LineWidth',3)
hold on
xlabel('Frequency, (MHz)','fontsize',42,'fontweight','b');
ylabel('Amplitude, (dBm)','fontsize',42,'fontweight','b');
grid on
hold on
```

To determine the effective loss tangent $\tan\delta_{eff}$ (Eq. 5) of all system and the effective dielectric permittivity of glass beads ϵ_{gb} the following function was used:

```
function F = bio_air_glass_coax_resonator(x,f)
em=1; % dielectric permittivity of the feed substrate, [-],
h=0.267+0.029; % the total length of the resonator with epoxy on the bottom [m],
% note: epoxy on the bottom of the sensor
h_epoxy=0.062; % the length of the layer of epoxy [m]
db=25e-3; % diameter of the resonator;
% e_epoxy=3.98 %from the simulation defined from the simulation models
e_epoxy_pol=1.96 %from the simulation defined from the simulation models
%using experimental data of the empty resonator with epoxy
%resin on the bottom
Vt=pi*h*db^2/4; %full volume of the empty resonator, [m^3]
Vt_epoxy=pi*h_epoxy*db^2/4 % volume of the part contains epoxy resin, [m^3]
f_epoxy=(pi*h_epoxy*db^2/4)/Vt % volume fraction of the part contains epoxy resin, [-]
Vt_feed=Vt-Vt_epoxy; %volume of the part of the resonator filled with epoxy resonator, [m^3]
f_feed_t=Vt_feed/Vt %volume fraction of air (feed) in the filled with epoxy resonator, [-]
Ng=2230; % the number of glass beads in the resonator, [-]
dg=4e-3; % diameter of the glass bead [m];
Vglass=(Ng*pi/6*dg^3); % volume of the glass beads, [m^3]
fgb=Vglass/(Vt_feed) % volume fraction of the glass beads, [-]
f_feed_t_gb=1-fgb % volume fraction of the air (feed) in a composition with glass beads, [-]
```

```

%dielectric constant of the composition (mixture) glass beads and air defined using the Lichtenecker equation
em_glass_1=f_feed_t_gb*(log10(em))+fgb*log10((x(2)));
em_glass_feed=10^em_glass_1
%parallel capacitance
em_glass_feed= f_feed_t_gb*((em))+fgb*((x(2))
check_s=f_feed_t_gb+fgb
% len =0.29; % length of the coax resonator, [m]
len =0.27+0.029; % length of the coax resonator [m]
b = 25e-3; % inner diameter of the outer conductor, [m]
a = 5e-3;% outer diameter of the inner conductor, [m]
c=3*1e+8; % speed of light in vacuum, [m/s]
Ur=1; %relative dielectric permeability of the dielectric between inner and outer conductors, [-]
u = Ur*4*pi*1e-7; % magnetic permeability of the dielectric, [H/m]
sigma_feed=0;%conductivity of the dielectric between inner and outer conductors, [S/m]
sigma_epoxy=1.41e-7%conductivity of epoxy resin, [S/m]
sigma_glass=1e-12%conductivity of glass glass bead, [S/m]
sigma_steel=1.45e+6;%conductance of the metal applied for inner and outer conductors (stainless steel),
[1/(Ohm*m)]
fgb_t=Vglass/(Vt)
f_of_feed=1-f_epoxy-fgb_t
sigma_eff = sigma_feed*f_of_feed + sigma_epoxy*f_epoxy + sigma_glass* fgb_t;% effective conductivity of
whole system, [S/m]
checkkk=fgb_t+f_epoxy+f_of_feed
Eeff=em_glass_feed*(f_feed_t)+e_epoxy_pol*f_epoxy% effective dielectric constant of whole system, [-]
E =Eeff * 1/(4*pi*1e-7*c*c); % vacuum permeability [H/m]
check1=f_feed_t+f_epoxy
C = ((2*pi*E)/log(b/a)); % capacitance of the open ended coaxial stub resonator [F]
L = ((u/(pi*2))*log(b/a));% inductance of the open ended coaxial stub resonator [H]
%Define the input voltage supplied by the function generator [V]
vin=120e-3; %input voltage supplied by the function generator [V]
omega = 2*pi*f;% angular frequency [rad/s]
Eim=((omega.*E.*x(1))-sigma_eff)./omega;%imaginary part of complex dielectric permittivity
skin_depth=sqrt(2./(omega.*u.*sigma_steel));%skin_depth
Rs=1./(sigma_steel.*skin_depth);% surface resistivity of the inner and outer conductor of the resonator
R=(Rs/(2*pi)*(1/(0.5*a)+1/(0.5*b)));% distributed element resistance R of the resonator [Ohm/m]
G=(omega.*Eim+sigma_eff)./(omega.*E).*omega.*C;%distributed element conductance of the resonator
[F/(m*s)]
gamma =(sqrt((R+1i.*omega.*L).*(G+1i.*omega.*C)));%complex propagation constant [1/m]
%notes on gamma: Re(gamma)=alfa = attenuation constant representing losses [Np/m];
Im(gamma)=beta=phase of the propagation constant [rad/m]
%since the signal is oscillating in time with omega rad/s, the propagation velocity of the wave [m/s] =
omega/beta; also, beta = 2*pi/wavelength.
Zc=sqrt(((R+1i.*omega.*L)./(G+1i.*omega.*C)));% complex characteristic impedance of the resonator [Ohm]
Zin=Zc.*coth(gamma.*len);%complex input impedance of the resonator [Ohm]
vout=sqrt((real(Zin.*(vin./(50+2*Zin))))).^2+(imag(Zin.*(vin./(50+2*Zin))))).^2);%modulus of vout, the is the
recorded voltage by the spectrum analyzer [V]
F =20.*log10(vout)+13;%vout as a power ratio in dBm i.e., the measured power referenced to one mWatt and
the underlying assumption of a 50 Ohm load resistance

```

The main program was:

```
clear all % Clear all variables in function workspace
close all % Close all figures
clc % Clear command window
load glass_new.txt % load the file with data of the day of experiment
%- See the Supplementary Information
f=glass_new(:,1); % Load experimental data; frequency
amplitude=glass_new(:,2); % Load experimental data; amplitude
f=f*1e+6; % Frequency conversion
%- Plot experimental data
plot(f/1e+6, amplitude, 'or')
hold on
x0 = [0 1];
ya0 = bio_air_glass_coax_resonator(x0,f);
% %- Plot initial values
% hold on;
% plot(f,ya0,'--m')
%-Boundary conditions
LB = [0 1]; % Lower bounds
UB = [1 50]; %Upper bounds
% -Solving nonlinear least-squares curve fitting
[x,resnorm] = lsqcurvefit('bio_air_glass_coax_resonator',x0,f,amplitude, LB, UB)
ya =bio_air_glass_coax_resonator(x,f);
%- Plot fit results
Hf = plot(f/1e+6,ya,'b');
set(Hf, 'LineWidth',3)
hold on
xlabel('Frequency, (MHz)', 'fontsize',42,'fontweight', 'b');
ylabel('Amplitude, (dBm)', 'fontsize',42,'fontweight', 'b');
grid on
hold on
```


To determine the effective loss tangent $\tan\delta_{eff}$ (Eq. 5) of all system and the effective dielectric permittivity of feed substrate ϵ_m the following function was used:

```
function F = bio_feed_epoxy_coax_resonator(x,f)
e_epoxy = 1.96; % dielectric constant of epoxy, defined from the simulation
    % x(2) dielectric permittivity of the feed substrate, [-],
h=0.267+0.029; % the total length of the resonator with epoxy on the bottom [m],
    % note: epoxy on the bottom of the sensor
h_epoxy=0.062; % the length of the layer of epoxy [m]
db=25e-3; % diameter of the resonator;
Vt=pi*h*db^2/4; %volume of the empty resonator [m^3]
Vt_epoxy=pi*h_epoxy*db^2/4 % volume of epoxy resin in the resonator
f_epoxy=(pi*h_epoxy*db^2/4)/Vt % volume fraction of epoxy resin in the resonator
Vt_feed=Vt-Vt_epoxy %volume of the filled with epoxy resonator [m^3]
f_feed=Vt_feed/Vt %volume of feed substrate in the filled with epoxy resonator [m^3]
f_feed_t=1-f_epoxy %volume fraction of feed substrate excluding epoxy in the filled with epoxy resonator
[m^3]
len =0.27+0.029; % length of the coax resonator [m]
b = 25e-3; % inner diameter of the outer conductor [m]
a = 5e-3;% outer diameter of the inner conductor [m]
c=3*1e+8; % speed of light in vacuum [m/s]
Ur=1; %relative dielectric permeability of the dielectric between inner and outer conductors [-]
u = Ur*4*pi*1e-7; % magnetic permeability of the dielectric [H/m]
sigma_feed=615e-4;%conductivity of the dielectric between inner and outer conductors [S/m]
sigma_epoxy=1.41e-7%conductivity of the epoxy resin
sigma_steel=7.7e+6;%conductance of the metal applied for inner and outer conductors (stainless steel)
[1/(Ohm*m)]
%effective conductance of both feed substrate and epoxy resin
sigma_eff=sigma_feed*f_feed_t+sigma_epoxy*f_epoxy;
%effective dielectric permittivity of both feed substrate and epoxy resin
Eeff=x(2)*(f_feed_t)+e_epoxy*f_epoxy
E = Eeff * 1/(4*pi*1e-7*c*c); % vacuum permeability [H/m]
C = ((2*pi*E)/log(b/a)); % capacitance of the open ended coaxial stub resonator [F]
L = ((u/(pi*2))*log(b/a));% inductance of the open ended coaxial stub resonator [H]
%Define the input voltage supplied by the function generator [V]
vin=120e-3; %input voltage supplied by the function generator [V]
omega = 2*pi*f;% angular frequency [rad/s]
Eim=((omega.*E.*x(1))-sigma_eff)./omega;%imaginary part of complex dielectric permittivity
skin_depth=sqrt(2./(omega.*u.*sigma_steel));%skin_depth
Rs=1./(sigma_steel.*skin_depth);% surface resistivity of the inner and outer conductor of the resonator
R=(Rs/(2*pi)*(1/(0.5*a)+1/(0.5*b)));% distributed element resistance R of the resonator [Ohm/m]
G=(omega.*Eim+sigma_eff)./(omega.*E).*omega.*C;%distributed element conductance of the resonator
[F/(m*s)]
gamma =(sqrt((R+1i.*omega.*L).*(G+1i.*omega.*C)));%complex propagation constant [1/m]
%notes on gamma: Re(gamma)=alfa = attenuation constant representing losses [Np/m];
Im(gamma)=beta=phase of the propagation constant [rad/m]
%since the signal is oscillating in time with omega rad/s, the propagation velocity of the wave [m/s] =
omega/beta; also, beta = 2*pi/wavelength.
Zc=sqrt(((R+1i.*omega.*L)./(G+1i.*omega.*C)));% complex characteristic impedance of the resonator [Ohm]
Zin=Zc.*coth(gamma.*len);%complex input impedance of the resonator [Ohm]
vout=sqrt((real(Zin.*(vin./(50+2*Zin))))).^2+(imag(Zin.*(vin./(50+2*Zin))))).^2);%modulus of vout, the is the
recorded voltage by the spectrum analyzer [V]
F =20.*log10(vout)+13;%vout as a power ratio in dBm i.e., the measured power referenced to one mWatt and
the underlying assumption of a 50 Ohm load resistance
```


The main program was:

```
clear all % Clear all variables in function workspace
close all % Close all figures
clc % Clear command window
load sub.txt % load the file with data of the day of experiment
%- See the Supplementary Information
f=sub(:,1); % Load experimental data; frequency
amplitude=sub(:,2); % Load experimental data; amplitude
f=f*1e+6; % Frequency conversion
%- Plot experimental data
plot(f/1e+6, amplitude, 'or')
hold on
x0 = [0 1];
ya0 = bio_feed_epoxy_coax_resonator(x0,f);
% %- Plot initial values
% hold on;
% plot(f,ya0,'--m')
%-Boundary conditions
LB = [0 1]; % Lower bounds
UB = [1 100]; %Upper bounds
% -Solving nonlinear least-squares curve fitting
[x,resnorm] = lsqcurvefit(' bio_feed_epoxy_coax_resonator',x0,f,amplitude, LB, UB)
ya = bio_feed_epoxy_coax_resonator(x,f);
%- Plot fit results
Hf = plot(f/1e+6,ya,'b');
set(Hf, 'LineWidth',3)
hold on
xlabel('Frequency, (MHz)','fontsize',42,'fontweight','b');
ylabel('Amplitude, (dBm)','fontsize',42,'fontweight','b');
grid on
hold on
```

To determine the effective loss tangent $\tan\delta_{eff}$ (Eq. 5) of all system and the effective dielectric permittivity of glass beads ϵ_{gb} by influence of the feed substrate the following function was used:

```
function F = bio_feed_glass_coax_resonator(x,f)
em=75.4; % dielectric permittivity of the feed substrate, [-],
h=0.267+0.029; % the total length of the resonator with epoxy on the bottom, [m],
% note: epoxy on the bottom of the sensor
h_epoxy=0.062; % the length of the layer of epoxy, [m]
db=25e-3; % diameter of the resonator, [m];
% e_epoxy=3.98 %from the simulation defined from the simulation models
e_epoxy=1.96 %from the simulation defined from the simulation models
%using experimental data of the empty resonator with epoxy
%resin on the bottom
Vt=pi*h*db^2/4; %full volume of the empty resonator, [m^3]
Vt_epoxy=pi*h_epoxy*db^2/4 % volume of the part contains epoxy resin, [m^3]
f_epoxy=(pi*h_epoxy*db^2/4)/Vt % volume fraction of the part contains epoxy resin, [-]
Vt_feed=Vt-Vt_epoxy; %volume of the part of the resonator filled with epoxy resonator, [m^3]
f_feed_t=Vt_feed/Vt %volume fraction of air (feed) in the filled with epoxy resonator, [-]
Ng=2230*1.05; % the number of glass beads in the resonator, [-]
dg=4e-3; % diameter of the glass bead [m];
Vglass=(Ng*pi/6*dg^3); % volume of the glass beads, [m^3]
fgb=Vglass/(Vt_feed) % volume fraction of the glass beads, [-]
f_feed_t_gb=1-fgb % volume fraction of the air (feed) in a composition with glass beads, [-]
%dielectric constant of the composition (mixture) glass beads and air defined using the Lichtenecker equation
em_glass_1=f_feed_t_gb*(log10(em))+fgb*log10((x(2)));
em_glass_feed=10^em_glass_1
%parallel capacitance
em_glass_feed= f_feed_t_gb*((em))+fgb*((x(2)))
check_s=f_feed_t_gb+fgb
len =0.267+0.029; % length of the coax resonator [m]
b = 25e-3; % inner diameter of the outer conductor, [m]
a = 5e-3;% outer diameter of the inner conductor, [m]
c=3*1e+8; % speed of light in vacuum, [m/s]
Ur=1; %relative dielectric permeability of the dielectric between inner and outer conductors, [-]
u = Ur*4*pi*1e-7; % magnetic permeability of the dielectric, [H/m]
sigma_feed=615e-4;%conductivity of the dielectric between inner and outer conductors, [S/m]
sigma_epoxy=1.41e-7%conductivity of epoxy resin, [S/m]
sigma_glass=1e-12%conductivity of glass glass bead, [S/m]
sigma_steel=1.45e+6;%conductance of the metal applied for inner and outer conductors (stainless steel),
[1/(Ohm*m)]
fgb_t=Vglass/(Vt)
f_of_feed=1-f_epoxy-fgb_t
sigma_eff = sigma_feed*f_of_feed + sigma_epoxy*f_epoxy + sigma_glass* fgb_t;% effective conductivity of
whole system, [S/m]
checkkk=fgb_t+f_epoxy+f_of_feed
Eeff=em_glass_feed*(f_feed_t)+e_epoxy*f_epoxy% effective dielectric constant of whole system, [-]
E =Eeff * 1/(4*pi*1e-7*c*c); % vacuum permeability [H/m]
check1=f_feed_t+f_epoxy
C = ((2*pi*E)/log(b/a)); % capacitance of the open ended coaxial stub resonator [F]
L = ((u/(pi*2))*log(b/a));% inductance of the open ended coaxial stub resonator [H]
%Define the input voltage supplied by the function generator [V]
vin=600e-3; %input voltage supplied by the function generator [V]
omega = 2*pi*f;% angular frequency [rad/s]
Eim=((omega.*E.*x(1))-sigma_eff)/omega;%imaginary part of complex dielectric permittivity
```

```

skin_depth=sqrt(2./(omega.*u.*sigma_steel));%skin_depth
Rs=1./(sigma_steel.*skin_depth);% surface resistivity of the inner and outer conductor of the resonator
R=(Rs/(2*pi)*(1/(0.5*a)+1/(0.5*b)));% distributed element resistance R of the resonator [Ohm/m]
G=(omega.*Eim+sigma_eff)./(omega.*E).*omega.*C;%distributed element conductance of the resonator
[F/(m*s)]
gamma =(sqrt((R+1i.*omega.*L).*(G+1i.*omega.*C)));%complex propagation constant [1/m]
%notes on gamma: Re(gamma)=alfa = attenuation constant representing losses [Np/m];
Im(gamma)=beta=phase of the propagation constant [rad/m]
%since the signal is oscillating in time with omega rad/s, the propagation velocity of the wave [m/s] =
omega/beta; also, beta = 2*pi/wavelength.
Zc=sqrt(((R+1i.*omega.*L)./(G+1i.*omega.*C)));% complex characteristic impedance of the resonator [Ohm]
Zin=Zc.*coth(gamma.*len);%complex input impedance of the resonator [Ohm]
vout=sqrt((real(Zin.*(vin./(50+2*Zin)))).^2+(imag(Zin.*(vin./(50+2*Zin)))).^2);%modulus of vout, the is the
recorded voltage by the spectrum analyzer [V]
F =20.*log10(vout)+13;%vout as a power ratio in dBm i.e., the measured power referenced to one mWatt and
the underlying assumption of a 50 Ohm load resistance
    
```

The main program was:

```

clear all % Clear all variables in function workspace
close all % Close all figures
clc % Clear command window
load feed_glass_epoxy.txt % load the file with data of the day of experiment
%- See the Supplementary Information
f=feed_glass_epoxy(:,1); % Load experimental data; frequency
amplitude=feed_glass_epoxy(:,2); % Load experimental data; amplitude
f=f*1e+6; % Frequency conversion
%- Plot experimental data
plot(f/1e+6, amplitude, 'or')
hold on
x0 = [0 1];
ya0 = bio_feed_glass_coax_resonator(x0,f);
% %- Plot initial values
% hold on;
% plot(f,ya0,'--m')
%-Boundary conditions
LB = [0 1]; % Lower bounds
UB = [1 10]; %Upper bounds
% -Solving nonlinear least-squares curve fitting
[x,resnorm] = lsqcurvefit('bio_feed_glass_coax_resonator',x0,f,amplitude, LB, UB)
ya =bio_feed_glass_coax_resonator(x,f);
%- Plot fit results
Hf = plot(f/1e+6,ya,'b');
set(Hf, 'LineWidth',3)
hold on
xlabel('Frequency, (MHz)','fontsize',42,'fontweight','b');
ylabel('Amplitude, (dBm)','fontsize',42,'fontweight','b');
grid on
hold on
    
```

To determine the effective loss tangent $\tan\delta_{\text{eff}}$ (Eq. 5) of all system and the effective dielectric permittivity of glass beads ϵ_{gb} by influence of the feed substrate the following function was used (main simulation for day 1 and day 2):

```

clc
clearvars
em=75.4; % dielectric permittivity of the feed substrate, [-],
h=0.267+0.029; % the total length of the resonator with epoxy on the bottom, [m],
% note: epoxy on the bottom of the sensor
h_epoxy=0.062; % the length of the layer of epoxy, [m]
db=25e-3; % diameter of the resonator, [m];
e_epoxy=1.96 %from the simulation defined from the simulation models
%using experimental data of the empty resonator with epoxy
%resin on the bottom
Vt=pi*h*db^2/4 %full volume of the empty resonator, [m^3]
Vt1=pi*h*5e-3^2/4
nu=(Vt1)*100/Vt
Vt_epoxy=pi*h_epoxy*db^2/4 % volume of the part contains epoxy resin, [m^3]
f_epoxy=(pi*h_epoxy*db^2/4)/Vt % volume fraction of the part contains epoxy resin, [-]
Vt_feed=Vt-Vt_epoxy %volume of the part of the resonator filled with epoxy resonator, [m^3]
f_feed_t=Vt_feed/Vt %volume fraction of air (feed) in the filled with epoxy resonator, [-]
Ng=2230; % the number of glass beads in the resonator, [-]
dg=4e-3; % diameter of the glass bead [m];
Vglass=(Ng*pi/6*dg^3); % volume of the glass beads, [m^3]
fgb=Vglass/Vt_feed % volume fraction of the glass beads, [-]
ebiol=60;
fbiol=0.138;
e_gb=5% dielectric constant of glass
f_feed_t_gb=1-fgb-fbiol
% volume fraction of the air (feed) in a composition with glass beads, [-]
%dielectric constant of the composition (mixture) glass beads and air defined using the Lichtenecker equation
%Lichtenecker's logarithmic law
% em_glass_1=f_feed_t_gb*(log10(em))+fgb*log10((e_gb))+fbiol*log10((ebiol));
% em_glass_feed=10^em_glass_1
%parallel capacitance
em_glass_feed=f_feed_t_gb*((em))+fgb*((e_gb))+fbiol*((ebiol));
check_s=f_feed_t_gb+fgb+fbiol
len =0.267+0.029; % length of the coax resonator, [m]
b = 25e-3; % inner diameter of the outer conductor, [m]
a = 5e-3;% outer diameter of the inner conductor, [m]
c=3*1e+8; % speed of light in vacuum, [m/s]
Ur=1; %relative dielectric permeability of the dielectric between inner and outer conductors, [-]
u = Ur*4*pi*1e-7; % magnetic permeability of the dielectric, [H/m]
sigma_feed=615e-4;%conductivity of the dielectric between inner and outer conductors, [S/m]
sigma_epoxy=1.41e-7%conductivity of epoxy resin, [S/m]
sigma_glass=1e-12%conductivity of glass glass bead, [S/m]
sigma_steel=1.45e+6;%conductance of the metal applied for inner and outer conductors (stainless steel),
[1/(Ohm*m)]
fgb_t=Vglass/Vt;
V_biol=fbiol*Vt_feed;
fbiolt=fbiol*Vt_feed/Vt
f_of_feed=1-f_epoxy-fgb_t-fbiolt
sigma_biol=615e-4;
sigma_eff = sigma_feed*f_of_feed + sigma_epoxy*f_epoxy + sigma_glass* fgb_t+sigma_biol*fbiolt;% effective
conductivity of whole system, [S/m]

```

```

check=fgb_t+f_epoxy+f_of_feed+fbiolt
Eeff=em_glass_feed*(f_feed_t)+e_epoxy*f_epoxy% effective dielectric constant of whole system, [-]
checkkkkkk=f_feed_t+f_epoxy
E =Eeff * 1/(4*pi*1e-7*c*c); % vacuum permeability [H/m]
tang_eff=0.08
C = ((2*pi*E)/log(b/a)); % capacitance of the open ended coaxial stub resonator, [F]
L = ((u/(pi*2))*log(b/a));% inductance of the open ended coaxial stub resonator, [H]
%Define the input voltage supplied by the function generator, [V]
f=220E+06:10000:320E+06;
vin=600e-3; %input voltage supplied by the function generator, [V]
omega = 2*pi*f;% angular frequency, [rad/s]
Eim=((omega.*E.*tang_eff)-sigma_eff)./omega;%imaginary part of complex dielectric permittivity
skin_depth=sqrt(2./(omega.*u.*sigma_steel));%skin_depth
Rs=1./(sigma_steel.*skin_depth);% surface resistivity of the inner and outer conductor of the resonator
R=(Rs/(2*pi)*(1/(0.5*a)+1/(0.5*b)));% distributed element resistance R of the resonator [Ohm/m]
G=(omega.*Eim+sigma_eff)./(omega.*E).*omega.*C;%distributed element conductance of the resonator
[F/(m*s)]
gamma =(sqrt((R+1i.*omega.*L).*(G+1i.*omega.*C)));%complex propagation constant [1/m]
%notes on gamma: Re(gamma)=alfa = attenuation constant representing losses [Np/m];
Im(gamma)=beta=phase of the propagation constant [rad/m]
%since the signal is oscillating in time with omega rad/s, the propagation velocity of the wave [m/s] =
omega/beta; also, beta = 2*pi/wavelength.
Zc=sqrt(((R+1i.*omega.*L)./(G+1i.*omega.*C)));% complex characteristic impedance of the resonator [Ohm]
Zin=Zc.*coth(gamma.*len);%complex input impedance of the resonator [Ohm]
vout=sqrt((real(Zin.*(vin./(50+2*Zin))))).^2+(imag(Zin.*(vin./(50+2*Zin))))).^2);%modulus of vout, the is the
recorded voltage by the spectrum analyzer [V]
vout =20.*log10(vout)+13;%vout as a power ratio in dBm i.e., the measured power referenced to one mWatt
and the underlying assumption of a 50 Ohm load resistance
hF = figure
hA = axes
set(hA, 'XGrid', 'off', 'YGrid', 'on')
hold on
set(0,'DefaultFontSize',36,'DefaultFontName','Times New Roman', 'DefaultFontWeight', 'bold');
%- See the Supplementary Information
load day_one.txt % load the file
MHz=day_one(:,1); % Load experimental data; frequency
CH1=day_one(:,2); % Load experimental data; amplitude
frequency=MHz;
amplitude=CH1;
plot(frequency,amplitude,'LineStyle','none','Marker','.', 'MarkerEdgeColor','r', 'MarkerSize',40)
hold on
plot(f/1e+6,vout, 'm', 'LineWidth', 3);
xlabel('Frequency, (MHz)', 'fontsize', 42, 'fontweight', 'b');
ylabel('Amplitude, (dBm)', 'fontsize', 42, 'fontweight', 'b');
hold on
%DAY TWO
em=75.4; % dielectric permittivity of the feed substrate, [-],
h=0.267+0.029; % the total length of the resonator with epoxy on the bottom, [m],
% note: epoxy on the bottom of the sensor
h_epoxy=0.062; % the length of the layer of epoxy, [m]
db=25e-3; % diameter of the resonator, [m];
e_epoxy=1.96 %from the simulation defined from the simulation models
%using experimental data of the empty resonator with epoxy
%resin on the bottom
Vt=pi*h*db^2/4 %full volume of the empty resonator, [m^3]
Vt1=pi*h*5e-3^2/4

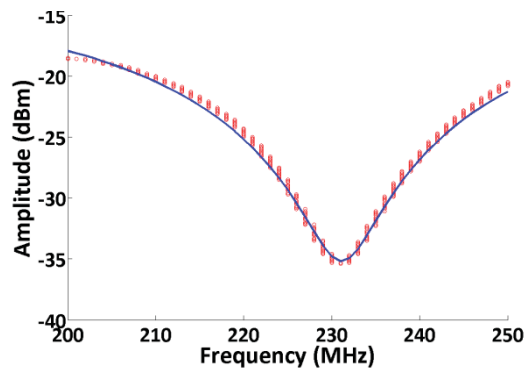
```

```

nu=(Vt1)*100/Vt
Vt_epoxy=pi*h_epoxy*db^2/4 % volume of the part contains epoxy resin, [m^3]
f_epoxy=(pi*h_epoxy*db^2/4)/Vt % volume fraction of the part contains epoxy resin, [-]
Vt_feed=Vt-Vt_epoxy %volume of the part of the resonator filled with epoxy resonator, [m^3]
f_feed_t=Vt_feed/Vt %volume fraction of air (feed) in the filled with epoxy resonator, [-]
Ng=2230; % the number of glass beads in the resonator, [-]
dg=4e-3; % diameter of the glass bead [m];
Vglass=(Ng*pi/6*dg^3); % volume of the glass beads, [m^3]
fgb=Vglass/Vt_feed % volume fraction of the glass beads, [-]
ebiol=60;
fbiol=0.290;
e_gb=5% dielectric constant of glass
f_feed_t_gb=1-fgb-fbiol
% volume fraction of the air (feed) in a composition with glass beads, [-]
%dielectric constant of the composition (mixture) glass beads and air defined using the Lichtenecker equation
%Lichtenecker's logarithmic law
% em_glass_1=f_feed_t_gb*(log10(em))+fgb*log10((e_gb))+fbiol*log10((ebiol));
% em_glass_feed=10^em_glass_1
%parallel capacitance
em_glass_feed=f_feed_t_gb*((em))+fgb*((e_gb))+fbiol*((ebiol));
check_s=f_feed_t_gb+fgb+fbiol
len =0.267+0.029; % length of the coax resonator, [m]
b = 25e-3; % inner diameter of the outer conductor, [m]
a = 5e-3;% outer diameter of the inner conductor, [m]
c=3*1e+8; % speed of light in vacuum, [m/s]
Ur=1; %relative dielectric permeability of the dielectric between inner and outer conductors, [-]
u = Ur*4*pi*1e-7; % magnetic permeability of the dielectric, [H/m]
sigma_feed=615e-4;%conductivity of the dielectric between inner and outer conductors, [S/m]
sigma_epoxy=1.41e-7%conductivity of epoxy resin, [S/m]
sigma_glass=1e-12%conductivity of glass glass bead, [S/m]
sigma_steel=1.45e+6;%conductance of the metal applied for inner and outer conductors (stainless steel),
[1/(Ohm*m)]
fgb_t=Vglass/Vt;
V_biol=fbiol*Vt_feed;
fbiolt=fbiol*Vt_feed/Vt
f_of_feed=1-f_epoxy-fgb_t-fbiolt
sigma_biol=615e-4;
sigma_eff = sigma_feed*f_of_feed + sigma_epoxy*f_epoxy + sigma_glass* fgb_t+sigma_biol*fbiolt;% effective
conductivity of whole system, [S/m]
check=fgb_t+f_epoxy+f_of_feed+fbiolt
Eeff=em_glass_feed*(f_feed_t)+e_epoxy*f_epoxy% effective dielectric constant of whole system, [-]
E =Eeff * 1/(4*pi*1e-7*c*c); % vacuum permeability [H/m]
tang_eff=0.08
C = ((2*pi*E)/log(b/a)); % capacitance of the open ended coaxial stub resonator, [F]
L = ((u/(pi*2))*log(b/a));% inductance of the open ended coaxial stub resonator, [H]
%Define the input voltage supplied by the function generator, [V]
f=220E+06:10000:320E+06;
vin=600e-3; %input voltage supplied by the function generator, [V]
omega = 2*pi*f;% angular frequency, [rad/s]
Eim=((omega.*E.*tang_eff)-sigma_eff)/omega;%imaginary part of complex dielctric permittivity
skin_depth=sqrt(2./(omega.*u.*sigma_steel));%skin_depth
Rs=1./(sigma_steel.*skin_depth);% surface resistivity of the inner and outer conductor of the resonator
R=(Rs/(2*pi)*(1/(0.5*a)+1/(0.5*b)));% distributed element resistance R of the resonator [Ohm/m]
G=(omega.*Eim+sigma_eff)/(omega.*E).*omega.*C;%distributed element conductance of the resonator
[F/(m*s)]
gamma =(sqrt((R+1i.*omega.*L)*(G+1i.*omega.*C)));%complex propagation constant [1/m]

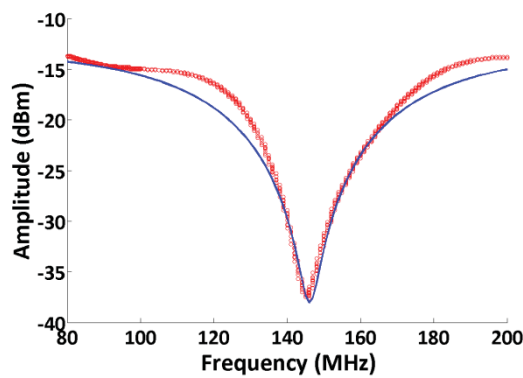
```

```
%notes on gamma: Re(gamma)=alfa = attenuation constant representing losses [Np/m];
Im(gamma)=beta=phase of the propagation constant [rad/m]
%since the signal is oscillating in time with omega rad/s, the propagation velocity of the wave [m/s] =
omega/beta; also, beta = 2*pi/wavelength.
Zc=sqrt(((R+1i.*omega.*L)/(G+1i.*omega.*C)));% complex characteristic impedance of the resonator [Ohm]
Zin=Zc.*coth(gamma.*len);%complex input impedance of the resonator [Ohm]
vout=sqrt((real(Zin.*(vin./(50+2*Zin))))).^2+(imag(Zin.*(vin./(50+2*Zin))))).^2;%modulus of vout, the is the
recorded voltage by the spectrum analyzer [V]
vout =20.*log10(vout)+13;%vout as a power ratio in dBm i.e., the measured power referenced to one mWatt
and the underlying assumption of a 50 Ohm load resistance
hold on
set(0,'DefaultFontSize',36,'DefaultFontName','Times New Roman', 'DefaultFontWeight', 'bold');
%- See the Supplementary Information
load day_two.txt % load the file
MHz=day_two(:,1); % Load experimental data; frequency
CH1=day_two(:,2); % Load experimental data; amplitude
frequency=MHz;
amplitude=CH1;
plot(frequency,amplitude,'LineStyle','none','Marker','*','MarkerEdgeColor','g', 'MarkerSize',10)
hold on
plot(f/1e+6,vout, 'b', 'LineStyle','--','LineWidth',3);
xlabel('Frequency, (MHz)','fontsize',42,'fontweight','b');
ylabel('Amplitude, (dBm)','fontsize',42,'fontweight','b');
hold on
```

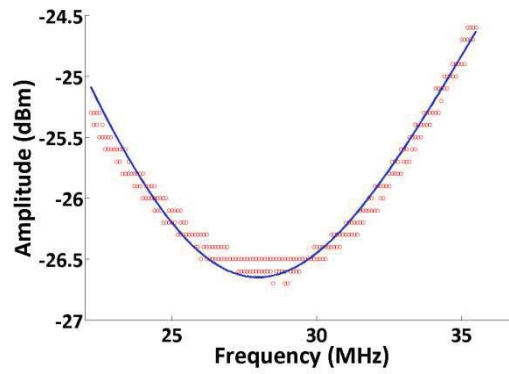
The output parameters of the simulation	Value
$\tan\delta_{eff}$	0.03
ϵ_{epoxy}	3.98

Fig. A.1. Experimentally obtained amplitude versus frequency plot of empty resonator with the layer of epoxy resin on the bottom (red) using a quarter wave length open-ended coaxial resonator. Fitting data are shown for comparison (blue).



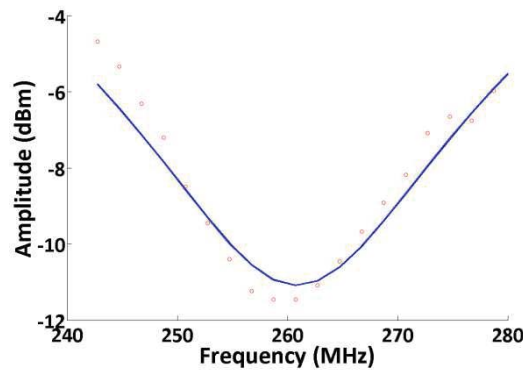
The output parameters of the simulation	Value
$\tan\delta_{eff}$	0.02
ϵ_{gb}	6.0

Fig. A.2. Experimentally obtained amplitude versus frequency plot of filled with glass beads resonator with the layer of epoxy resin on the bottom (red) and glass beads using a quarter wave length open-ended coaxial resonator. Fitting data are shown for comparison (blue).



The output parameters of the simulation	Value
$\tan\delta_{eff}$	0.75
ϵ_m	75.4

Fig. A.3. Experimentally obtained amplitude versus frequency plot of filled with feed substrate resonator with the layer of epoxy resin on the bottom (red) and feed substrate using a quarter wave length open-ended coaxial resonator. Fitting data are shown for comparison (blue).



The output parameters of the simulation	Value
$\tan\delta_{eff}$	0.08
ϵ_{gb} Lichtenecker's logarithmic law	3.5
ϵ_{gb} parallel capacitance	5

Fig. A.4. Experimentally obtained amplitude versus frequency plot of filled with glass beads resonator with the layer of epoxy resin on the bottom (red), feed substrate and glass beads using a quarter wave length open-ended coaxial resonator. Fitting data are shown for comparison (blue).

Appendix B

Taking into account the presumptions made in section 6.2. The assumption that volume fraction of biofilm in the system can be calculated based on the values of total organic carbon (TOC) was made to simulate the behavior of the coaxial stub resonator.

The procedure to find the volume fraction of biofilm includes following steps:

1. The TOC form the laboratory will be named TOC_{lab} in [mg/ml].
2. Since, glass beads were immersed in 100 ml of PBS, the mass of TOC, further TOC_m in [kg]:

$$TOC_m = \frac{TOC_{lab} \cdot Volume_of_PBS}{1 \cdot 10^6} \quad (B.1)$$

3. Using Eq. (10) the factor to converting the TOC_m to total organic biomass TOB in [kg] was calculated as 2.25:

$$TOB = 2.25 \cdot TOC_m \quad (B.2)$$

4. For the limiting cases that the mass fraction of total organic biomass in the biofilm f_{mass} are assumed to amount 2% and 10% respectively, this means that the total mass of the biofilm TOB , total can be calculated as:

$$TOB_{total} = TOB_m / f_{mass} \quad (B.3)$$

5. Assuming the density of biofouling $\rho_{biofouling}$ is 1000 kg/m³ the volume of total biomass $V_{biomass}$ in [m³] by A.4:

$$V_{biomass} = \frac{TOB_{total}}{\rho_{biofouling}} \quad (B.4)$$

6. So, the volume fraction of biomass φ_l is expressed by following equation:

$$\varphi_l = \frac{V_{biomass}}{V_{resonator} - V_{epoxy}} \quad (B.5)$$

It is noted that in our estimate of the biofilm volume, we neglected the decreasing dry mass of salts in the system with time. This decrease is caused the fact that bacteria contain inorganic salts whereas the EPS hardly contains any inorganic material. As a result the overall mass fraction of salts in the biofilm decreases as a function of time due to the increasing EPS volume fraction as compared to bacteria. It is also should mentioned that despite fact that the value of 1000 kg/m³ $\rho_{biofouling}$ were taken for the simulation in reality this number can be higher depending on EPS content and amount up to 1300 kg/m³ [57].

Appendix C

Cost-reducing suggestions for design and operation

As a receiver, a simple rectifier can be used and the rectified signal can be fed into a 10 bit ADC of the same microcontroller. The software in the microcontroller realizes in such case the following steps in an endless loop:

- 1) program the frequency generator to produce a signal with frequency f ;
- 2) read the amplitude of the rectified signal on the ADC input of the microcontroller;
- 3) write the amplitude and frequency to a data logger using a RS232 protocol;
- 4) increase the frequency f with a small step Δf ;
- 5) repeat steps 1 to 4 until the desired AF plot is obtained.

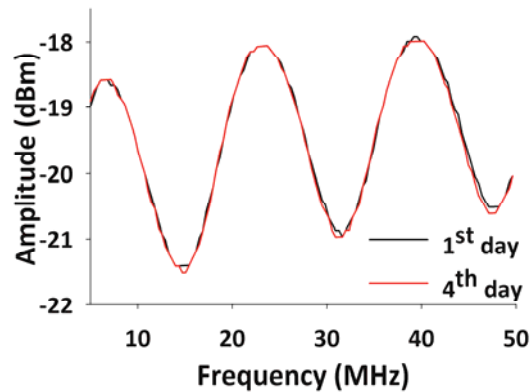
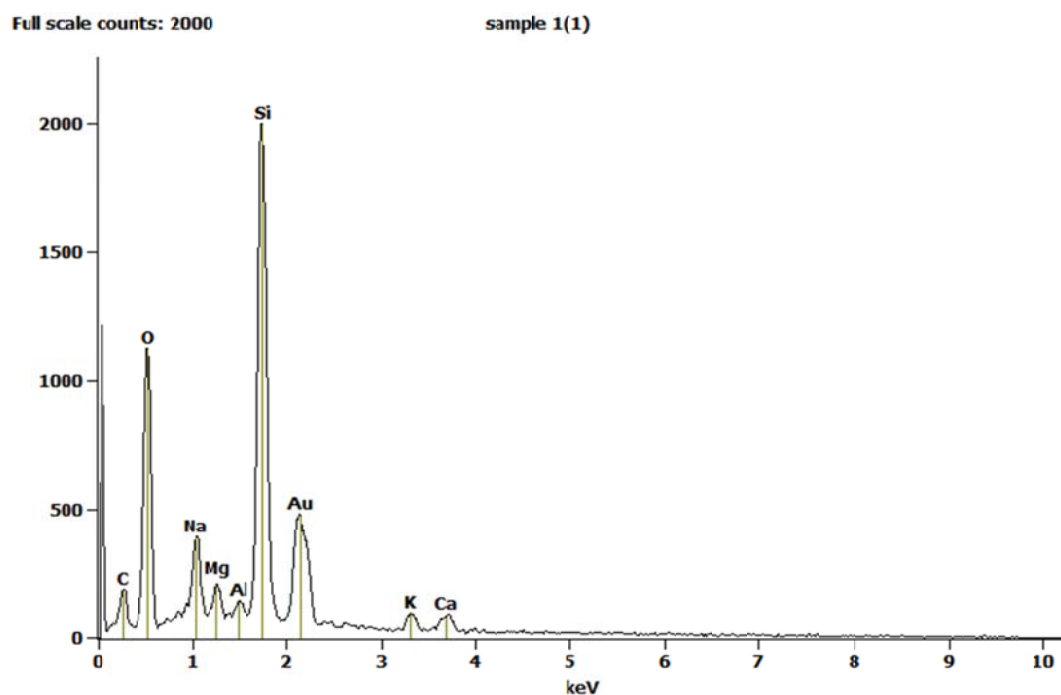


Fig. C.1. AF plots in the presence of biofilm on the surface of inner conductor during 4 days of operation using tap water from laboratory of WETSUS in frequency range of 5-50 MHz. The temperature t and conductivity σ of used water were controlled and constant 22 °C and $550 \cdot 10^{-4} [\text{S} \cdot \text{m}^{-1}]$, respectively.

Appendix D

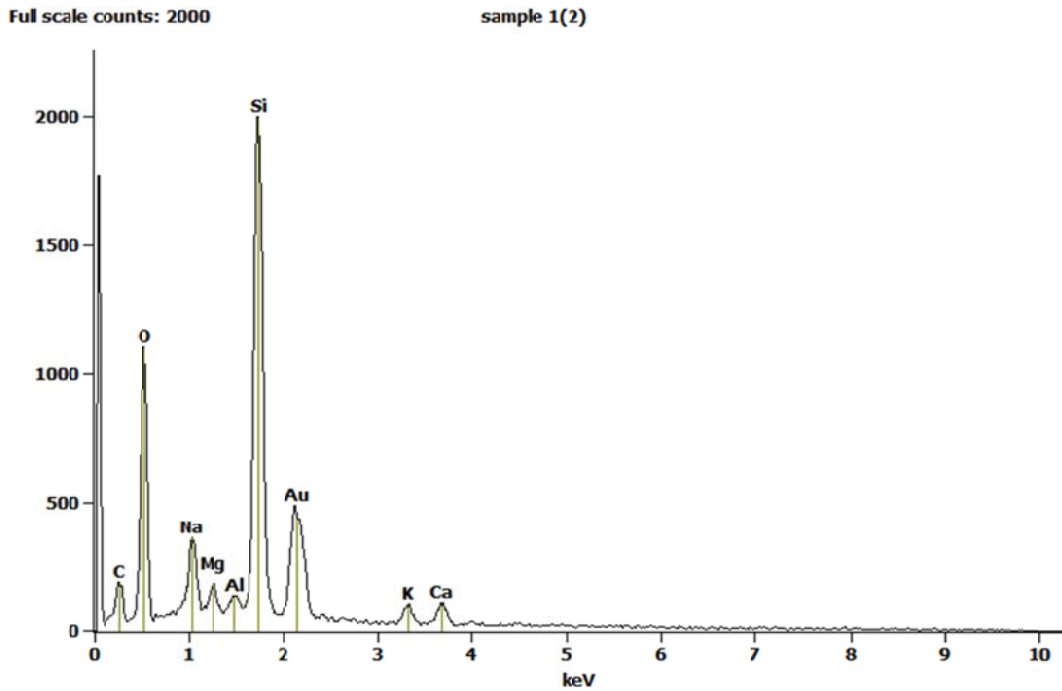
Results of energy Dispersive X-ray (EDX) spectroscopy

Sample1 was a clean glass bead and sample 2 was glass bead with adsorbed layer of AgCl.



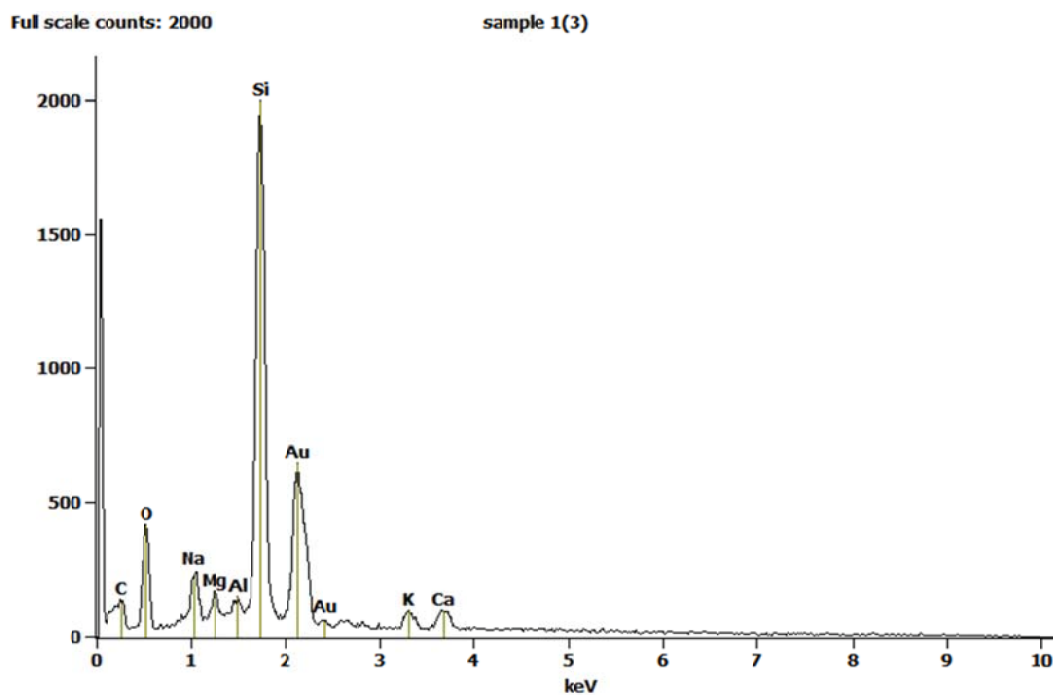
Quantitative Results for: sample 1(1)

Element Line	Net Counts	Z	A	F	Weight %	Atom %
C K	1184	0.838	3.736	1.000	6.04	11.17
O K	7810	0.892	2.130	1.000	46.94	65.14
Na K	2510	0.990	1.588	0.998	3.17	3.06
Mg K	936	0.973	1.366	0.997	1.00	0.91
Al K	478	1.010	1.221	0.993	0.47	0.39
Si K	18819	0.988	1.133	0.996	18.75	14.82
K K	743	1.062	1.071	0.998	1.68	0.96
Ca K	906	1.043	1.054	1.000	2.44	1.35
Au M	7501	1.554	0.994	1.000	19.49	2.20
Total					100.00	100.00



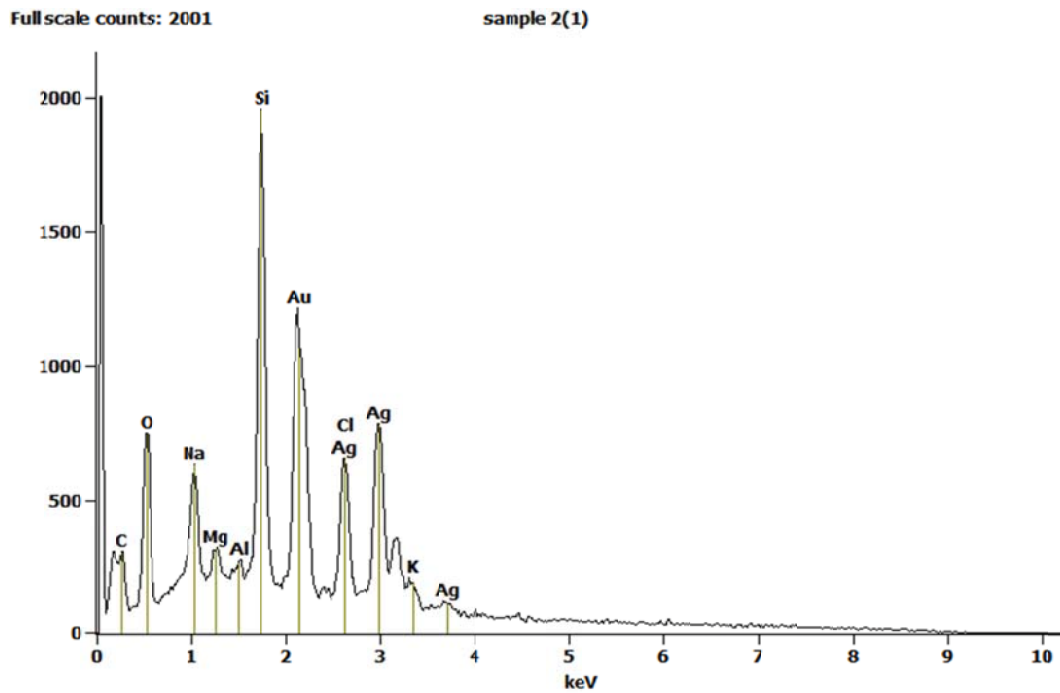
Quantitative Results for: sample 1(2)

Element Line	Net Counts	Z	A	F	Weight %	Atom %
C K	1174	0.834	3.825	1.000	6.47	12.15
O K	6840	0.888	2.191	1.000	44.63	62.88
Na K	2304	0.985	1.581	0.998	3.06	3.00
Mg K	855	0.969	1.361	0.997	0.96	0.89
Al K	535	1.006	1.218	0.993	0.56	0.46
Si K	18792	0.983	1.132	0.996	19.73	15.84
K K	710	1.057	1.073	0.998	1.70	0.98
Ca K	924	1.038	1.056	1.000	2.63	1.48
Au M	7363	1.547	0.997	1.000	20.25	2.32
Total					100.00	100.00



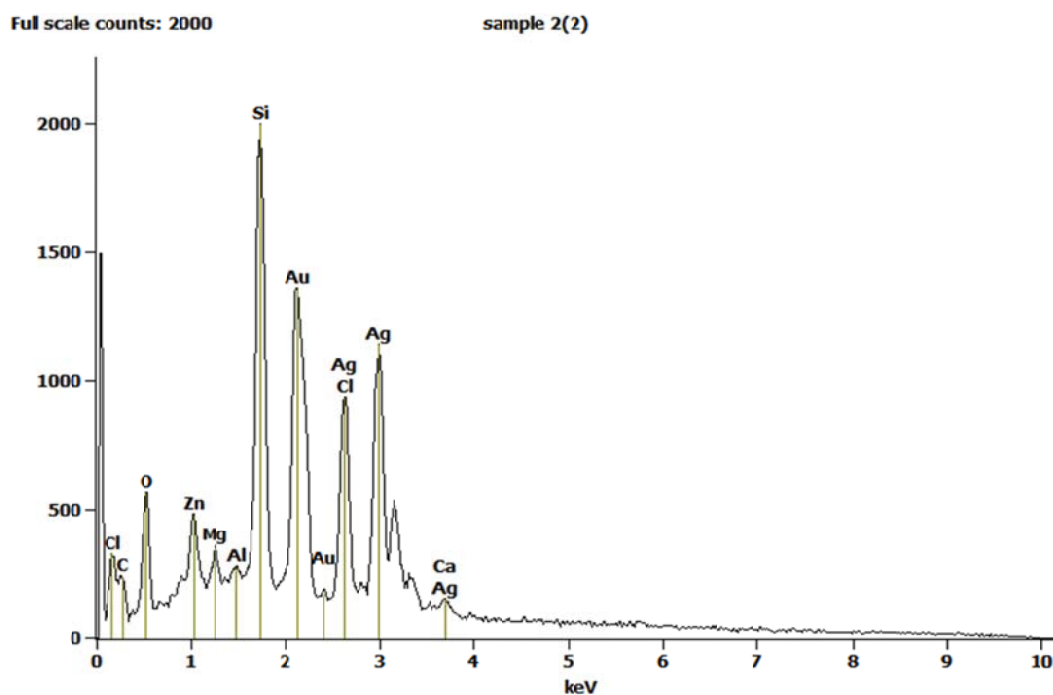
Quantitative Results for: sample 1(3)

Element Line	Net Counts	Z	A	F	Weight %	Atom %
C K	703	0.786	4.348	1.000	5.60	13.05
O K	2811	0.837	2.646	1.000	28.20	49.30
Na K	1315	0.929	1.568	0.998	2.20	2.68
Mg K	680	0.913	1.354	0.996	0.97	1.11
Al K	446	0.947	1.220	0.991	0.59	0.61
Si K	18190	0.925	1.137	0.995	24.34	24.23
K K	867	0.987	1.109	0.998	2.71	1.94
Ca K	1008	0.968	1.085	1.000	3.71	2.59
Au M	8895	1.454	1.018	0.999	31.68	4.50
Total					100.00	100.00



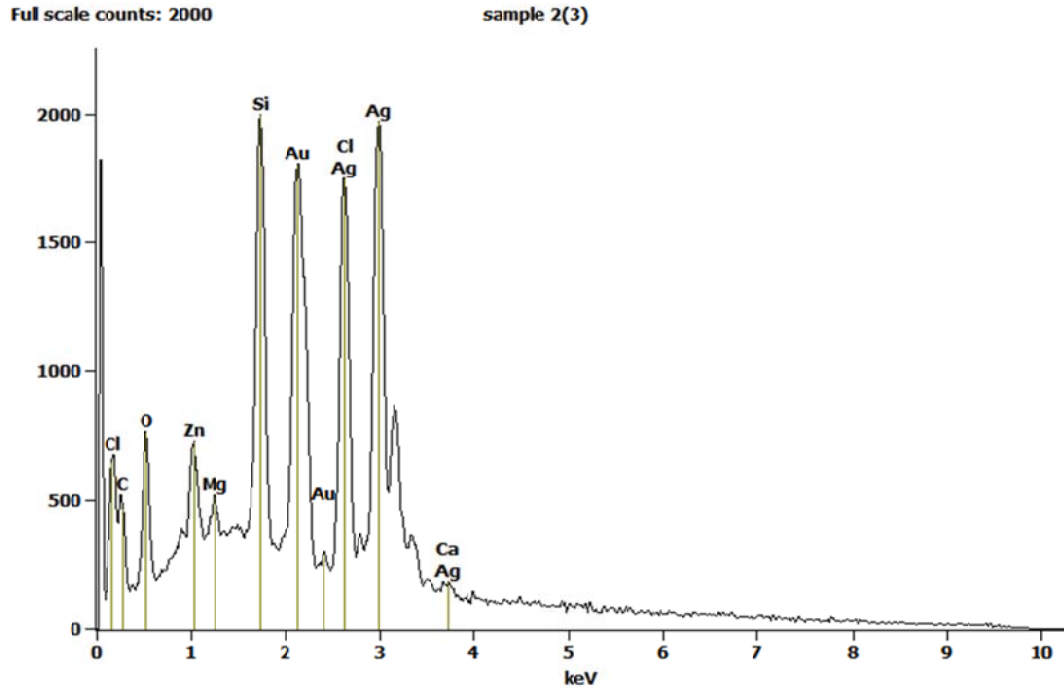
Quantitative Results for: sample 2(1)

Element Line	Net Counts	Z	A	F	Weight %	Atom %
C K	0	0.708	4.063	1.000	0.00	0.00
O K	5090	0.780	3.198	1.000	26.39	60.28
Na K	3271	0.865	1.799	0.999	2.69	4.28
Mg K	863	0.850	1.508	0.997	0.58	0.88
Al K	353	0.881	1.316	0.995	0.22	0.29
Si K	16526	0.861	1.198	0.994	9.94	12.93
Cl K	5838	0.916	1.152	0.991	5.76	5.93
K K	1133	0.915	1.100	1.000	1.49	1.40
Ag L	13505	1.182	1.071	1.000	27.32	9.25
Au M	17245	1.353	0.998	0.996	25.61	4.75
Total					100.00	100.00



Quantitative Results for: sample 2(2)

Element Line	Net Counts	Z	A	F	Weight %	Atom %
C K	0	0.686	4.153	1.000	0.00	0.00
O K	3577	0.751	3.558	1.000	18.33	50.92
Mg K	987	0.818	1.547	0.997	0.61	1.11
Al K	352	0.848	1.343	0.995	0.19	0.32
Si K	17242	0.828	1.218	0.993	9.35	14.80
Cl K	8735	0.880	1.158	0.990	7.67	9.62
Ca K	902	0.859	1.138	1.000	1.31	1.45
Zn L	2359	1.011	1.647	0.999	3.08	2.09
Ag L	18553	1.135	1.080	1.000	33.52	13.82
Au M	19515	1.301	1.006	0.995	25.93	5.85
Total					100.00	100.00



Quantitative Results for: sample 2(3)

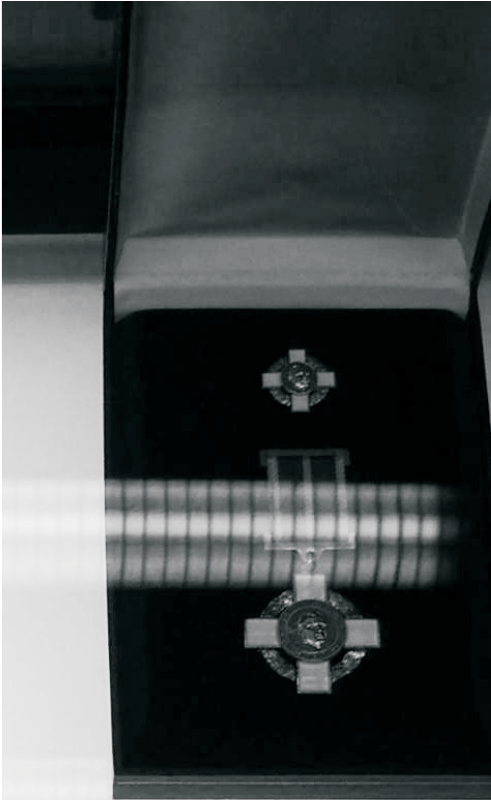
Element Line	Net Counts	Z	A	F	Weight %	Atom %
C K	0	0.676	3.938	1.000	0.00	0.00
O K	4620	0.741	3.779	1.000	16.65	49.36
Mg K	1299	0.808	1.578	0.998	0.54	1.06
Si K	15991	0.818	1.229	0.993	5.80	9.79
Cl K	17285	0.869	1.142	0.987	9.88	13.22
Ca K	816	0.848	1.145	1.000	0.79	0.93
Zn L	3468	0.998	1.694	0.999	3.08	2.24
Ag L	34594	1.121	1.072	1.000	41.09	18.07
Au M	25383	1.284	0.999	0.994	22.16	5.34
Total					100.00	100.00



zachstaans kostuum van André
reeg bij de landing na zijn eerste



Space Expo, Noorwijk, RME 2013



Chapter 7

A Coaxial Stub Resonator-Based Sensor for the On-line Monitoring of the Loading of Ion Exchange Resins



Abstract

In this study, we demonstrate the proof-of-principle of a new type of sensor to monitor the loading of ion exchange resins (IER). The sensing device outlined here is based on the operating principle of a quarter wave length open-ended stub resonator with an IER present between its inner and outer conductor. Loading of the IER by binding of the substrate of interest affects both the real and imaginary parts of the complex dielectric permittivity of both the IER and the fluid under investigation. As a result, the recorded amplitude-frequency (AF) plot shows a shift of the resonance frequency and/or a change of shape of the resonance peak(s). Two types of stub resonator designs were explored, either with a straight (classical) or a helically-shaped inner conductor. Because of the different electrical length of the inner conductor, the two types of resonator operate in different frequency ranges, which, in turn has implications for the sensitivity of the sensor. Irrespective the design, the method outlined here offers an equipment-undemanding, low maintenance and cost-efficient in-line early warning system to monitor the load of IERs. Experimental evidence is provided showing that measuring the load degree of an anion exchange resin (AER) with humic acid (HA) is technically feasible, opening possibilities to assess the HA load of the AER continuously and before significant breakthrough is detected in the effluent. Hence, the proposed method provides an efficient tool to optimize the regeneration cycles of AER columns. Apart from experimental data, the AF response of the sensor was simulated showing that the HA load and regeneration of the AER can be described in terms of the real part of its dielectric permittivity and its loss tangent up to HA load degrees of about 1 gram HA per liter of AER. At higher load degrees, a different AF response was observed and at the same time, regeneration of the AER was strongly inhibited indicating that the proposed method may be an efficient tool as an early warning system or to study the behavior of composite dielectrics immersed in water.

This chapter is based on the article submitted as:

N.A. Hoog, M.J.J. Mayer, H. Miedema, S. M. Bakker, W. Olthuis, T. Hubert, A. van den Berg: *A Coaxial Stub Resonator-Based Sensor for the On-line Monitoring of the Loading of Ion Exchange Resins*, Sensing and Bio-Sensing Research.

7.1 Introduction

Adsorption to an ion exchange resin (IER) is a widely used technique to remove an unwanted component out of a solution. In many Northern European countries IER technology is common practice during the production of drinking water from surface water [3]. In contrast to ground water, surface water contains humic acids (HA), the main fraction of an intricate mixture of organic compounds resulting from the decomposition of dead natural organic matter (NOM). These components are present at different degrees and variations, not only giving the surface water a yellowish/brownish color but causing taste and odor problems as well. It is for these reasons that HA need to be removed.

One of the most widely used AER in the drinking water industry for HA removal is Purolite® A860S with a total organic carbon removal capacity of 3g/L. Inherently to any IER-based adsorption process is that, over time, the IER saturates and needs to be regenerated. Timing of this regeneration process is crucial. Postponing the regeneration process too much implies a compromised quality of the IER effluent and in addition may damage the resin in the sense that (most) resins can beyond a certain degree of loading no longer be regenerated completely. If the regeneration is started too early, on the other hand, precious rest capacity of the IER is wasted. This all implies the operational window of IERs to be rather narrow. Apart from these direct costs, the regeneration procedure is time consuming and labor intensive [4, 5]. There thus is a strong economically-driven incentive in the drinking water industry to have the timing of IER regeneration right [6-8]. Recently, several IER sensors have been introduced, all monitoring a different characteristic of the IER [9 - 11]. Despite the fact that the working mechanism is not always obvious [12, 13], these sensors lack a certain simplicity in construction and have not been tested under field conditions yet [14]. Moreover, they assess IER properties by chemical rather than physical methods [15], are often off-line [16 - 20] and sometimes require rather labor-intensive data analysis [17].

Dielectrometry [18-20] has shown the ability to monitor the dielectric properties of IERs by recording its complex impedance. This development implies that chemical analysis of the IER effluent is no longer necessary. Another advantage is that, in contrast to chemical analysis, dielectric monitoring can be performed continuously.

Here we introduce a sensor to assess the dielectric properties of an IER, and by that its degree of loading, based on coaxial stub resonator technology. Previously, it has been demonstrated that stub resonators can be used successfully to determine the dielectric properties of fluids, including those with lossy dielectrics [21 -25]. As will be shown here, the amplitude-frequency (AF) response of the resonator is affected by changes of the dielectric properties of the IER upon adsorption or desorption (during degeneration) of the particular compound of interest (here HA). A model description based on the dielectric properties of mixtures and composites adds to understanding the sensor response and the ability to predict IER behaviour during operation.

7.2 Sensor description

Fig. 1. shows a schematic outline and the basic elements of a sensor based on a stub resonator coaxial transmission line, discussed in detail previously in [21-25], but here filled with ion exchange resin.

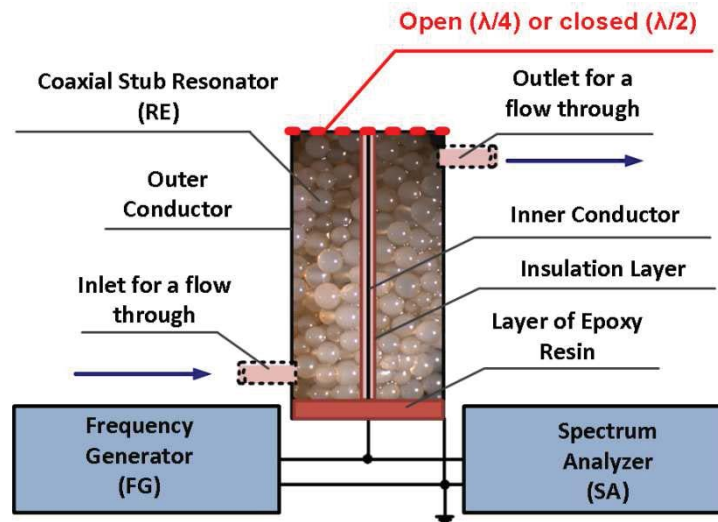


Fig. 1. Schematic outline of the coaxial stub resonator sensing system consisting of a function generator (FG), a spectrum analyzer (SA) and the coaxial stub resonator (RE). The dotted inlet and outlet indicate that the flow-through resonator can be optionally used as batch resonator.

The dielectric properties of composites

As shown in Fig. 1, the system comprises several layers of different dielectric properties. Working from the inside to the outside we distinguish the inner conductor, an isolation layer, the IER submerged in the fluid under investigation and the outer conductor. The effective dielectric permittivity ϵ_{eff} and the effective loss tangent $\tan\delta_{eff}$ of a coaxial resonator with multiple concentric layers of different dielectric permittivity has been described in [21 - 25] and is expressed by:

$$\epsilon_{eff} = f(\epsilon_{r1}, \epsilon_{r2}, \dots, \epsilon_{rn}) \quad (1)$$

$$\tan\delta_{eff} = f(\tan\delta_1, \tan\delta_2, \dots, \tan\delta_n) \quad (2)$$

In an ideal resonator, i.e., one without any losses, the resonance frequency f_{res} of an open ended ($\lambda/4$) and closed ended ($\lambda/2$) resonator are given by Eqs. 3a and 3b, respectively, directly rendering the dielectric constant ϵ_{re} [21 - 25].

$$f_{res} = \frac{2n-1}{2 \cdot \pi \cdot \sqrt{LC}} = \frac{c \cdot (2n-1)}{4l \sqrt{\epsilon_{re} \epsilon_0 \mu_{re} \mu_0}} \quad (3a)$$

$$f_{res} = \frac{n}{2 \cdot \pi \cdot \sqrt{LC}} = \frac{c \cdot n}{2l \sqrt{\epsilon_{re} \epsilon_0 \mu_{re} \mu_0}} \quad (3b)$$

where c represents the speed of light in vacuum (m/s), n the order number of f_{res} (Hz), l the length of the resonator (m), μ_r relative magnetic permeability of the dielectric between inner and outer conductors (-), μ_0 the absolute vacuum permeability (H/m), ϵ_0 the absolute vacuum permittivity (F/m) and ϵ_{re} the real part of the relative effective dielectric constant. Note that the capacitance C in Eqs. 3a and 3b is determined by the real part ϵ_{re} of ϵ_r .

For a lossy resonator, polarization and conductivity losses in the dielectric under investigation, as well as resistance losses in the inner and outer conductors, must be taken into account. A detailed model accounting for these losses, essentially based on telegrapher's equations, is explained in [25].

The IER sensor represents a lossy resonator packed with ion exchange resin of which the properties change upon adsorption or desorption (during regeneration) of humic acid (HA). In order to theoretically describe the behavior of this system, the model described in [25] has been extended with expressions for both the effective dielectric permittivity ϵ_{re} and the effective conductivity of the composite dielectric, consisting of IER, with or without HA adsorbed to it, and immersed in feed substrate.

For a lossy dielectric, the complex dielectric permittivity is given by:

$$\epsilon_r = \epsilon_{re} - j\epsilon_{im} \quad (4)$$

where ϵ_{re} and ϵ_{im} represent the real and imaginary parts of ϵ_r , respectively.

The effective loss tangent $\tan\delta_{eff}$ (-), which is a measure for the dielectric losses in the system, is expressed by Eq. 5:

$$\tan\delta_{eff} = \frac{\omega\varepsilon_{im} + \sigma_{eff}}{\omega\varepsilon_{re}} \quad (5)$$

where ε_{im} and σ_{eff} reflect the polarization losses and the conductivity losses in the dielectric, respectively, and $\omega=2\pi f$ the angular frequency, in rad/s.

The presence of IER (including the counter charge attached to it) and (but to a lesser extent) the amount of free HA and other ions in solution substantially increase the conductivity of the system causing dispersion of the signal. The insulation around the inner conductor serves to limit this dispersion effect. The effective conductivity σ_{eff} of the composite dielectric between inner and outer conductors is a parameter hard to assess since it is not possible to discriminate between signal changes due to polarization losses and signal changes due to conductivity losses [32]. The difficulty is related to the aforementioned high fluid conductivity as well as several different processes that may occur in the resin phase: ion exchange, interactions other than ion exchange, (de)protonation of functional groups, IER (de)swelling and diffusive processes. All these processes may affect the conductivity and polarization losses of the system. However, because it remains unknown to what extent these processes actually occur, σ_{eff} was lumped into $\tan\delta_{eff}$ (see Eq. 5), which, in turn, represents a fitting parameter in the model used. It is noted that lumping of σ_{eff} into $\tan\delta_{eff}$ is common practice [26].

The real part of ε_r and $\tan\delta_{eff}$ can also be expressed in terms of the capacitance and tangent loss of the individual system elements:

$$\varepsilon_{re} = C_{eff} / C_{vacuum} \quad (6)$$

where C_{vacuum} is the capacitance of the resonator with vacuum between both conductors.

According to [27], the effective capacitance C_{eff} of a coaxial capacitor with a two-layer dielectric is given by Eqs. 7 and 8:

$$C_{eff} = \left[\frac{1}{C_1} + \frac{1}{C_2} \right]^{-1} \quad (7)$$

where C_1 and C_2 are the capacitances related to the insulation layer and the fluid, respectively, each given by:

$$C_1 = \frac{2\pi\epsilon_0\epsilon_1}{\ln(r_1/r_0)} \text{ and } C_2 = \frac{2\pi\epsilon_0\epsilon_2}{\ln(r_2/r_1)} \quad (8)$$

where

ϵ_1 , real part of dielectric permittivity of the insulation layer (-);

ϵ_2 , real part of the effective dielectric permittivity of the fluid (-);

r_0 , radius of the inner conductor of the resonator (m);

r_1 , radius of the insulation layer (m);

r_2 , inner radius of the outer conductor (m).

Taking into account Eqs. 6 - 8, ϵ_{eff} of a cylindrical capacitor with dielectrics ϵ_1 and ϵ_2 in radial direction can be expressed by [27]:

$$\epsilon_{eff} = \frac{\epsilon_1\epsilon_2\ln\left(\frac{r_2}{r_0}\right)}{\epsilon_1\ln\left(\frac{r_2}{r_1}\right) + \epsilon_2\ln\left(\frac{r_1}{r_0}\right)} \quad (9)$$

It is noted that until now we assumed that the second dielectric, with real part of dielectric permittivity ϵ_2 , is a fluid. In reality, the resonator is packed with IER particles immersed in the fluid pumped through the resonator under plug flow regime. This means that, in our IER process, ϵ_2 represents the real part of the effective dielectric permittivity of the packed bed with IER particles immersed in the fluid. It is noted that, theoretically, it is possible to express ϵ_2 in terms of the volume fraction of IER, φ_{IER} , ϵ_{IER} , the volume fraction of fluid φ_{fluid} and ϵ_{fluid} . However, as also noted in the discussion on Eq. 5, the system of IER immersed in the fluid that is being purified is rather complex. In addition, in a flow-through

resonator, both the fluid composition and the composition of the IER are functions of the length coordinate of the resonator, due to directionality of perfusion (from bottom to top) and the continuous removal of HA from the fluid by adsorption to the IER. In effect, the real part of the dielectric permittivity ϵ_2 becomes a function of the length coordinate of the resonator as well. In case the dependence of ϵ_2 as a function of the length coordinate of the resonator is known, theoretically, the “length averaged value” of ϵ_2 provides the effective value of ϵ_2 . This can easily be understood by deriving the expression for ϵ_{eff} for a system of two resonators in series, each filled with a different dielectric. Underlying assumption in this reasoning however, is that the change in ϵ_2 per 1 gram of adsorbed HA onto the AER at low AER load degrees is nearly equal to the change in ϵ_2 per 1 gram of adsorbed HA onto the AER at high AER load degrees. In practice the change of ϵ_2 as a function of the load degree of HA on the AER may not be linear and it may be required to also account for this non linearity. It should be noted however that too large differences in dielectric properties between these two resonators might cause the impedance difference become too large, causing reflection effects. In such case the resonator would not work properly anymore.

It is important to realize that the effective value of ϵ_2 is determined by the length averaged value of ϵ_2 (l) since it means that the shifts in AF response are expected to depend on the amount of adsorbed HA only and not on the distribution of the adsorbed HA over the length coordinate of the resonator. This brings along the advantage that the sensitivity of this stub resonator does not depend on the load degree of the IER column. On the other hand, it should be realized that the developed method will not detect malfunction of the IER column due to for example a too short residence time of the fluid in the column. In such case, the sensor signal would indicate that the column is still only partly loaded with HA and yet there would be HA in the effluent because of a too short adsorption time.

With the aforementioned assumptions, Eqs. 3-9 give a full description of the behavior of the coaxial stub resonator.

Using the model, the dielectric properties of the composite dielectric mixture between inner and outer conductors of the resonator in terms of ϵ_r and $\tan\delta_{eff}$ can be determined from experimentally determined AF plots. This procedure was applied in this study to quantify the loading (and regeneration) capacity of the IER column used in terms of ϵ_{eff} and $\tan\delta_{eff}$ (see also “**Supplementary Information**”).

We investigated two different types of resonators with slightly different design as for their inner conductor, either straight or helically-shaped. The rationale of the latter design is its longer inner conductor, i.e., it behaves as a resonator with a straight inner conductor of the same length as its helical counterpart [28]. The advantage of the helical type is that it shows more resonances in the same frequency range, implying larger f_{res} differences at the highest resonances in that particular frequency range.

7.3 Material and Methods

Experimental setup

Fig. 2 shows the experimental set-up, including two resonators (1, 2) with either a straight inner conductor (4a) or helical type of inner conductor (4b). Apart from the different type of inner conductor, the system comprises two identical flow-through systems, each of them equipped with a peristaltic pump (Masterflex), a vessel of 120 L and a pump generating a flow rate of $3 \text{ ml}\cdot\text{min}^{-1}$. The experiments to load the IER in Fig. 2 with HA typically lasted about 144 hours. During the experiments, the temperature and conductivity fluctuations of the feed solution and effluent were measured to amount less than $2 \text{ }^\circ\text{C}$ and $200 \text{ }\mu\text{S}/\text{cm}$, respectively. Further, it was shown that these temperature and conductivity fluctuations did not significantly influence the AF plots shown in this study (see also Appendix A).

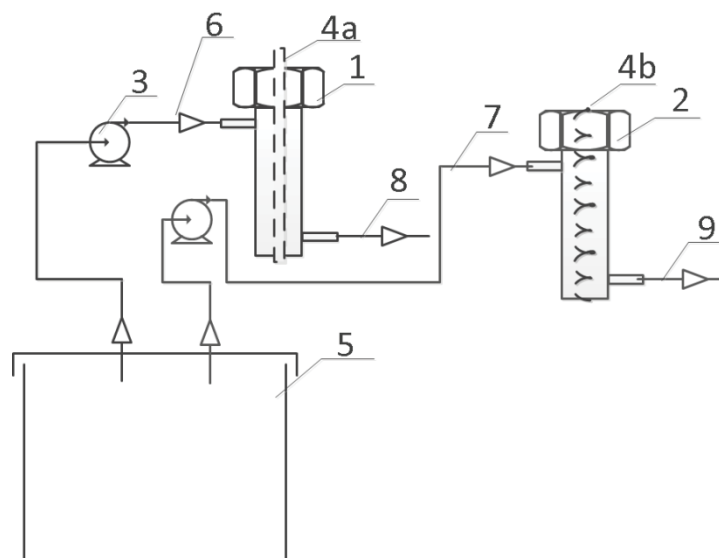


Fig. 2. Schematic view of the experimental set-up consisting of a coaxial resonator (1) with straight inner conductor (4a), coaxial resonator (2) with helical inner conductor (4b), pump (3), storage tank for tap water (5), inlet hoses (6,7) and outlet hoses for waste (8,9).

Quarter-wave open-ended coaxial stub resonator with straight and helical inner conductors

Table 1 and Table 2 give an overview of the dimensions of the quarter-wave coaxial stub resonators applied in this study, see also Fig. 1 and Fig. 2.

Table 1

Geometric parameters of the flow-through resonator with a straight inner conductor. The outer and the inner conductors of the resonator were made from stainless steel 316L and copper, respectively.

Parameter	Flow-through Resonator
Length, l	$29 \cdot 10^{-1}$ [m]
Inner conductor diameter, d	$4 \cdot 10^{-3}$ [m]
Outer diameter of inner conductor including the polymer insulation material, dd	$5.5 \cdot 10^{-3}$ [m]
Inner diameter of the outer conductor, D	$25 \cdot 10^{-3}$ [m]
Diameters of the fluid inlet and outlet	$27 \cdot 10^{-3}$ [m]
Conductivity of stainless steel 316L, σ	$1.45 \cdot 10^6$ [$S \cdot m^{-1}$]
Conductivity of copper, σ	$5.96 \cdot 10^7$ [$S \cdot m^{-1}$]

Table 2

Geometric parameters of the flow-through resonator with a helical inner conductor. The outer and the inner conductors of the resonator were made from stainless steel 316L and copper, respectively.

Parameter	Flow-through Resonator
Length of the outer conductor, l_{out}	$29 \cdot 10^{-1}$ [m]
Length of the inner conductor, l_{inner}	$9 \cdot 10^{-1}$ [m]
Inner conductor diameter, d	$1 \cdot 10^{-3}$ [m]
Outer diameter of inner conductor including the polymer insulation material, dd	$1.5 \cdot 10^{-3}$ [m]
Inner diameter of the outer conductor, D	$25 \cdot 10^{-3}$ [m]
Diameters of the fluid inlet and outlet	$27 \cdot 10^{-3}$ [m]
Conductivity of stainless steel 316L, σ	$1.45 \cdot 10^6$ [$S \cdot m^{-1}$]
Conductivity of copper, σ	$5.96 \cdot 10^7$ [$S \cdot m^{-1}$]

In order to control variations in the resonance frequency and the shape of the response signal, a HAMEG HMS3010 3 GHz Spectrum Analyzer with Tracking Generator was used. It should be mentioned that the output voltages of the three Spectrum Analyzers of this type used in this study appeared to be different. This was taken into account in the model simulations see also the MATLAB codes in the Appendix C.

The interconnecting transmission lines used all had characteristic impedance Z_0 of 50 Ohm. The transmission lines were connected to the resonator by using SMA (SubMiniature version A) connectors, all with a total length of 20 mm.

To prevent corrosion of the SMA connectors the sensors were filled with a 1-1.5 cm layer of epoxy resin at the bottom of the sensor, thereby fully immersing the SMA connectors in the resin. The real part of dielectric permittivity ϵ_{re} of epoxy resin is 3-6 [38]. The influence of the epoxy resin layer on the model simulations was taken into account in the model simulations, see also the MATLAB codes in the Appendix C.

Analytical procedures

An overview of the measured water parameters as well as the equipment used is given in Appendix B. Samples were collected in 300 ml amber glass vials with screw cap. Ultraviolet Absorbance (UV₄₅₅) absorbance was measured at 455 nm using 5 cm quartz cells.

To avoid interference due to turbidity, prior to the measurements, samples for DOC, humic acid-C and humic acid-N were filtered through pre-washed 0.45 μm membrane filters (Whatman). Milli-Q filtered water served as background correction for the spectrophotometer.

Anion exchange resin (AER)

The anion exchange resin used in this study is Purolite® A860S (Brenntag NV, Belgium), a commonly used resin by the drinking water industry to remove HA. The specifications of Purolite® A860S are listed in the Appendix B [33, 34].

In order to ensure a certain consistency and repeatability of experimental results, we followed the pre-treatment protocol for AER as described in [33]. In short, AER was regenerated with 5 bed volumes (BV) of washing solution containing 10% (w/v) NaCl solution and 2% (w/v) NaOH. The washing solution passed the AER at a rate of 0.5 BV/hr for >3 hrs. The resin was subjected to two of such regeneration cycles and subsequently washed with demi-water until the pH of the washing solution was < 11.

Feed solution of HA in tap water

A synthetic HA solution (Sigma-Aldrich Chemie GmbH, 53680 Humic acid,)) containing 10 mg HA per 1 L of tap water, was used as experimental feed solution. The choice of taking a solution of HA in tap water as a feed stream for the feasibility tests was based on the practical relevance of removing HA from tap water and to investigate the influence of replacing chloride ions in the anion exchange resin (AER) with large organic molecules on the dielectric properties of the AER.

The properties of the feed solution are summarized in Table 3.

Table 3

Characteristics of the experimental feed solution obtained by dissolving 10 mg HA per liter tap water.

No	Characteristics	Values
1.	Temperature, T ($^{\circ}\text{C}$)	18.2
2.	pH, (-)	8.02
3.	Conductivity, ($\mu\text{S}/\text{cm}$)	497
4.	UV ₄₅₅ , (-)	0.029
5.	TOC, (mg/L)	3.63
6.	DOC, (ppb)	4730
7.	IC, (mg/L)	50.3
8.	Humus acids-C, (ppb)	3450

Since HA are a complex mixture of organic components [29], all having different affinity to the AER, the HA in the feed solution and the effluent were characterized by measuring parameters 4-8 in Table 3. For the same reason, the total amount of absorbed HA per volume unit of AER [g/l] was not related to one of these individual parameters 4-8 but calculated directly from the concentration of solid HA dissolved in the feed solution, the flow rate of feed solution through the resonator filled with AER and the total filtration time, assuming a time scale of adsorption short enough compared to the residence time of HA in the resonator. As a double check, the parameters 4-8 in Table 3 were also determined in the effluent of the resonator packed with AER. Comparing both methods justified indeed the assumption that during the experimental conditions applied by far most of the perfused HA is adsorbed by the AER.

7.4 Results and Discussion

Effect of adsorption

Examples of the effect of HA adsorption by the AER on the AF response are shown in Fig. 3 and 4, for a resonator with straight and helical inner conductor, respectively. As shown, a higher load, i.e., more HA adsorbed, causes two effects on the AF-response. Firstly, f_{res} shifts to the right, i.e., to higher frequencies and secondly, the entire curve shifts in upward direction, indicating enhanced dielectric losses.

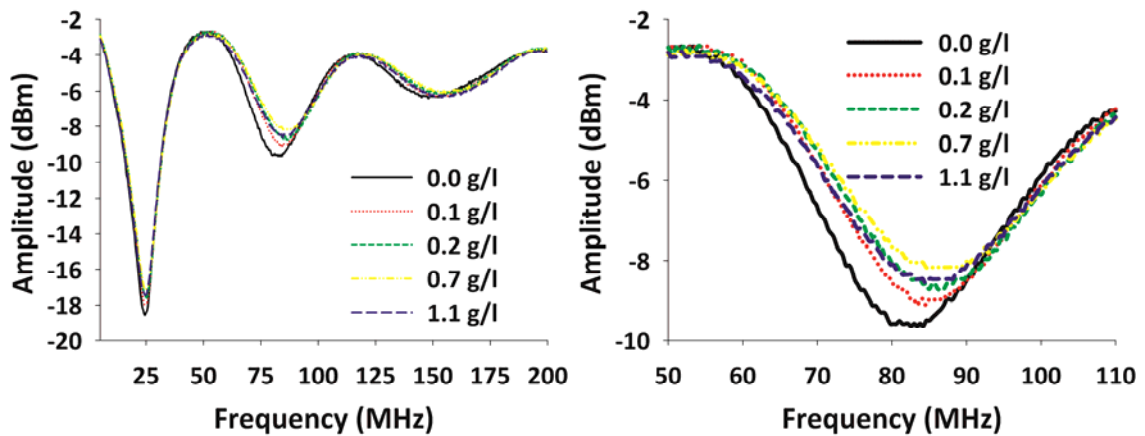


Fig. 3. On the left, AF plots in the 1-200 MHz range in response to HA adsorption by AER using a resonator with straight inner conductor. The right panel shows the 2nd resonance in more detail.

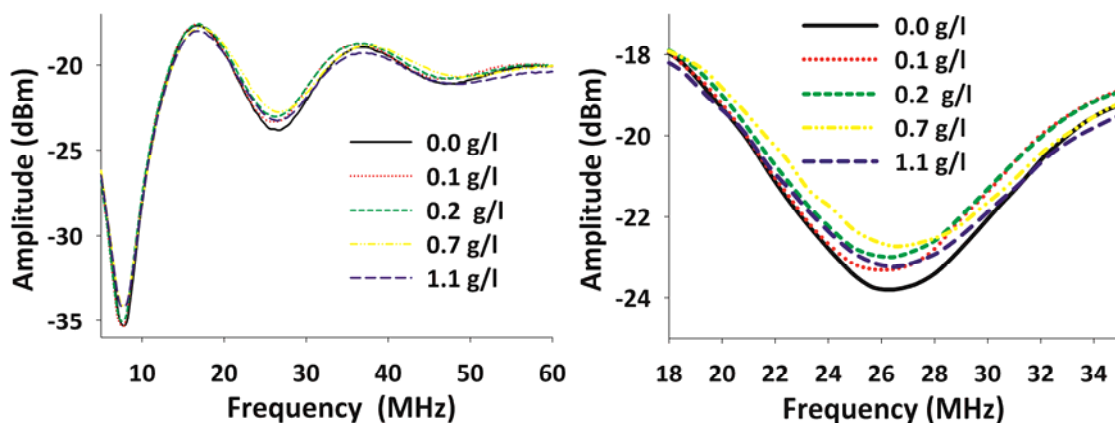


Fig. 4. On the left, AF plots in the 1-200 MHz range in response to HA adsorption by AER using a resonator with helically-shaped inner conductor. The right panel shows the 2nd resonance in more detail.

Fig. 5 delineates the changes of resonant frequency (top) and amplitude ratio (bottom) separately for the first (left) and second (right) resonances shown in Fig. 3 and Fig. 4 for both types of resonators, those with a straight inner conductor (A panels) and those with the helical one (B panels). The experiments were performed for five different HA concentrations. As can be seen, observed shifts of f_{res} as recorded by the two types of resonators were quite similar. The similarity is valid for the amplitude ratio as well (but to a slightly lesser extent). From these similarities in response changes we conclude that the mechanism responsible is the same for each resonance. An important conclusion as it declassifies other, possible interfering, processes causing similar changes. It also implies that this type of measurements can be performed in either a lower or higher frequency range, depending on the specific application. Recording at low frequency reduces the cost of the required electronics involved but this comes at the expense of sensitivity. For operation at high frequency the arguments are exactly opposite, an enhanced sensitivity but at higher cost.

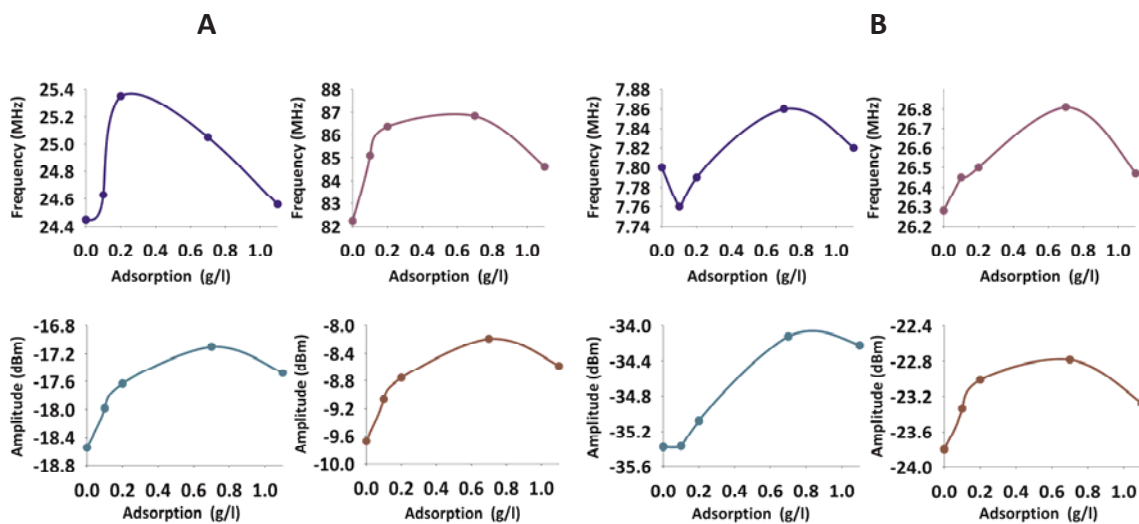


Fig. 5. Changes of resonant frequency (top row) and amplitude (bottom row) of the first (left) and second (right) resonance, in response to HA adsorption and using either a resonator with straight (A panels) or helical inner conductor (B panels).

The shift of the minimum in each resonance of the AF plots to a higher frequency in Fig. 3 and Fig. 4 points to a decrease of the real part of dielectric permittivity of the dielectric material between inner and outer conductors of the stub resonator ϵ_{eff} , see Eqs. 3a, 9. Since the insulation layer on the inner conductor does not change during the experiments, this decrease of ϵ_{eff} is caused by a decrease of the real part of the effective dielectric permittivity of the AER immersed in the solution pumped through the resonator, ϵ_2 . Apparently, the overall effect of replacing chloride ions in the AER by HA in the order of 1 g/l HA results in a lower value of ϵ_2 .

In order to gain more insight in the mechanism by which HA adsorption by AER affects the AF-response, model simulations were executed and results are summarized in Table 4. Major objective was to investigate whether the changes in the AF responses, measured during HA adsorption, can be explained by changes in the dielectric properties of the composite material in the resonator, applying the model described in [219]. Given the rather close fit between experimental and model data, notably at frequencies in the vicinity of f_{res} , we conclude that adsorption of HA does indeed affect the dielectric properties of AER. The real part ϵ_{re} of the effective dielectric constant of the AER decreases with increasing HA load whereas the dielectric loss of the AER changes with increasing HA load. This result will now be discussed in more detail. Replacing the chloride ions in the AER by the much larger HA anions will swell the AER particles. A second effect will be a net replacement of “volume elements of water” by “volume elements of HA anions” in the resonator. Since organic material has a considerably lower dielectric constant than water [28], the overall effect will be a decrease of the effective dielectric constant of the AER. However, adsorption of in the order of 1 gram HA per liter AER will only replace a very small volume fraction of water in the resonator with organic material. Assuming densities of the AER, the water and HA of around 1000 kg/m³, an AER load degree of 1 g/l would mean that order of magnitude 0.1% of the total volume in the resonator might be replaced by HA. In case replacing water by HA (anions) would be the only phenomenon affecting ϵ_{eff} during the HA adsorption process, changes in ϵ_{fluid} would be negligible [30]. However, the model simulations in Table 4 reveal a considerable decrease of ϵ_{eff} with increasing HA load of the AER. In fact changes of the real part of dielectric permittivity of the AER are even larger than the simulated changes of ϵ_{eff} in Table 4 since, besides the dielectric properties of the AER, these values also contain information on the insulation layer of the inner conductor and the water in the resonator.

Table 4

Simulation of HA adsorption by AER, using the coaxial resonator with straight and helical inner conductors. Red dots represent experimental data, solid blue line simulation data.

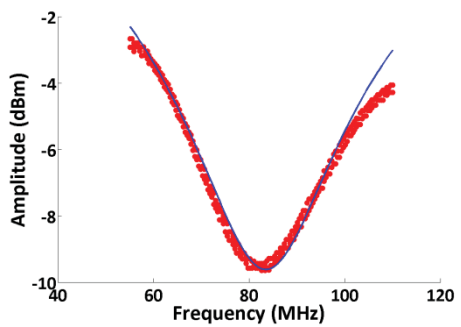
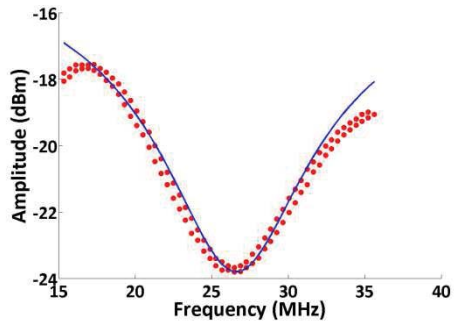
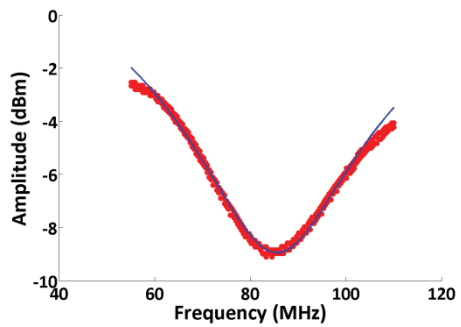
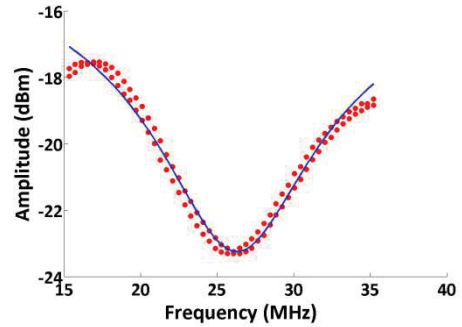
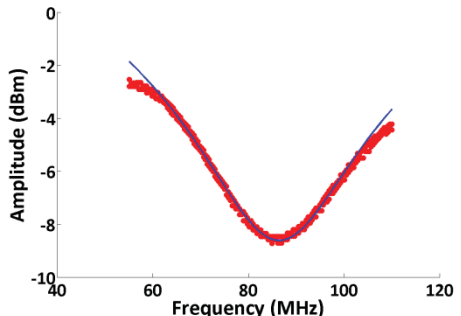
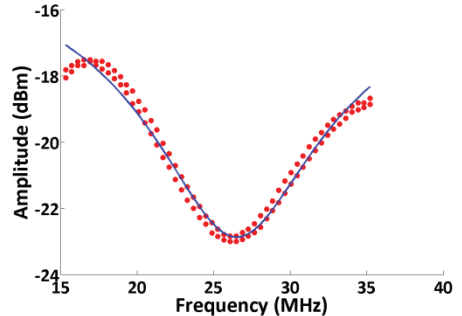
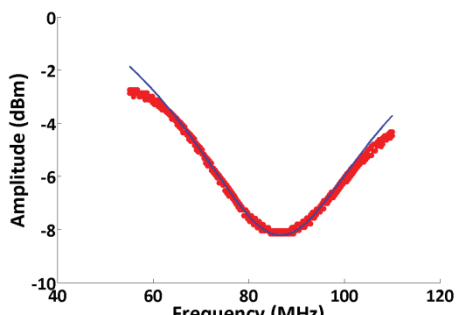
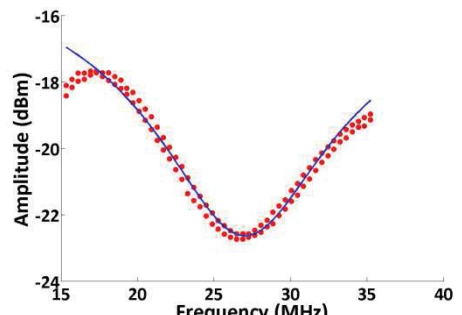
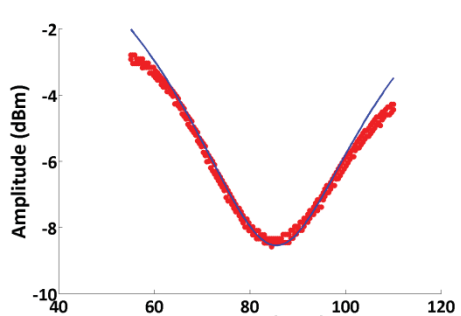
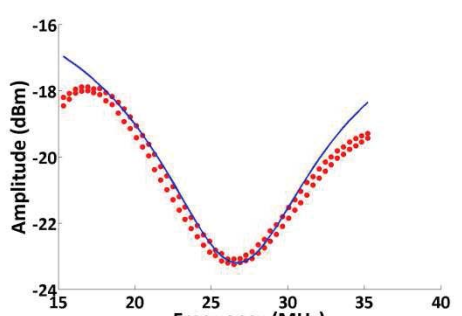
Adsorption, (g/l)	Simulated 2 nd resonance: the straight inner conductor	Simulated 2 nd resonance: the helical inner conductor		
0.0				
	$\tan\delta_{eff}, (-)$ 0.28	$\epsilon_{eff}, (-)$ 23.8	$\tan\delta_{eff}, (-)$ 0.26	$\epsilon_{eff}, (-)$ 17.9
0.1				
	$\tan\delta_{eff}, (-)$ 0.31	$\epsilon_{eff}, (-)$ 20.3	$\tan\delta_{eff}, (-)$ 0.29	$\epsilon_{eff}, (-)$ 18.2

Table 4 (continued)

Adsorption, (g/l)	Simulated 2 nd resonance: the straight inner conductor	Simulated 2 nd resonance: the helical inner conductor
0.2	 <p style="text-align: center; margin-top: 5px;"> $\tan\delta_{eff}, (-)$ $\epsilon_{eff}, (-)$ 0.32 19.1 </p>	 <p style="text-align: center; margin-top: 5px;"> $\tan\delta_{eff}, (-)$ $\epsilon_{eff}, (-)$ 0.32 17.3 </p>
0.7	 <p style="text-align: center; margin-top: 5px;"> $\tan\delta_{eff}, (-)$ $\epsilon_{eff}, (-)$ 0.35 18.4 </p>	 <p style="text-align: center; margin-top: 5px;"> $\tan\delta_{eff}, (-)$ $\epsilon_{eff}, (-)$ 0.33 16.0 </p>
1.1	 <p style="text-align: center; margin-top: 5px;"> $\tan\delta_{eff}, (-)$ $\epsilon_{eff}, (-)$ 0.33 19.9 </p>	 <p style="text-align: center; margin-top: 5px;"> $\tan\delta_{eff}, (-)$ $\epsilon_{eff}, (-)$ 0.29 17.2 </p>

It is critically noted that the minimum in the AF plot of each resonance is not exclusively determined by ϵ_{eff} but also affected to some extent by losses in the system. In other words, Eq. 3 is only valid for lossless transmission lines or distortionless transmission lines [25]. However, the simulations in Table 4, using the model outlined in the appendix, clearly reveal that measured AF plots can only be explained by a significant decrease of ϵ_{eff} with increasing AER load. Further, a close inspection of Fig. 3 and Fig. 4 and Table 4 reveals that for high AER loads i.e., going from an AER load of 0.7 g/l HA to 1.1 g/l HA, the values of ϵ_{eff} increase with increasing HA load. This observation points to a different binding mechanism of HA molecules to the AER in the load region of 0.7 g/l HA to 1.1 g/l HA as compared to 0 g/l HA to 0.7 g/l HA and will be discussed in more detail in the section on regeneration of the AER.

The experiments in Fig. 3 and Fig. 4 and the simulations in Table 4 also show that the dielectric losses in the AER increase with increasing AER load until HA load degrees of about 0.7 g/l and decrease with increasing AER load in the HA load region between 0.7 g/l and 1 g/l. The dielectric losses in the AER consist of conductivity losses and polarization losses, see Eq. 5. By insulating the inner conductor of the resonator, the effects of conductivity losses in the composite dielectric on the AF plots are suppressed. To some extent, introduction of the dielectric for insulating the inner conductor, will also suppress the effect of polarization losses in the composite mixture of AER and fluid on the AF plots since in such case the dielectric properties are not anymore exclusively determined by the properties of the AER – fluid composite mixture but also by the properties of the insulating dielectric. Discriminating between both conductivity losses and polarization losses was beyond the scope of this work.

During the AER loading experiments, the composition of the effluent solution as well as its temperature and conductivity were determined. The analysis results show that nearly all HA were loaded on the AER, see Appendix B. In Appendix A, it is shown that the effects of temperature and conductivity changes in the fluid, measured during the loading experiments, on the measured AF plots were negligible.

Effect of regeneration

From the point of view of cost-effective operation, evenly important as the adsorption capacity is the regeneration capacity. For that reason the regeneration process was studied in more detail as well. An example of typical regeneration experiments are given in Fig. 6 and Fig. 7, using either a straight (Fig. 6) or helical inner conductor (Fig. 7). After loading the AER to a level of 1.1 g/L, the resonator tube was perfused with regeneration solution (10% w/v NaCl + 2% w/v NaOH) and an AF-response was recorded after 1.5 and 2.5 hrs, respectively. Clearly, under these experimental conditions, the effect of perfusing the AER with the regeneration fluid has a large effect on the AF-response: the minimum in the resonances of the AF plots shifts to lower frequencies (ϵ_{eff} increases) whereas the quality factor of each resonance increases ($\tan\delta_{eff}$ decreases). This indicates that the regeneration solution may have affected the binding of HA, chloride and hydroxide ions to the AER. Figures 6 and 7 also show that there is hardly a difference between the AF plots after 1.5

hours and 2.5 hours of regeneration respectively. This result indicates that equilibrium is nearly achieved or that the time scale for regeneration is orders of magnitude longer than expected and feasible in practice. After the regeneration procedure, the AER was perfused with tap water again and, surprisingly, the measured AF plot was similar to that obtained with AER column loaded with 1.1 g/l HA.

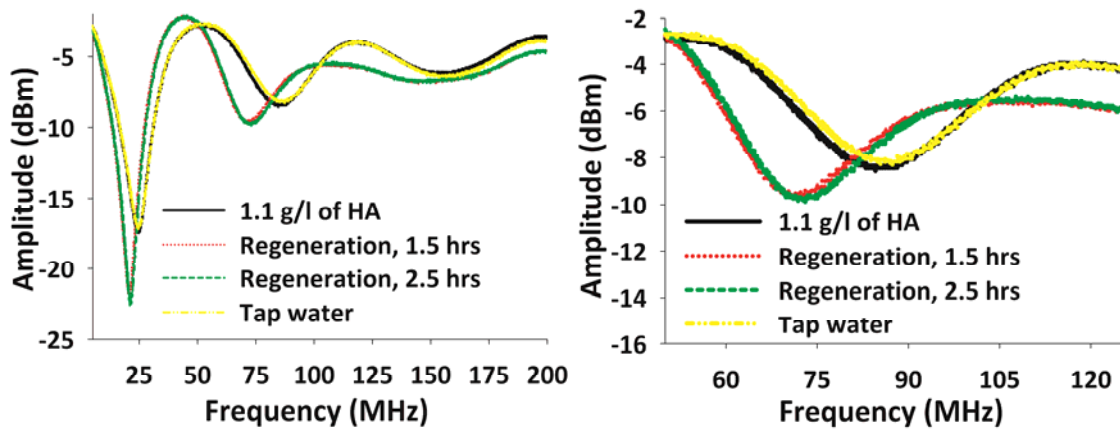


Fig. 6. On the left, AF plots in the 1-200 MHz range in response to regeneration of AER using a resonator with straight inner conductor. The right panel shows the 2nd resonance in more detail. The black curves correspond to AER loaded with 1 g/l of HA during perfusion with tap water and the yellow curves to the situation after the regeneration procedure and perfusion of the AER with tap water.

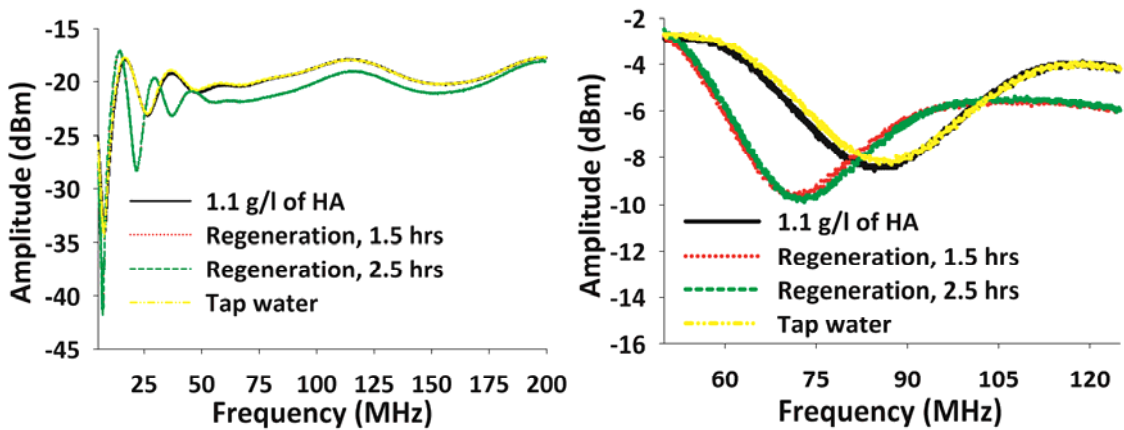


Fig. 7. On the left, AF plots in the 1-200 MHz range in response to regeneration of AER using a resonator with helically-shaped inner conductor. The right panel shows the 2nd resonance in more detail. The black curves correspond to AER loaded with 1 g/l of HA during perfusion with tap water and the yellow curves to the situation after the regeneration procedure and perfusion of the AER with tap water.

Following the analysis of the adsorption process, the AF-responses obtained from the regeneration experiments were also delineated in terms of changes in resonant frequency and amplitude ratio. Results are shown in Fig. 8 and the conclusion is the same as for the adsorption experiments: the AF response of the two types of resonators explored here with inner conductors of different geometries are very similar.

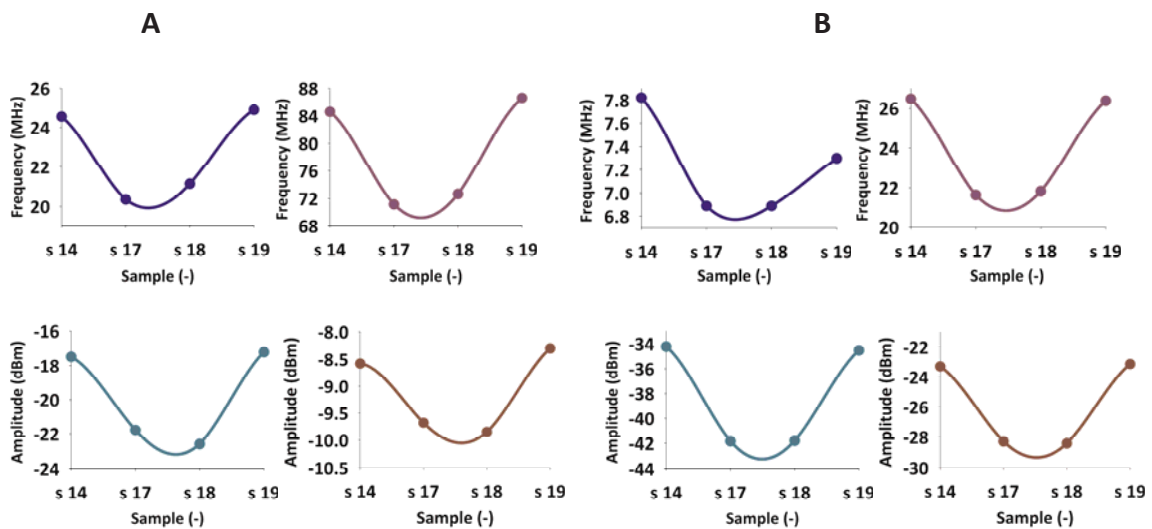
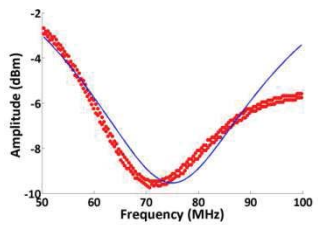
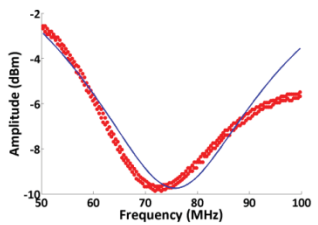
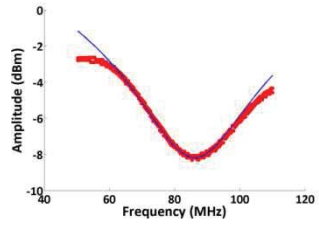
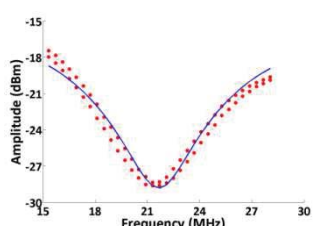
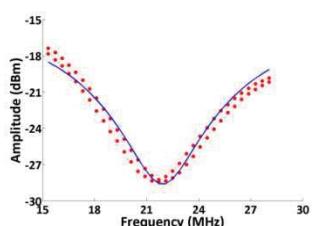
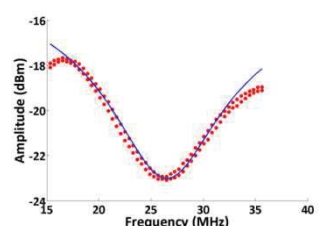


Fig. 8. Changes of resonant frequency (top row) and amplitude (bottom row) of the first (left) and second (right) resonance, in response AER regeneration, using either a resonator with straight (A panels) or helical inner conductor (B panels). Where S14 represents the experimental curve for the adsorption of 1.1 g/l of HA; S17 represents the experimental curve for the regeneration during 1.5 hrs; S18 represents the experimental curve for the regeneration during 2.5 hrs; S19 represents the experimental curve for the experiment using tap water.

Table 5

Simulation of AER regeneration, using the coaxial resonator with straight and helical inner conductors. Red dots represent experimental data, solid blue line simulation data.

	Regeneration, 1.5 hrs	Regeneration, 2.5 hrs	Tap water
The straight inner conductor	 <p>$\tan\delta_{eff}, (-)$ 0.29</p> <p>$\epsilon_{eff}, (-)$ 48.2</p>	 <p>0.30</p> <p>45.0</p>	 <p>0.35</p> <p>18.7</p>
The helical inner conductor	 <p>$\tan\delta_{eff}, (-)$ 0.12</p> <p>$\epsilon_{eff}, (-)$ 57.9</p>	 <p>0.12</p> <p>52.8</p>	 <p>0.31</p> <p>17.5</p>

As was done for the adsorption experiments, the regeneration process was simulated also, with the same purpose, i.e., to understand the AF-response in terms of changed AER dielectric properties [24]. Results are shown in Table 5, for a resonator with straight and helical inner conductors. From the data we conclude that perfusion of the AER with regeneration solution results in an increase of ϵ_{eff} and a decrease of $\tan\delta_{eff}$. Partly, this increase of ϵ_{eff} is caused by the sodium chloride and hydroxide ions in the solution, see Appendix E. The decrease of $\tan\delta_{eff}$ is caused by changes of the AER properties since the dielectric losses measured in tap water are smaller than those in the regeneration solution, see also Appendix E. Comparing the values for ϵ_{eff} and $\tan\delta_{eff}$ determined for tap water i.e., the values for tap water in Tables 5, with those in Table 4 for AER loaded with 1.1 g HA per liter AER resulted in the hypothesis that the regeneration procedure was not effective. A number of batch experiments, where the AER was loaded with different amounts of AER and subsequently regenerated with the standard regeneration solution, confirmed this hypothesis, see Appendix E. The batch experiments reveal that the AER can be regenerated up to HA loads on the AER of about 1 g/l. If the AER is loaded with more than about 1 g/l HA, higher HA load degrees are achieved but in this case, the regeneration procedure applied is not effective anymore to regenerate the AER.

Additional remarks

The results presented here are a first step towards the development of a transmission line based sensor for measuring on - line the load degree of ion exchange resin columns. The proposed method brings along the advantage that the load degree of the IER is measured in the column and not by analysis of the components of interest in the effluent of the column, allowing quantifying loading of the column long before breakthrough occurs. An interesting experimental observation in this study was the relation between the AF plots and the IER load observed up to HA load degrees of about 1 g/l. At these load degrees and the applied experimental conditions, ϵ_{eff} decreases with increasing load degree whereas $\tan\delta_{eff}$ increases with increasing load degree. In a sensor, the values of ϵ_{eff} and $\tan\delta_{eff}$ could be determined on - line from the AF plots using the model discussed in [25] and applied in this study. This opens possibilities to calculate the load degree of the AER from the fitted values of ϵ_{eff} and $\tan\delta_{eff}$. At higher HA load degrees than about 1g HA/l, an opposite trend was observed for the relation between the AF plots and the HA load degree. Most interestingly, this load degree of 1 g/l was also the critical HA load degree above which the regeneration procedure of the IER applied in this study was hardly effective anymore. This finding suggests that the binding interactions between HA and IER are stronger at HA loads above about 1 g/l as compared to HA loads below about 1 g/l. By definition, ion exchange is a reversible process. The irreversibility occurring at HA loads >1 g/l indicates an interaction between HA and IER of different nature than those occurring at lower loads, representing truly ion exchange. One possibility is the formation of a complex network of neighboring HA molecules with binding charge interaction via complexing cations such as calcium ions [40]. The observation that HA loading of >1 g/l coincidences with a different AF response indicates that the developed sensor technology may be a promising tool to for the on - line

assessment of the IER loading process. Finally it is noted that the results in this study indicate that transmission line based sensors may be a useful tool for collecting additional data in studies on interactions in composite dielectrics such as IER, nanofiltration, reverse osmosis and reverse electrodialysis membranes and chromatography columns.

7.5 Conclusions

- The feasibility of using a flow-through stub resonator for measuring the load degree of an AER column with HA was demonstrated for a solution of HA in tap water.
- Both the AER loading and regeneration can be theoretically described in terms of changed dielectric properties of the system i.e., ϵ_r and $\tan\delta_{eff}$, due to adsorption and desorption of the particular analyte (here HA) to the AER.
- At the experimental conditions applied, the sensor response to increasing AER loads with HA changed for HA load degrees above 1 gram per liter AER which was also the critical load degree above which regeneration of AER was seriously inhibited. Hence, the flow-through stub resonator is a promising tool to assess the loading process of the AER.
- Resonators with inner conductors of different electrical length (straight vs helical) give qualitatively similar results. Depending on the application one may opt for either type of resonator. The straight version shifts f_{res} to a higher frequency range, thereby increasing the sensitivity of the sensor. The helical type, on the other hand, shifts f_{res} in opposite direction. This illustrates that transmission line resonators as described here offer a large freedom of design, allowing in-line operation under “real life process conditions”.

7.6 Acknowledgement

This work was performed in the TTIW-cooperation framework of Wetsus, Centre of Excellence for Sustainable Water Technology (www.wetusus.nl). Wetusus is funded by the Dutch Ministry of Economic Affairs, the European Union Regional Development Fund, the Province of Fryslân, the City of Leeuwarden and the EZ/Kompas program of the “Samenwerkingsverband Noord-Nederland”. The authors thank the participants of the research theme Sensoring for the fruitful discussions and their financial support.

7.7 References

1. E.R. Cornelissen, N. Moreau, W. G. Siegers, A. J. Abrahamse, L. C. Rietveld, A. Grefte, M. Dignum, G. Amy, L.P. Wessels, Selection of anionic exchange resins for removal of natural organic matter fractions, *Water research*, n°42, p 413-423, 2008.
2. <http://www.waterbedrijfgroningen.nl/en/water-at-home/Paginas/default.aspx>
3. B. Eikebrokk, R.D. Vogt, H. Liltved, NOM increase in Northern European source waters: discussion of possible causes and impacts on coagulation/contact filtration processes, *Water Science & Technology: Water Supply*. Vol. 4 Issue 4, pp. 47-54. 8p, 2004.
4. http://dardel.info/IX/resin_structure.html
5. http://www.gewater.com/handbook/ext_treatment/ch_8_ionexchange.jsp#COMMON_ION_EXCHANGE_SYSTEM_PROBLEMS
6. S.D. Alexandratos, Ion-Exchange Resins: A Retrospective from Industrial and Engineering Chemistry Research, *Industrial & Engineering Chemistry Research* 48 (1), 388-398, 2009.
7. http://msdssearch.dow.com/PublishedLiteratureDOWCOM/dh_0886/0901b80380886357.pdf?filepath=liquidseps/pdfs/noreg/177-01772.pdf&fromPage=GetDoc
8. W.E. Bernahl, W. Bernahl, Ion Exchange Resins and Processes for Industrial Water Treatment, Enterprises, Ltd, (<http://www.wqpmag.com/ion-exchange-resins-and-processes-industrial-water-treatment>).
9. G.N. Rao, Sandeep Srivastava, S. K. Srivastava, Manendra Singh, Chelating ion-exchange resin membrane sensor for nickel(II) ions, *Talanta*, Volume 43, Issue 10, October 1996, Pages 1821-1825, ISSN 0039-9140, [http://dx.doi.org/10.1016/0039-9140\(96\)01959-5](http://dx.doi.org/10.1016/0039-9140(96)01959-5).
10. Tatsuro Nakagama, Masaaki Yamada, Toshiyuki Hobo, Chemiluminescence sensor with uranine immobilized on an anion-exchange resin for monitoring free chlorine in tap water, *Analytica Chimica Acta*, Volume 231, 1990, Pages 7-12, ISSN 0003-2670, [http://dx.doi.org/10.1016/S0003-2670\(00\)86390-4](http://dx.doi.org/10.1016/S0003-2670(00)86390-4).
11. L. Niedrach, Sensor with ion exchange resin electrolyte, US3714015 A, 30 January, 1973.
12. H. Waki, S. Noda, M. Yamashita, Spectroscopy of ion exchangers and its applications. Ion-exchanger phase absorptiometry and spectrofluorometry using a crosslinked dextran ion exchanger, *Reactive Polymers, Ion Exchangers, Sorbents*, Volume 7, Issues 2–3, January 1988, Pages 227-237, ISSN 0167-6989, [http://dx.doi.org/10.1016/0167-6989\(88\)90144-4](http://dx.doi.org/10.1016/0167-6989(88)90144-4).
13. Kazuhisa Yoshimura, Hirohiko Waki, Ion-exchanger phase absorptiometry for trace analysis, *Talanta*, Volume 32, Issue 5, May 1985, Pages 345-352, ISSN 0039-9140, [http://dx.doi.org/10.1016/0039-9140\(85\)80097-7](http://dx.doi.org/10.1016/0039-9140(85)80097-7).
14. <http://pac.iupac.org/publications/pac/pdf/1971/pdf/2504x0797.pdf>
15. Yu.G. Vlasov, E.A. Bychkov, Chalcogenide glass chemical sensors: Relationship between ionic response, surface ion exchange and bulk membrane transport, *Journal of Electroanalytical Chemistry*, Volume 378, Issues 1–2, 21 November 1994, Pages 201-204, ISSN 1572-6657, [http://dx.doi.org/10.1016/0022-0728\(94\)87072-1](http://dx.doi.org/10.1016/0022-0728(94)87072-1).
16. http://www3.panasonic.biz/ac/e_download/fasys/lasermarker/lasermarker/catalog/lp-f_e_cata.pdf?f_cd=401694
17. D.S. Stefan, I. Meghea, Mechanism of simultaneous removal of Ca²⁺, Ni²⁺, Pb²⁺ and Al³⁺ ions from aqueous solutions using Purolite® S930 ion exchange resin, *Comptes Rendus Chimie*, Volume 17, Issue 5, May 2014, Pages 496-502, ISSN 1631-0748, <http://dx.doi.org/10.1016/j.crci.2013.09.010>.
18. J. Bessière, A. Kléber, I. Sutapa, M. Perdicakis, Dielectric control of the behaviour of ion-exchange resins, *Sensors and Actuators B: Chemical*, Volume 27, Issues 1–3, June 1995, Pages 411-413, ISSN 0925-4005, [http://dx.doi.org/10.1016/0925-4005\(94\)01629-V](http://dx.doi.org/10.1016/0925-4005(94)01629-V).
19. A. Ishikawa, T. Hanai and N. Koizumi, Dielectric properties of ion-exchange beads of sulfonic acid type dispersed in aqueous solutions — effect of fixed charge density, *Colloid and Polymer Science*, 1985, Volume 263, Issue 5, pp. 428-432.
20. A. Ishikawa, T. Hanai and N. Koizumi, Dielectric study of some ion exchange resins, *Bull. Inst. Chem. Res. Kyoto Univ. Bol.*, 62 (4), 1984.
21. N.A. Hoog-Antonyuk, W. Olthuis, M.J.J. Mayer, D. Yntema, H. Miedema, A. van den Berg, On-line fingerprinting of fluids using coaxial stub resonator technology, *Sensors and Actuators B* 163, 2012, <http://dx.doi.org/10.1016/j.snb.2012.01.012>.

22. N.A. Hoog-Antonyuk, W. Olthuis, M.J.J. Mayer, H. Miedema, F.B.J. Leferink, A. van den Berg, Extensive Modeling of a Coaxial Stub Resonator for Online Fingerprinting of Fluids, *Procedia Engineering*, pp. 310-313, 2012, <http://dx.doi.org/10.1016/j.proeng.2012.09.145>.
23. M.J.J. Mayer, N.A. Hoog, RF antenna filter as a sensor for measuring a fluid, WO Patent 005084, 13 January, 2011.
24. M.J.J. Mayer, N. A. Hoog, Werkwijze en inrichting voor ingerprinting of het behandelen van een dielectricum in het algemeen en van water in het bijzonder, NL1038869, 16 August, 2012.
25. N.A. Hoog, M. J.J. Mayer, H. Miedema, W. Olthuis, F. B. J. Leferink, A. van den Berg, Modeling and Simulations of the Amplitude-Frequency Response of Transmission Line Type Resonators Filled with Lossy Dielectric Fluids, *Sensors & Actuators: A. Physical*, Volume 216, 2014, pp.147-157 <http://dx.doi.org/10.1016/j.sna.2014.05.006>.
26. W. Richards, Yuen Lo, D. Harrison, An improved theory for microstrip antennas and applications, *Antennas and Propagation, IEEE Transactions on*, vol.29, no.1, pp.38, 46, (1981).
27. N.A. Hoog, M.J.J. Mayer, H. Miedema, R. M. Wagterveld, J. Tuinstra, M. Saakes, W. Olthuis, A. van den Berg, Stub Resonators for Online Monitoring Early Stages of Corrosion, Manuscript Number: SNB-D-14-00307 has been accepted for publication in *Sensors and Actuators B: Chemical* on th 9th, 2014.
28. G. C. Topp, J. L. Davis, A. P. Annan, G. C. Topp, J. L. Davis, A. P. Annan, Electromagnetic determination of soil water content: Measurements in coaxial transmission lines, *Water Resources Research*, Vol 16 Issue 3, 2010, <http://dx.doi.org/10.1029/WR016i003p00574>.
29. A. Rodrigues, A. Brito, P. Janknecht, M.F. Proença, R. Nogueira, Quantification of humic acids in surface water: effects of divalent cations, pH, and filtration, *J Environ Monit.* 2009 Feb;11(2):377-82. <http://dx.doi.org/10.1039/b811942b>
30. A.V. Goncharenko, V.Z. Lozovski, E.F. Venger, Lichtenecker's equation: applicability and limitations, *Optics Communications*, Volume 174, Issues 1–4, 15 January 2000, Pages 19-32, ISSN 0030-4018, [http://dx.doi.org/10.1016/S0030-4018\(99\)00695-1](http://dx.doi.org/10.1016/S0030-4018(99)00695-1).
31. W.W. Macalpine, R.O Schildknecht, Coaxial Resonators with Helical Inner Conductor, *Proceedings of the IRE*, vol.47, no.12, pp.2099 - 2105, Dec. 1959, doi: <http://dx.doi.org/10.1109/JRPROC.1959.287128>.
32. D.M. Pozar, *Microwave Engineering*, Wiley, 2004.
33. R.E. Collin, *Foundations for Microwave Engineering*, Wiley IEEE, 2000.
34. P.A. M. Steeman, F. H. J. Maurer, M. A. van Es, Dielectric monitoring of water adsorption in glass-bead-filled high-density polyethylene, *Polymer*, Volume 32, Issue 3, pp. 523-530, 1991.
35. A.D. Archer, and P. C. Singer, An evaluation of the relationship between SUVA and NOM coagulation using the ICR database, *Journal of American Water Work Association*, 98(7): (2006), pp. 110-123.
36. <http://www.purolite.com/default.aspx?RelID=606288&ProductID=226>
37. <http://www.brenntag.be/>
38. M. S. Bhatnagar, EPOXY RESINS (Overview), *The Polymeric Materials Encyclopedia*, © 1996 CRC Press, Inc.
39. H. T. Dang, R. M. Narbaitz, T. Matsuura and K. C. Khulbe, A comparison of commercial and experimental ultrafiltration membranes via surface property analysis and fouling tests, *Water Quality Research Journal of Canada*, 2006 • Volume 41, No. 1, 84–93.
40. Chendong Shuang, Fei Pan, Qing Zhou, Aimin Li, Penghui Li, and Weiben Yang, Magnetic Polyacrylic Anion Exchange Resin: Preparation, Characterization and Adsorption Behavior of Humic Acid, *Industrial & Engineering Chemistry Research* 2012 51 (11), pp. 4380-4387.

7.8 Supplementary Information

Appendix A

During the experiments on the loading of AER with HA, temperature and conductivity fluctuations were measured to amount less than 2 °C and 200 $\mu\text{S}/\text{cm}$, respectively. Figures A.1 and A.2 reveal that changes in the AF plots due to these conductivity and temperature changes are negligible.

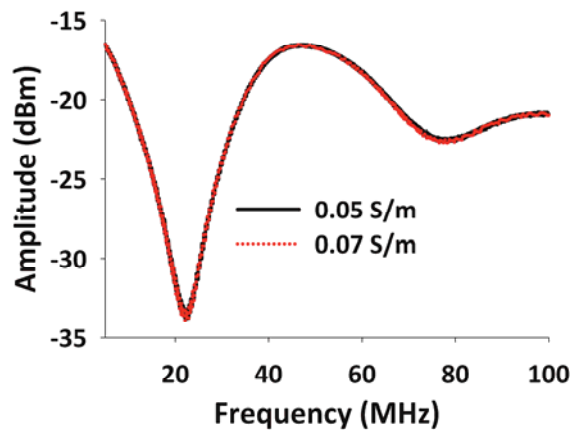


Fig. A.1. AF plots in the 1-100 MHz range obtained for a resonator with straight inner conductor that was filled with AER and perfused with feed solutions with a conductivity of 0.05 S/m and 0.07 S/m respectively.

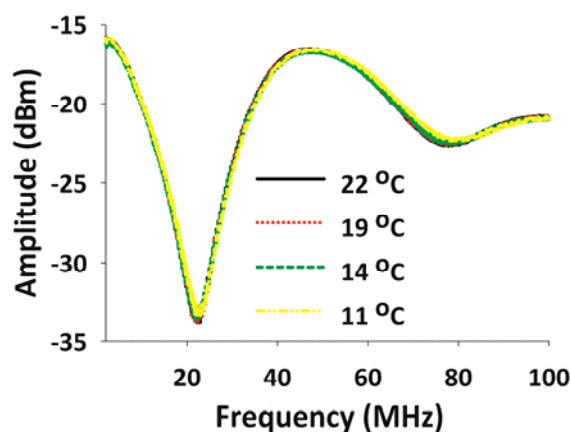


Fig. A.2. AF plots in the 1-100 MHz range obtained for a resonator with straight inner conductor that was filled with AER and perfused with feed solutions with a temperature of 22, 19, 14 and 11 °C respectively.

It should be mentioned that differences Δf_{res} for 2nd resonance in the experiments of monitoring of the load of AER using the straight inner conductor between 0 g/l and 0.1 g/l and experiments to measure difference in temperature within 3 oC are 3 MHz and 0.2 MHz, respectively.

Table A.1 summarized of the measured water parameters as well as the equipment used in this study.

Table A.1.

Parameters and apparatus.

No	Parameters	Apparatus
	Temperature	Thermometer, WTW, (Germany)
	pH	pH meter, WTW, (Germany)
	Conductivity	Conductivity meter, WTW, (Germany)
	UV absorbance	Spectrophotometer, type UV-1650PC, Shimadzu (Japan)
	TOC	TOC analyzer, Shimadzu (Japan)
	IC	TOC analyzer, Shimadzu (Japan)
	DOC	LC-OCD, Model 8, DOC-LABOR (Germany)
	Humus acids-C	LC-OCD, Model 8, DOC-LABOR (Germany)

The anion exchange resin used in this study is Purolite® A860S (Brenntag NV, Belgium), a commonly used resin by the drinking water industry to remove HA. The specifications of Purolite® A860S are listed in Table A.2

Table A.2

Specifications of Purolite® A860S anion exchange resin.

No	Characteristics	Values
Physical characteristics		
	Physical form	Uniform particle size spherical beads
1.	Shipping weight	680 - 730 g/l
2.	(approx.)	
3.	Uniformity coefficient	<1.6
4.	Particle size Range	425 - 1200 μ m
5.	Temp Limit, Cl ⁻ Form	80°C
6.	Temp Limit, OH ⁻ Form	40°C
Chemical characteristics		
	Specific Gravity	1.08
7.	Reversible Swelling,	<20 %
8.	Cl ⁻ → OH ⁻	Cl ⁻
9.	Ionic Form as Shipped	Quaternary Ammonium
10.	Functional Group	>0.8 eq/l (Cl ⁻ form)
11.	Total exchange capacity	66 - 72 % (Cl ⁻ form)
12.	Moisture Retention	0.8% (Cl ⁻ form)
13.	Polymer Structure	Macroporous polyacrylic crosslinked with divinylbenzene

Appendix B

In order to check the loading efficiency of HA on the AER, samples were collected simultaneously and used for the analysis of pH, humic acids-C and dissolved organic carbon (DOC) (See Supplementary Information for analysis of total organic carbon (TOC), inorganic carbon (IC) and total carbon (TC) as well as for UV₄₅₅, temperature, and conductivity). Results are shown in Fig. B.1.

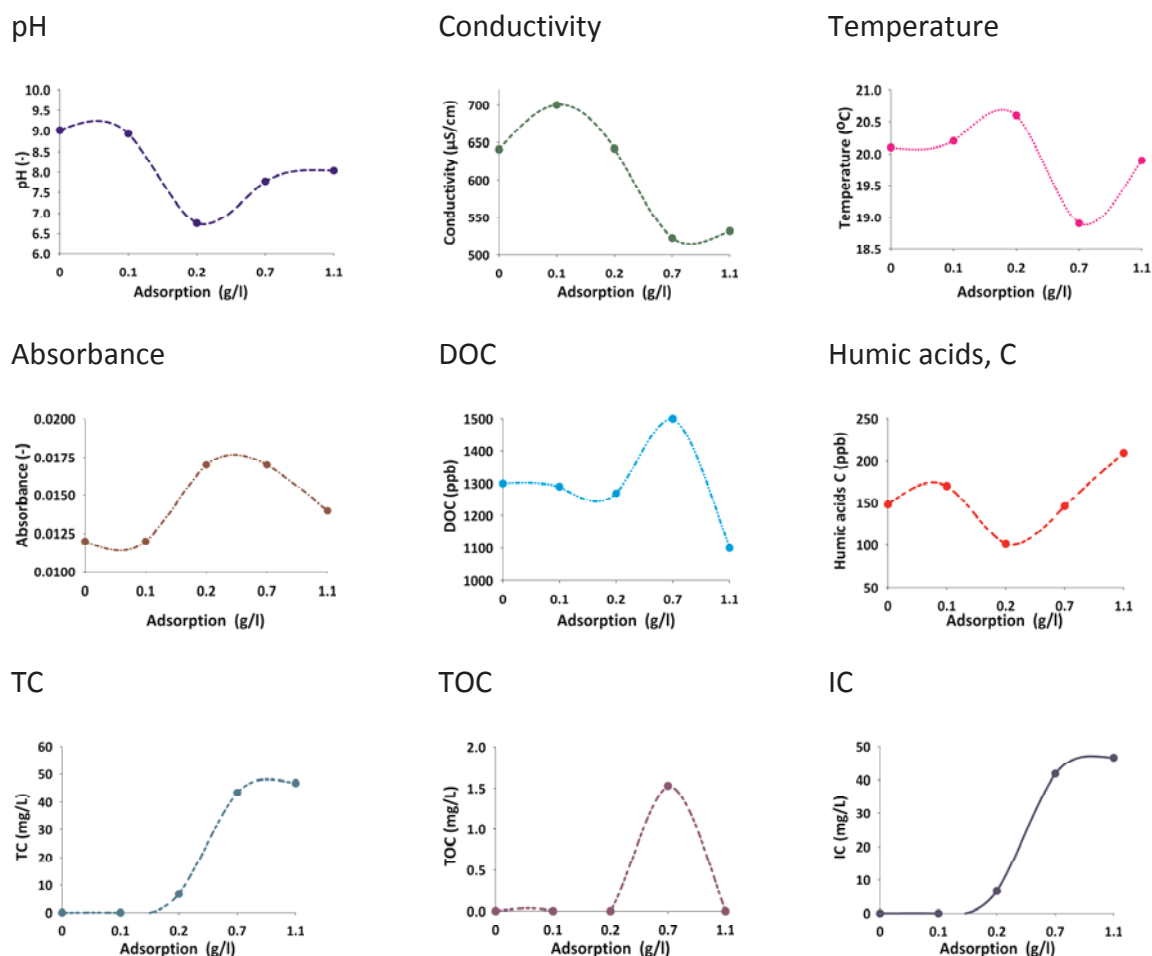


Fig. B.1. Recorded effluent solution values of pH, temperature, conductivity, UV₄₅₅, humic acid-C and dissolved organic carbon (DOC), total organic carbon (TOC), and inorganic carbon (IC) all as function of the amount of HA adsorbed per unit volume of AER.

The data of Fig. B.1 was obtained during the same experiment as those of Fig. 3. The experiment started out with perfusion the resonator with tap water. After perfusion with several resonator tube volumes (150 ml), the actual experiment started by switching to perfuse with the analytical HA-containing feed solution. At this point, with no HA adsorbed yet, the first sample (100 ml) was taken and the first AF response recorded. After 50 min, i.e., with a perfusion rate of 3 ml/min the time needed to flow through one resonator tube volume, the second sample was taken and the second AF-response recorded. The data of Fig. B.1 is plotted against the over-time integrated adsorbed amount of HA as calculated from the HA concentration in the feed (Table 5), the HA concentration in effluent and the perfusion rate. After 100 min, the third sample was taken and the third AF-response recorded, and so on. The 100 ml sample was split into 10 ml samples, which were used for the analysis of the parameters shown in Fig. A.3. Even though derived from the same experiment, these different types of measurements were independent in terms of chemical analysis.

The plots for pH and humic acids-C show similar trends, between the first two data points, i.e., rather constant (pH) or a slight increase, reflecting the switch from tap water to HA-containing feed. Between the second and third data point, both parameters show a rather steep decline. The drop in pH is caused by the appearance of HA in the effluent, the one in humic acids-C because AER adsorbs HA very efficiently (note the very low concentration in the effluent, 100-150 ppb, compared to the content of the feed, 3450 ppb). From data point #3 off, both parameters start to increase, indicating the very beginning of IER saturation. However, even though AER might start to saturate, the final saturation level has not reached yet as it is expected that at that point the effluent concentration of humic acids-C becomes close to its concentration level in the feed solution, 3450 ppb. It is not entirely clear why the pH increases as well.

Compared to the time course of humic acids-C, that of DOC is completely different. Most remarkable is the peak at a load of 0.7 g/L. This might be an artefact, to our opinion, and caused, for example, by the presence of a larger undissolved particular, temporarily increasing the absorbance and by that suggesting an increased DOC level. These points to an essential difference between measurements of the effluent and monitoring the status of the IER itself. During IER operation, the DOC peak might have evoked a false alarm, interpreted as saturation of the IER, followed by starting the regeneration procedure too early. Monitoring the IER itself represents an integrated measurement as the IER accumulates the analyze of interest over time. Obviously, such type of measurement is less prone to false positives due to temporal anomalies in the effluent.

Finally, in analogy to Fig. B.1, we aimed to correlate observed regeneration-induced changes in AF response to effluent composition measurements. Results for pH, humic acids-C and DOC are shown in Fig. B.2. Both the pH and DOC response show a clear peak, representing, in the effluent, the presence of highly alkaline regeneration solution and dissolved organic carbon compounds due to the regeneration process, respectively.

Remarkably, the response of humic-acids-C clearly shows two peaks, suggesting the presence of two populations of HA with different adsorption affinity for this particular AER.

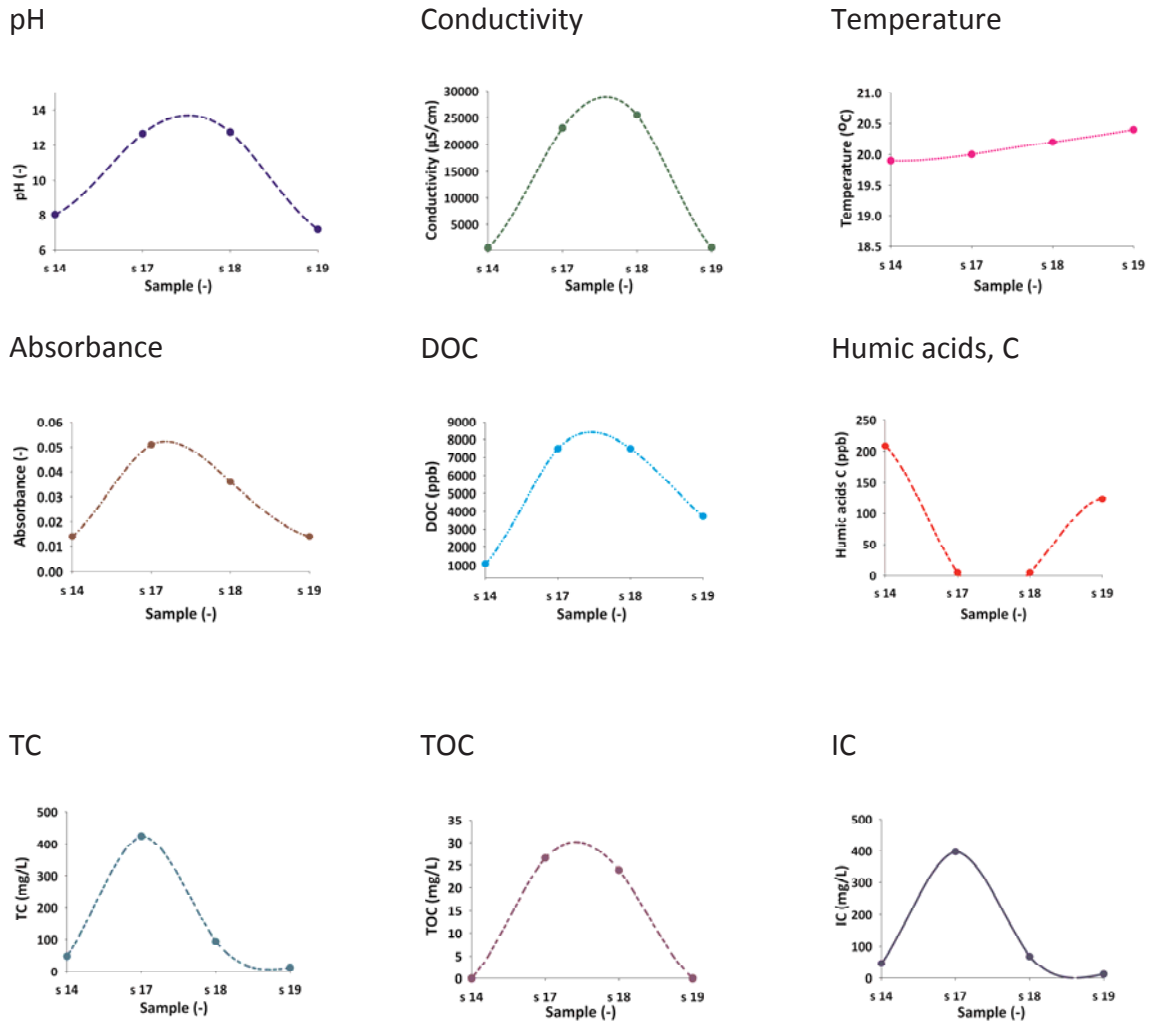


Fig. B.2. Recorded effluent solution values of pH, temperature, conductivity, UV₄₅₅, humic acid-C and dissolved organic carbon (DOC), total organic carbon (TOC), and inorganic carbon (IC), all in response to the regeneration protocol and as function of the amount of HA adsorbed per unit volume of AER.

Appendix C

To exclude the effect of the epoxy resin on the bottom of the resonator the following function was used:

```
function F = iox_air_epoxy_coax_resonator_1(x,f)
% dielectric constant of epoxy, defined from the simulation in the
% previously work
e_epoxy = 1.96;
h=0.267+0.029; % the total length of the resonator with epoxy on the bottom [m],
% note: epoxy on the bottom of the sensor
h_epoxy=0.062; % the length of the layer of epoxy [m]
db=25e-3; % diameter of the resonator;
%Er1 = 2.4; %dielectric permittivity of polymer layer, [-]
Er1=x(2)%dielectric permittivity of polymer layer, [-]
Vt=pi*h*db^2/4; %volume of the empty resonator [m^3]
Vt_epoxy=pi*h_epoxy*db^2/4 % volume of epoxy resin in the resonator
f_epoxy=(pi*h_epoxy*db^2/4)/Vt % volume fraction of epoxy resin in the resonator
Vt_feed=Vt-Vt_epoxy %volume of the filled with epoxy resonator [m^3]
f_feed=Vt_feed/Vt %volume of feed substrate in the filled with epoxy resonator [m^3]
f_feed_t=1-f_epoxy %volume fraction of feed substrate excluding epoxy in the filled with epoxy resonator
[m^3]
len =0.27+0.029; % length of the coax resonator [m]
b = 25e-3; % inner diameter of the outer conductor [m]
a = 4e-3;% outer diameter of the inner conductor [m]
c=3*1e+8; % speed of light in vacuum [m/s]
Ur=1; %relative dielectric permeability of the dielectric between inner and outer conductors [-]
u = Ur*4*pi*1e-7; % magnetic permeability of the dielectric [H/m]
sigma_stainless_steel=1.45e+6;%conductance of the metal applied for inner and outer conductors (stainless
steel) [1/(Ohm*m)]
sigma_copper=5.96e+7;%conductance of the metal applied for inner conductor ( copper), [1/(Ohm*m)]
%effective conductance of both feed substrate and epoxy resin
% sigma_eff=sigma_feed*f_feed_t+sigma_epoxy*f_epoxy;
%effective dielectric permittivity of both feed substrate and epoxy resin
Er_air=1;
Eeff_ep_air=Er_air*(f_feed_t)+e_epoxy*f_epoxy;
r2 = (25.4e-3)/2; %inner radius of the outer conductor, [m]
r0 = (4e-3)/2; %radius of the inner conductor of the resonator, [m]
Er2 =Eeff_ep_air % dielectric permittivity of a fluid substrate, [-]
Ur =1; %relative dielectric permeability of the dielectric between inner and outer conductors, [-]
e = 8.854e-12; % vacuum permeability [H/m]
u = Ur*1.257e-6;% magnetic permeability of the dielectric, [H/m]
r1=r0+1.5e-3/2; %radius of the inner conductor and outer radius of the polymer layer (m);
c=3*1e+8; % speed of light in vacuum, [m/s]
% capacitance of the open ended coaxial stub resonator, contains the oxide layer, [F/m]
C1=2*pi*e*Er1/(log(r1/r0))
% capacitance of the open ended coaxial stub resonator, contains a fluid, [F/m]
C2=2*pi*e*Er2/(log(r2/r1))
% total capacitance of the open ended coaxial stub resonator, [F/m]
C=1/(1/C1+1/C2)
% inductance of the open ended coaxial stub resonator, [H/m]
L = ((u/(pi*2))*log(r2/r0))
Eeff_coax=(Er1*Er2*log(r2/r0))/((Er1*log(r2/r1)+Er2*log(r1/r0)))% effective dielectric constant of whole
system, [-]
Eeff=Eeff_coax
```



```

E= Eeff * 1/(4*pi*1e-7*c*c); % vacuum permeability [H/m]
sigma_eff=0; % effective conductivity of the system, [S/m]
%Define the input voltage supplied by the function generator [V]
vin=500e-3; %input voltage supplied by the function generator [V]
omega = 2*pi*f;% angular frequency [rad/s]
Eim=((omega.*E.*x(1))-sigma_eff)./omega;%imaginary part of complex dielectric permittivity
skin_depth1=sqrt(2./(omega.*u.*sigma_stainless_steel));%skin_depth
skin_depth2=sqrt(2./(omega.*u.*sigma_copper));%skin_depth
Rs1=1./(sigma_stainless_steel.*skin_depth1);% surface resistivity of the outer conductor of the resonator
Rs2=1./(sigma_copper.*skin_depth2);% surface resistivity of the inner conductor of the resonator
R=Rs2/r0+Rs1/r2;% distributed element resistance R of the resonator [Ohm/m]
G=(omega.*Eim+sigma_eff)./(omega.*E).*omega.*C;%distributed element conductance of the resonator
[F/(m*s)]
gamma =(sqrt((R+1i.*omega.*L).*(G+1i.*omega.*C)))/omega;%complex propagation constant [1/m]
%notes on gamma: Re(gamma)=alfa = attenuation constant representing losses [Np/m];
Im(gamma)=beta=phase of the propagation constant [rad/m]
%since the signal is oscillating in time with omega rad/s, the propagation velocity of the wave [m/s] =
omega/beta; also, beta = 2*pi/wavelength.
Zc=sqrt(((R+1i.*omega.*L)./(G+1i.*omega.*C)));% complex characteristic impedance of the resonator [Ohm]
Zin=Zc.*coth(gamma.*len);%complex input impedance of the resonator [Ohm]
vout=sqrt((real(Zin.*(vin./(50+2*Zin)))).^2+(imag(Zin.*(vin./(50+2*Zin)))).^2);%modulus of vout, the is the
recorded voltage by the spectrum analyzer [V]
F =20.*log10(vout)+13;%vout as a power ratio in dBm i.e., the measured power referenced to one mWatt and
the underlying assumption of a 50 Ohm load resistance

```

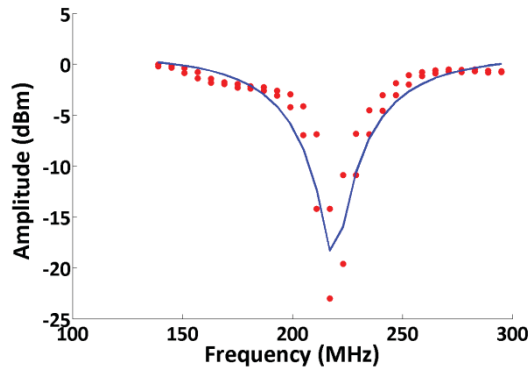
The main program was:

```

clear all % Clear all variables in function workspace
close all % Close all figures
clc % Clear command window
clearvars
format longE
load air_straight.txt % load the file with data of the day of experiment
f=air_straight(:,1); % Load experimental data; frequency
amplitude=air_straight(:,2); % Load experimental data; amplitude
f=f*1e+6; % Frequency conversion
%- Plot experimental data
hF = figure
hA = axes
set(hA, 'XGrid', 'off', 'YGrid', 'on')
hold on
set(0,'DefaultFontSize',36,'DefaultFontName','Times New Roman','DefaultFontWeight','bold');
plot(f/1e+6, amplitude, 'LineStyle','none','Marker','.', 'MarkerEdgeColor','r', 'MarkerSize',35);
hold on
x0 = [0.01 1];
ya0 = iox_air_epoxy_coax_resonator_1(x0,f);
% % - Plot initial values
% hold on;
% plot(f,ya0,'--m')
%-Boundary conditions
LB = [0 0]; % Lower bounds
UB = [1 10]; %Upper bounds
% LB = [0]; % Lower bounds
% UB = [1]; %Upper bounds
% -Solving nonlinear least-squares curve fitting

```

```
[x,resnorm] = lsqcurvefit('iox_air_epoxy_coax_resonator_1',x0,f,amplitude, LB, UB)
ya = iox_air_epoxy_coax_resonator_1(x,f);
%- Plot fit results
Hf = plot(f/1e+6,ya,'b');
set(Hf, 'LineWidth',3)
hold on
xlabel('Frequency, (MHz)','fontsize',42,'fontweight','b');
ylabel('Amplitude, (dBm)','fontsize',42,'fontweight','b');
hold on
```



The output parameters of the simulation	Value
$\tan\delta_{eff}$	0.03
$\epsilon_{polymer\ layer}$	2.32

Fig. C.1. Experimentally obtained amplitude versus frequency plot of empty resonator with the layer of epoxy resin on the bottom (red) and the polymer layer on the inner conductor using a quarter wave length open-ended coaxial resonator with the straight inner conductor. Fitting data are shown for comparison (blue).

To determine the effective loss tangent $\tan\delta_{eff}$ (Eq. 5) and dielectric permittivity ϵ_{eff} (Eq. 4) the following function was used for the straight inner conductor:

```
function F = iox_feed_epoxy_coax_resonator_m(x,f)
% dielectric constant of epoxy, defined from the simulation in the
% previously work
e_epoxy = 1.96;
h=0.267+0.029; % the total length of the resonator with epoxy on the bottom [m],
% note: epoxy on the bottom of the sensor
h_epoxy=0.062; % the length of the layer of epoxy [m]
db=25e-3; % diameter of the resonator;
%Er1 = 2.4; %dielectric permittivity of polymer layer, [-]
Er1=2.32%dielectric permittivity of polymer layer, [-]
Vt=pi*h*db^2/4; %volume of the empty resonator [m^3]
Vt_epoxy=pi*h_epoxy*db^2/4 % volume of epoxy resin in the resonator
f_epoxy=(pi*h_epoxy*db^2/4)/Vt % volume fraction of epoxy resin in the resonator
Vt_feed=Vt-Vt_epoxy %volume of the filled with epoxy resonator [m^3]
f_feed=Vt_feed/Vt %volume of feed substrate in the filled with epoxy resonator [m^3]
f_feed_t=1-f_epoxy %volume fraction of feed substrate excluding epoxy in the filled with epoxy resonator
[m^3]
len =0.27+0.029; % length of the coax resonator [m]
```

```

b = 25e-3; % inner diameter of the outer conductor [m]
a = 4e-3;% outer diameter of the inner conductor [m]
c=3*1e+8; % speed of light in vacuum [m/s]
Ur=1; %relative dielectric permeability of the dielectric between inner and outer conductors [-]
u = Ur*4*pi*1e-7; % magnetic permeability of the dielectric [H/m]
sigma_stainless_steel=1.45e+6;%conductance of the metal applied for inner and outer conductors (stainless
steel) [1/(Ohm*m)]
sigma_copper=5.96e+7;%conductance of the metal applied for inner conductor ( copper),
[1/(Ohm*m)]%effective conductance of both feed substrate and epoxy resin
% sigma_eff=sigma_feed*f_feed_t+sigma_epoxy*f_epoxy;
%effective dielectric permittivity of both feed substrate and epoxy resin
Er_feed_iox=x(2);
Eeff_ep_air=Er_feed_iox*(f_feed_t)+e_epoxy*f_epoxy;
r2 = (25.4e-3)/2; %inner radius of the outer conductor, [m]
r0 = (4e-3)/2; %radius of the inner conductor of the resonator, [m]
Er2 =Eeff_ep_air % dielectric permittivity of a fluid substrate, [-]
Ur =1; %relative dielectric permeability of the dielectric between inner and outer conductors, [-]
e = 8.854e-12; % vacuum permeability [H/m]
u = Ur*1.257e-6;% magnetic permeability of the dielectric, [H/m]
r1=r0+1.5e-3/2; %radius of the inner conductor and outer radius of the polymer layer (m);
c=3*1e+8; % speed of light in vacuum, [m/s]
% capacitance of the open ended coaxial stub resonator, contains the oxide layer, [F/m]
C1=2*pi*e*Er1/(log(r1/r0))
% capacitance of the open ended coaxial stub resonator, contains a fluid, [F/m]
C2=2*pi*e*Er2/(log(r2/r1))
% total capacitance of the open ended coaxial stub resonator, [F/m]
C=1/(1/C1+1/C2)
% inductance of the open ended coaxial stub resonator, [H/m]
L = ((u/(pi*2))*log(r2/r0))
Eeff_coax=(Er1*Er2*log(r2/r0))/((Er1*log(r2/r1)+Er2*log(r1/r0)))% effective dielectric constant of whole
system, [-]
Eeff=Eeff_coax
E= Eeff * 1/(4*pi*1e-7*c*c); % vacuum permeability [H/m]
sigma_eff=0; % effective conductivity of the system, [S/m]
%Define the input voltage supplied by the function generator [V]
vin=600e-3; %input voltage supplied by the function generator [V]
omega = 2*pi*f;% angular frequency [rad/s]
Eim=((omega.*E.*x(1))-sigma_eff)./omega;%imaginary part of complex dielectric permittivity
skin_depth1=sqrt(2./(omega.*u.*sigma_stainless_steel));%skin_depth
skin_depth2=sqrt(2./(omega.*u.*sigma_copper));%skin_depth
Rs1=1./(sigma_stainless_steel.*skin_depth1);% surface resistivity of the outer conductor of the resonator
Rs2=1./(sigma_copper.*skin_depth2);% surface resistivity of the inner conductor of the resonator
R=Rs2/r0+Rs1/r2;% distributed element resistance R of the resonator [Ohm/m]
G=(omega.*Eim+sigma_eff)./(omega.*E).*omega.*C;%distributed element conductance of the resonator
[F/(m*s)]
gamma =(sqrt((R+1i.*omega.*L).*(G+1i.*omega.*C)));%complex propagation constant [1/m]
%notes on gamma: Re(gamma)=alfa = attenuation constant representing losses [Np/m];
Im(gamma)=beta=phase of the propagation constant [rad/m]
%since the signal is oscillating in time with omega rad/s, the propagation velocity of the wave [m/s] =
omega/beta; also, beta = 2*pi/wavelength.
Zc=sqrt(((R+1i.*omega.*L)./(G+1i.*omega.*C)));% complex characteristic impedance of the resonator [Ohm]
Zin=Zc.*coth(gamma.*len);%complex input impedance of the resonator [Ohm]
vout=sqrt((real(Zin.*(vin./(50+2*Zin))))).^2+(imag(Zin.*(vin./(50+2*Zin))))).^2);%modulus of vout, the is the
recorded voltage by the spectrum analyzer [V]
F =20.*log10(vout)+13;%vout as a power ratio in dBm i.e., the measured power referenced to one mWatt and
the underlying assumption of a 50 Ohm load resistance

```

The main program was:

```
clear all % Clear all variables in function workspace
close all % Close all figures
clc % Clear command window
clearvars
format longE
load nd_fith_straight.txt % load the file with data of the day of experiment
f=nd_fith_straight(:,1); % Load experimental data; frequency
amplitude=nd_fith_straight(:,2); % Load experimental data; amplitude
f=f*1e+6; % Frequency conversion
%- Plot experimental data
hF = figure
hA = axes
set(hA, 'XGrid', 'off', 'YGrid', 'on')
hold on
set(0,'DefaultFontSize',36,'DefaultFontName','Times New Roman', 'DefaultFontWeight', 'bold');
plot(f/1e+6, amplitude, 'LineStyle','none','Marker','.', 'MarkerEdgeColor','r', 'MarkerSize',35);
hold on
x0 = [0 1];
ya0 = iox_feed_epoxy_coax_resonator_m(x0,f);
% % - Plot initial values
% hold on;
% plot(f,ya0,'--m')
%-Boundary conditions
LB = [0 1]; % Lower bounds
UB = [1 100]; %Upper bounds
% LB = [0]; % Lower bounds
% UB = [1]; %Upper bounds
%-Solving nonlinear least-squares curve fitting
[x,resnorm] = lsqcurvefit('iox_feed_epoxy_coax_resonator_m',x0,f,amplitude, LB, UB)
ya = iox_feed_epoxy_coax_resonator_m(x,f);
%- Plot fit results
Hf = plot(f/1e+6,ya,'b');
set(Hf, 'LineWidth',3)
hold on
xlabel('Frequency, (MHz)','fontsize',42,'fontweight','b');
ylabel('Amplitude, (dBm)','fontsize',42,'fontweight','b');
hold on
```

To determine the effective loss tangent $\tan\delta_{eff}$ (Eq. 5) and dielectric permittivity ϵ_{eff} (Eq. 4) the following function was used for the helical inner conductor:

```
function F = iox_feed_epoxy_coax_resonator_spiral(x,f)
% dielectric constant of epoxy, defined from the simulation in the
% previously work
e_epoxy = 1.96;
h=0.267+0.029; % the total length of the resonator with epoxy on the bottom [m],
% note: epoxy on the bottom of the sensor
h_epoxy=0.062; % the length of the layer of epoxy [m]
db=25e-3; % diameter of the resonator;
%Er1 = 2.4; %dielectric permittivity of polymer layer, [-]
Er1=2.32%dielectric permittivity of polymer layer, [-]
Vt=pi*h*db^2/4; %volume of the empty resonator [m^3]
Vt_epoxy=pi*h_epoxy*db^2/4 % volume of epoxy resin in the resonator
```

```

f_epoxy=(pi*h_epoxy*db^2/4)/Vt % volume fraction of epoxy resin in the resonator
Vt_feed=Vt-Vt_epoxy %volume of the filled with epoxy resonator [m^3]
f_feed=Vt_feed/Vt %volume of feed substrate in the filled with epoxy resonator [m^3]
f_feed_t=1-f_epoxy %volume fraction of feed substrate excluding epoxy in the filled with epoxy resonator
[m^3]
len =0.9+0.029; % length of the coax resonator [m]
b = 25e-3; % inner diameter of the outer conductor [m]
a = 1e-3;% outer diameter of the inner conductor [m]
c=3*1e+8; % speed of light in vacuum [m/s]
Ur=1; %relative dielectric permeability of the dielectric between inner and outer conductors [-]
u = Ur*4*pi*1e-7; % magnetic permeability of the dielectric [H/m]
sigma_stainless_steel=1.45e+6;%conductance of the metal applied for inner and outer conductors (stainless
steel) [1/(Ohm*m)]
sigma_copper=5.96e+7;%conductance of the metal applied for inner conductor ( copper),
[1/(Ohm*m)]%effective conductance of both feed substrate and epoxy resin
% sigma_eff=sigma_feed*f_feed_t+sigma_epoxy*f_epoxy;
%effective dielectric permittivity of both feed substrate and epoxy resin
Er_feed_iox=x(2);
Eeff_ep_air=Er_feed_iox*(f_feed_t)+e_epoxy*f_epoxy;
r2 = (25.4e-3)/2; %inner radius of the outer conductor, [m]
r0 = (1e-3)/2; %radius of the inner conductor of the resonator, [m]
Er2 =Eeff_ep_air % dielectric permittivity of a fluid substrate, [-]
Ur =1; %relative dielectric permeability of the dielectric between inner and outer conductors, [-]
e = 8.854e-12; % vacuum permeability [H/m]
u = Ur*1.257e-6;% magnetic permeability of the dielectric, [H/m]
r1=r0+0.5e-3/2; %radius of the inner conductor and outer radius of the polymer layer (m);
c=3*1e+8; % speed of light in vacuum, [m/s]
% capacitance of the open ended coaxial stub resonator, contains the oxide layer, [F/m]
C1=2*pi*e*Er1/(log(r1/r0))
% capacitance of the open ended coaxial stub resonator, contains a fluid, [F/m]
C2=2*pi*e*Er2/(log(r2/r1))
% total capacitance of the open ended coaxial stub resonator, [F/m]
C=1/(1/C1+1/C2)
% inductance of the open ended coaxial stub resonator, [H/m]
L = ((u/(pi*2))*log(r2/r0))
Eeff_coax=(Er1*Er2*log(r2/r0))/((Er1*log(r2/r1)+Er2*log(r1/r0)))% effective dielectric constant of whole
system, [-]
Eeff=Eeff_coax
E= Eeff * 1/(4*pi*1e-7*c*c); % vacuum permeability [H/m]
sigma_eff=0; % effective conductivity of the system, [S/m]
%Define the input voltage supplied by the function generator [V]
vin=80e-3; %input voltage supplied by the function generator [V]
omega = 2*pi*f;% angular frequency [rad/s]
Eim=((omega.*E.*x(1))-sigma_eff)./omega;%imaginary part of complex dielectric permittivity
skin_depth1=sqrt(2./(omega.*u.*sigma_stainless_steel));%skin_depth
skin_depth2=sqrt(2./(omega.*u.*sigma_copper));%skin_depth
Rs1=1./(sigma_stainless_steel.*skin_depth1);% surface resistivity of the outer conductor of the resonator
Rs2=1./(sigma_copper.*skin_depth2);% surface resistivity of the inner conductor of the resonator
R=Rs2/r0+Rs1/r2;% distributed element resistance R of the resonator [Ohm/m]
G=(omega.*Eim+sigma_eff)./(omega.*E).*omega.*C;%distributed element conductance of the resonator
[F/(m*s)]
gamma =(sqrt((R+1i.*omega.*L).*(G+1i.*omega.*C)))/omega;%complex propagation constant [1/m]
%notes on gamma: Re(gamma)=alfa = attenuation constant representing losses [Np/m];
Im(gamma)=beta=phase of the propagation constant [rad/m]
%since the signal is oscillating in time with omega rad/s, the propagation velocity of the wave [m/s] =
omega/beta; also, beta = 2*pi/wavelength.

```

```
Zc=sqrt(((R+1i.*omega.*L)/(G+1i.*omega.*C)));% complex characteristic impedance of the resonator [Ohm]
Zin=Zc.*coth(gamma.*len);%complex input impedance of the resonator [Ohm]
vout=sqrt((real(Zin.*(vin./(50+2*Zin))).^2+(imag(Zin.*(vin./(50+2*Zin))).^2);%modulus of vout, the is the
recorded voltage by the spectrum analyzer [V]
F =20.*log10(vout)+13;%vout as a power ratio in dBm i.e., the measured power referenced to one mWatt and
the underlying assumption of a 50 Ohm load resistance
```

The main program was:

```
clear all % Clear all variables in function workspace
close all % Close all figures
clc % Clear command window
clearvars
format longE
load spiral_fith_nd.txt % load the file with data of the day of experiment
f=spiral_fith_nd(:,1); % Load experimental data; frequency
amplitude=spiral_fith_nd(:,2); % Load experimental data; amplitude
f=f*1e+6; % Frequency conversion
%- Plot experimental data
hF = figure
hA = axes
set(hA, 'XGrid', 'off', 'YGrid', 'on')
hold on
set(0,'DefaultFontSize',36,'DefaultFontName','Times New Roman', 'DefaultFontWeight', 'bold');
plot(f/1e+6, amplitude, 'LineStyle','none','Marker','.', 'MarkerEdgeColor','r', 'MarkerSize',35);
hold on
x0 = [0 1];
ya0 = iox_feed_epoxy_coax_resonator_spiral(x0,f);
% % - Plot initial values
% hold on;
% plot(f,ya0,'--m')
%-Boundary conditions
LB = [0 1]; % Lower bounds
UB = [1 100]; %Upper bounds
% LB = [0]; % Lower bounds
% UB = [1]; %Upper bounds
% -Solving nonlinear least-squares curve fitting
[x,resnorm] = lsqcurvefit('iox_feed_epoxy_coax_resonator_spiral',x0,f,amplitude, LB, UB)
ya = iox_feed_epoxy_coax_resonator_spiral(x,f);
%- Plot fit results
Hf = plot(f/1e+6,ya,'b');
set(Hf, 'LineWidth',3)
hold on
xlabel('Frequency, (MHz)', 'fontsize',42, 'fontweight', 'b');
ylabel('Amplitude, (dBm)', 'fontsize',42, 'fontweight', 'b');
hold on
```

Appendix D

In order to obtain a qualitative impression on the influence of the HA load of the AER on the regeneration efficiency of the AER, a number of batch experiments were executed, applying the following procedure:

1. The batch resonator was filled with new (never used) AER that was loaded with chloride ions according to the procedure in the Materials and Methods part, section Anion Exchange Resin (AER).

2. A desired concentration of HA was dissolved in 150 ml of tap water, resulting in a HA solution, such that an AER load degree of 0.5 g/l (1 g/l, 1.5 g/l, 2 g/l, and 3 g/l) was obtained.

3. A photo was made of the HA solution obtained in step 2 to get a qualitative impression on the HA concentration in the solution.

4. 100 ml of AER were added to the HA solution and the mixture was stirred during 30 minutes using a magnetic stirrer (slow stirring speed)

5. The dispersion of AER in the HA solution was filtered using a Buchner filter.

6. A photo was taken of the filtrate to get an impression on the HA concentration in solution after the AER loading process.

7. A photo was made from the AER to get a qualitative impression of the amount of HA adsorbed by the AER.

8. The AER loaded with 0.5 g/l (1 g/l, 1.5 g/l, 2 g/l, and 3 g/l) HA was regenerated using the procedure in the Materials and Methods part, section Anion Exchange Resin (AER).

9. Photos were made from the AER and the regeneration solution to get an impression on the efficiency of the regeneration procedure.

10. Subsequently, this regenerated AER was loaded for the second time with 0.5 g/l (1 g/l, 1.5 g/l, 2 g/l, and 3 g/l) of HA load, applying steps 3 to 5.

11. Finally, pictures were made from the AER and the filtrate to get a qualitative impression on the efficiency of the second adsorption step.

Tables D.1 a D.2 show the results of the batch experiments executed according to the procedure in steps 1-11.

Table D.1.

Color of the different solutions.



































Solution	HA	After 1 st adsorption	After regeneration	After 2 nd adsorption
0.5 g/l				
1 g/l				
1.5 g/l				
2 g/l				
3 g/l				

Table D.2.

Colour of the ion exchange resin for the different steps.

Resin	After 1 st adsorption	After regeneration	After 2 nd adsorption
0.5 g/l			
1 g/l			
1.5 g/l			
2 g/l		X	
3 g/l			

^xPicture of sample reg_2HA is not there because a sample of was not taken.

The results in table D1 and D2 reveal that for HA load degrees on the AER higher than about 1 g/l, the AER is not regenerated efficiently using the procedure applied in the Materials and Methods part, section Anion Exchange Resin (AER).

Fig. D. 6 shows SEM pictures of the surface of AER beads after the first and second adsorption of 1 g/l of HA. In the image for second adsorption, dark spots appear pointed towards a modification of the AER surface after the second adsorption step.

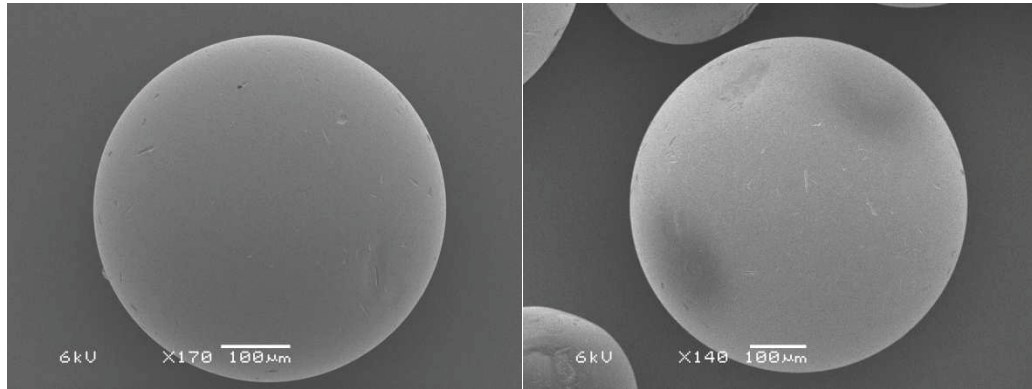


Fig. C.6. SEM images of ion exchange resin, respectively after 1st and 2nd adsorption of 1 g/l HA.

Appendix E

Figure E.1 shows the changes in the AF plots due to an effect of tap water and the regeneration fluid (10%NaCl+2%NaOH).

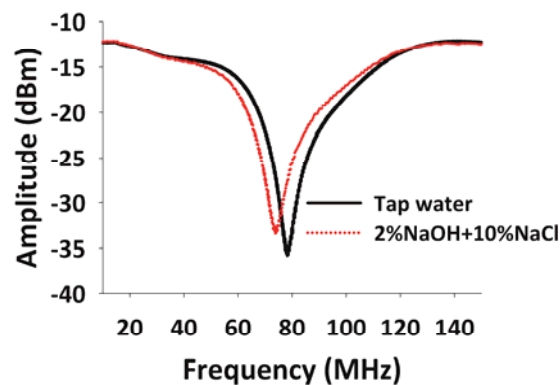


Fig. E.1. The amplitude versus frequency or AF plots as an effect of tap water and the regeneration fluid (10%NaCl+2%NaOH) using the batch resonator in the frequency range of 5-150 MHz.



Little Tower of Drienerlo, University Twente, Enschede

Chapter 8

General Discussion and Perspectives



Abstract

Even though currently existing technology is able to monitor the presence of microorganisms and pollutions, quite often the detection limits remain too high [1 - 3]. To remedy this lack of sensitivity demands sensor designs based on entirely different concepts. This thesis focuses on the development of a new sensor platform based on transmission line resonators and suitable for different sensor applications. The preceding chapters demonstrated the proof-of-principle of this technology for several applications, ranging from fluid composition to biofilm formation. In this final chapter we discuss several technical improvements to enhance resonator behavior:

- inner conductors of different periodic structure;
- minimization of the finite length of transmission line connectors;
- combining stacks of PCBs and transmission line technology;
- miniaturization of the coaxial type resonator;
- inner conductors coated with selective absorption layers;
- determination of the complex characteristic of a dielectric;
- role of temperature.

8.1 Inner conductors of different periodic structure

The shape of the inner conductor of stub resonators can adopt different geometries, with the straight one (discussed most frequently so far) perhaps just as the most obvious option. But there are alternatives and Fig. 1 shows two of them based on a different periodic structure, either the helical (1A) or the rack-type (1B) [4].

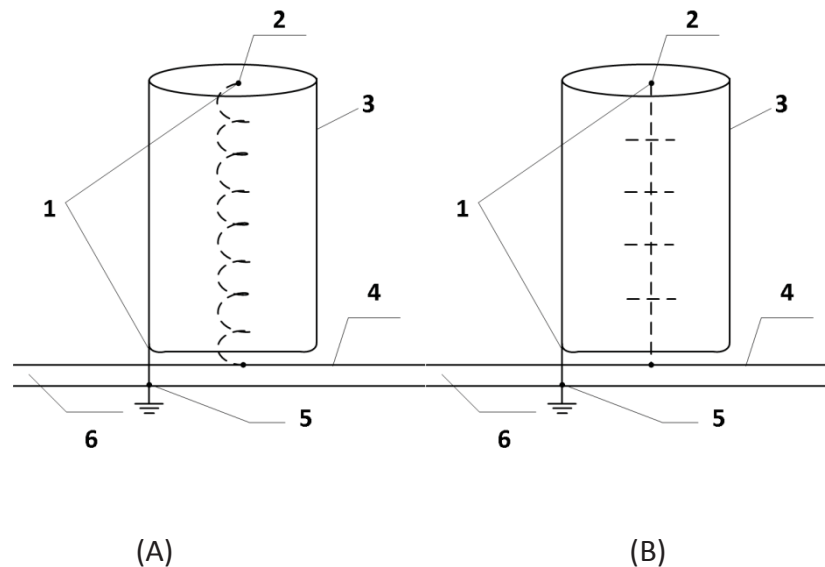


Fig. 1. Schematic overview of a coaxial stub resonator (1) with an inner conductor (2) of different periodic geometry, either helical (A) or rack-type (B). Indicated are: outer conductor (3), signal wire (4), ground wire (5), and main transmission line (6).

The behavior of the resonator depends to a certain extent on the type of inner conductor applied. Fig. 2 and 3 compare AF plots obtained with a resonator possessing a straight (SIC) inner conductor with those obtained using a resonator with either the helical-type (SSIC) or rack-type (RSIC) resonator, with the resonator filled with air (Fig. 2) or tap water (Fig. 3). As is obvious from Figs. 2 and 3, the higher the periodicity (SSIC>RSIC>SIC), the larger the number of resonances in a given frequency range. In addition, a higher periodicity and by implication, a longer total (effective) electric length of the inner conductor, shifts the resonance frequency of the first (base) resonance to a lower frequency.

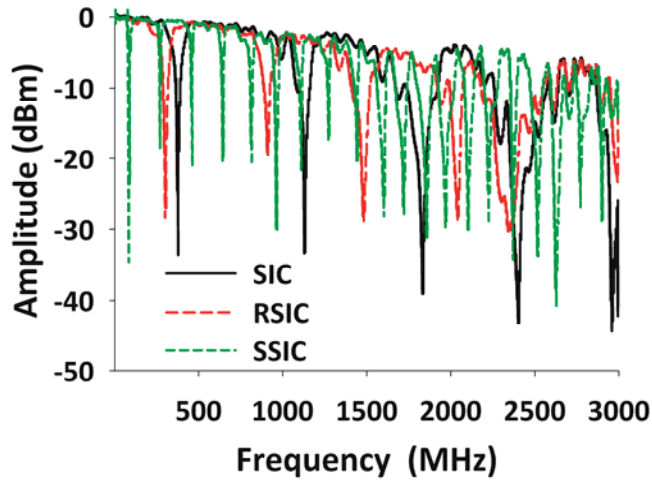


Fig. 2. AF plots with air as dielectric between the two conductors of the resonator. Used geometry of inner conductor: SIC-straight, SSIC-spiral (or helical) and RSIC-rack. (1000 point/scan).

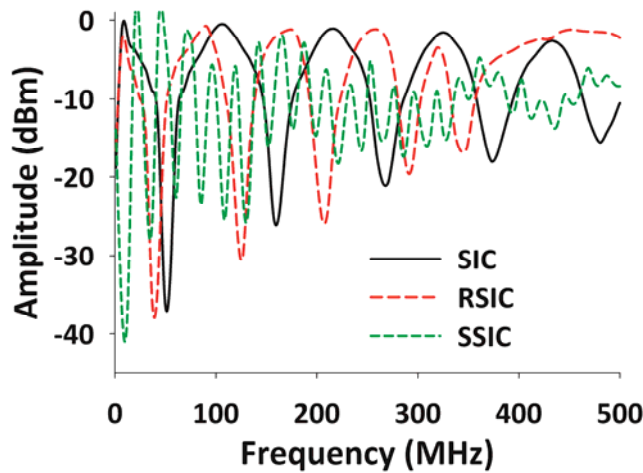


Fig. 3. AF plots with tap water as dielectric between the two conductors of the resonator. Used geometry of inner conductor: SIC-straight, SSIC-spiral (or helical) and RSIC-rack. (1000 point/scan).

Figure 4 shows an entirely different design of a transmission line-based resonator, the stripline, essentially the 2D analog of the coaxial-type resonator. Also for this design can the (effective) electric length be increased by applying the concept of an inner conductor with periodic structure, in this particular case rectangular-shaped.

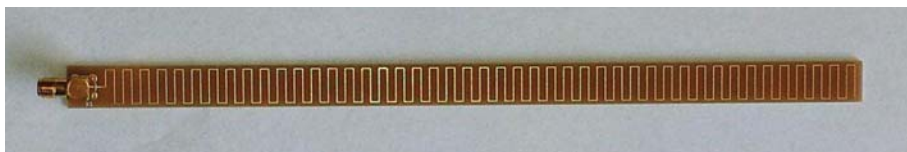


Fig. 4. Stripline resonator with meandering rectangular-shaped inner conductor.

Fig. 5 features preliminary results obtained with this design, showing the AF response after applying water with different sugar content (0-100 gr/l equivalent to 0-0.29 mol/l). As shown by Fig. 5 and 6, an effect is observable at a concentration of 0.015 mol/l, the lowest sugar concentration tested, notably at higher frequencies. Another conclusion arising from Fig. 5 is that, in general, effects of sugar are more pronounced at higher frequencies. This increased sensitivity at higher frequencies can be explained in general by the fact that for a certain change in ϵ_r (e.g., due to a change in sugar concentration), the shift of f_{res} (Δf_{res}) is proportional to $c(2n-1)/4l$, implying a larger shift at higher n , i.e., at higher resonance frequencies.

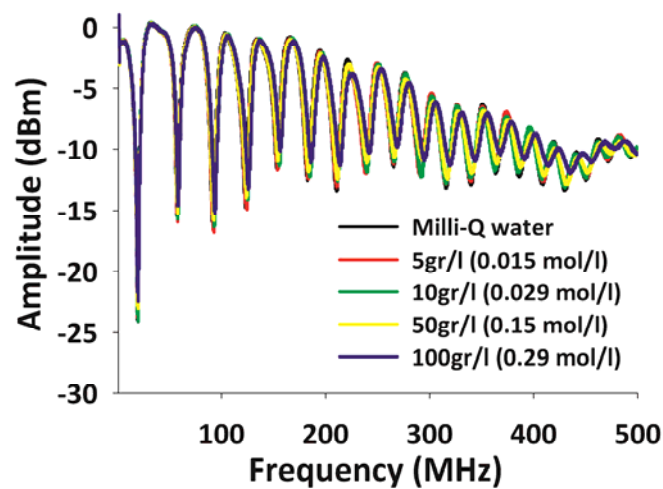


Fig. 5. AF plots obtained with the stripline resonator of Fig. 4 in response to Milli-Q water (with conductivity of 10^{-4} S/m) containing different concentration of sugar (1000 point/scan). Temperature: 18 ± 0.5 °C.

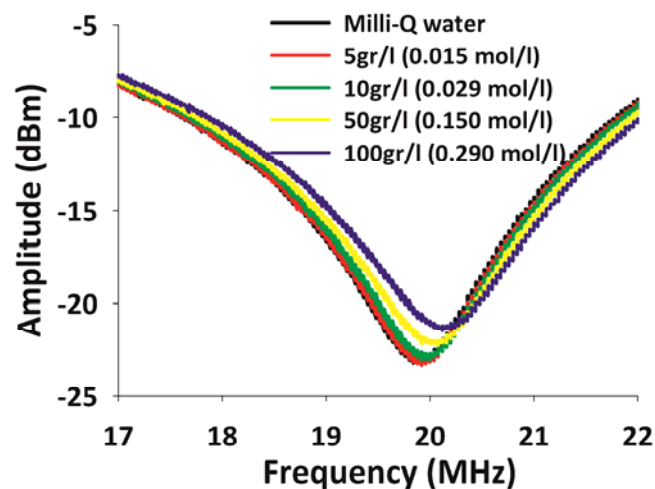


Fig. 6. The first resonance of Fig. 5 shown in more detail.

In conclusion, a straight (i.e., short) inner conductor evokes resonance frequencies at relatively high frequency, resulting in enhanced sensitivity of the measurement because dielectric dispersions effects become more prominent at higher frequency. On the other hand, the helical or rack-type (i.e., long) inner conductor shifts the resonance frequency into a lower frequency range. The practical, if not commercial, implication is that the measurement can be performed with substantially less expensive electronic equipment, for instance, a low price function generator and detector (spectra analyzer in this particular case).

Future experiments will shed more light on the pro's and contra's of the different designs, all in the context of the intended application and desired cost price of the sensor device.

8.2 Minimization of the finite length of transmission line connectors

As argued and demonstrated in the previous paragraph, the (effective electric) length of the stub resonator plays a significant role in the AF response of the system. It is for this reason that connecting the stub resonator to the main transmission line can be quite challenging, especially for the coaxial stub resonator [13 - 16]. The reason is that the connectors used increase the (effective) length of the total transmission line because they function and behave as transmission line themselves. A possible solution is to avoid generally used SMA and/or BNC connectors all together or, alternatively, to connect them entirely differently. Fig. 7 shows an example of how that can be achieved, based on printed circuit transmission lines [14].

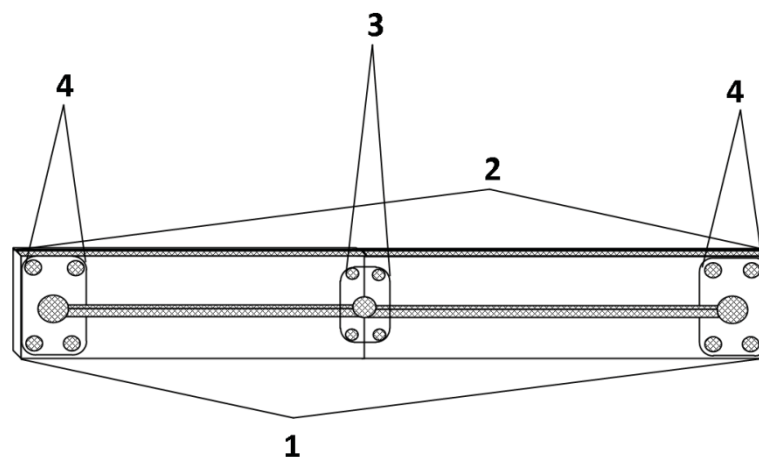


Fig. 7. Schematic view of a printed circuit transmission line (1), positioned on a metal ground plane (2), with slots for inner and outer conductor (3) of the coaxial stub resonator (in the center) and two SMA connectors (4).

One consequence of the design of Fig. 7 is however that we substitute a classic coax transmission line of $50\ \Omega$ by a printed circuit transmission line with different impedance. To account for the resulting impedance mismatch, the structure shown in Fig. 8 can be used.

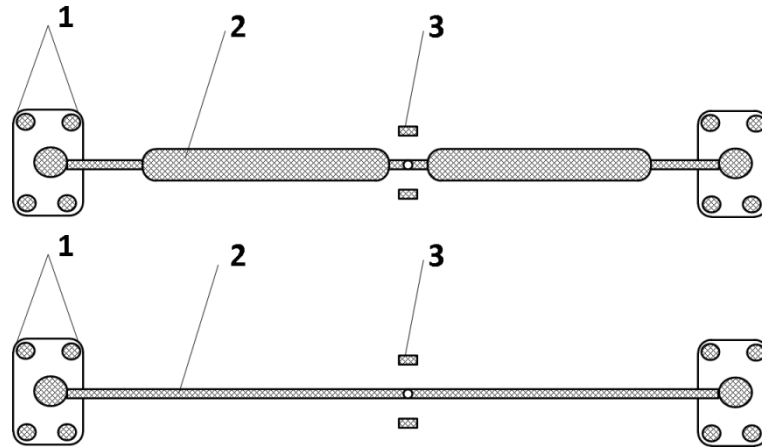


Fig. 8. Back (top) and front (bottom) of the printed circuit transmission line shown in Fig. 7, with slots for SMA connectors (1), the signal transmission line (2) and the connection of the outer conductor to the ground plane (3).

A photo of such a printed circuit transmission line is shown in Fig. 9.

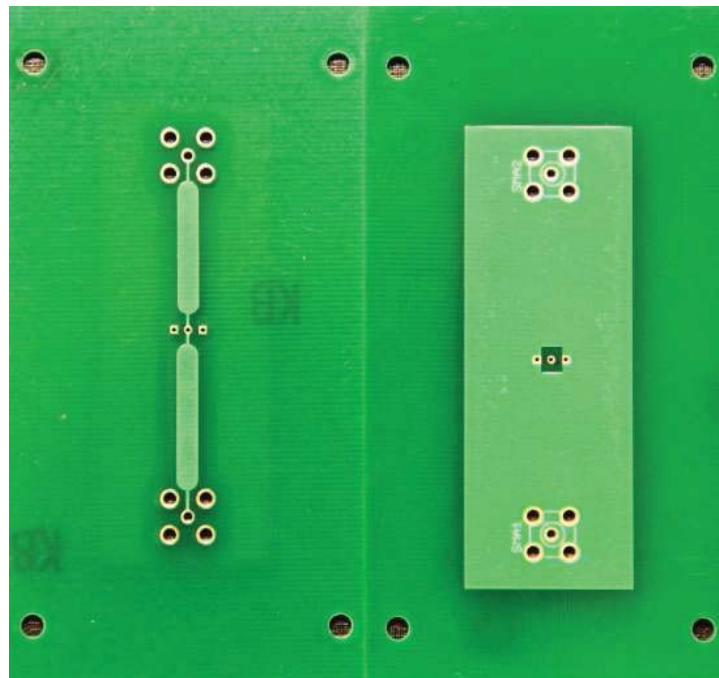


Fig. 9. Photo of a printed circuit transmission line with slots for inner and outer conductor of the coaxial stub resonator (in the center) and two SMA connectors.

8.3 Combining stacks of PCBs and transmission line technology

As argued in the previous paragraph, the sensitivity of transmission line resonators is determined not only by the design of the stub resonator but in addition also by the electric connections between stub resonator and the main the transmission line. Here we demonstrate a design solution using stacks of PCBs [17 - 20].

Fig. 10 shows a design comprising three layers of printed circuit board (PCB) with the stripline resonator printed on PCB no. 1. The two remaining PCBs form the electrical interface for connecting the resonator to the main transmission line.

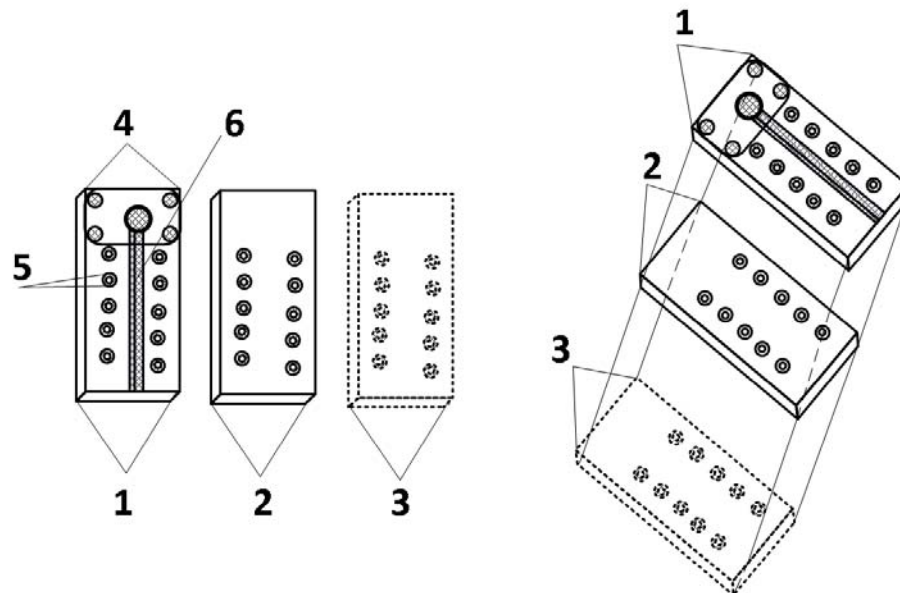


Fig. 10. Schematic view of a stack of three PCBs (1-3). The stripline resonator with signal wire (6) is printed on PCB no. 1, also containing a slot for a SMA connector (4). Conductive (metal) holes (5) in PCB no. 1 and 2 are distributed uniformly all over the PCB surface area.

8.4 Miniaturization of the stub resonator sensor

In general, miniaturization increases the sensitivity of stub resonators because they shift the resonance frequency even further into the high frequency range. One way to achieve miniaturization of the system is combining a prototype based on coaxial stub microfluidic impedance transformer (COSMIX) technology [8] and the coaxial stub resonator technology presented in this thesis. An example is shown in Fig. 11, a coax stub resonator of 2 cm length with the main transmission lines connected using printed circuit transmission lines. Note that this design allows flow-through of the measured solution.

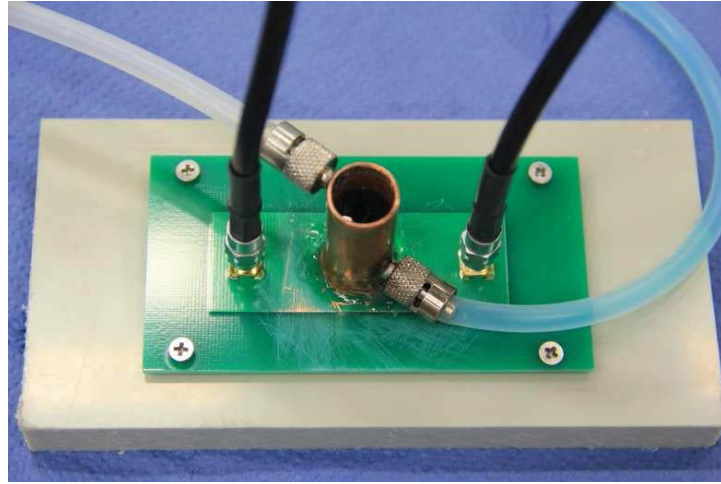


Fig. 11. A coaxial stub resonator of 2cm length connected to the main transmission line by means of printed circuit transmission lines.

As an example, combining the designs of [8] and [12] results in a quarter-wave stub resonator (with length of around 0.5 cm) with a base resonance frequency of 1.6 GHz if filled with water of dielectric permittivity of 80.

The (measured) dielectric permittivity of both liquids and solids depends to a large extent on the frequency used, from constant (ϵ_0) at low frequencies to a smaller limiting value ϵ_∞ at higher frequencies. This effect of frequency on the calculated ϵ value is caused by polarization effects of the material under investigation. Debye theory provides a theoretical framework to quantify this effect using a single dielectric relaxation time constant τ . The value of ϵ_0 and ϵ_∞ are related by the following expressions:

$$\epsilon_r = \epsilon_{re} - j\epsilon_{im} \quad (1)$$

$$\epsilon_{re} = \epsilon_\infty + \frac{\epsilon_0 - \epsilon_\infty}{1 + \omega^2 \tau^2} \quad (2)$$

$$\epsilon_{im} = (\epsilon_0 - \epsilon_\infty) \frac{\tau}{1 + \omega^2 \tau^2} \quad (3)$$

where

ϵ_r , relative dielectric permittivity (-);

ϵ_{re} , the real part of the complex dielectric permittivity ϵ_r (-);

- ϵ_{im} , the imaginary part of the complex dielectric permittivity ϵ_r (-);
- ϵ_0 , static dielectric constant of the solution (-);
- ϵ_{∞} , optical dielectric constant of the solution (-);
- τ , relaxation time (s);
- σ , ionic conductivity of the dissolved salts, (S/m, mho/m 1S/m=1mho/m);
- ω , angular frequency, $\omega=2\pi f$ (rad/s).

Measuring at high frequency (accomplished by miniaturization) thus offers extra information of the dielectric properties of the sample under study, ϵ_{im} , i.e., the dielectric losses of the system representing a material characteristic, as is ϵ_0 . In case of a composite material, e.g., a mixture of fluids, the system is characterized by multiple τ values, one for each component [9 - 11].

Moreover, considering the skin effect, characteristic impedance and even multi-modes, future plans include improving the sensitivity and miniaturization of the sensor based on the optimization of the geometry and depending on the application.

8.5 Inner conductors coated with selective absorption layers

In parallel to the PhD study presented here, in the framework of the Wetsus Sensoring theme, at Delft university PhD student Judith Stagnus explored the feasibility of a so-called capacitive sensor. Aim of this project is to develop a sensor that measures impurities in water [1, 6]. Figure 12 shows a schematic view of the concept of the Delft sensor. The working mechanism is based on the capacitive response of interdigitated electrodes (IDEs) coated with a selective absorption polymer layer. The selectivity of the sensor arises from the chemical properties of the coating used. The work of Judith Stagnus reveals that the capacitive response of the IDEs, covered with a thin layer of polydimethyl siloxane, enables detection of volatile organic compounds (VOCs) in water. Further, that the sensor response changes during absorption and desorption of VOCs were fully reversible.

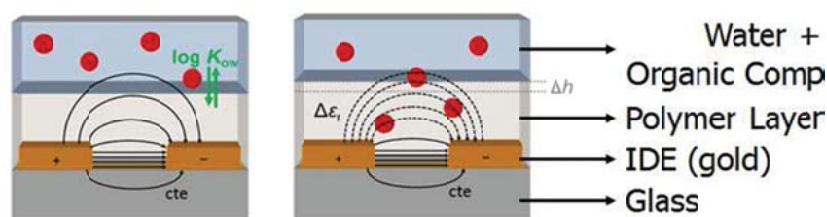


Fig. 10. Artistic view of the Delft capacitive sensor with the IDE electrode coated with a selective polymer absorption layer (PhD project of Judith Stagnus [7]).

Aim of a next Wetsus/Delft project, starting July 1st 2014, is to integrate the two lines of research i.e., the R&D on the capacitive sensor platform with a polymer adsorption layer [1 - 6] and the R&D on transmission line sensors presented in this thesis into a completely new sensor platform technology. In a nutshell, this new technology comprises the coating of a microstripline shown in Fig. 4 with polymers having very specific and reversible absorption properties.

The new platform is expected to combine the “best of two worlds” i.e.,:

- high sensitivity (impurity concentration through absorption);
- high selectivity (specific absorption properties of the polymer combined with broad frequency range dielectric spectroscopy);
- low noise (very small parasitic capacities due to the use of transmission line technology);
- low / no drift (possibilities to use the transient of the response rather than absolute signal changes to detect the level of impurities);
- possibilities for miniaturization (e.g., meander stripline as consumable in a hand held device);
- no need of using expensive electrical equipment thanks to the “long effective resonator length” resulting from the meander microstrip technology and the related high quality factor of the resonator.

8.6 Determination of the complex characteristic of a dielectric

The diagram of Fig. 13 schematically depicts the steps required to determine the (complex) dielectric properties of a fluid (or solid) using transmission line-based technology. The obtained parameters can then be used for extensive modeling (as outlined in Chapter 3) or simulation of AF responses allowing comparison with experimental data.

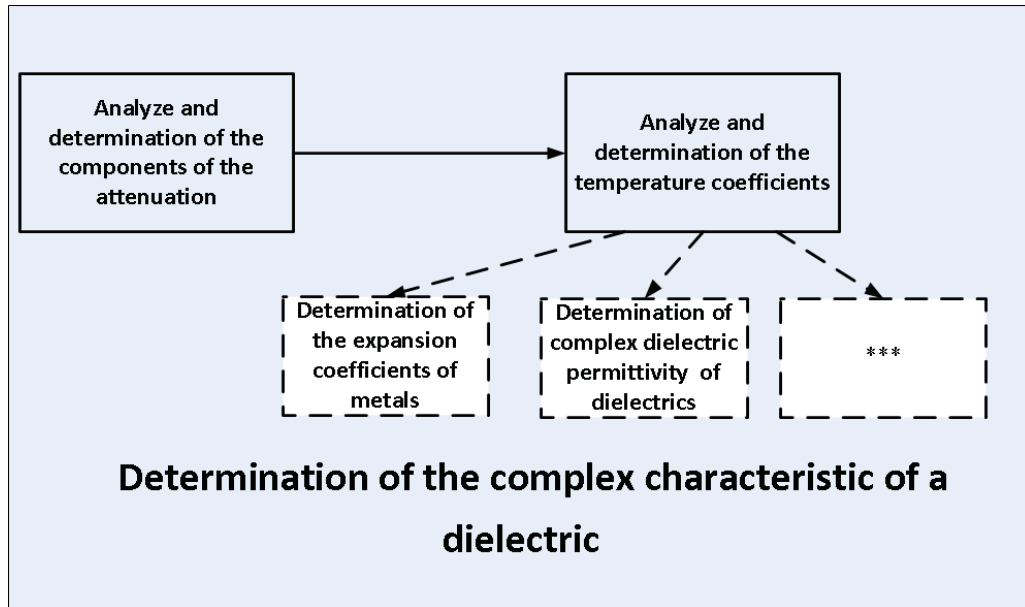


Fig. 11. General algorithm for the determination of the complex dielectric properties of materials. Dotted lines and ellipsis (***) indicate an available and/or additional components which depend on the type of the resonator.

Starting on the left in the diagram, the four main sources of attenuation in a lossy-type of transmission line are losses due to metal loss α_C , dielectric loss tangent α_D , dielectric conductivity α_G and stray radiation α_R [21 - 22].

$$\alpha = \alpha_C + \alpha_D + \alpha_G + \alpha_R \quad (4)$$

In the microwave frequency range, the overall loss of transmission lines filled with a low-loss dielectric is dominated by α_C (5):

$$\alpha_C = \frac{R_s}{2Z_c} \quad (5)$$

where

R_s , surface resistivity [Ω],

Z_c , complex characteristic impedance [Ω].

Losses due to dielectric loss tangent $\tan\delta_{eff}$ are given by [12]:

$$\alpha_D = \tan\delta_{eff} \frac{\omega CZ_c}{2} \quad (6)$$

In general, the loss due to the conductivity of the dielectric α_G is considered to be a frequency-independent parameter, given by Eq. (4). However, this assumption is valid only for low-loss dielectrics, as shown by Eqs. (7-10):

$$\alpha_G = \frac{GZ_c}{2} \quad (7)$$

$$G = \omega \cdot C \cdot \tan\delta_{eff} \quad (8)$$

$$\tan\delta_{eff} = \frac{\omega\epsilon_{im} + \sigma}{\omega\epsilon_{re}} \quad (9)$$

$$G = \omega \cdot C \cdot \tan\delta = \omega \cdot \frac{\omega\epsilon_{im} + \sigma}{\omega\epsilon_{re}} \cdot C \quad (10)$$

where

C , distributed capacitance (F/m);

$\tan\delta_{eff}$, dielectric loss tangent (-);

G , distributed dielectric conductance (S/m).

The contribution of stray radiation α_R to the overall attenuation is normally very small, around 2% [24].

Temperature coefficients

Changes in temperature not only lead to changes in resonance frequency but also affect the shape of the AF response. Four temperature coefficients (TC) can be distinguished: TC of the dielectric constant, TC of the cavity, TC of thermal expansion and TC of the resonance frequency, actually a function of the three other TCs mentioned [22]:

TC of dielectric permittivity

$$\tau_{\varepsilon} = \frac{1}{\varepsilon_{\tau}} \cdot \frac{\Delta\varepsilon_{\tau}}{\Delta T} \quad (11)$$

TC of cavity

$$\tau_c = \frac{1}{L} \cdot \frac{\Delta L}{\Delta T} \quad (12)$$

TC of thermal expansion

$$\alpha_L = \frac{1}{H} \cdot \frac{\Delta H}{\Delta T} = \frac{1}{D} \cdot \frac{\Delta D}{\Delta T} \quad (13)$$

TC of resonant frequency

$$\tau_f = \frac{1}{f_0} \cdot \frac{\Delta f_0}{\Delta T} \quad (14)$$

where

Δf_0 , the total frequency variation corresponding to the temperature shift ΔT ,

ε_{τ} , the variation of dielectric permittivity,

ΔL , the cavity expansion,

ΔH and ΔD , the resonator material linear expansions.

Complex characteristic impedance

The general expression for the complex characteristic impedance Z_c of a transmission line filled with lossy dielectric is given by:

$$Z_c = \sqrt{(R + j\omega L)/(G + j\omega C)} \quad (15)$$

where

C , distributed capacitance (F/m);

L , inductance per meter (H/m)

R , resistance per meter (Ω /m)

G , distributed dielectric conductance (S/m).

Example of using TC for coaxial resonator

In the following example cavity expansion was considered to be negligible, implying that it is assumed that the temperature change does not affect the length of the sample.

At the initial temperature, the characteristic impedance of the coaxial transmission line is defined by:

$$Z_c = \sqrt{\frac{\mu_0 \mu_r}{\epsilon_0 \epsilon_r}} \cdot \frac{\ln(b/a)}{2\pi} \quad (16)$$

where

μ_0 , magnetic permeability of free space (vacuum permeability), (H·m-1): $\mu_0 = 4\pi \cdot 10^{-7}$;

μ_r , relative magnetic permeability (-);

ϵ_0 , dielectric permittivity of free space (vacuum permittivity), (F·m-1): $\epsilon_0 = 1/(\mu_0 \cdot c^2)$;

b , inner diameter of outer conductor (m);

a , outer diameter of inner conductor (m).

The change in impedance ΔZ_0 as function of temperature, due to thermal expansion αL , can be written as:

$$\Delta Z_0 = \sqrt{\frac{\mu_0 \mu_r}{\epsilon_0 \epsilon_r}} \cdot \frac{\ln(b(1 + \alpha(b) \cdot \Delta T) / a(1 + \alpha(a) \cdot \Delta T))}{2\pi} \quad (17)$$

where

$\alpha(a)$, expansion coefficient of inner conductor,

$\alpha(b)$, expansion coefficient of outer conductor.

For instance, the expansion coefficients of copper and steel are $17 \cdot 10^{-6}/^{\circ}\text{C}$ and $11 \cdot 10^{-6}/^{\circ}\text{C}$, respectively [24].

Taking into account the TC of dielectric permittivity τ_{ϵ} , the expression for the characteristic impedance of the coaxial line is defined as:

$$Z_c = \frac{V_0}{I_0} = \sqrt{\frac{\mu_0 \mu_r}{\epsilon_0^* \epsilon_r (1 + \tau_{\epsilon})}} \cdot \frac{\ln(b(1 + \alpha(b) \cdot \Delta T) / a(1 + \alpha(a) \cdot \Delta T))}{2\pi} \quad (18)$$

Mathematical models and solutions

The complex dielectric permittivity of saline water is given by Debye:

$$\epsilon = \epsilon_{\infty} + \frac{\epsilon_0 - \epsilon_{\infty}}{1 - i\tau\omega} + \frac{i\sigma}{\epsilon_0\omega} \quad (19)$$

There are several well-known dielectric models describing both the static dielectric constant ϵ_0 and optical dielectric constant ϵ_{∞} of a solution as function of salt concentration and temperature [25 - 27].

Fig. 12 shows typical AF responses obtained from tap water at different temperature using the coaxial stub resonator. The preliminary results show experimental data close to the theoretical predictions by Eqs. 17 and 18. It should be mentioned that temperature affects both the real ϵ_{re} and imaginary ϵ_{im} part of the complex dielectric permittivity ϵ_{eff} . Since the proposed system measures the module of the complex effective dielectric permittivity ϵ_{eff} , the resonance frequency shifts to lower or higher frequency, depending on the relative sensitivity to temperature of ϵ_{im} (related to conductivity losses due to the ion species present) and ϵ_{re} (related to the stored energy). As can be seen in Fig. 11, the temperature response of the 1st resonance is dominated by the temperature effect on ϵ_{re} , whereas the response of the 2nd and 3rd resonance is dominated by the temperature effect on ϵ_{im} .

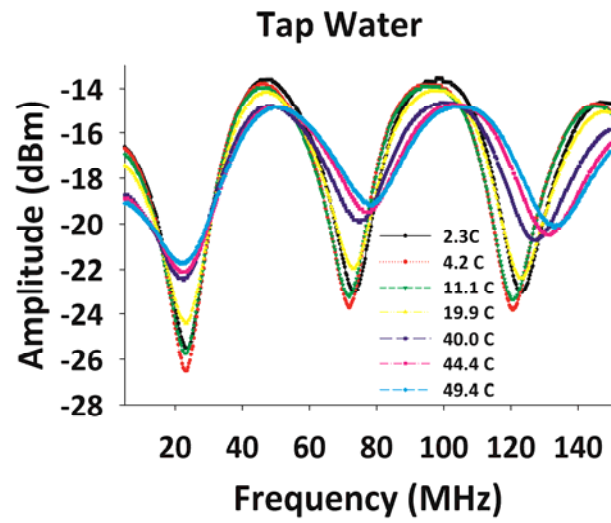


Fig. 12. AF responses obtained with a coaxial batch resonator of 34 cm length, with tap water of different temperature as dielectric.

8.7 References

1. T. Fen-Chong, A. Fabbri, J.-P. Guilbaud, O. Coussy, Determination of liquid water content and dielectric constant in porous media by the capacitive method *Comptes Rendus Mecanique*, Volume 332, Issue 8, August 2004, 639-645.
2. Fl.-G. Banica, Chemical sensors and biosensors: Fundamentals and applications, *J Analytical and Bioanalytical Chemistry*, V 405, N 16, 15 AUG 2012, doi: <http://dx.doi.org/10.1007/s00216-013-6870-9>
3. <http://epa.gov/ncer/publications/workshop/pdf/microproceedings061807.pdf>
4. V.V.Nikol'skii, T. I. Nikol'skaia, *Electrodynamics and propagation of radio waves*, Moscow, Izdatel'stvo Nauka, 1989, 544 p. In Russian.
5. J. Stagnus, I. M Aerts, Z.-Y. Chang, G.C.M. Meijer, L.C.P.M. de Smet, E.J.R. Sudhölter, Capacitive Response of PDMS-coated IDE Platforms Directly Exposed to Aqueous Solutions Containing Volatile Organic Compounds, *Sensors & Actuators, B: Chemical* 2013, 184, 130-142.
6. M.J.J. Mayer, L.C.P.M. de Smet, E.J.R. Sudhölter, Capacitance electrode and sensor-system capable of sensing contaminants and method therefor, International Patent Application WO2010/050806 A1.
7. <http://si.epfl.ch/page-67214-en.html>
8. G. H. Huff, S. Goldberger, A Coaxial Stub Microfluidic Impedance Transformer (COSMIX), *Microwave and Wireless Components Letters, IEEE* , vol.20, no.3, pp.154,156, March 2010 doi: 10.1109/LMWC.2010.2040217
9. Sudo, Naoki Shinyashiki, Yusuke Kitsuki, and, and Shin Yagihara, Dielectric Relaxation Time and Relaxation Time Distribution of Alcohol–Water Mixtures Seiichi, *The Journal of Physical Chemistry A* 2002 106 (3), 458-464.
10. C. M. Roland and K. L. Ngai, Segmental relaxation and the correlation of time and temperature dependencies in poly (vinyl methyl ether)/polystyrene mixtures, *Macromolecules* 1992 25 (1), 363-367.
11. Satoru. Mashimo, Shinichi. Kuwabara, Shin. Yagihara, and Keniti. Higasi, Dielectric relaxation time and structure of bound water in biological materials, *The Journal of Physical Chemistry* 1987 91 (25), 6337-6338.
12. N. A. Hoog, M. J.J. Mayer, H. Miedema, W. Olthuis, F. B. J. Leferink, A. van den Berg, Modeling and Simulations of the Amplitude-Frequency Response of Transmission Line Type Resonators Filled with Lossy Dielectric Fluids, Manuscript Number: SNA-D-13-01258R2 has been accepted for publication in *Sensors & Actuators: A. Physical* on the 12th of May, 2014.
13. <http://chemandy.com/technical-articles/stub-filter/how-does-a-stub-filter-work.htm>
14. Hung-Yuet Yee; Kuang Wu, Printed Circuit Transmission-Line Characteristic Impedance by Transverse Modal Analysis, *Microwave Theory and Techniques, IEEE Transactions on* , vol.34, no.11, pp.1157,1163, Nov 1986: doi: 10.1109/TMTT.1986.1133513
15. Hung-Yuet Yee, Transverse Modal Analysis of Printed Circuit Transmission Lines, *Microwave Theory and Techniques, IEEE Transactions on* , vol.33, no.9, pp.808,816, Sep 1985 doi: 10.1109/TMTT.1985.1133128
16. <http://pdfserv.maximintegrated.com/en/an/AN2093.pdf>
17. N. Hoog and M.J.J. Mayer: Method and device for measuring dielectric properties of a fluid through an array of cavities in a stack of printed circuit boards: Ref. No: NL1039729, Year: 01/2014.
18. N. Hoog and M.J.J. Mayer: Method and device for measuring dielectric properties of individual fluid samples present in an array of cavities in a stack of printed circuit boards: Ref. No: NL1039730, Year: 01/2014.
19. N. Hoog and M.J.J. Mayer: Method and device for measuring dielectric properties of a fluidum using dipole antenna and/or wave guide cavity technology: Ref. No: NL1039731, Year: 01/2014.
20. N. Hoog and M.J.J. Mayer: Method and device for measuring dielectric properties of a fluid and suppressing wave reflections: Ref. No: NL1039732, Year: 01/2014.
21. R. E. Collin, *Foundations for Microwave Engineering*, Wiley IEEE, pp.156-157, 2000.
22. E. J. Sterba and C. B. Feldman, "Transmission Lines for Short-Wave Radio Systems", *Bell Telephone Laboratories, New York City Proceedings of the Institute of Radio Engineers*, Volume 20, Number 7 July, 1932, 175
23. Tech-Brief No. "831 Note Application – Temperature Coefficients of Dielectric Resonators", *Trans-Tech Proprietary Information* • Products and Product Information are Subject to Change without Notice. • March 9, 2007, http://www.trans-techinc.com/products_detail.asp?ID=11&Name=Dielectric-Resonators.

24. Ch. Kittel, Introduction to Solid State Physics, 7th Ed., John Wiley & Sons, 1996.
25. D. H. Gadani, V. A. Rana, S. P. Bhatnagar, A. N. Prajapati⁴ and A. D. Vyas Effect of salinity on the dielectric properties of water, Indian Journal of Pure&Applied Physics, Vol. 50, June 2012, pp.405-410.
26. L. A. Klein, C. T. Swift, IEEE Transactions on Antennas Propagation, AP-25/1 (1977), 104
27. A. Stogryn, IEEE Trans on Microwave Theory and Techniques, (1971) 733.

Drinking water, surface water and waste water may contain toxic or otherwise undesired components at a wide range of concentration levels. In order to safeguard water quality, the early detection of pollutants and control of process conditions by continuous monitoring is mandatory. However, currently existing (bio) chemical detection methods are offline and by implication labor-intensive and thus expensive. This conclusion drives the search to develop a new class of inline sensors for the cost-effective monitoring of water quality. The focus of this PhD study was to explore the use of antenna or transmission-line-based technology to measure water quality in terms of its composition. In addition, several other applications of this technology has been investigated, ranging from biofilm and corrosion development to measuring the load of ion exchange columns.

Chapter 2 demonstrates that coaxial stub resonators can be used to assess the dielectric properties of fluids. This technology, essentially radio-frequency spectroscopy, comprises quarter wave length open-ended resonators, filled with a liquid sample that serves as dielectric between inner and outer conductor. Changes in the dielectric properties of the liquid sample result in changes of the electric properties of the resonator, e.g., its resonance frequency and quality factor. Results obtained with either a batch or flow through-type resonator indicate that the concept can be further developed into a cost-efficient and low-maintenance sensor for the on-line fingerprinting of the dielectric properties of fluids, such as drinking or waste water, ethanol and glycerol.

Chapter 3 elaborates on a theoretical description of the AF response of stub resonators. The resonance frequency, derived from the AF response, is defined predominantly by the permittivity of the fluid while damping arises from dielectric losses. Even though this methodology has been extensively reported in the literature, without almost any exception these studies refer to (near) ideal behavior regarding for example, geometry and negligibly low conductivity of the fluid studied. Online stub resonator-based sensors (i.e., flow-through) in use for industrial applications, however, quite often suffer from high dielectric losses, non-ideal material choice of the conductors from an electrical point of view and unconventional resonator geometry. Therefore, in order to ensure correct data interpretation, a straightforward model accounting for the effects of dielectric losses, conductor losses (skin effect) and impedance mismatches on the AF response is highly desirable. In addition, such a model can help to optimize future sensor designs. Here, we present a lumped parameter model, essentially based on telegrapher's equations, that accounts for the skin effect, dielectric losses and impedance mismatches between the transmission lines to the resonator and in the resonator itself. The adequacy of the method, even in the case of impedance mismatch, is demonstrated by comparing these model simulations with experimentally obtained AF curves.

Chapter 4 demonstrates the proof-of-principle to use stub resonators for evaluating bulk solvent properties of water-ethanol mixtures. Experimental results are in close agreement with theoretical models predicting the dielectric properties of binary mixtures. However, the potential applicability of the technique reaches further than assessing the dielectric properties of binary water – ethanol mixtures. Indeed, the method introduced

here might be a useful tool in the field of food industry, organic chemistry, biochemistry and microbiology for on-line monitoring the content of ethanol.

Chapter 5 introduces an entirely different application of stub resonators, i.e., to assess effects due to corrosion of metal surfaces. The method can be applied to all situations where metals are exposed to a corrosive (fluidic) environment, including, for instance, the interior of pipes and tubes. In the absence of corrosion, inner and outer conductors of the resonator are separated by a single dielectric, i.e., a fluid. Oxidation of the metal surface of inner and/or outer conductor changes the properties of the dielectric between inner and outer conductor because it introduces a dielectric permittivity that differs from that of the fluid. The two types of transmission line designs explored are coaxial and coplanar stripline (CPS). Irrespective the design, the method outlined here offers an equipment-undemanding, low maintenance and cost-efficient in-line early warning system to detect (the onset of) corrosion. As for its geometry, the additional advantage of the system is its freedom of design, from coax to one embedded in printed circuit boards.

Chapter 6 explores the possibility to use coaxial stub resonators for the detection of (early stages of) biofilm formation. The sensitivity of the system was improved by using a relatively short resonator (higher frequencies, better measurement of dispersion) and applying glass beads embedded in feed solution as dielectric between inner and outer conductors. The rationale of the glass beads is providing a larger surface area for biofilm formation. Analysis of the biofilm and the resonator signal as functions of time indicates that the sensor can be used to detect early stages of biofilm formation. It was observed that the sensor signal discriminates between biofilm formation (spots of bacterial growth on the glass beads) and the presence of a nearly homogeneous biofilm.

Chapter 7 discusses yet another application of stub resonators, i.e., to monitor the loading of ion exchange resins, used for, for instance, the reduction of natural organic matter (NOM) from drinking water. Fouling of anion-exchange resins (e.g. Purolite® A860S) by adsorption of (colored) organic substances in present surface water (e.g. humic acid) affects both the real and imaginary part of the complex dielectric permittivity of the system. As a result, the AF plot shows a shift of the resonance frequency and/or a change of shape of the resonance peak(s).

Chapter 8 provides conclusions and recommendations for further research.

Drink-, oppervlakte en afval water kunnen veel ongewenste chemische stoffen bevatten die bovendien kunnen voorkomen in heel verschillende concentraties. Waarborging van de veiligheid van de waterkwaliteit vereist daarom permanente monitoring en bovenal een vroege detectie van verontreinigingen. Huidige (bio)chemische analyse- en meettechnieken zijn echter veelal off-line en om die reden arbeidsintensief en dus kostbaar. Dit laatste aspect is een belangrijke (economische) drijfveer om een nieuw type sensoren te ontwikkelen die niet alleen kostenbesparend zijn maar bovendien de waterkwaliteit continue kunnen bewaken. Mijn PhD onderzoek was er op gericht om te kijken of een sensor gebaseerd op antenne (of transmissielijn) technologie kan worden gebruikt om water kwaliteit, in termen van samenstelling, te bepalen. In aanvulling hierop werden ook andere mogelijke toepassingen onderzocht, variërend van een sensor om biofilm- en corrosie (roest)vorming te detecteren tot een sensor om de verzadigingsgraad (load) van ionenwisselaars, zoals veel gebruikt binnen de watertechnologie, te meten.

Hoofdstuk 2 laat zien dat zogeheten coaxiale stub resonatoren kunnen worden gebruikt om de dielectrische eigenschappen van vloeistoffen te bepalen. Deze technologie, feitelijk een variant van radio-frequentie spectroscopie, berust op de toepassing van een kwart-golflengte open resonator, met de te onderzoeken vloeistof als dielectricum tussen de binnen en buiten geleider. Veranderingen in de dielectrische eigenschappen van de vloeistof vertalen zich in een verandering in de elektrische eigenschappen van de resonator, bv de resonantiefrequentie en Q- of quality factor. Resultaten verkregen hetzij met een batch-, hetzij met een doorstroom uitvoering van de sensor, laten zien dat dit concept verder kan worden ontwikkeld en kan leiden tot een sensor om on-line de dielectrische eigenschappen van vloeistof te meten. De sensor is niet alleen naar verhouding goedkoop in aanschaf maar stelt tevens lage eisen aan onderhoud zodat ook de operationele kosten laag zijn.

Hoofdstuk 3 behandelt een theoretische beschrijving van de amplitude – frequentie of AF response van stub resonatoren. De resonantie frequentie, zoals afgeleid van de gemeten AF response, wordt hoofdzakelijk bepaald door de permittiviteit van de vloeistof terwijl dielectrische verliezen demping van het signaal veroorzaken. Hoewel deze technologie al uitgebreid in de literatuur is beschreven, bijna zonder een enkele uitzondering is daarbij altijd uitgegaan van een ideale geometrie en een resonator die ideaal gedrag vertoont doordat bv gekozen is voor vloeistoffen met een te verwaarlozen geleiding. In de praktijk komt dit zelden voor en hebben on-line resonatoren voor industriële toepassingen te lijden van hoge dielectrische verliezen in de vloeistof en, gezien vanuit electrisch perspectief, bv een niet-ideale geometrie en materiaalkeuze wat betreft de geleiders. Dit alles betekent dat een juiste interpretatie van de data gegenereerd door dit type resonatoren sterk afhangt van een model die al deze niet-ideale eigenschappen en gedrag (dielectrische verliezen, skin effect en impedantie mismatch) meeneemt in haar theoretische beschrijving. Een dergelijk model kan tevens helpen om het ontwerp van toekomstige resonatoren te verbeteren. Het model dat hier wordt gepresenteerd is een zogeheten lumped parameter model dat gebaseerd is op de telegrapher's equations en dat bovengenoemd niet-ideaal gedrag

meeneemt in de beschrijving. Een vergelijk met experimentele data laat zien dat dit model, zelfs in het geval van impedantie mismatch, de AF response van resonatoren redelijk goed beschrijft.

In **Hoofdstuk 4** worden stub resonatoren gebruikt om de bulk eigenschappen van water-ethanol mengsels te bepalen. De experimentele data vertoont goede overeenkomst met de theoretische modellen voor dit soort binaire mengsels. De mogelijke toepassingen van deze technologie reiken echter veel verder dan metingen aan water – ethanol mengsels. Voor deze sensor zien we toepassing in de voedselindustrie, de organische en biochemie en bv de microbiologie om on-line het ethanolgehalte te kunnen meten.

Hoofdstuk 5 introduceert een geheel andere toepassing van stub resonatoren, het detecteren van vroege stadia van corrosievorming op metaaloppervlakken. De methode kan worden toegepast in alle situaties waarbij metalen worden blootgesteld aan corroderende (vloeistof) condities, ook indien dit proces plaats vindt in het binnenste van pijpen en buizen. In de afwezigheid van corrosie zijn beide geleiders van de resonator gescheiden door een enkel dielectricum, de vloeistof. Oxidatie van het metaaloppervlak van binnen en/of buitengeleider verandert de eigenschap van het dielectricum omdat het een dielectrische permittiviteit toevoegt aan het systeem die verschilt van die van de vloeistof. Twee verschillende resonator ontwerpen zijn onderzocht, de coax uitvoering en de stripline. Ongeacht het ontwerp, de methode hier beschreven biedt een eenvoudige en goedkope manier om vroege stadia van corrosie te detecteren.

Hoofdstuk 6 onderzoekt een andere toepassing op het gebied van oppervlaktemodificatie, waarneming van vroege stadia van biofouling. De gevoeligheid van het systeem was verhoogd door gebruikt te maken van een relatief korte resonator (hogere frequenties en bijgevolg een nauwkeuriger meting van dispersie) en door toepassing van glas korrels in de ruimte tussen beide geleiders. Deze laatste aanpassing leidt tot een enorme toename van oppervlak waarop de vorming van een biofilm kan plaats vinden. Analyse van zowel de biofilm als de AF response van de resonator laat zien dat deze uitvoering van de sensor inderdaad geschikt is om biofouling in een vroeg stadium waar te nemen. De resultaten laten tevens zien dat de sensor onderscheid maakt tussen afzonderlijke spots van bacteriegroei, in een vroeg stadium, en de aanwezigheid van een bijna homogene biofilm in een later stadium.

Hoofdstuk 7 beargumenteert wederom een andere toepassing van stub resonatoren, bepaling van de verzadigingsgraad van ionenwisselaars, bv die welke worden gebruikt binnen de watersector voor de reductie van organisch materiaal (NOM) dat van nature in oppervlaktewater voorkomt. Vervuiling van anionenwisselaars (bv Purolite® A860S) door adsorptie van organisch materiaal aanwezig in het oppervlaktewater, bv humus zuren, heeft een effect op zowel het gemeten reële deel van de complexe dielectrische permittiviteit als op het imaginaire gedeelte. Het gevolg is dat de waargenomen AF-response verschuift naar een andere resonantiefrequentie en dat de vorm van de resonantiecures verandert.

Hoofdstuk 8 tenslotte bevat de eindconclusies alsmede aanwijzingen voor vervolg onderzoek.

Journal Publications

- N. A. Hoog-Antonyuk, W. Olthuis, M. J. J. Mayer, D. Yntema, H. Miedema, Berg van den A: *On-line fingerprinting of fluids using coaxial stub resonator technology*, Sensors and Actuators B: Chemical, Volume 163, Issue 1, 1 March 2012, Pages 90-96.
- N.A. Hoog-Antonyuk, W. Olthuis, M.J.J. Mayer, H. Miedema, F.B.J. Leferink, A. van den Berg: *Extensive Modeling of a Coaxial Stub Resonator for Online Fingerprinting of Fluids*, Procedia Engineering, Volume 47, 2012, Pages 310-313.
- N.A. Hoog-Antonyuk, M.J.J. Mayer, H. Miedema, W. Olthuis, F.B.J. Leferink, A. van den Berg: *Coaxial Stub Resonator for Online Monitoring Early Stages of Corrosion*, Key Engineering Materials Vol. 605 (2014) pp. 111-114.
- N.A. Hoog, M.J.J. Mayer, H. Miedema, W. Olthuis, F.B.J. Leferink, A. van den Berg: *Modeling and Simulations of the Amplitude-Frequency Response of Transmission Line Type Resonators Filled with Lossy Dielectric Fluids*, Sensors and Actuators A: Physical, Volume 216, 1 September 2014, Pages 147-157.
- N.A. Hoog, M.J.J. Mayer, H. Miedema, R. M. Wagterveld, J. Tuinstra, M. Saakes, W. Olthuis, A. van den Berg, *Stub Resonators for Online Monitoring Early Stages of Corrosion*, Sensors and Actuators B: Chemical, Volume 202, 31 October 2014, Pages 1117-1136
- N.A. Hoog, H. Miedema, M.J.J. Mayer, W. Olthuis, S.G. Kataev, A. van den Berg, *On-line Method for Assessing the Ethanol Content of Solutions Using Coaxial Stub Resonator Technology*, (2014) submitted manuscript.
- N.A. Hoog, M.J.J. Mayer, H. Miedema, W. Olthuis, A. A. Tomaszewska, A. H. Paulitsch-Fuchs, A. van den Berg, *Online Monitoring of Biofouling Using Coaxial Stub Resonator Technique*, (2014) submitted manuscript (invited paper).
- N. A. Hoog, M. J. J. Mayer, H. Miedema, S. M. Bakker, W. Olthuis, T. Hubert, A. van den Berg, *A Coaxial Stub Resonator-Based Sensor for the On-line Monitoring of the Loading of Ion Exchange Resins*, (2014) submitted manuscript.

Patents

- N. Hoog and M.J.J. Mayer: *Method and device for measuring dielectric properties of a fluid through an array of cavities in a stack of printed circuit boards*: Ref. No: NL1039729, Year: 01/2014.
- N. Hoog and M.J.J. Mayer: *Method and device for measuring dielectric properties of individual fluid samples present in an array of cavities in a stack of printed circuit boards*: Ref. No: NL1039730, Year: 01/2014.
- N. Hoog and M.J.J. Mayer: *Method and device for measuring dielectric properties of a fluidum using dipole antenna and/or wave guide cavity technology*: Ref. No: NL1039731, Year: 01/2014.
- N. Hoog and M.J.J. Mayer: *Method and device for measuring dielectric properties of a fluid and suppressing wave reflections*: Ref. No: NL1039732, Year: 01/2014.
- N. A. Hoog M.J.J. Mayer: *Werkwijze en inrichting voor fingerprinting of het behandelen van een dielectricum in het algemeen en van water in het bijzonder*. Ref. No: NL1038869, Year: 08/2012.
- M.J.J. Mayer, N. A. Hoog: *RF antenna filter as a sensor for measuring a fluid*. Ref. No: WO2011005084, Year: 01/2011

Conference Proceedings

- N. Hoog, M. J.J. Mayer, H. Miedema, W. Olthuis, Albert van den Berg, *Coaxial Stub Resonator for Online Monitoring Early Stages of Corrosion*, The 3rd International Conference on Materials and Applications for Sensors and Transducers, IC-MAST, 09/2013.
- N. Hoog-Antonyuk, *On-line fingerprinting of fluids for quality control using coaxial stub resonator technology*, The RME Conference Series - Bastiaanse Communication, 22 January, 2013.
- V.V. Zagoskin, A.S. Shostak, B.I. Avdochenko, L.P. Ligthart, A.G. Yarovoy, V.N. Iljushenko, A.P. Batsula, N.A. Antonyuk, I.S. Kruglov: *Experimental investigation of profile distribution of complex dielectric permittivity of soils*. Ground Penetrating Radar, 2004. GPR 2004. Proceedings of the Tenth International Conference on; 02/2004
- N.A. Antonyuk, I.S. Kruglov, L.P. Ligthart, V.V. Zagoskin, A.S. Shostak, V.N. Iljushenko: *Measurement of the complex dielectric permittivity of stratified media with dipole antenna sensors*. Radar Conference, 2004. EURAD. First European; 02/2004
- N.A. Antonyuk, I.S. Kruglov, V.V. Zagoskin, L.P. Ligthart, A.S. Shostak, V.N. Iljushenko, B.I. Avdochenko: *Measurement of the complex dielectric permittivity of homogeneous media with dipole antenna sensors*. Radar Conference, 2004. EURAD. First European; 02/2004
- V.V. Zagoskin, A.S. Shostak, B.I. Avdochenko, L.P. Ligthart, V.N. Iljushenko, A.P. Batsula, N.A. Antonyuk, I.S. Kruglov: *Dipole antenna sensors for measurement of complex dielectric permittivity of soils and their application under field conditions*. Ground Penetrating Radar, 2004. GPR 2004. Proceedings of the Tenth International Conference on; 02/2004.

International Scientific Reports

- V. N Iljushenko, V V. Zagoskin, L. P. Ligthart, B.I. Avdochenko N.A Antonyuk, I.S. Kruglov and others, Project IS 030126. *Proof of Principle on the use of Dipole Antenna Measurements Techniques for Experimental Determination of Soil Characteristics and the Development of a Statistical Electrophysical Model of Soils*, Report IS 030126-3, Tomsk State University of Control Systems and Radioelectronics, Delft University of Technology, Tomsk-Delft, 2003.
- V. N Iljushenko, V V. Zagoskin, L. P. Ligthart, B.I. Avdochenko N.A Antonyuk, I.S. Kruglov and others, Project IS 030126. *Proof of Principle on the use of Dipole Antenna Measurements Techniques for Experimental Determination of Soil Characteristics and the Development of a Statistical Electrophysical Model of Soils*, Report IS 030126-2, Tomsk State University of Control Systems and Radioelectronics, Delft University of Technology, Tomsk-Delft, 2003.
- V. N Iljushenko, V V. Zagoskin, L. P. Ligthart, B.I. Avdochenko, N.A Antonyuk, I.S. Kruglov and others, Project IS 030126. *Proof of Principle on the use of Dipole Antenna Measurements Techniques for Experimental Determination of Soil Characteristics and the Development of a Statistical Electrophysical Model of Soils*, Report IS 030126-1, Tomsk State University of Control Systems and Radioelectronics, Delft University of Technology, Tomsk-Delft, 2003.
- V. N. Iljushenko, V. V. Zagoskin, L. P. Ligthart, A.S. Shostak, B.I. Avdochenko, N.A Antonyuk, I.S. Kruglov and others, *The Experimental Investigations of Electrodinavic Characteristics of Soils in an Ultrawide Band Frequency Range (50 MHz - 6 GHz) and the development of a statistical elektrophysical model of Siols*, Report-TD-006-02, International Research Centre for Telecommunication-Transmission and Radar, Delft University of Technology, Department of Electrical Engineering, The Netherlands, 2002.

My story as being PhD student has come to the logical end. I must say, it was an awesome event of that length in more than 5 years. It is time now to express my utmost gratitude to all people who made me the person I am today.

My endless thanks to Dr. Ir. **Mateo** (M.J.J.) **Mayer** who patiently withstood my zero-level English, my emotional outbursts in frustration, and my enthusiasm over the edge. Mateo, You always had a patient and time for our uncountable discussions about science and life. Although, You could all of a sudden disagree with Yourself from scientific point of view, You supported all my weekends activities as well. I had a great freedom in choosing my research direction, to plan and execute my ideas. Thank You for Your believe in me. I want to extend the warmest words of thanks (heel erg hartelijk bedankt) to Your beautiful family: **Mia**, **Lise**, and **Maartje**.

My sincere gratitude and appreciation goes to Dr. **Henk Miedema** who has played a key role in this research project by constantly reading and editing the parts of writing. Henk, You amazingly, could solved all my social dilemmas in a very tactful and diplomatic way of communicating during all these years. I cannot thank You enough for Your bright suggestion, teaching me a lot, and the daily talks about everything.

I would also like to extend a special thanks to Dr. Ir. **Wouter Olthuis** for his critical knowledge, inspiration, dedication, and patience. Wouter, You decorated an every part of my research project with Your advises and ideas.

I would like to thank Prof. Dr. Ir. **Albert van den Berg** for his acceptance me into the BIOS group. It was unforgettable the Workweek BIOS in French Alps. I admire Your incredible contributions to the world of science.

I am indebted and eternally grateful to scientific Director Prof. Dr. Ir. **Cees** (C.J.N.) **Buisman** and managing director Mr. **Johannes Boonstra** for the opportunity of my life to do my PhD research at **WETSUS**, centre of excellence for sustainable water technology.

Sincere thanks to Dr. Ir. **Maarten** (P.M.) **Biesheuvel** who convinced me to start working at WETSUS.

I would like to deeply thank Dr. Ir. **Bert** (H.V.M.) **Hamelers** and Prof. Dr. **Gert-Jan** (G.J.W) **Euverink** for the scientific advices and support.

I would like also to thank Mr. **Gerrit Oudakker**, who always had some kind words for me.

My very warm thanks to my first roommates Ir. **Heleen** Sombekke and **Hester** Henstra who was an example for me to follow as being a Woman

I would like to express my appreciation to Dr. Ir. **Martijn** (R.M.) Wagterveld and Dr. Ir. **Doekle** Yntema, for their important contribution to my research project and who answered on my thousands questions.

My sincere thanks to my “communist comrades” Zhao **Ran** and Liu **Fei**. We have been at the same office for over 4 years, therefore, we know about each other a lot, including our strengths and weaknesses.

This project could not have been carried out without the substantial help and guidance from technical and analytical staff at WETSUS: **Wim** Borgonje, **Harrie** Bos, **Janneke** Tempel, **Ernst** Pandstra, **Foppe** Westra, **Rienk** Smit, **Mieke** Kersaan-Haan, and **Ton** van der Zande. Your patience, tolerance and understanding are immeasurable. I know that I was in our laboratory like a bull in a china shop.

Besides, I would especially like to thank **Harm** van der Kooi for his efforts in building and maintaining the first coaxial sensor by using hundreds of meters of aluminium foil for wrapping; **Jelmer** Dijkstra for an umpteen number of beautiful SEM images and the nice story about horses; **Marianne** Heegstra for analyzing my innumerable amount of TOC samples and the awesome experience of mud walking (wadlopen); **Jan** Tuinstra for improving the stability and aesthetic look of the coaxial sensor; **Agnieszka** Tomaszewska who was dare enough to teach me microbiology.

Then I would like to thank human resource manager **Nynke** Broekens but also the great team of secretaries at WETSUS, especially, **Helena** van der Werff, **Linda** van der Ploeg, **Geke** Wijma, and **Trienke** and de Vries, for their excellent communication and organizational skills.

Thanks a lot to co-authors participated in the work represented by my publications, and who was not yet mentioned: Dr. Ir. **Michel Saakes**, Ir. **Simon** (S.M.) **Bakker**, Dr. Dipl.-Ing. **Astrid** (A.H.) **Paulitsch-Fuchs**, and Prof. Dr. Ir. **Sergey** (S.G.) **Kataev**.

I am grateful to Dipl.-Ing. **Martina** Sammer, Dr. **Lucia** Hernandez Leal, Dr. **Johannes** Kuipers, M.Sc. **Florian** Beyer, Dr. Ir. **Tom** Sleutels, M.Sc. **Lieven** De Temmerman, Dr. **David** Vermaas, Dr. **Elsemiek** Croese, Dr. **Sanne** van den Hengel, and Dr. **Yvette** Lubbersen, M.Sc. **Prashanth** Kumar, Dr. **Marco** de Graaff, Dr. **Agata** Brzozowska, Dr. **Justina** Racyte, Dr. **Sławomir** Porada, M.Sc. **Zlatica** Novotná, M.Sc. **Oane** Galama, Dr. **Paula** van den Brink and Dr. **Arie** Zwijnenburg for the technical and personal help but also for the friendly talks.

I want to thank also Dr. **Enver** Güler for guiding me in preparation of the layout of my thesis.

My gratitude also goes to all my colleagues at **BIOS group** for the all “gezellig tijden” and fruitful discussions during the BIOS presentations. I want thank to **Hermine Knol** for the countless times that You helped me.

I would also like to extend my thanks to my great students **Thomas** Hubert and **Tereza** Rusková who not only have helped me a lot within the project, but also have taught me being a teacher.

I gratefully acknowledge all the members of my committee, Prof. Dr. Ir. J.H.A. **de Smit**, Prof. Dr. Ir. P.M.G. **Apers**, Prof. Dr. Ir. A. **van den Berg**, Dr. Ir. W. **Olthuis**, Dr. H. **Miedema**, Prof. Dr. H. **Morgan**, Prof. Dr. Ir. P.J. **French**, Prof. Dr. Ir. F.B.J. **Leferink**, Prof. Dr. Ir. F.E. **van Vliet**, and Dr. Ir. M.J.J. **Mayer**, who have given their time to read this thesis. Sincere appreciation is also extended to Prof. Dr. Ir. F. **Leferink** and Prof. Dr. Ir. F.E. **van Vliet** who have also offered valuable advices to complete this thesis.

I would like to thank all members of the **Sensing theme at WETSUS** and, in the first place, **Maurice** Tax who believes in everyone of his theme. And, of course, thousand thanks for sensinging PhD’s: **Martijn** Wagterveld, **Petra** van Daltsen, **Nienke** Stein, **Thijs** van Leest, **Jeroen** Heldens, **Judith** Staginuis, **Marjolein** Woutersen, **Gerwin** Steen and **Jorick** van 't Oever, who always provided useful feedback when I had to give presentations.

I owe my sincere gratitude to family van Daltsen (**Jos** and **Petra**) for the warmest feelings they bring around and nice dinners together.

Lastly, I would like to thank my paranimfs, **Jan** Tuinstra and **Agnieszka** Tomaszewska, who supported me in organizing and coordinating not only in the final steps of my PhD event. Your huge help, knowledge, and nice talks lighted up many of my days in our laboratory.

My tender thanks to all hard workers around me for the *innovation, partnership, cooperation, reliability, and joy*.

My most heartfelt thanks go to my the Prof. Dr. Ir. **Vladimir Nikolaevich Iljushenko**, Dr. Ir. **Vladimir Viktorovich Zagoskin**, Dr. Ir. **Boris Ivanovich Avdochenko**, Prof. Dr. Ir. **Arkadii Stepanovich Shostak**, Dr. Ir. **Aleksandr Panteleevich Batsula**, Prof. D.r Ir. **Sergei Grigorievich Kataev**, and Prof. Dr. Ir. **Leo (L.P) Lighthart** who introduced me the fascinating world of dielectric antennas.

I would also like to thank my childhood friend **Assem** Tyishkombaeva (Sekochka), my nanny **Natalia** Belyaeva (Natalechka), my soul mate **Yulia** Lavrenova (Yulechka) who supported my crazy ideas, and incited me to strive towards my goal.

I am so grateful to my **Family** for their unconditional love and support.

Дорогая моя **Ольга Васильевна**, спасибо Вам и **Владимиру Александровичу**, за то, что всегда мне были рады в Вашем доме, за Вашу поддержку.

Самые теплые слова благодарности моей тетушке **Вере Михайловне**, за ее доброту и заботу.

Спасибо огромное **Валентину Николаевичу** и **Алене Владимировне**, за Ваше бесконечное добро, за нашу классную поездку в Гент, за совместные у Вас и у нас прогулки и кофе (чае) питья. **Валентин Николаевич**, без Вашей помощи книга не выглядела бы такой красивой и полноценной, еще раз тысячу раз спасибо. (I would like to extend my special thanks to **Valentin N. Dolgov** for helping me with the book cover design).

Мишанечка, мой любимый братик, ты всегда был рядом, когда мне это было так необходимо, а за спасение от кота, отдельные благодарности 😊. Спасибо также и Твоей семье: **Бэле** и **Таиси**. Совместная поездка в Париж, одно из самых ярких и теплых моих воспоминаний.

Самые дорогие и любимые **Бабушка** и **Дедушка**, спасибо Вам, мои замечательные за все. Вы только не болейте, балуйте меня тем, что вы у меня есть.

Мои **Мамочка** и **Папочка**, а дороже Вас у меня никого нет и не будет. Вы всегда верили в меня, для Вас я всегда самая лучшая. Спасибо Вам, за то, что меня любите такой какая я есть, за все счастье в моей жизни.

My final but very special thanks go to my beloved **Husband Richard** for his listening to me these years about my research, willing help in everything, and taking care of me. Thank You my wonderful Husband, my **Richardik**, for Your loving patience with me. You promised to my Farther that that one day I will have the degree of doctor and You kept Your words...



Natalia Hoog (Antonyuk) was born on 25th of January 1980 in Shevchenko, Kazakhstan (USSR). She studied and received her Engineer Diploma within specialization “Organization and Technology of Information Security”, at Tomsk State University of Control Systems and Radioelectronics (TSUCSR), Russia in 2002. After she worked as an engineer and an assistant in the Department of Radioelectronics and Data Protection, (TSUCSR), at the same time, she was a member of international project The Netherlands (TU Delft)-Russian (TSUCSR) with research activities in the area of advanced Ground-Penetrating Radar (GPR) technology. At present time, she is PhD in the Laboratory of Biosensors, the Lab-on-a-Chip group, part of the MESA+ Research Institute, of the University of Twente and a researcher at Wetsus center of excellence for sustainable water technology, the Netherlands. In 2013 her research was awarded the Marcel Mulder prize.

This work was performed in the TTIW-cooperation framework of Wetsus, Centre of Excellence for Sustainable Water Technology (www.wetusus.nl). Wetusus is funded by the Dutch Ministry of Economic Affairs, the European Union Regional Development Fund, the Province of Fryslân, the City of Leeuwarden and the EZ/Kompas program of the “Samenwerkingsverband Noord-Nederland”. The authors thank the participants of the research theme Sensoring for the fruitful discussions and their financial support.

The image for the cover of the chapter 7 was made by Yulia Lavrenova

